Ce:$LiLuF_4$ Lasers

Kristie Shureen Johnson
Wolfson College, University of Oxford

Thesis submitted for the degree of Doctor of Philosophy in the Faculty of Physical Sciences, Hilary Term 2003.

Funded by The Beit Trust 09.1999-09.2002.



RADCLIFFE SCIENCE LIBRARY OXFORD
21 AUG 2003

Ce:$LiLuF_4$ Lasers

Kristie Shureen Johnson

Wolfson College, University of Oxford

Thesis submitted for the degree of Doctor of Philosophy in the Faculty of Physical Sciences, Hilary Term 2003.

The research in this project was directed, firstly towards gaining an understanding of the effect excited-state absorption (ESA) has on gain and lasing in broadly tunable Ce:LiLuF lasers and secondly towards the development of Ce:LiLuF lasers suitable for spectroscopic applications.

Detailed measurements of the single-pass, small-signal gain in Ce:LiLuF were undertaken, with a gain coefficient as high as 30±1 cm^{-1} at 309 nm, with an absorbed pump fluence of 0.46 Jcm^{-2}. Further, the ESA in Ce:LiLuF at 261 nm and 349 nm was measured. Using both the gain and ESA results in a computer model, the effective gain cross-sections at 309 nm and 327 nm and the ESA cross-sections at 261 nm, 309 nm, 327 nm and 349 nm were determined. The ESA cross-sections were found to be of the order of 10^{-18} cm^2. The effective gain cross-section in Ce:LiLuF was found to increase with decreasing temperature. This was proposed to arise from a decrease in the ESA cross-section with decreasing temperature in the Ce:LiLuF.

An in-depth parametric study of Ce:LiLuF laser operation and tunability was undertaken. The results of these studies, together with computer modelling, enabled the importance of ESA and other effects on lasing to be established. In particular, the gain competition effects and ESA were found to lead to inefficient laser operation unless σ-polarised lasing was suppressed. With polarisation selection, efficient operation was obtained, with continuous tunability between 305 nm - 335 nm.

Narrow bandwidth operation of Ce:LiLuF for use in OH radical detection in the atmosphere was investigated. Narrow bandwidth operation was achieved for the first time in Ce:LiLuF using a Littrow grating with a telescopic and prism beam expansion system. Tunable lasing between 306.5 nm and 311.5 nm was obtained, with a spectral bandwidth of 0.7 cm^{-1}.

Finally, highly efficient Ce:LiLuF lasing was achieved with a new all-solid-state, 289 nm frequency-quadrupled Raman-shifted Nd:YAG laser. Slope efficiencies as high as 62±3% were achieved. This slope is believed to be the highest obtained in any cerium laser to date. The IR-to-UV conversion efficiency was 0.41% and the UV-to-UV conversion efficiency was 41%. These high efficiencies were attributed to high pump beam quality and good mode matching.

Do not follow where the path leads.
Rather go where there is no path and leave a trail.

Acknowledgements

- DC, thank you for supervising me through thick and thin, as well as putting up with my rowing and anti-rowing phases. Thanks for your patience with the Grinch and with me, we were a demanding team.

- The Beit Trust, thank you for giving me the chance to study not only in the UK but in Oxford. You gave me this once in a lifetime chance and I hope one day you'll feel what I have achieved was worth your while.

- Graham, as with David, thanks for loving CVL's so much that you were patient enough to help fix Grinch week in and week out with never a foul word to the defenceless laser.

- Colin and Simon, thanks for all the help on basic laser theory, which I was always lacking in.

- Macquarie CLA people, particularly Mick, Helen, Pete, Rich, Jenn and Bron. You helped make my work in Sydney successful (see Chapter 5) and my 3 months there great fun.

- My David, thanks for being my true support through my captaincy in the boat club and my writing up. You've seen me at my worst, it's all good from here on in I promise.

- Helen and Sarah, I'm so glad you were also writing up when I was, as least I had someone to gauge my insanity against. What a scary combination of doctors we make!!!

- Mr B you get a special mention, one, because you are still writing and I wish you the best with it and two, because you always made me look good by getting in after me, but then again you make me look bad by leaving after me.

- Past teachers and lectures, yes I'm getting soppy, but in all honesty I wouldn't be here without your guidance and constant encouragement in particular the staff at Rhodes physics department. If you hadn't been such a great bunch I wouldn't have carried on in physics

- Miss Walker, Miss Wallace, Mrs Simpson, Sister Luguera and Sister Angela and the Convent in general for converting me, if not into a nun into a keen scientist.

- Going back a bit further since these are my acknowledgements and I'll write what I want to, thanks to Whitestone School in particular Mr Ramand for giving my first glimpse of enjoyment in maths and Mrs Judge at for seeing the potential and dragging at least some of it out.

- And of course last and probably most importantly, thanks to my dear family, scattered all over the world. You all did more than your fair share getting me here, whether it being your shoulder, your support, encouragement or your "gentle" nudging, I appreciate it all.

Table of Contents

[1] INTRODUCTION 1

1.1 SOLID-STATE TUNABLE ULTRA-VIOLET LASERS 1

1.1.1 GENERATION OF TUNABLE LASER EMISSION IN THE ULTRA-VIOLET 1

1.1.2 APPLICATIONS OF TUNABLE UV LASERS 3

1.2 CERIUM-DOPED LASER MATERIALS 4

1.2.1 GENERAL TRIVALENT CERIUM SPECTROSCOPY 4

1.2.2 CE:$Y_3AL_5O_{12}$ (CE:YAG) 9

1.2.3 CE:CAF_2 11

1.2.4 CE:$LIYF_4$ (CE:LIYF) 12

1.2.5 CE:LAF_3 15

1.2.6 CE:$LICAALF_6$ (CE:LICAF) AND CE:$LISRALF_6$ (CE:LISAF) 15

1.2.7 CE:$LILUF_4$ (CE:LILUF) 19

1.3 PUMP SOURCES FOR CERIUM LASERS 26

1.3.1 COPPER VAPOUR LASERS (CVLS) AS CERIUM LASER PUMP SOURCES 28

1.3.2 FREQUENCY-QUADRUPLED RAMAN-SHIFTED ND:YAG LASERS AS CERIUM LASER PUMP SOURCES 33

1.4 THESIS OUTLINE 35

[2] DETAILED SPECTROSCOPIC CHARACTERISATION OF CE^{3+}:$LILUF_4$ 38

2.1 EMISSION CROSS-SECTION MEASUREMENT AND CALCULATION 38

2.1.1 EXPERIMENTAL CONFIGURATION 39

2.1.2 RESULTS 39

2.2 ABSORPTION COEFFICIENT DETERMINATION AT 289 NM FOR π-POLARISED LIGHT... 40

2.2.1 EXPERIMENTAL CONFIGURATION 40

2.2.2 RESULTS 41

2.3 SMALL SIGNAL GAIN MEASUREMENTS FOR CE:LILUF 43

2.3.1 EXPERIMENTAL CONFIGURATION 43

2.3.2 RESULTS 47

2.4 EXCITED STATE ABSORPTION MEASUREMENTS FOR CE:LILUF AT 261 NM AND 349 NM..... 54

2.4.1 EXPERIMENTAL CONFIGURATION 55

2.4.2 RESULTS 56

2.5 SIMULATED SMALL-SIGNAL GAIN AND ESA CROSS-SECTION DETERMINATION. 60

2.5.1 PROGRAM DESCRIPTION 60

2.5.2 TRANSMISSION SIMULATION RESULTS 66

2.5.3 SMALL-SIGNAL GAIN SIMULATION RESULTS 68

2.6 DISCUSSION 75

2.6.1 ORIGIN OF ESA IN CE:LILUF 76

2.6.2 CREATION, DISSOCIATION AND RELAXATION OF COLOUR CENTRES AND THE ORIGIN OF THE TEMPERATURE DEPENDENCE OF ESA AND SMALL-SIGNAL GAIN IN CE:LILUF. 81

2.6.3 POLARISATION OF THE ESA CROSS-SECTIONS IN CE:LILUF 86

[3] LASING IN CE:LILUF$_4$ 91

3.1 INTRODUCTION 91

3.2 CE:LILUF LASING WITH NON-WAVELENGTH SPECIFIC OUTPUT COUPLERS..... 92

3.2.1 EXPERIMENTAL CONFIGURATION 92

3.2.2 RESULTS 1 - CAVITY DEPENDENCE OF CE:LILUF LASING..... 94

3.2.3 RESULTS 2 -TEMPERATURE DEPENDENCE OF 309 NM LASING IN CE:LILUF 100

3.3 LASING OF CE:LILUF WITH WAVELENGTH-DEPENDENT OUTPUT COUPLING REFLECTIVITIES. 102

3.3.1 EXPERIMENTAL CONFIGURATION 102

3.3.2 RESULTS 1: LASING IN CE:LILUF WITH THE M302 OUTPUT COUPLER (R=54% @ 309 NM AND R=92% @ 327 NM). 104

3.3.3 RESULTS 2: LASING IN CE:LILUF WITH THE M303 OUTPUT COUPLER (R=9% @309 NM AND R=70% @ 327 NM) 108

3.4 TUNABLE LASING IN CE:LILUF 114

3.4.1 EXPERIMENTAL CONFIGURATION 114

3.4.2 RESULTS OF PRISM-TUNED LASING IN CE:LILUF 115

3.5 SIMULATION OF LASING IN CE:LILUF 122

3.5.1 PROGRAM DESCRIPTION 123

3.5.2 MODELLING RESULTS 1 - SIMULATIONS OF LASING IN CE:LILUF WITH NON-WAVELENGTH SELECTIVE OUTPUT COUPLERS. 129

3.5.3 MODELLING RESULTS 2: SIMULATIONS OF LASING IN CE:LILUF WITH WAVELENGTH-SELECTIVE OUTPUT COUPLERS 135

3.5.4 MODELLED RESULTS 3: SIMULATIONS OF LASING IN A PRISM-TUNED CAVITY 140

3.6 DISCUSSION 144

3.6.1 DEPENDENCE OF CE:LILUF LASING CHARACTERISTICS ON THE LASER CAVITY USED. 145

3.6.2 TEMPERATURE DEPENDENCE OF THE LASER OUTPUT IN CE:LILUF 146

3.6.3 PRESENCE OF MULTIPLE POLARISATION AND WAVELENGTH COMPONENTS IN THE LASER OUTPUT OF CE:LILUF WITH M302, M303 AND PRISM-TUNED CAVITY 147

3.6.4 FLUCTUATIONS IN THE LASER OUTPUT IN THE PRESENCE OF σ-POLARISED 327 NM LASING. 155

3.6.5 CONCLUSIONS 157

[4] NARROW- BANDWIDTH LASING IN CE:LILUF$_4$ 158

4.1 INTRODUCTION 158

4.2 METHODS OF NARROWBAND TUNING 160

4.3 CAVITY 1- THREE-MIRROR, SMALL-MODE CAVITY 162

4.3.1 EXPERIMENTAL CONFIGURATION 162

4.3.2 UN-TUNED RESULTS USING CAVITY 1 166

4.3.3 RESULTS: NARROW BANDWIDTH ADAPTATIONS OF CAVITY 1. 170

4.4 CAVITY 2-TELESCOPE CAVITY 174

4.4.1 EXPERIMENTAL CONFIGURATION 174

4.4.2 RESULTS 177

4.5 DISCUSSION 188

[5] ALL-SOLID-STATE UV LASER BASED ON CE:LILUF$_4$ 191

5.1 INTRODUCTION 191

5.2 EXPERIMENTAL CONFIGURATION 191

5.3 RESULTS 192

5.4 DISCUSSION 195

[6] CONCLUSION 198

6.1 SUMMARY OF RESULTS 198

6.2 IMPLICATIONS OF RESULTS 202

6.3 FUTURE WORK 203

BIBLIOGRAPHY 207

APPENDIX 216

[1] Introduction

1.1 Solid-State Tunable Ultra-Violet Lasers

1.1.1 Generation of Tunable Laser Emission in the Ultra-Violet

Perhaps the most common laser used, until recently, for the generation of tunable ultra-violet (UV) laser light has been the frequency-doubled dye laser. Dye lasers have broadly tunable emission and very high gains and the large number of laser dyes available, used sequentially, gives access to most of the visible spectrum and some of the IR spectrum. Frequency doubling, tripling and sum-frequency mixing of tunable dye lasers are all easily achieved using BBO and LBO non-linear crystals. The dyes used in dye lasers however, have a limited lifetime and are toxic; as such these lasers are very wasteful and require frequent maintenance.

Another laser commonly used in the generation of tunable UV laser light is the frequency-doubled Ti:Sapphire laser. These lasers are tunable between ~700 nm-1.1 μm, which when doubled in LBO, give access to tunable laser emission between 350 nm and 550 nm with frequency-conversion efficiencies, over most of this range, of 30% (Skripko *et al.* 1991). Frequency-tripling and fourth-harmonic generation of Ti:Sapphire laser emission have also been achieved, giving tunable laser emission at wavelengths as low as 205 nm (Nebel and Beigang 1991). Other methods of tunable UV laser emission include using optical parametric oscillators and fibre Raman lasers (Ilev *et al.* 1997).

UV light, by definition, includes wavelengths lying between 185 nm and 400 nm, with VUV wavelengths lying between 105 nm and 185 nm. There are a number of problems encountered when developing solid-state optical materials to be used in the UV. Firstly, most solid-state materials have a short spectral transmittance. Fortunately, in recent years, optical materials

which are transparent in the UV have become more readily available. Problems start to arise when the laser wavelengths being used lie in the VUV, as most optical materials that can be used in the UV have a transmittance cut-off between 150 nm (fused silica) and 100 nm (LiF). Another limitation of optical materials used for lasing in the UV, is the relatively short lifetime of these materials resulting from degradation by the high energy UV photons (~7eV).

There are two main mechanisms used in the generation of tunable ultra-violet (UV) laser emission. The first is the use of the nonlinear optical properties of certain materials to convert the laser emission from existing tunable infra-red (IR) and visible lasers into tunable UV laser light. Nonlinear processes such as nonlinear harmonic generation (2^{nd}, 3^{rd}, 4^{th} and 5^{th}), sum-frequency mixing and nonlinear frequency upconversion are frequently used today. The nonlinear crystals presently available are of an excellent optical quality and can provide relatively high efficiency frequency conversion. Such crystals include BBO (β-BaB_2O_4), KTP ($KTiO_2PO_3$) and LBO (LiB_3O_5) and more recently developed crystals such as CLBO ($CsLiB_6O_{16}$). For harmonic generation one selects the non-linear crystal which fulfils the phase-matching criteria best, such as the acceptance angle, walk off angle, temperature and wavelength acceptance. One of the main disadvantages of some non-linear crystals is their large hygroscopy (water absorption) which requires the crystal to be in a controlled temperature environment to prevent damage to the crystal. (CLBO requires a high temperature (~150°C) environment to be maintained at all times in order for the crystal not to degrade as a result of the absorption of moisture.)

The second and possibly more efficient method of generating UV laser light is the use of rare-earth doped, wide band-gap fluoride laser crystals which lase directly in the UV. It is only in the last decade that such lasers have been shown to have efficiencies high enough to compete with the non-linear method of tunable UV generation. The turn-key reliability, high average output power and high repetition rates accessible from solid-state lasers as well as their relatively low maintenance, low cost and minimal toxicity make them advantageous over dye lasers.

Much research has been done on obtaining laser emission from rare-earth doped crystals, based on the high energy *5d→4f* transition. To date, broad-band UV lasing has only been achieved in Ce^{3+} doped crystals. (It was initially thought that lasing in Nd^{3+}:LaF_3 had been seen (Waynant and Klein 1985) however more recently Nd:LaF_3 has been shown to have a net loss making the lasing achievements questionable (Cashmore 1995). Nd:$LiYF_4$ has been similarly shown to have a net loss coincident with the *5d→4f* transition (Cashmore *et al.* 1997)). UV laser emission based on the *5d→4f* transition was first achieved in Ce:$LiYF_4$

(Ehrlich *et al.* 1979) in which lasing at 325 nm was achieved using a KrF pump laser. Since these first successes in obtaining UV laser emission directly from these rare-earth doped crystals, a number of cerium-doped fluoride crystals namely Ce:LiCaAlF$_6$ (Ce:LiCAF), Ce:LiSrAlF$_6$ (Ce:LiSAF) and Ce:LiLuF$_4$ (Ce:LiLuF), have been shown to provide efficient performance in the range of tunability available (281-315 nm, in Ce:LiCAF (Pinto *et al.* 1995) and 305-334 nm in Ce:LiLuF (McGonigle *et al.* 1999c)) with high slope efficiencies obtained in general, for example, up to 47% in Ce:LiSAF (Bayramian *et al.* 1996) and 55% in Ce:LiLuF (Rambaldi *et al.* 1998).

1.1.2 Applications of Tunable UV Lasers

UV spectroscopy is extensively used in chemical, biological and material sciences. Detection applications in which UV lasers are used, are wide spread, such as in the local detection of OH^- molecules (Evans and Webb 1994; Corner *et al.* 2002), and the remote sensing of molecules such as O_3, NO (Hanna *et al.* 2002) and SO_2 (Rambaldi *et al.* 1995). These molecules all have strong absorption in the UV spectral region which enables them to be detected by such remote sensing. The detection of aerosols such as these in the atmosphere is vital for research leading to a fuller understanding of climatic conditions on earth.

A wide range of methods have been used to obtain laser output at specific wavelengths. In the search of a laser for use in the detection of OH, all-solid state lasers have been developed such as the sum-frequency generation of 20 nW of 309 nm using a violet and near IR distributed feedback diode laser (Corner *et al.* 2002), or the intra-cavity tripled Ti:Sapphire laser from which 1.5 mW of tunable output between 275-285 nm was obtained (Mohamed *et al.* 2002). Cerium lasers have also been used in remote sensing applications, in particular, the tunable output of Ce:LiSAF between 284 nm and 299 nm has been used to detect SO_2 and O_3 simultaneously (Rambaldi *et al.* 1995). Dubinskii *et al.* (Dubinskii *et al.* 1995) have also reported the use of a 0.15 cm^{-1} (0.0015 nm) bandwidth Ce:LiCAF laser for the detection of CH_3O. A Ce:LiCAF laser, tunable between 280 nm and 315 nm was commercially available from Lambda Physik for use in such applications. The spectral bandwidth of this laser was ~0.3 nm. As will be discussed later in Chapter 5 and 6, research into the use of Ce:LiLuF in the detection of OH is currently underway.

A new and fast moving field using tunable UV lasers is the generation of and amplification of ultra-short, high-energy laser pulses. The broad gain bandwidth present in cerium laser crystals is sufficient to amplify pulses with durations down to a few femtoseconds, which makes these lasers very attractive for short-pulse generation. Such lasers are very desirable for

applications in a number of fields such as micromachining, plasma interaction and x-ray generation.

1.2 Cerium-Doped Laser Materials

1.2.1 General Trivalent Cerium Spectroscopy

Trivalent cerium laser transitions are based on the *5d*→*4f* transition as shown in Figure 1.1. Ce^{3+} has been doped into a variety of optical materials, including $Y_3Al_5O_{12}$ (YAG), $LiYF_4$, $LiCaAlF_6$, $LiSrAlF_6$, CaF_2, LaF_3 and $LiLuF_4$ and more recently in $KMgF_3$, $LuPO_4$, $LiSrGaF_6$ and $LiBaF_3$. The Ce^{3+} ion has only one unbound electron and the ground state of the Ce^{3+} ion is the $4f^1$ state. In the free ion, the $4f^1$ state is split by spin-orbit coupling into two levels, namely $F_{7/2}$ and $F_{5/2}$, of which the lowest lying level is the $F_{5/2}$ level.

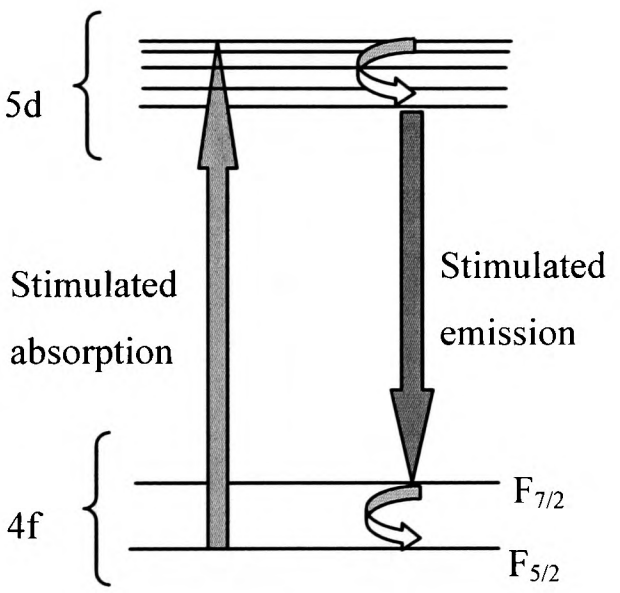


Figure 1.1 shows a simplified energy level diagram representative of the four-level laser system on which cerium lasers are based.

The wave-functions of the $4f^1$ states are of relatively small spatial extent and when Ce^{3+} is doped into a crystals these *4f* states are shielded from the crystal field by the larger closed *5s* and *5p* shells, thus, in general, the $4f^1$ energy levels are relatively unchanged from their free ion values when placed in a crystal field. For instance, the separation between the Ce^{3+} $F_{5/2}$ and $F_{7/2}$ levels in the free ion is ~2300 cm^{-1} (Jacobs *et al.* 1978) and when doped into a LiLuF crystal this separation is ~1900 cm^{-1} (Ranieri *et al.* 2000). The crystal field however does lead to a Stark splitting of the $F_{5/2,\ 7/2}$ levels with a separation between the Stark levels of only ~100 cm^{-1}. In a crystal the two Ce^{3+} *4f* bands overlap, forming a continuous band with two peaks. The extent of the overlap and bandwidth is governed by the crystal host. At room

temperature, the thermal distribution of the *4f* population is such that only the lowest 5% of the *4f* band has any significant thermal population. In cerium laser crystals the relaxation within the 4f band is however non-radiative, with a picosecond timescale characteristic of such band structure.

The excited 4f $5d^1$ configuration of Ce^{3+}, in the free ion form, is split by spin-orbit coupling into two states namely the $D_{3/2}$ and $D_{5/2}$ states, which lie approximately 50000 cm^{-1} and 52000 cm^{-1} respectively, above the ground state. However, the radial wave-function of the 5d states extends well beyond the closed *5s* and *5p* shells and, as such, when Ce^{3+} is doped into a crystal these *5d* states are strongly perturbed by the crystal field of the host.

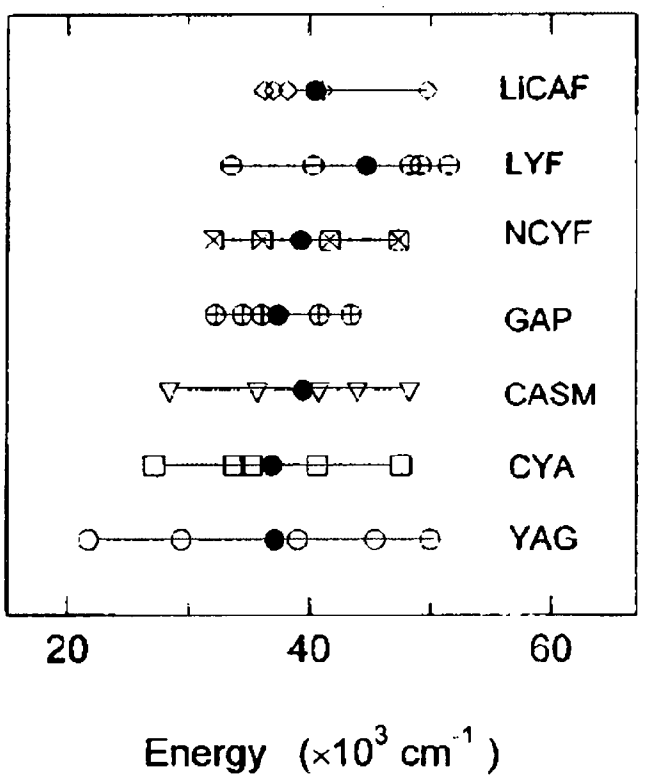


Figure 1.2 Energy levels of the 5d excited states of Ce^{3+} ions estimated from the absorption spectra in various host crystals (Kodama *et al.* 1998). Abbreviations are as follows: ($NaCaYF_6$ = NCYF, $Ca_2Al_2SiO_7$ = CASM, $CaYAlO_4$ = CYA, $GdAlO_3$ = GAP). Solid circle is representative of the average energy of the 5d levels, and the hollow symbols represent the energies of the 5d levels for the specified host.

The extent to which these *5d* states are perturbed by the crystal field depends solely on the crystal host, more specifically on the site symmetry of the Ce^{3+} ion in the lattice. In general, the average of the Ce^{3+} *5d* levels, in a variety of host crystals, lies between 35000 cm^{-1} and 45000 cm^{-1} above the *4f* ground state as shown in Figure 1.2. The crystal field splitting in Ce^{3+} arising from YAG is very large, with the energy between the highest and lowest lying excited *5d* levels being ~30000 cm^{-1}. The splitting of Ce^{3+} in LiCAF is less dramatic with the

energy difference between the highest and lowest lying excited *5d* levels being only 15000 cm^{-1}.

Figure 1.3 shows the positions of the absorption and emission spectra of some Ce^{3+} doped crystals. In all the host crystals investigated by Kodama *et al.* (Kodama *et al.* 1998), only Ce:LiCAF, Ce:LiYF and Ce:NCYF show the fluorescence (from the *5d*→*4f* transition) in the UV, due to the high energy of the lowest *5d* band in these hosts. Because of the larger energy gap between the lowest *5d* band to the highest *4f* band in these UV emitting Ce^{3+} doped crystals, the probability of multi-phonon non-radiative relaxation is small and as a result the *5d*→*4f* quantum efficiency of the fluorescence is near unity.

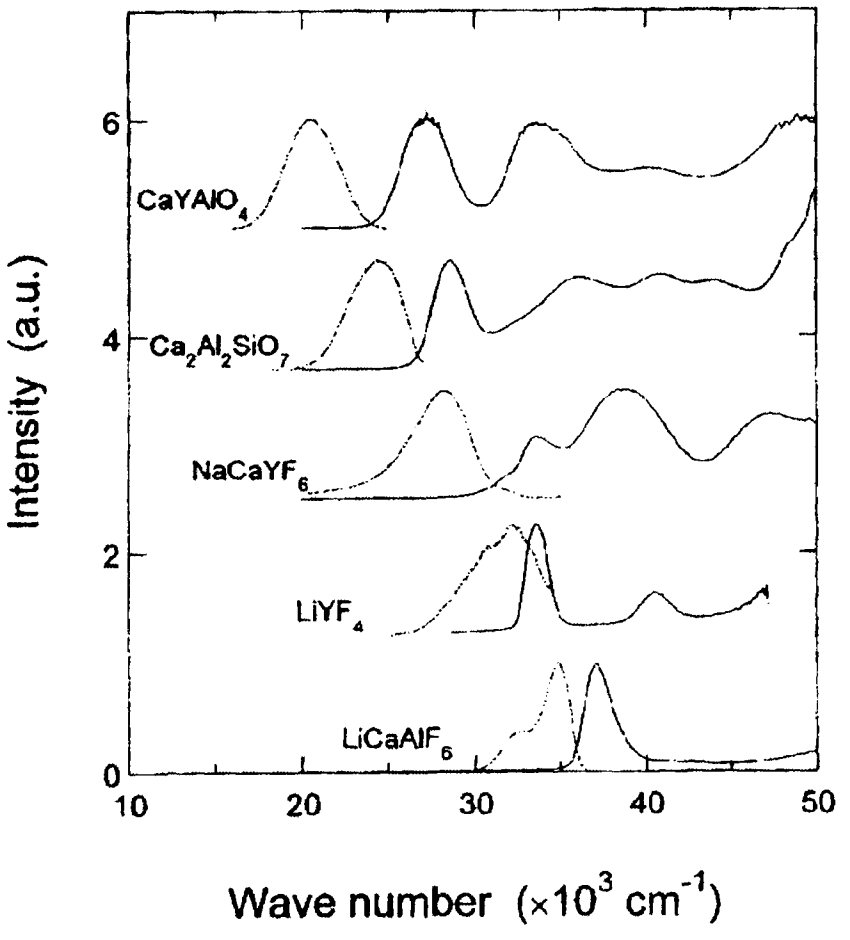


Figure 1.3 Optical emission and absorption spectra of Ce^{3+} in various crystals hosts (Kodama *et al.* 1998).

The positions and number of levels into which the excited *5d* state is split depends on the site symmetry and coordination number of the Ce^{3+} ion in the crystal lattice. Research into the assignment of absorption peaks and emission peaks in trivalent cerium doped crystals has grown dramatically in recent years. Studies of various cerium doped crystals have been undertaken by Yamaga and colleagues on Ce:LiYF (Yosida *et al.* 1997), Ce:LiLuF (Yamaga *et al.* 2002) as well as many others (Yamaga *et al.* 1997; Yamaga *et al.* 1999; Yamaga *et al.* 2000; Yamaga *et al.* 2001a; Yamaga *et al.* 2001b). Such research is vital to understanding the

crystal field effects on cerium in the various hosts and as such aids in the development of new cerium-doped laser crystals.

The *5d*→*4f* transition is a highly electric-dipole parity-allowed transition. Thus the decay from the lowest *5d* level to the *4f* level is very fast, with a fluorescence lifetime of the order of 10 ns, such as that of 28 ns in Ce:LiCAF (Marshall *et al.* 1994) and that of 40 ns in Ce:LiLuF (Sarukura *et al.* 1995a). The optical absorption and emission spectra presented in Figure 1.3 show the *4f*↔*5d* transitions to be broad-band transitions with bandwidths of the order of 1000 cm^{-1}. This broadening of the absorption bands is the result of phonon broadening of the *5d* levels (Okada *et al.* 1994). The broadening of the emission bands is the due to Stark and phonon broadening of the *4f* bands. The broad emission bands seen in the trivalent cerium doped crystals make these crystals ideal as sources of tunable emission in the UV. It has been found that the non-radiative decay from the higher lying *5d* bands to the lowest *5d* bands is very fast, of the order of a few nanoseconds (Okada *et al.* 1994). This is very advantageous when using these crystals as laser crystals, as pumping into any of the *5d* bands can result in a population in the lowest *5d* band with very little time delay, making this ideal for a four-level laser system. Further, the broad nature of the absorption bands means the Ce^{3+} doped crystals do not require precision wavelength selection for pumping of the *4f*→*5d* transition. A more detailed overview of the pump lasers used to date for pumping cerium lasers is given in §1.3.

Investigation of lasing in cerium doped laser crystals has shown that excited-state absorption processes are important to the lasing behaviour and cannot be ignored. In some case, such as in Ce:YAG and Ce:CaF_2, these excited-state processes have resulted in a net loss at the wavelengths of the *5d*→*4f* transition as opposed to gain. Other crystals such as Ce:LiYF and Ce:LiCAF have also been detrimentally affected by excited-state processes, however gain and, in the case of Ce:LiCAF, highly efficient lasing has still been achieved.

Excited-state absorption (ESA) includes any process involving the transition of an electron from an excited laser level to a higher lying level. These transitions reduce the upper laser level population and as such act as a loss mechanism to lasers. ESA has been observed in many of the transition-metal lasers and the rare-earth metal lasers. ESA has been found in transition-metal laser materials such as Cr^{3+}:Glasses (Koepke *et al.* 2001) and Cr^{4+}:Garnets (Kuck *et al.* 1997; Burshtein *et al.* 1998) as well as in Ni^{2+} and V^{2+} in MgF_2 (Moncorge and Benyattou 1988; Payne *et al.* 1988) to name only a few reported cases. Of perhaps more relevance to this thesis is the ESA seen in rare-earth metals such as Eu^{2+}, Pr^{3+} and Ce^{3+}.

Research has been directed towards finding more about the transitions leading to ESA in Eu^{2+} and Pr^{3+}-doped fluorides. The ESA in Eu^{2+}:CaF_2 investigated by Lawson *et al.* (Lawson and

Payne 1993) and Owen *et al.* (Owen *et al.* 1981) showed the ESA spectrum to overlap with the emission spectrum, preventing gain from being achieved in this crystal. The ESA was thought to result from the *5d→Conduction band (CB)* transition. The ESA in Pr^{3+}:YAG was found to originate from the lowest excited *5d* state (Cheung and Gayen 1994) and the terminal state for this ESA was also thought to be the conduction band, as in Eu^{2+}:CaF. The excited-state processes in Nd^{3+} doped fluorides have also been investigated and shown to result in a net loss at the *5d→4f* transition wavelengths (Cashmore 1995; Cashmore *et al.* 1997) due to ESA transitions to the conduction band and the formation of colour centres.

Owen *et al.* (Owen *et al.* 1981) gave two main guidelines to crystal design to aid the development of crystals which are not affected by ESA. Firstly, one requires that no sequential transitions to excited states of the dopant are accessible with two pump or emission photons, from the ground state. Many electron atoms thus should be avoided as dopants because as the number of electrons increase, the abundance of excited states also increases, making the number of transitions accessible from the ground state large. Secondly, the dopant energy levels must lie well below the conduction band. This requires that the host material has a large band gap, which restricts host crystals to fluorides and some oxides and chlorides.

Excited-state absorption includes the absorption by colour centres. Colour centres can be formed by direct absorption from the upper laser level to an impurity site or via excitation of an electron from an excited state to the conduction band, this electron then gets trapped in an impurity site to form a colour centre. Colour centres or photo-chromic centres are by definition point defects in specific charge states which have optical absorption bands in the transparent wavelength region of the host crystal (Henderson and Bartram 2000). One normally refers to colour centres which can be optically bleached as photo-chromic centres. In cerium lasers, colour centres have been found to be detrimental to lasing, as seen in $Ce:CaF_2$ and Ce:LiYF (see §1.2.3 and §1.2.4). F centres, Ce^{4+} and Ce^{2+} ions are all possible colour centres or colour centre precursors in cerium fluoride lasers. A variety of different types of colour centres exist and each is different in the different hosts, thus the identification of the exact type of colour centre is difficult. The formation, excitation, recombination and relaxation of colour centres in cerium doped fluorides are not well understood either. Colour centres can be defined by their behaviour, namely transient or stable. Transient colour centres are characterised by short lifetimes. These colour centres can result in absorptions which vary on the scale of the Ce^{3+} emission lifetime. The more stable, longer lived colour centres act more to create constant, stable background absorption. Both types of colour centre have been observed in cerium lasers.

In the next section of this chapter, the overall lasing performance characteristics of cerium doped materials are summarised. Where excited-state absorption (ESA) and colour-centre formation has been investigated, the results of these investigations are also summarised.

1.2.2 Ce^{3+}:$Y_3Al_5O_{12}$ (Ce:YAG)

Ce:YAG was one of the first cerium-doped crystals to be investigated as a possible broadband tunable laser. The crystal development of YAG as a host crystal for use in rare-earth doped lasers (such as Nd:YAG) was reasonably advanced when investigations into Ce:YAG lasers began. Gain, however, has never been achieved in Ce:YAG due to ESA and as such ESA in Ce:YAG has been the subject of much research (Jacobs *et al.* 1978; Miniscalco *et al.* 1978; Owen *et al.* 1981; Hamilton *et al.* 1989).

Using a pump-probe experiment with Ce:YAG pumped with a 353 nm XeF laser and probed using a cw-argon ion pumped dye laser at 590 nm, Jacobs *et al.* (Jacobs *et al.* 1978) found absorption at 590 nm when the pump was present. The excited-state absorption was found to have two distinguishable lifetimes, firstly one similar to that of the excited *5d* level (~75 ns) and secondly, one between 400-800 ns. The absorption characterised by the longer lifetime was tentatively assigned to absorption by transient colour centres. For an ESA transition originating from the *lowest 5d* band and terminating in the conduction band, the wave function of the terminal state would be diffuse enough to overlap intrinsic trap sites which could cause such colour centres.

The 75 ns lifetime suggested that some of the absorption of the probe originated at the excited *5d* level, implying the lowest *5d* state to be the initial state of the ESA. Confirming this was the obvious depletion of the *5d*→*4f* fluorescence observed by Hamilton *et al.* (Hamilton *et al.* 1989) when a pumped Ce:YAG crystal was irradiated with an intense probe. The intense probe resulted in the depletion of the *5d* population which in turn resulted in a decrease in fluorescence intensity. Once the probe pulse ended, it was found that the fluorescence did not recover but continued to drop with a decay rate similar to that of the *5d*→*4f* fluorescence decay rate. This suggested that the relaxation of electrons from the terminal ESA state back to the Ce^{3+} *5d* levels was slow and inefficient. At much later times the fluorescence decay was found to become non-exponential and to develop a long tail with a limiting lifetime of ~10 μs. This long lifetime tail was only observed in the presence of both the pump and a strong saturating probe and was proposed to be the result of delayed *5d*→*4f* phosphorescence arising from the back-transfer of electrons from the terminal ESA state to the Ce^{3+} *5d* levels.

A combination of ESA measurements by various groups (Jacobs *et al.* 1978; Miniscalco *et al.* 1978; Owen *et al.* 1981; Hamilton *et al.* 1989) enabled the ESA cross-sections between ~450 nm-900 nm to be determined. Figure 1.4 shows this ESA spectrum in Ce:YAG. The peak of the ESA spectrum was found to lie at ~700 nm with an ESA cross-section of $\sim 10 \times 10^{-18}$ cm^2 at this wavelength (Hamilton *et al.* 1989). The ESA peak at 700 nm was not found to correlate in energy to any feature on the ground state absorption spectrum. The wavelength range of the ESA transition did however overlap the lowest $5d \rightarrow 3^{rd}$ lowest $5d$ level transition wavelength. The cross-sections determined were thought to be too large for a disallowed $5d \rightarrow 5d$ transition. However, Miniscalo *et al.* (Miniscalco *et al.* 1978) suggested that the close proximity of the conduction band to these higher lying $5d$ levels may have reduced the purity of these higher lying states, causing the $5d \rightarrow 5d$ transition to be less parity forbidden, allowing for a relatively large cross-section. The other possible terminal ESA state proposed was the conduction band. The large cross-sections were thought to be realistic for a $5d \rightarrow CB$ transition. In support of the latter terminal ESA state assignment, photocurrent measurements in Ce:YAG by Hamilton *et al.* (Hamilton *et al.* 1989), showed an increase in the photocurrent on exposure to a coincident 460 nm pump beam and 700 nm probe beam, suggesting an increase in the number of electrons in the conduction band arising from the coincident pump and probe beams. Further, using a highly focussed 460 nm pump beam, with no incident probe beam, an increase in the photocurrent was observed, however this increase was not as large as with the 700 nm probe incident. This suggested that ESA at the pump wavelength was present; however it was much less than that at 700 nm, the peak of the ESA spectrum.

The photocurrent was also measured using a 355 nm pump beam. At this wavelength, the excitation was directly from the lower $4f$ band to the 2^{nd} $5d$ band of the Ce^{3+} ions. A large photocurrent was measured with this wavelength pump and a linear dependence of the photocurrent on the pump intensity was also found. This linear dependence suggested that this excitation into the 2^{nd} $5d$ band was caused by a one-step photo-ionisation of the Ce^{3+} ions from the ground state. This one-step transition caused an increase in the photocurrent which gave evidence placing the 2^{nd} $5d$ band inside the conduction band. This overlap of the conduction band and the higher lying $5d$ bands is thought to be the overall reason for the lack of gain in Ce:YAG.

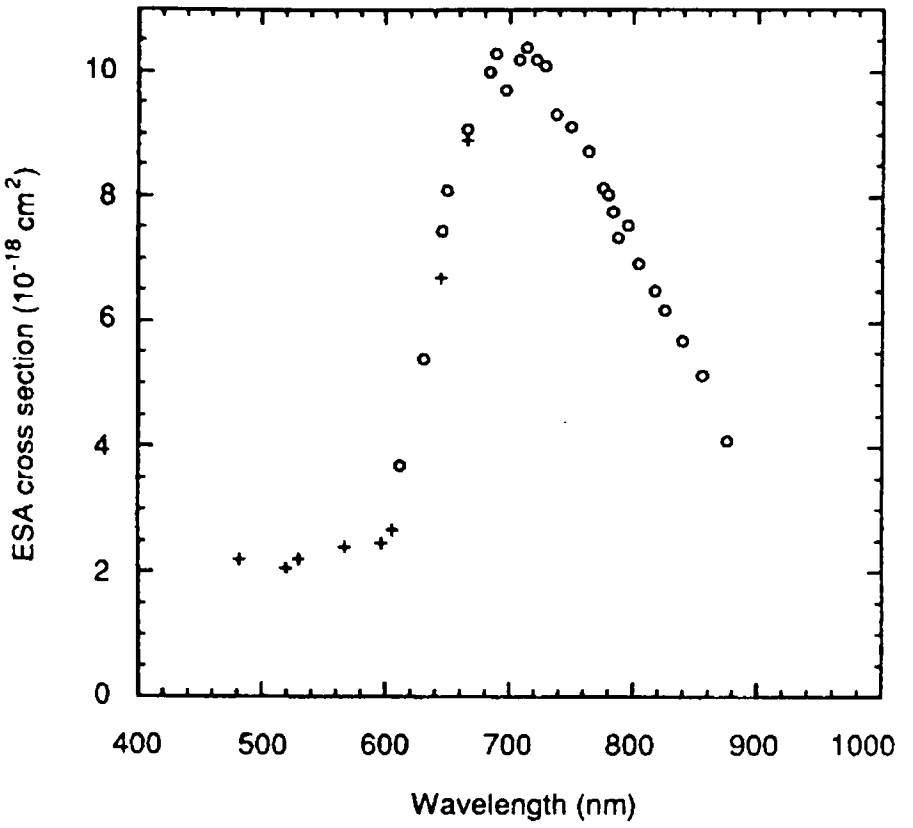


Figure 1.4 ESA spectrum of Ce:YAG derived from a combination of results from (Miniscalco *et al.* 1978; Owen *et al.* 1981; Hamilton *et al.* 1989).

1.2.3 Ce:CaF_2

Ce:CaF_2 has been haunted by excited-state absorption losses coincident with the emission spectrum of Ce:CaF_2. The initial signs of colour centre formation in Ce:CaF_2 was the change in the pumped region of the crystal from being transparent to having a dirty brown colouration on irradiation with on-resonance 308 nm pump light. Off resonant pumping did not result in any discolouration of the crystal suggesting the centres were created in a process involving excited cerium ions (Pogatshnik and Hamilton 1987). The absorption spectrum of the 308 nm induced colour centres had peaks at 390 nm, 510 nm and 800 nm and resulted in strong absorption over the Ce:CaF_2 emission spectral region preventing gain from being obtained in Ce:CaF_2. These colour centres were shown to be bleached by exposure to 351 nm, 532 nm or 633 nm light, returning the crystal to its original transparent state (Hamilton 1985).

Early research by Staebler and Schnatterly (Staebler and Schnatterly 1971) showed that colour centres in rare-earth doped CaF_2 consisted of a combination of a divalent cerium ion next to an F^- centre. These colour centres were found to be photo-chromic (PC), in that their colour could be changed by irradiation with light as shown in equation 1.1.

$$PC + RE^{3+} \underset{kT}{\overset{\text{Visible/UV Light}}{\rightleftharpoons}} PC^{+} + RE^{2+} \qquad 1.1$$

These photo-centres, in the form of a divalent cerium ion with a neighbouring fluorine ion, could be formed by irradiation of a trivalent rare-earth ion fluorine-vacancy complex with visible or UV light. This process was reversible either thermally or by absorption of light by the RE^{2+}. These colour centres were found to be stable for a day or more at room temperature.

The origin of the colouration of the $Ce:CaF_2$ laser crystals in particular has been investigated in detail by Pogatshnik *et al.* (Pogatshnik *et al.* 1984; Pogatshnik and Hamilton 1987) and a mechanism of colour centre formation similar to that determined by Staebler and Schnatterly was proposed as follows. In $Ce:CaF_2$, the trivalent cerium ions replace the divalent calcium (Ca^{2+}) in the lattice, requiring a F^- ion in the nearest body-centred cubic site to compensate for the charge difference between Ce^{3+} and Ca^{2+}. The presence of the fluorine ion results in a tetragonal distortion of the Ca^{2+}/Ce^{3+} site. Some trivalent cerium ions however do not have a closely located fluorine ion, in this case the site remains in a cubic symmetry. It was proposed by Pogatshnik and Hamilton that these trivalent cerium ions in cubic sites were the colour centre precursor sites. Ce^{2+} is known to be stable in a cubic site and hence, the acceptance of an electron by a trivalent cerium ion forms a stable Ce^{2+} colour centre. The colour centres were thought to have been formed via excited state absorption of the pump wavelength from the Ce^{3+} *5d* level to the conduction band. The free electron was then trapped in an electron acceptor site, in particular a Ce^{3+} site with cubic symmetry, thus forming a stable Ce^{2+} colour centre (Pogatshnik and Hamilton 1987). Thus these colour centres are not thought to involve parasitic impurities but rather are the result of an alternate metastable valence state of the cerium atoms (Pogatshnik and Hamilton 1987). The extreme stability of Ce^{2+} ions in $Ce:CaF_2$ may be exceptional, however it may also be present in other cerium doped fluorides.

1.2.4 $Ce:LiYF_4$ (Ce:LiYF)

1.2.4.1 Lasing in Ce:LiYF

The emission and ground state absorption spectrum for Ce:LiYF is shown in Figure 1.5. As can be seen there are a number of absorption peaks suitable for pumping of a Ce:LiYF laser. The emission spectrum shows a broad doubled peaked emission between 300-350 nm. The two peaks were located at ~309 nm and ~327 nm. As mentioned earlier, Ce:LiYF was the first cerium-doped material to show gain and lasing (Ehrlich *et al.* 1979). Peak single pass gains of >2 at 325 nm were measured (corresponding to the longer wavelength emission peak shown in Figure 1.5) when excited with a KrF laser (pumping into the second absorption band); however, above ~1J/cm^2 the gain was observed to saturate. Stimulated emission was also observed with a maximum output energy of ~1 mJ for an absorbed KrF pump fluence of ~100 mJ/cm^2, giving an overall conversion efficiency of ~0.1%. Improvements in the laser

crystal growth methods resulted in an optical-to-optical conversion efficiency of 1.2% (Okada *et al.* 1994). Okada *et al.* (Okada *et al.* 1994) further showed that gain could be achieved between ~320-330 nm, showing this laser could possibly be tuned when pumped with either a 193 nm ArF laser or a 248 nm KrF laser. Gain was not reported at the shorter wavelength peak. The small signal gain variation with repetition rate was measured by Lim and Hamilton and at repetition rates greater than 1 Hz a net loss was seen at 325 nm (Lim and Hamilton 1989). Efficient lasing in Ce:LiYF was never achieved and further research on Ce:LiYF was directed towards discovering the reason for the limited lasing efficiency achieved. Initial investigations by Okada *et al.* showed the formation of colour centres in Ce:LiYF to limit the lasing efficiency achievable.

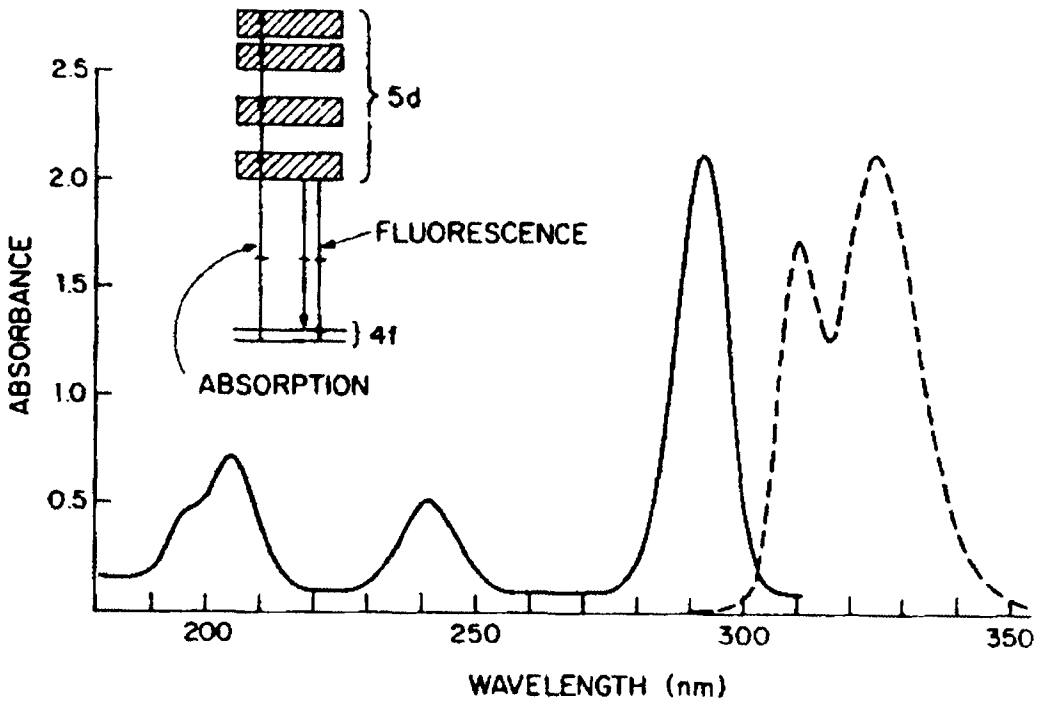


Figure 1.5 shows the ground state absorption and emission spectra for Ce:LiYF as measured by Ehrlich *et al.* (Ehrlich *et al.* 1979). (Dashed line is emission spectrum).

1.2.4.2 Excited-state Absorption effects in Ce:LiYF

Pump-probe measurements by Okada *et al.* to investigate the gain in Ce:LiYF showed the presence of absorption below 315 nm. This absorption, coincident with the shorter wavelength emission region of Ce:LiYF, was investigated further and was attributed to be the result of absorption by transient colour centres. No obvious absorption occurred with an undoped LiYF crystal, nor was any absorption seen when the Ce:LiYF crystal was irradiated with non-resonant pump wavelengths. This suggested that, in both cases, the formation of colour centres was directly dependent on the excitation of Ce^{3+} ions in the lattice, and hence the result of an excited-state absorption process. Even though colour centres are evident in

Ce:LiYF, unlike Ce:CaF_2, gain was still achievable. Two types of colour centres were observed in Ce:LiYF by Lim and Hamilton (Lim and Hamilton 1989), the main features of which are described next.

1.2.4.2.1 Stable Longer-lived Colour Centres

These stable colour centres have a characteristic lifetime of ~30 s (Lim and Hamilton 1989). The absorption by these colour centres was thought to be the result of a two-photon process since the absorption was found to vary quadratically with pump intensity. The absorption was anisotropic in nature, with the π-polarised (parallel to the *c*-axis of the crystal) absorption being much larger than the σ-polarised absorption. Two different measurements of the absorption spectrum arising from these colour centres have been measured (Lim and Hamilton 1989; Sarukura *et al.* 1995a), each showing a dominant absorption peak at ~340 nm. The presence of these almost identical spectra from crystals from different origins does suggest these colour centres are inherent to cerium doped LiYF. The position of the 340 nm peak is coincident with a gamma-ray formed F centre absorption in Ce:LiYF and as such was assigned to an F centre absorption (Lim and Hamilton 1989). These colour centres were found to be thermally stable, in that neither the lifetime nor the absorption changed with temperature variation (Lim and Hamilton 1989). The absorption by the colour centres was found to saturate after a number of pump pulses. The extent of the absorption experienced by the probe once saturation was reached was found to be dependent on the pump pulse energy. Lim *et al.* proposed this to indicate an upper bound for the number of deep trapping sites.

It was found that these long-lived colour centres could be bleached by short wavelengths such as 266 nm and 308 nm. Bleaching at 355 nm was however not evident, but absorption of the 355 nm probe was still obvious. The limited wavelength range for which bleaching occurred is evident of a photo-ionisation threshold for bleaching which in turn possibly indicates the presence of bound excited states in the colour centre (Lim and Hamilton 1989). The bleaching at 308 nm was found to be most effective at low temperatures (77 K). This was thought to be due to the narrowing of the $4f \rightarrow 5d$ absorption band, resulting in a decrease in the $4f \rightarrow 5d$ absorption, in turn increasing the number of remaining photons available for bleaching of the colour centres. It is possible, however, that the bleaching itself was temperature dependent, with an increase in bleaching efficiency with decreasing temperature.

1.2.4.2.2 Transient/Short-lived Colour Centres

The lifetime of the short-lived colour centres varied between 50 ns and 50 ms. Measurements made by Lim *et al.* (Lim and Hamilton 1989) found a decrease in the transient absorption

towards the shorter wavelengths. The origin of these transient colour centres was not discussed by Lim *et al.*

No afterglow phosphorescence was observed in Ce:LiYF, suggesting that the decay of the transient colour centres was neither radiative nor via the excited Ce^{3+} *5d* levels. Lim and Hamilton (Lim and Hamilton 1988) showed the transient colour centre lifetime τ in Ce:LiYF to be temperature dependent. The temperature dependence was found to vary as shown in equation 1.2, which is suggestive of the thermally activated decay process of these colour centres. This in turn is suggestive of non-radiative decay and possibly a dependence of the decay on electron mobility, hence resulting in a dependence on temperature.

$$\frac{1}{\tau} = s\exp(-\Delta E/kT) \qquad 1.2$$

where k is Boltzmann's constant, T is the temperature, ΔE is the activation energy and s is a rate parameter.

1.2.5 Ce:LaF_3

Ce:LaF_3 is another cerium laser which has shown gain and lasing in the UV, however use of this laser crystal has not been pursued very far. The emission and absorption spectra of Ce:LaF_3 are not shown here but can be found in the paper by Ehrlich *et al.* (Ehrlich *et al.* 1980). Lasing was achieved at 285.5 nm when pumped with more that 3 mJ of 248 nm KrF pump power (Ehrlich *et al.* 1980). A maximum power of ~5 μJ was achieved under full pumping. Lasing was not realised using the 193 nm ArF laser as the pump source. Ce:LaF_3 has not produced as much output as the Ce:LiYF laser to date. The limitations of Ce:LaF_3 as a laser crystal were assigned to the difficulty in obtaining laser-quality crystals, as the crystals used showed high scattering losses as well as unidentified absorption bands across the wavelength spectrum.

1.2.6 Ce:$LiCaAlF_6$ (Ce:LiCAF) and Ce:$LiSrAlF_6$ (Ce:LiSAF)

1.2.6.1 Lasing in Ce:LiSAF and Ce:LiCAF

The absorption and emission spectra of Ce:LiSAF and Ce:LiCAF are shown in Figure 1.6. The absorption peak lies between 265-270 nm and the peak emission occurs at ~290 nm in both crystals. The position of the absorption peak in both Ce:LiSAF and Ce:LiCAF give these crystals the great advantage over other cerium lasers, in that they can be pumped by the

all-solid-state, 266 nm frequency-quadrupled Nd:YAG laser. To date Ce:LiCAF is the only cerium laser to be produced commercially, and this is most likely because of the convenience of this pump source (this is discussed in more detail in §1.3).

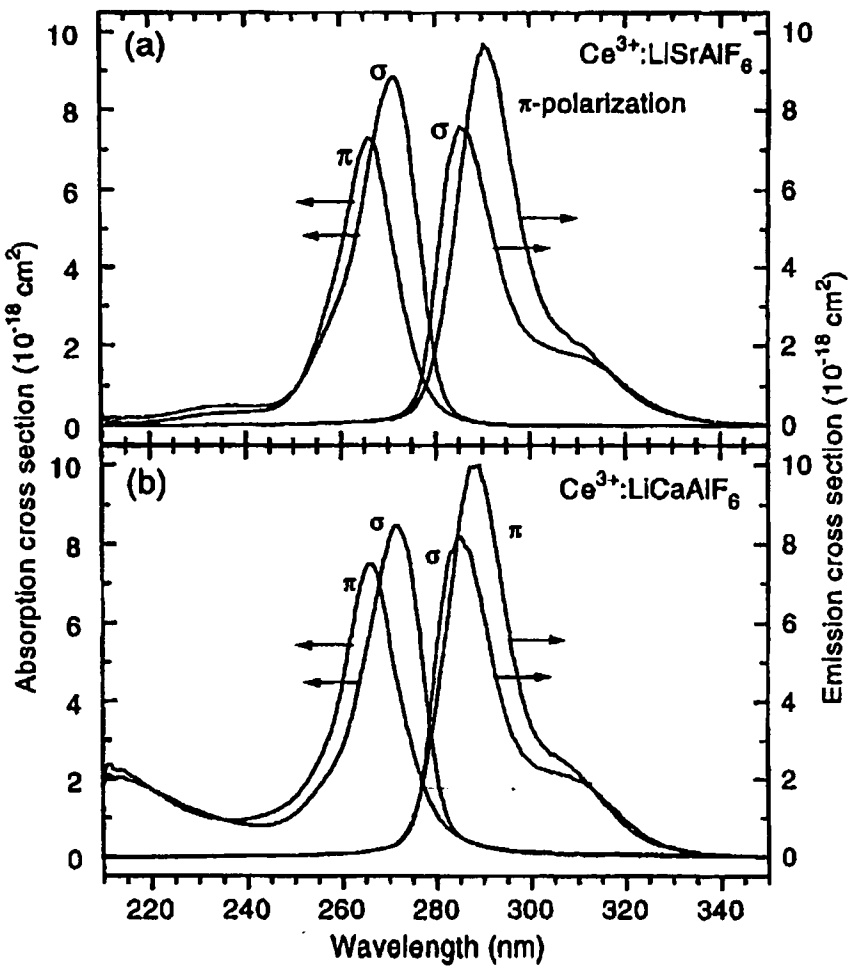


Figure 1.6 shows the absorption and emission spectra of Ce:LiSAF and Ce:LiCAF as measured by Marshall *et al.* (Marshall *et al.* 1994).

Tunable gain was first observed in Ce:LiCAF by Dubinskii *et al.* (Dubinskii *et al.* 1993b) with single pass gains of up to 2.3 and tunability between 280 nm and 320 nm. Lasing was first achieved in Ce:LiCAF and Ce:LiSAF by Dubinskii *et al.* (Dubinskii *et al.* 1993a) and Pinto *et al.* (Pinto *et al.* 1994). Single-pass gains as high as 11 (~4cm^{-1}) have been achieved at 290 nm in Ce:LiSAF and 4 (~2.5 cm^{-1}) at 290 nm in Ce:LiCAF with a pump fluence of 2 J/cm^2 from a 266 nm Nd:YAG pump laser. Tunable laser output in Ce:LiSAF was first accomplished by Pinto *et al.* (Pinto *et al.* 1994) with lasing between 285-297 nm. Since then gain has been achieved between ~280-325 nm in both Ce:LiCAF and Ce:LiSAF. Further highly efficient, broadly tunable lasing has been achieved between ~280-315 nm and 283-313 nm in Ce:LiCAF (Pinto *et al.* 1995; Gororkov *et al.* 1998; McGonigle *et al.* 1999b) and Ce:LiSAF (Pinto *et al.* 1995) respectively. Narrow bandwidth lasing (<0.1 nm) has also been achieved in Ce:LiCAF and Ce:LiSAF by Pinto *et al.* (Pinto and Esterowitz 1997) at 288 nm and 290 nm respectively, by using a distributed feedback laser. Narrower bandwidth

operation (<0.15 cm^{-1}) has also been achieved by Dubinskii *et al.* (Dubinskii and Schepler 1998) using an injection-seeded laser cavity. Tunable laser emission has been achieved between 223-243 nm by Pinto *et al.* (Pinto *et al.* 1998) by frequency-mixing the tunable output from Ce:LiCAF and the 1.064 μm radiation from a Nd:YAG laser in BBO. Similar results have been achieved by Petersen using the 1.064 μm output from a Nd:YVO_4 laser giving up to 50 mW of average power between 228-240 nm (Petersen 1997).

Laser slope efficiencies as high as 47% have been achieved in Ce:LiSAF, with anti-solarant pumping, and 33%, with no anti-solarant pumping (Bayramian *et al.* 1996) and slope efficiencies of 33% have been achieved in Ce:LiCAF (Petersen *et al.* 1996). Using larger Ce:LiCAF crystals (15 mm diameter), slope efficiencies of up to 39% have been achieved (Liu *et al.* 1998).

In Ce:LiSAF output powers of 0.25 mJ have been observed (with anti-solarant pumping) from 0.6 mJ of 266 nm pump power at 10Hz, giving a conversion efficiency (266 nm to ~290 nm) of 42% (Bayramian *et al.* 1996). Ce:LiCAF has given up to 550 mW of output power from 1.9 W of 1 kHz 266 nm pump power . Using the 10 kHz sum-frequency-mixed CVL output (see §1.3) at 271 nm, up to 530 mW of Ce:LiCAF output from 1.9 W of pump power was achieved, giving a conversion efficiency of 28% (McGonigle *et al.* 1999b). In these high repetition rate experiments, no active cooling of the laser crystal was required as there were no noticeable degradation effects at these high repetition rates and no noticeable thermal lensing either. Thus in general, lasing in Ce:LiCAF and Ce:LiSAF is not restricted to low repetition rates as was found to be the case in Ce:LiYF (Lim and Hamilton 1989).

Most recently the work on Ce:LiCAF has been focussed on using these crystals for short pulse generation (<1 ns) and amplification of such pulses. Amplification of single short 289 nm laser pulses in a Ce:LiCAF master oscillator power amplifier (MOPA) system has shown a 14 times amplification of a 1 mJ laser pulse with no noticeable pulse broadening (Sarukura *et al.* 1997). Further, using a large (1 x 2 x 2 cm^3) Ce:LiCAF crystal based four-pass amplification system, up to 98 mJ of 290 nm laser output has been achieved from an input pulse energy of ~13 mJ (Ono *et al.* 2002).

Further work by this Liu *et al.* has shown that Ce:LiCAF can be used in chirped pulse amplification (CPA) in the ultraviolet. Using a frequency tripled Ti:Sapphire amplifier system at 289 nm and a four-pass Ce:LiCAF amplifier, Liu *et al.* produced 6 mJ 289 nm pulses which could be then compressed down to 115 fs with a pulse energy of 3.5 mJ. This was the first reported ultra-violet, all-solid-state, high peak power CPA system (Liu *et al.* 2001).

As can be seen the development of Ce:LiCAF and Ce:LiSAF has been pursued in many directions. Overall this laser has proved highly efficient, with high gains and with broad-band tunability.

1.2.6.2 Excited-state absorption effects in Ce:LiSAF and Ce:LiCAF

The ESA cross-sections in Ce:LiSAF and Ce:LiCAF were determined by Marshall *et al.* (Marshall *et al.* 1994) at 266 nm (pump wavelength) and 290 nm (peak emission wavelength). The ESA cross-sections were determined using a combination of experimentally determined small-signal gain measurements and a finite-difference computer simulation of the gain behaviour in trivalent cerium-doped LiSAF and LiCAF. The ESA was found to be anisotropic with a higher ESA cross-section for the σ-polarised transitions than for the π-polarised transition in all cases looked at, except at 290 nm in Ce:LiCAF where the π-polarised ESA cross-section was found to be larger than the σ-polarised transition. The ESA cross-sections were of the order of 10^{-18} cm^2 for all polarisations and wavelengths except for the σ-polarised 266 nm ESA transition in Ce:LiSAF, where the cross-section was found to be ten times larger than this. This large σ-polarised ESA cross-section at the pump wavelength of Ce:LiSAF of 23 x 10^{-18} cm^2 was found to be highly detrimental to the gain achievable with a σ-polarised 266 nm pump in Ce:LiSAF. The σ-polarised gain at 290 nm in this crystal, with the σ-polarised pump, was non-existent and the π-polarised gain at 290 nm was only 1.2 ($0.3cm^{-1}$). The highest gain achievable in these two crystals was found in Ce:LiSAF when pumped with π-polarised 266 nm, with a π-polarised 290 nm probe. This gain was ~11 ($4cm^{-1}$) with an incident pump fluence of 2 Jcm^{-2}. The effective gain cross-section at this wavelength and polarisation was 6.8 x 10^{-18} cm^2.

The origin of the ESA in Ce:LiSAF and Ce:LiCAF was proposed to arise from the lowest *5d→CB* transition, as was suggested for the Ce:YAG transition. The polarisation dependence of the ESA was suggested to arise from the layered structure of LiSAF and LiCAF. These crystals are made up of four layers perpendicular to the *c*-axis of the crystals. The Ce^{3+} ion was expected to replace the Sr^{2+}/Ca^{2+} ion in the lattice. From the perspective of the Ce^{3+} ion, in the direction perpendicular to the crystal *c*-axis (σ-polarisation) the Ce^{3+} ion mainly interacts with the Sr^{2+}/Ca^{2+} wave-functions and parallel to the *c*-axis (π-polarisation) the Ce^{3+} ion interacts mainly with the Li^{+} and Al^{3+} ion wave-functions. The different extents of the Sr^{2+}/Ca^{2+} and Li^{+} and Al^{3+} wave-functions were thought to cause the wave-function of the conduction band perpendicular to Ce^{3+} ion wave-function to have a larger spatial extent than the wave-function of the conduction band parallel to the Ce^{3+} ion wave-function. With this

proposal the transition probability of the σ-polarised ESA transition was higher than a π-polarised ESA transition, resulting in the polarisation dependence of the ESA observed.

Yamaga *et al.* (Yamaga *et al.* 1998) using electron spin resonance results suggested a similar dependence of the ESA on polarisation. It was proposed that the polarisation dependence arose from the shape of the wave-function of the lowest *5d* state. The lowest excited-state was found to be an ^2E_g state which was characterised by an eigenfunction which extended in the *aa*-plane of the crystal, perpendicular to the *c*-axis. The shape of this ^2E_g eigenfunction implies that the *5d*→*CB* transition would occur more readily with σ-polarised light as the interaction between σ-polarised light and the lowest *5d* level is stronger. Both Marshall *et al.*'s model and Yamaga *et al.*'s model contribute towards a viable explanation of the anisotropic nature of ESA in Ce:LiSAF and Ce:LiCAF.

1.2.7 Ce:$LiLuF_4$ (Ce:LiLuF)

1.2.7.1 Lasing in Ce:LiLuF

Ce:LiLuF lasers have an emission and absorption spectrum almost identical to that of Ce:LiYF. LiYF and LiLuF are both scheelite-type materials (shown in Figure 1.7) which result in an almost identical crystal field splitting in a Ce^{3+} dopant (Sarukura *et al.* 1995a). In Ce:LiLuF, the Ce^{3+} ion substitutes the Lu^{3+} ions in the LiLuF lattice, in S_4 symmetry.

A detailed energy level diagram of Ce:LiLuF, based on the absorption spectrum measured by Ranieri *et al.* (Ranieri *et al.* 2000) (shown in Figure 1.8) is shown in Figure 1.9. The rising Ce:LiLuF absorption at ~170 nm in Figure 1.8 gives an approximate *4f* band→*CB* energy separation of 59000 cm^{-1} and the undoped LiLuF absorption shown in Figure 1.9, starting at ~130 nm gives an energy separation *VB*→*CB* of ~77000 cm^{-1} (~10eV). There are five excited *5d* levels in Ce:LiLuF as shown in the energy level diagram, corresponding to the five ground-state absorption (GSA) peaks at 186 nm, 196 nm, 206 nm, 244 nm and 292 nm. Figure 1.8 does not show the separate polarisation components of the absorption spectrum however this absorption is actually anisotropic (Rambaldi *et al.* 1998) (see Figure 3.25). In particular, for the two lower energy peaks, the 244 nm peak has a stronger π-polarised absorption cross-section and the 292 nm peak has a stronger σ-polarised absorption cross-section. A similar polarisation dependence is seen in Ce:LiYF (Yosida *et al.* 1997) (see Figure 3.25).

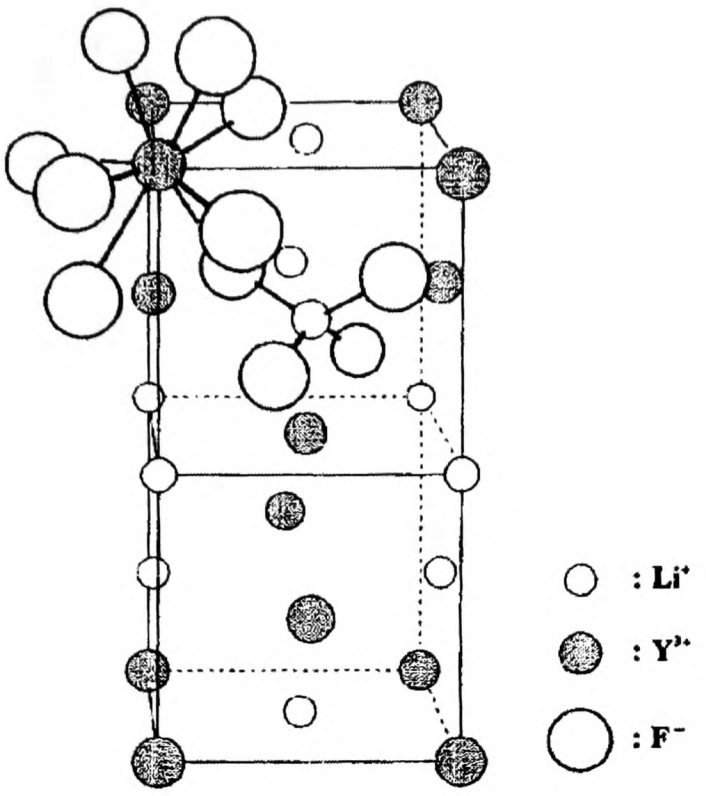


Figure 1.7 shows the scheelite crystal structure of $LiYF_4$, which is identical to the $LiLuF_4$ crystal structure. In Ce:LiLuF the Y^{3+} ions are replaced by Lu^{3+} ions. (Yosida *et al.* 1997)

The origin of the polarised GSA in Ce:LiYF and Ce:LiLuF has been investigated by Yosida *et al.* (Yosida *et al.* 1997) and Yamaga *et al.* (Yamaga *et al.* 2002). Qualitatively they suggested that the polarisation dependence of these *4f→5d* transitions was the result of the localisation of the *5d* wave-functions. In the case of the 2nd *5d* band (244 nm), this level was found to correspond to the $|2z^2 - x^2 - y^2\rangle$ e_g level. The wave-function of this level is localised in *z*-plane (*c*-axis), thus interacts more readily with π-polarised light. In the same way the lowest *5d* band is the $|x^2 - y^2\rangle$ e_g level which is localised more in the *xy* plane (*aa*-axis), hence interacts more readily with σ-polarised light. The localisation of the *4f* wave-function was not explicitly defined in this report, thus the extent to which the *5d* bands influence the polarisation dependence of each transition cannot be derived. The presence of absorption of both polarisations at both the 244 nm and 292 nm peaks for both of the lower energy *5d* levels suggests these levels are not actually pure but are mixed (Yosida *et al.* 1997).

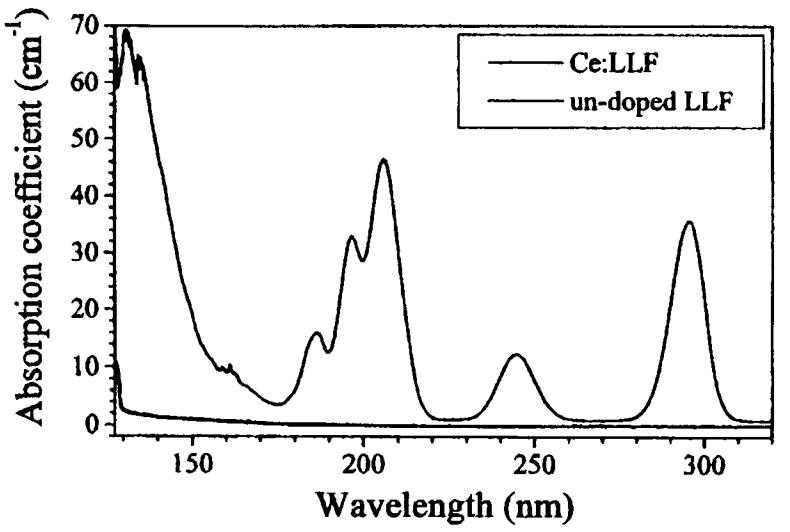


Figure 1.8 Ground-state absorption spectrum for Ce:LiLuF as measured by Ranieri *et al.* (Ranieri *et al.* 2000).

The emission spectrum of Ce:LiLuF is shown in Figure 1.10. The emission corresponds to the *lowest 5d→4f* transition with the double-peaked appearance resulting from the two *4f* levels ($F_{5/2}$ and $F_{7/2}$). The emission is anisotropic, with the π-polarised emission consisting of a larger 309 nm emission peak and a smaller 327 nm emission peak. The σ-polarised emission on the other hand has a larger 327 nm peak and a smaller 309 nm emission peak. The localisation of the *4f* wave-functions may be responsible for the polarisation dependence of the emission, in a similar manner to the GSA. The fluorescence lifetime of the *5d* level in Ce:LiLuF is ~40±2 ns. This fluorescence lifetime was found to be temperature independent between 200 and 400 °K (Sarukura *et al.* 1995a). The fluorescence *intensity* however was found to be temperature dependent by McGonigle *et al.* (McGonigle *et al.* 2001b), with the fluorescence intensity increasing with decreasing temperature. This temperature dependence was independent of pump intensity in that the change in fluorescence intensity was independent of whether a focussed pump or unfocussed pump was used. The quantum yield of Ce:LiLuF was measured by Sarukura *et al.* to be 0.88±0.08, which was high compared to the quantum yield of Ce:LiYF which was determined to be 0.44, using an method identical to that used for the Ce:LiLuF quantum yield determination.

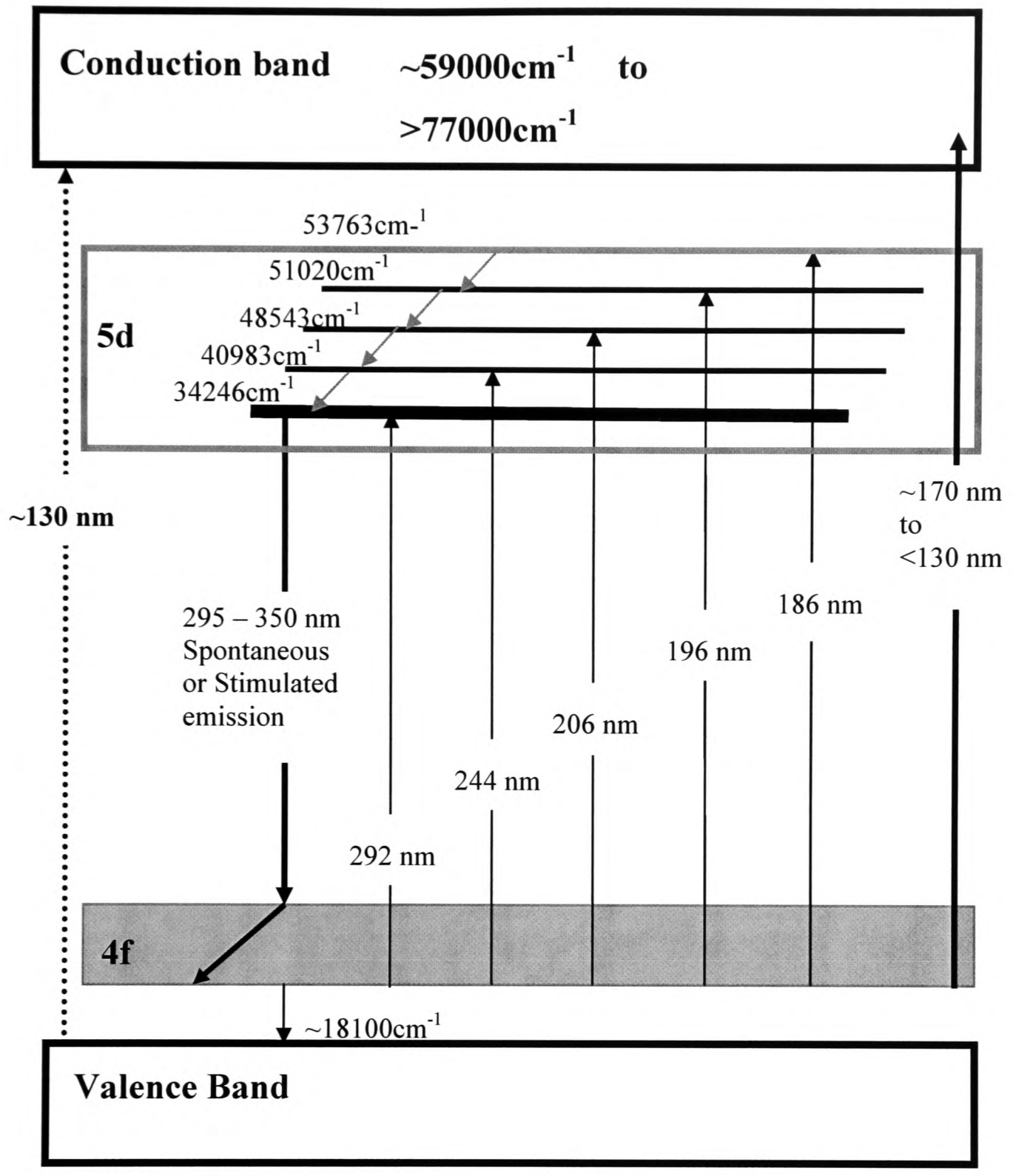


Figure 1.9 shows a simplified energy level diagram of Ce^{3+} doped into LiLuF, based on the absorption spectrum shown in Figure 1.8. All the energies are shown assuming that the Ce^{3+} ground state ($F_{5/2}$) has an energy of 0 cm^{-1}.

Sarukura *et al.* carried out a detailed comparison of Ce:LiYF and Ce:LiLuF and overall Ce:LiLuF was found to be superior to Ce:LiYF as a fluorescence or laser material. The small-signal gain was measured to be >1 between ~323-335 nm. Lasing at 311 nm was achieved in Ce:LiLuF, with a threshold which was approximately two times lower than was required for the Ce:LiYF laser. The slope efficiency of 18.5% was achieved without careful optimisation, which was twice as high as the Ce:LiYF laser slope efficiency using the same laser cavity configuration. Tunable gain was first achieved in Ce:LiLuF by Sarukura *et al.*

(Sarukura *et al.* 1995a), in which a single-pass gain of up to 4.5 (1.46 cm^{-1}) was achieved with a pump fluence of 0.5 J/cm^2 from a 248 nm KrF laser. Lasing at the longer wavelength peak of 326.5 nm was achieved by Coutts *et al.* (Coutts *et al.* 1996), with a repetition rate of 6.2 kHz. The maximum slope efficiency obtained was 5%. More recently, laser slope efficiencies as high as 55% have been reported by Rambaldi *et al.* (Rambaldi *et al.* 1998), with up to 2 mJ of 311 nm output from 6 mJ of pump power.

Ce:LiLuF has shown high gains which make these laser crystals ideal for use as amplification media for UV pulses, as was found to be the case for Ce:LiCAF. Sarukura *et al.* (Sarukura *et al.* 1995b) reported the amplification of short pulses in Ce:LiLuF. Large laser-quality Ce:LiLuF crystals have been grown (Liu *et al.* 2000) for use in such amplification media. Most recently Buhr and Fedosejevs have conducted simulations which indicate the possibility of producing peak powers of the order of terra-watts through amplification in a three stage Ce:LiLuF CPA system (Buhr and Fedosejevs 2002).

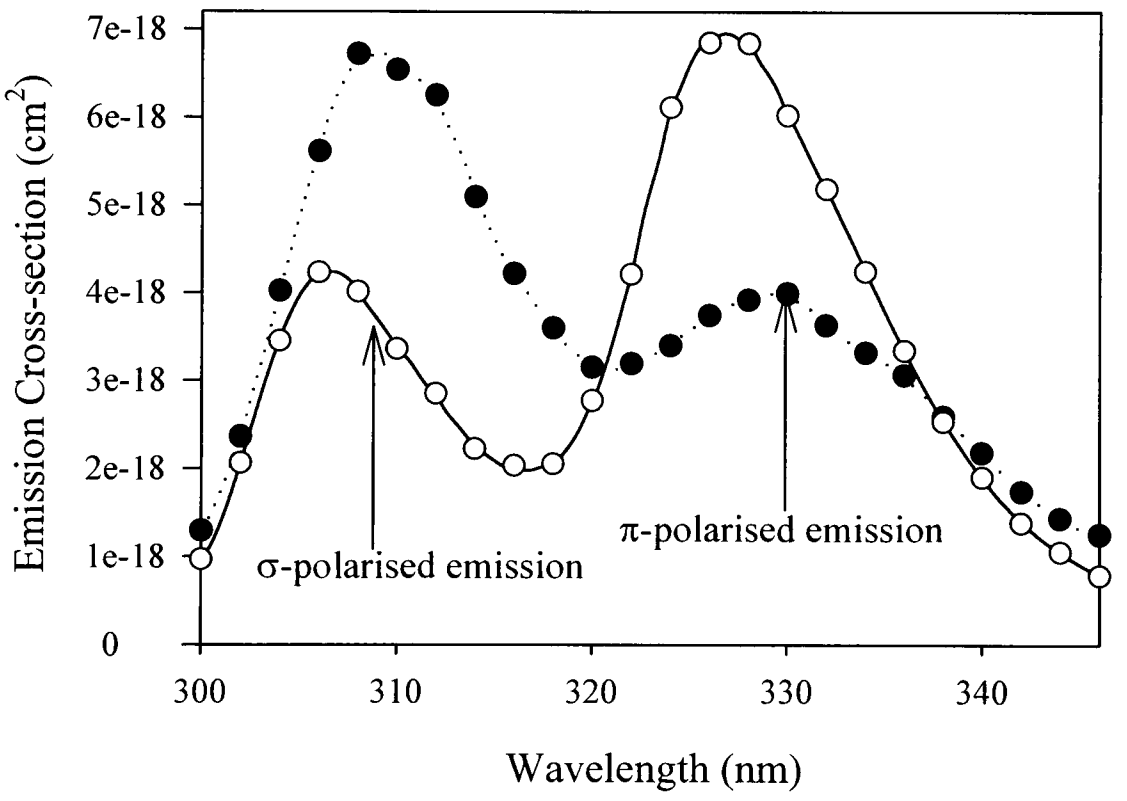


Figure 1.10 shows the polarised emission spectrum of Ce:LiLuF determined by the author (as described in §3.1).

Initially, tunable laser output was only achievable between 307.6-313.5 nm and 324-328.5 nm, coincident with the peaks of the laser emission curves. Continuous tuning was first achieved by McGonigle *et al.* (McGonigle *et al.* 1999c) pumping a French grown Ce:LiLuF crystal with a 10 kHz frequency-doubled copper vapour laser (see §1.3). Using single-prism tuning, laser output was achieved between 305 nm and 333.2 nm with a slope

efficiency of 51% at 309 nm. The output was found to be all π-polarised. Since then they have generated outputs as high as 380 mW using 1.2 W of 289 nm pump power. Further McGonigle *et al.* (McGonigle *et al.* 1999c; McGonigle *et al.* 2001b) found the laser output of Ce:LiLuF to increase with decreasing temperature, with the 309 nm output increasing from 150 mW at room temperature to 240 mW at -2°C. This increase in laser output however was not across the whole laser emission spectrum. At 327 nm the output actually decreased with cooling of the laser crystal, from 120 mW to ~75 mW. Figure 1.11 shows the variation of the Ce:LiLuF laser spectrum with a temperature change from room temperature to -2°C. The temperature dependence of the laser output was investigated more fully and it was found that the π-polarised 311 nm laser output increased approximately linearly with decreasing temperature.

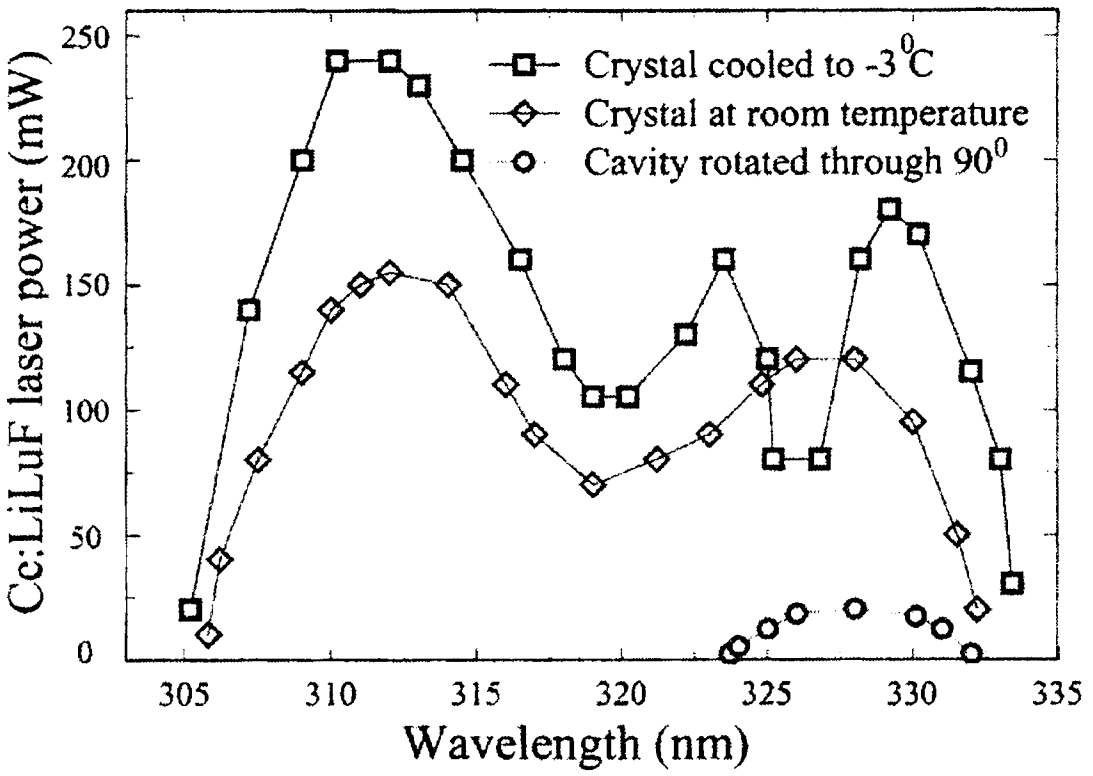


Figure 1.11 shows the Ce:LiLuF laser output versus wavelength at room temperature and -2°C as achieved by McGonigle *et al.* (McGonigle *et al.* 1999c)

The 327 nm output however increased with decreasing temperature until ~10°C, below which the output started to decrease and fluctuate considerably. It was also noticed that the laser output at 327 nm became predominantly σ-polarised as the crystal temperature was decreased or the pump power increased. It was found that two competing 327 nm modes existed in the laser cavity, a σ-polarised mode characterised by a shorter build up time and a π-polarised mode characterised by a longer build-up time and longer lasting laser pulse.

Before these results were published, Coutts *et al.* (Coutts *et al.* 1996) showed similar anomalous lasing behaviour in Ce:LiLuF lasers, in as much that at low pump fluence or with a low loss cavity, the σ-polarised 327 nm emission was dominant. As the pump fluence was increased or the cavity loss increased the lasing became dominated by π-polarised 312 nm emission. This decreased efficiency of the σ-polarised 327 nm laser emission with higher pump fluence or laser mode intensity suggested some pump or laser induced loss effects were present. The results of further investigations of this Russian grown Ce:LiLuF crystal are reported in detail next.

McGonigle *et al.* (McGonigle *et al.* 2001b) postulated that the lasing behaviour seen was the result of a temperature and polarisation dependent excited-state absorption mechanism between the *5d* level and the conduction band. Polarisation-dependent ESA had been seen previously in Ce:LiCAF and Ce:LiSAF (Marshall *et al.* 1994) (which is described in detail in §1.2.6.2). In a similar manner to that used in Ce:LiSAF, the affect of anti-solarant pumping was investigated in Ce:LiLuF. Results showed an increase in output peak power of up to 30% with the coincident pumping of Ce:LiLuF with 289 nm GSA pump wavelength and 578 nm anti-solarant pump wavelength (McGonigle *et al.* 1999a).

1.2.7.2 Excited-state Absorption effects in Ce:LiLuF

The anomalous lasing behaviour of Ce:LiLuF has suggested the presence of some form of excited state absorption, resulting from either *5d→CB* absorption as in Ce:YAG or colour centre absorption, as in Ce:LiYF. A colour centre absorption spectrum, similar to that seen in Ce:LiYF, was observed by Sarukura *et al.* (Sarukura *et al.* 1995a) in Ce:LiLuF showing an absorption peak at ~340 nm. Since then very little work has been undertaken on the presence of colour centres in Ce:LiLuF; however, an excited state absorption spectrum has been measured by Laroche *et al.* (Laroche *et al.* 10 -15 September 2000). In these ESA experiments the Ce:LiLuF crystal was pumped with the 290 nm output of a Ce:LiSAF laser and probed between 300-700 nm. The percentage absorption was found to be less than 10% between 300-700 nm. The ESA was found to be stronger for the σ-polarised probe light than with a π-polarised probe. The ESA was also found in general to increase towards the shorter wavelengths, as was observed in the stable colour centre absorption in Ce:LiYF. This absorption was tentatively suggested to be due to the presence of pump-induced colour centres.

Cashmore (Cashmore 1995) observed the formation of colour centres, manifested as a grey/blue colouration in the pumped region of one of the earlier Russian-grown Ce:LiLuF

crystals. These colour centres were found to be thermally removable or optically bleached with the UV output of a Hg lamp. The transient absorption of a He-Ne 633 nm laser in the pumped Ce:LiLuF crystal was investigated in order to gain some understanding of the colour centre formation. The colour centres were found to have a lifetime of ~10 μs, however some absorption was found to persist for >50 ms. The 633 nm absorption was found to be anisoptropic with more absorption of σ-polarised 633 nm probe than the π-polarised probe. This absorption provided evidence supporting the postulation that the anomalous lasing behaviour in the Ce:LiLuF crystal described in §1.2.7.1, in which the σ-polarised lasing occurred only at low pump fluence or low crystal field intensities, was the result of an anisotropic colour centre absorption. In general, this Ce:LiLuF crystal, one of the earliest Ce:LiLuF crystals grown at the former Kazan State University in Russia, was shown to be inferior to the more recently grown Ce:LiLuF crystals. Other than in this crystal, no colouration of Ce:LiLuF crystals on pumping has been reported, thus it is presumed that the inferior optical-quality of this crystal was the reason for the discolouration arising from extensive colour centre formation.

1.3 Pump sources for cerium lasers

In order for a pump source to be ideal for a solid-state tunable cerium laser one looks for a pump source which is at the ideal pump wavelength as well as compact and reliable (such as a solid-state or diode laser at the ideal pump wavelength). For Ce:LiCAF and Ce:LiSAF a pump source with a wavelength between ~255-275 nm is required. For Ce:LiLuF or Ce:LiYF a pump source lasing between 285-303 nm, 239-250 nm or 180-220 nm is required. There are various sources available which emit within these bands; however, of these, only a couple are solid-state lasers. To date the most convenient laser to act as a pump source for the cerium lasers is the frequency-quadrupled Nd^{3+} laser which lases at 266 nm. The Nd:YAG and Nd:YVO_4 laser wavelengths coincide almost perfectly with the peak of the Ce:LiCAF and Ce:LiSAF ground-state absorption bands, making them ideal pump sources for these lasers, (Marshall *et al.* 1994; Pinto *et al.* 1994; Rambaldi *et al.* 1995). A more bulky but equally good pump source for Ce:LiCAF is the sum-frequency mixed output of a copper vapour laser (CVL). In this pump source the green (511 nm) and yellow (578 nm) outputs of the CVL are sum-frequency mixed in BBO to give an output at 271 nm which also lies in the absorption band of Ce:LiCAF (McGonigle *et al.* 1999b).

For Ce:LiLuF lasers, solid-state pump sources have not been as readily available, however a less efficient, all-solid-state, frequency-quintupled Nd:YAG laser has been used to pump Ce:LiLuF at 213 nm (Sarukura *et al.* 1998) as has the all-solid-state Nd:YAG pumped

Ce:LiSAF laser at 290 nm, (Laroche *et al.* 10 -15 September 2000; Rambaldi *et al.* 1998). Other more bulky pump sources for pumping Ce:LiLuF include the frequency-doubled yellow output (578 nm) or frequency-doubled green output (511 nm) of a CVL, giving laser emission at 289 nm (McGonigle *et al.* 1999a; McGonigle *et al.* 1999c) and 255 nm respectively. KrF excimer lasers are possibly the most commonly used pump source for Ce:LiLuF at present, with laser emission at 248 nm (Sarukura *et al.* 1995a; Buhr and Fedosejevs 2002). All the pump sources used, except the CVLs, are all at low pulse repetition rates of the order of 10 Hz.

It has been found that pumping at the longer wavelengths has produced the most efficient operation due to the minimal solarisation and colour centre formation effects at the longer wavelength (Rambaldi *et al.* 1998). The 213 nm pump source has an undesirable quantum defect of only 65% compared to that with the 290 nm pump sources of 89% for lasing at 327 nm and when pumped with the 213 nm pump source showed solarisation and laser performance degradation during several hours of continuous operation. The UV-to-UV conversion efficiency with this 213 nm pump was only 0.5% (Sarukura *et al.* 1998).

CVLs are excellent pump sources for cerium laser characterisation and development because of their ability to pump Ce:LiCAF, Ce:LiSAF, Ce:LiYF and Ce:LiLuF. In particular, the sum-frequency-mixed 511 nm and 578 nm CVL output at 271 nm, has been used to pump Ce:LiCAF and Ce:LiSAF. In Ce:LiCAF up to 530 mW of 288 nm was achieved from ~1.8 W of 271 nm pump power (McGonigle *et al.* 1999b). In Ce:LiSAF 70 mW has been achieved from 550 mW of pump power at 10 kHz (McGonigle *et al.* 2001a). In previous work, Ce:LiLuF has been pumped by the frequency-doubled yellow output of the CVL giving pump light at 289 nm (McGonigle *et al.* 1999a; McGonigle *et al.* 1999c; McGonigle *et al.* 2001b). It is also conceivable that the frequency-doubled green CVL output at 255 nm could also be used to pump Ce:LiLuF, however this has not been undertaken to date, possibly due to the lower absorption coefficient at 255 nm compared to 289 nm. In this thesis the main pump source used to pump Ce:LiLuF was the frequency-doubled yellow output (578 nm) of a CVL, giving an output at 289 nm.

Although the CVL is a good pump source for cerium laser research, in order for cerium lasers to become commercially viable an all-solid-state pump source is required. Thus an efficient all-solid-state laser with output matching the longer wavelength Ce:LiLuF absorption band is required. 266nm pumped Ce:LiCAF is such a source, however these lasers are relatively inefficient in that three frequency conversion steps are involved. New all-solid-state laser sources lasing between 578 and 590 nm, developed by Pask and Piper (Pask and Piper 3-6 Feb. 2002; Pask and Piper 1998; Pask and Piper 1999; Pask and Piper 2000) which can be

frequency-doubled to give UV laser output between 295 and 289 nm have recently become available. These highly efficient frequency-quadrupled Raman-shifted Nd:YAG lasers may be the pump source required to make Ce:LiLuF commercially viable. In this thesis use of such a pump source is investigated for use in Ce:LiLuF. The details of the frequency-doubled CVL and frequency-quadrupled Raman-shifted Nd:YAG laser sources are described in full detail next.

An interesting aside is that, more recently instead of looking for pump sources which can be used to pump the *4f→5d* transition in cerium laser crystals, research is moving towards the development of cerium laser crystals which have absorption bands which coincide with the 263 and 266 nm emission of a frequency-quadrupled Nd lasers. Such work has been reported by Dubinskii *et al.* (Dubinskii *et al.* 1998) and an overview of 5d energy levels in some cerium laser materials is shown in Figure 1.12.

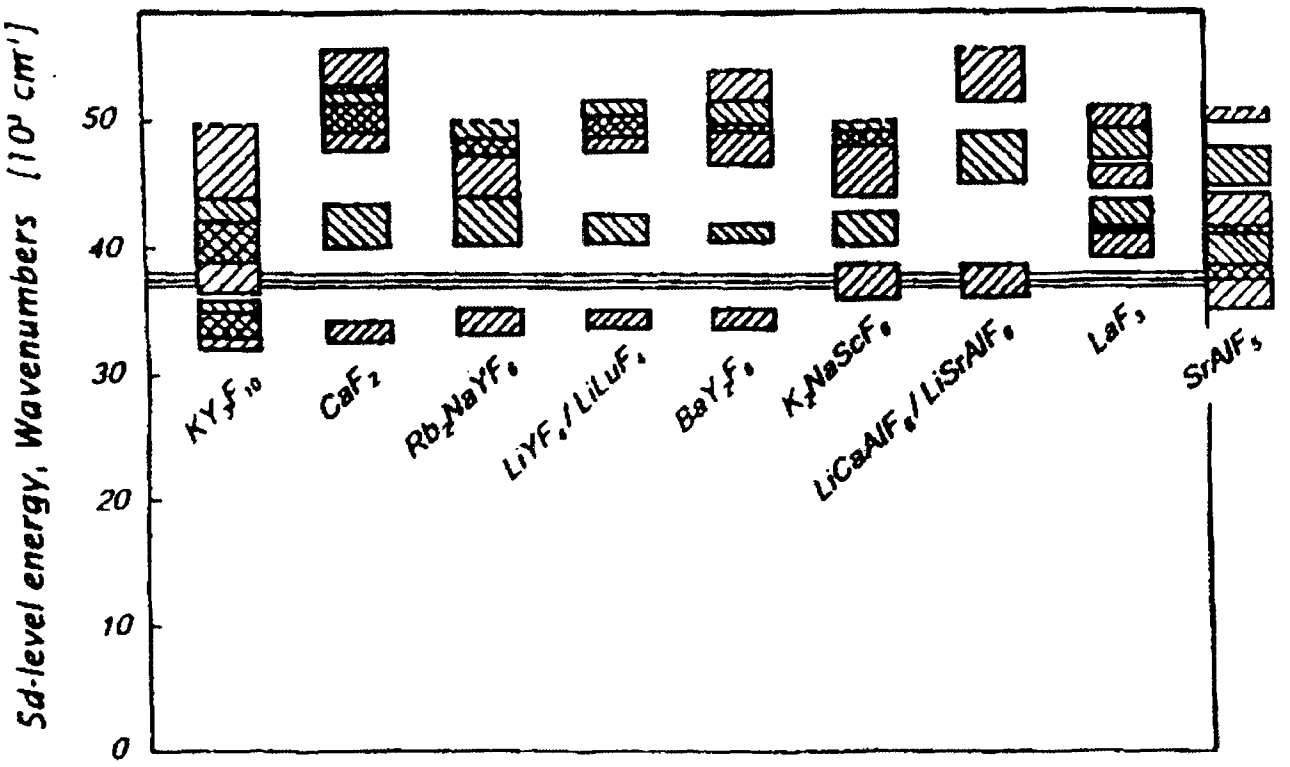


Figure 1.12 Simplified 5d energy level diagram indicating the relative positions of the 4f→5d absorption bands in cerium doped fluoride materials (Dubinskii *et al.* 1998).

1.3.1 Copper Vapour Lasers (CVLs) as cerium laser pump sources.

Copper lasers are metal vapour lasers which are renowned for their high average powers (up to several hundred of watts) and excellent performance at high pulsed repetition rates (1-100 kHz). There are two main copper laser transitions at 510.6 nm in the green and 578.2 nm in the yellow, which arise from the 4p $^2P^o_{3/2} \rightarrow 4s^2\ ^2D_{5/2}$ and the 4p $^2P^o_{1/2} \rightarrow 4s^2\ ^2D_{3/2}$ transitions in atomic copper, respectively, as shown in Figure 1.13.

Little (Little 1999) reviews metal vapour lasers in detail, CVLs in particular, thus only a brief summary of CVLs in general is given here. An electrical discharge passed down a thermally insulated ceramic laser tube containing solid copper and neon gas, causes the ceramic tube to be heated to ~1500°C, hence vaporising the copper into the neon buffer gas, while simultaneously pumping the upper $^2P_{1/2,\ 3/2}$ laser levels by direct electron impact. The ground-state to upper laser level transition is a fully allowed (resonant) transition. The population inversion lasts for only a short time thus the gain duration is short (~40 ns) which limits the number of round trips that can occur in the presence of the high gain. Direct-impact pumping from the ground state favours population of the lower resonance levels ($P_{3/2}$). Lasing occurs simultaneously from the both the excited *P levels* to both of the lower metastable *D levels,* giving green and yellow laser emission simultaneously as previously mentioned.

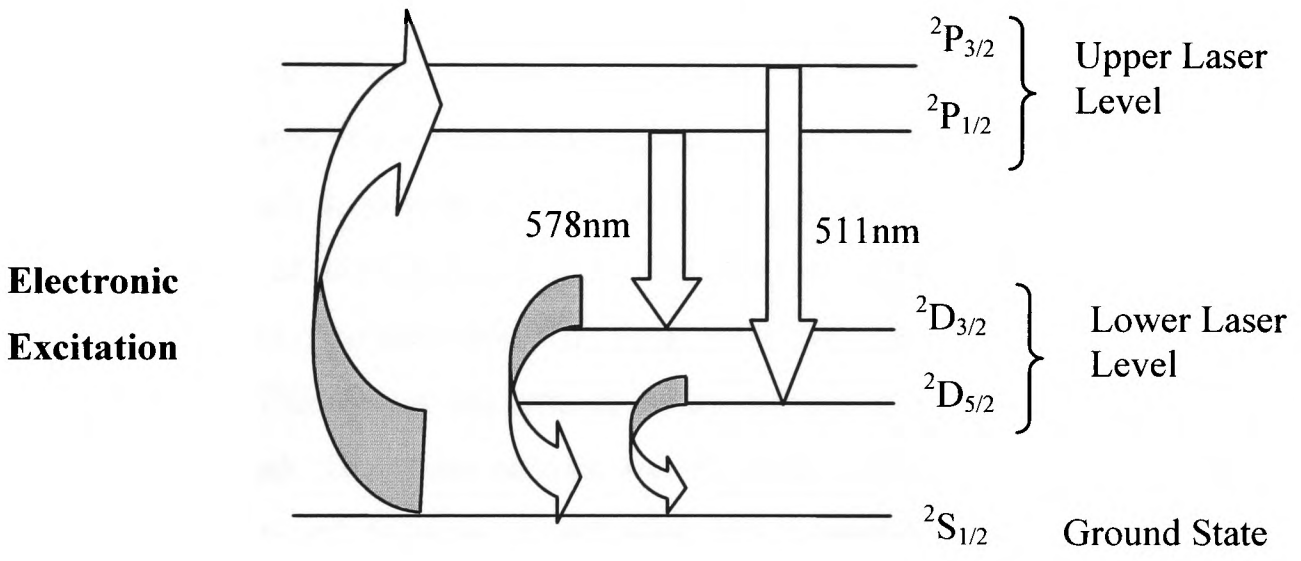


Figure 1.13 Shows a schematic diagram of part of the atomic copper energy level diagram and the lasing levels in a CVL.

A CVL is usually run with a low Q, plane-plane resonator with the mirror reflectivity of ~4%. The beam quality from such resonators is relatively poor, limited only by the aspect ratio of the plasma tube. In order to improve the beam quality of the CVL output, high magnification unstable resonators are often employed. The output of such lasers is less but the beam quality of the laser output is much better. The beam quality has been shown to evolve in a stepwise fashion from low beam quality amplified stimulated emission (ASE) in the first round trip to increasing beam quality in the later round trips. The output of the 3rd or higher round trips can be almost diffraction limited (Coutts *et al.* 1993).

The addition of hydrogen (<5%) and/or halogen donor gases such as HCl and HBr to the CVL neon buffer gas mix has been shown to improve the CVL performance dramatically (Withford

et al. 1996; Withford *et al.* 1997; Withford *et al.* 1998a; Withford *et al.* 1998b). These lasers are commonly referred to as kinetically enhanced CVLs (KE-CVL). These additives in the laser tube are thought to contribute towards decreasing the pre-pulse electron density in the laser tube and as a result improve the spatial uniformity of the copper density profile by increasing the gain at the centre of the axis of the laser tube. The beam quality of a KE-CVL is markedly improved as the peak power of the higher beam quality components of the KE-CVL are increased significantly (Withford *et al.* 1995). The pulse repetition frequencies accessible to CVLs are also found to be markedly higher for kinetically enhanced CVLs compared to CVLs with no H_2, HCl or HBr additives (Marshall and Coutts 2000).

1.3.1.1 CVL's used in this thesis

The CVL used in all the experiments conducted by the author and reported in Chapter 3, 4 and 5 in this thesis was an in-house build CVL based on the Oxford Lasers LS 20-10 system. The laser tube consisted of a 1.14 m long, 102mm (inner) diameter silica tube inside of which was a 1 m long ceramic tube with a diameter of 3.4 cm. The ceramic laser tube was insulated using an outer layer of alumina paper (~2 cm thickness) and an inner layer of Rath alumina fibre (2 cm thickness). The laser tube was fluted with 18 x 2 cm, 25 mm diameter flutes, each separated by 3 cm. The copper was placed between flutes to prevent copper reservoirs from blocking the laser path. The active volume was 1m long with a 25 mm inner (flute) diameter. A neon gas pressure of between 65-90 mbar was maintained within the laser tube. A thyratron-switched LC-Inverter excitation circuit was used with a two stage magnetic pulse compression (MPC). The operating electrical input power was ~3.2 kW. The pulse repetition frequency (PRF) was maintained at 10 kHz throughout the experiments. The laser was operated with an M=128 on-axis negative branch unstable resonator, consisting of a 3.2 m radius of curvature (ROC) high reflector and a 2.5 cm ROC concave reflector. The laser output was derived from a 45° centre hole scraper mirror as shown in Figure 1.14.

In the experiments undertaken using this CVL as the pump source, some experiments were carried out with a pure neon buffer gas and some were carried out with a H_2-HCl-Ne gas mixture. In the case where the CVL was kinetically-enhanced, a mixture of 1% H_2, 0.2% HCl with a balance of neon was used. The non-kinetically enhanced CVL gave, on average, output powers (green + yellow) of between 12-20W and for the KE-CVL, the average output powers obtained were between ~17-25W. The ratio of green output to yellow output was ~2:1. The beam quality of the green + yellow KE-CVL output was determined have an M^2 ~8. The beam quality of the non-kinetically enhanced CVL was not determined here but was previously measured by McGonigle (McGonigle 2000) to have an M^2 ~9.

1.3.1.2 UV-CVL at 289 nm

In all the experiments described in this thesis for which the CVL was the pump source, the green + yellow output of the CVL was vertically polarised using an intra-cavity polarising cube. The CVL output was de-magnified from ~25 mm to between 4-6 mm and by using a Keplerian mirror telescope consisting of a 1 m radius of curvature (ROC) focussing mirror and a 0.15 mm ROC recollimating mirror identical to that used previously by McGonigle (McGonigle 2000). This mirror telescope is shown in Figure 1.14. Near the focus of the visible CVL output, a dye-cell containing Rhodamine 6G dye was placed. The dye, pumped by the 511 nm green output and seeded by the yellow output, acted to boost the yellow output of the CVL. This "green to yellow converter" described in detail by Coutts *et al.* (Coutts *et al.* 1990) gave up to 7 W of 578 nm from 19 W of green and yellow CVL output.

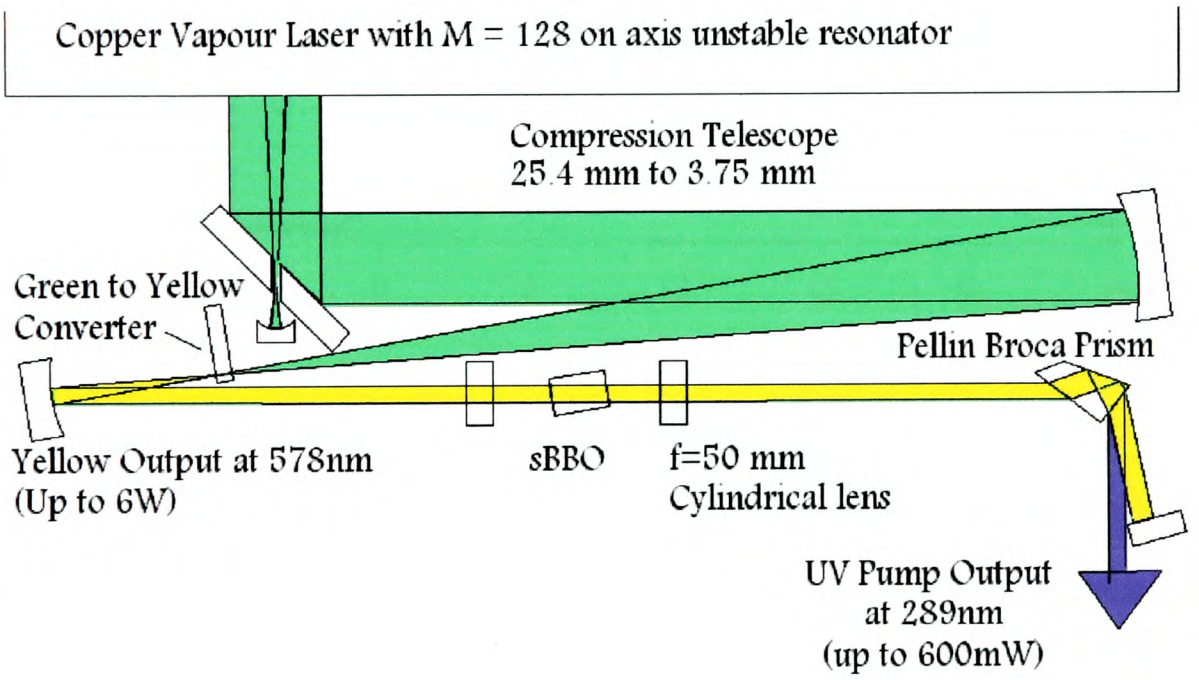


Figure 1.14 Schematic diagram showing CVL pump scheme used to pump Ce:LiLuF at 289nm as used by McGonigle *et al.* (McGonigle *et al.* 1999a).

The boosted yellow output was then focussed into an sBBO frequency-doubling crystal (4 mm x 6 mm x 8 mm) using a nominal focal length of 50 mm cylindrical lens. The crystal was oriented to phase match for TYPE I frequency-doubling of the vertically polarised 578nm yellow light (phase match angle = 42.5°) to give horizontally polarised 289nm UV light. A 578 nm to 289 nm average power conversion efficiency of ~11% was achieved for both the CVL and KE-CVL outputs. The maximum output powers available from the UV-CVL and UV-KE-CVL lasers were ~600 mW and ~1 W respectively. The beam quality of the 289nm output was measured (McGonigle 2000) to be similar to that of the green and yellow CVL output, with an M^2 between 8 and 9. The UV-CVL 289 nm pump pulses are shown in Figure

1.15. The presence of the relatively high pulse intensity towards the back end of the UV-KE-CVL pulse is indicative of the higher beam quality at the back end of this pulse due to the higher frequency-doubling efficiency with the better beam quality. The KE-UV-CVL laser pulse shape was distinguishable from the non-kinetically enhanced UV-CVL pulse as can be seen in Figure 1.15.

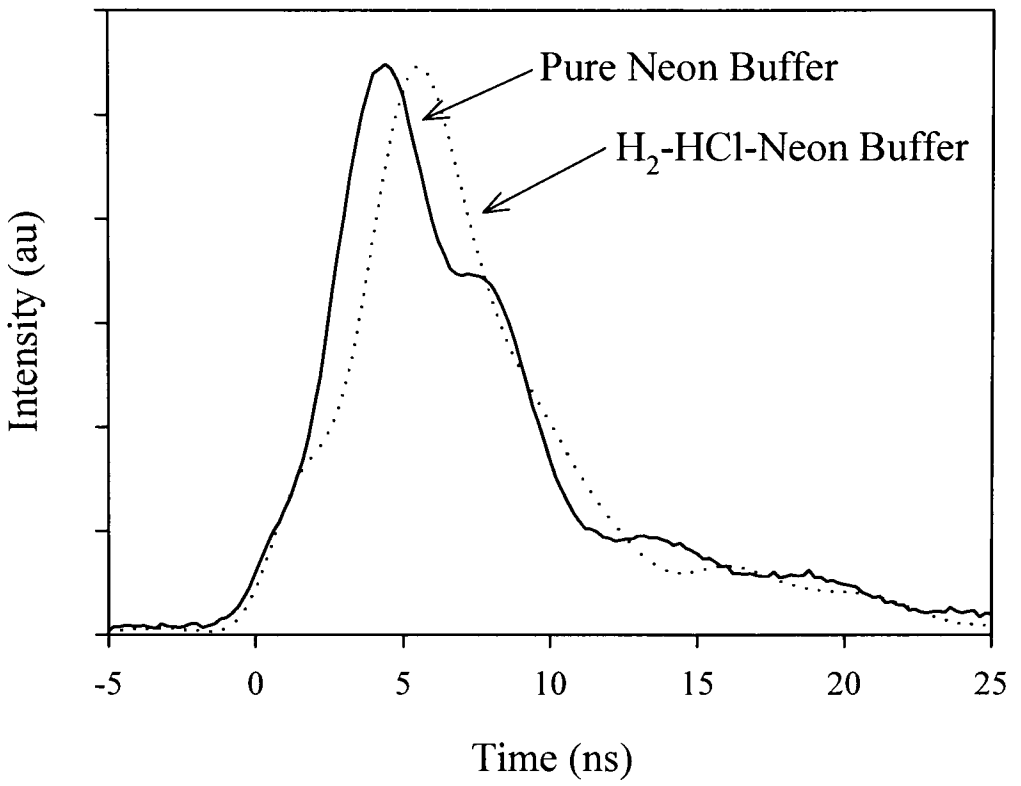


Figure 1.15 UV-CVL laser pulses from the non-kinetically enhanced CVL and the KE-CVL. The gas mix in the KE-CVL contained 1%H_2 + 0.2%HCl with the balance being Neon. The intensities are not on the same scale.

The two harmonics were dispersed using a Pellin-Broca prism. The yellow output was stopped by a beam dump and the UV output was passed through a combination of a ½ -wave plate and polarising cube, aligned such as to allow only horizontally polarised light through. Rotation of the ½ -wave plate allowed excellent control of the pump power. The UV pump beam was then reflected through a focussing lens onto the laser crystal using a 45°, 289 nm turning mirror. The focal length of the focussing lens used in each set of experiments varied between f = 200 mm to f = 80 mm, and is indicated in the experimental configuration description in each section.

The position of the Ce:LiLuF crystal was oriented such that the *c*-axis of the crystal was parallel to the UV 289 nm horizontally polarised pump, throughout the experiments described. Thus for the extent of this thesis, horizontally polarised light shall be referred to as π-polarised and vertically polarised light referred to as σ-polarised. In other words, using this

notation, a π-polarised pumping configuration was maintained throughout the experiments described in this thesis.

1.3.2 Frequency-quadrupled Raman-shifted Nd:YAG lasers as cerium laser pump sources.

In the development and promotion of the tunable all-solid-state UV Ce:LiCAF and Ce:LiSAF lasers (which have a maximum reported slope efficiency of 47%) have received much more attention than the more efficient Ce:LiLuF lasers (maximum slope efficiency ~55%). This is mainly due to the lack of an efficient, convenient, compact and reliable pump source for Ce:LiLuF. As mentioned previously Ce:LiSAF lasers (290 nm) have been successfully used to pump Ce:LiLuF (Laroche *et al.* 10 -15 September 2000; Rambaldi *et al.* 1998), as has the quintupled Nd:YAG laser (213 nm) (Sarukura *et al.* 1998). Although the frequency-quadrupled Nd:YAG-pumped Ce:LiSAF (or Ce:LiCAF) laser and the quintupled-Nd:YAG lasers are all-solid-state pump sources that do provide pump light at an appropriate wavelength for Ce:LiLuF, they are relatively inefficient. In general, so as to get a suitable pump source for Ce:LiLuF using Nd lasers as the all-solid-state pump source, one requires either 5^{th} harmonic generation or 4^{th} harmonic generation with one non-harmonic conversion step to get to a suitable wavelength.

In the last few years efficient Raman-shifted frequency-doubled Nd:YAG lasers have been developed by Pask and Piper at Macquarie University in Sydney, Australia (Pask and Piper 3-6 Feb. 2002; Pask and Piper 1998; Pask and Piper 1999; Pask and Piper 2000). These lasers can provide up to 1.4 W of yellow output at 10 kHz, at a wavelength 577.8 nm (almost identical to the wavelength of the CVL yellow output of 578.2 nm). This yellow laser was possibly ideal as an all-solid-state pump source for Ce:LiLuF. The 578 nm output of the frequency-doubled Raman-shifted Nd:YAG laser could be frequency-doubled to give light at 289 nm, falling in the 292 nm absorption band for Ce:LiLuF. A long-standing collaboration has existed between Macquarie University and the Clarendon Laboratory at Oxford University and as such the frequency-doubled Raman-shifted Nd:YAG laser was made available to investigate the possibility of pumping Ce:LiLuF with this efficient all-solid-state pump source.

The more recent availability of solid-state Raman crystals has made Raman-shifting more user-friendly compared to the use of gaseous or liquid media to induce a Raman shift in laser output. The intra-cavity design capability of solid-state Raman crystals is a particular advantage over Raman-shifting in a liquid or gaseous media (Basiev and Powell 1999). The yellow Raman lasers developed by Pask and Piper were developed initially for use in

dermatology for the removal of vascular lesions, for which the main requirement of the laser was to be strongly absorbed by haemoglobin. The sources used presently for such medical procedures are dye lasers (~585 nm), Krypton ion lasers (568 nm) and CVLs (578 nm). An all-solid-state alternative with the turn-key reliability and compactness of a solid-state laser is thought particularly attractive for use in dermatology.

The approach taken by Pask and Piper (Pask and Piper 1998) in developing an all-solid-state Raman laser was to use intra-cavity stimulated Raman shifting (SRS) in $LiIO_3$ to shift 1064 nm Nd:YAG output to 1156 nm and then intra-cavity frequency-doubling the 1156 nm output in LBO to generate 578 nm. In contrast to the all-solid-state laser sources used previously to pump Ce:LiLuF, in the Raman laser used in the experiments reported in this thesis, both the non-harmonic step (Raman conversion of 1064 nm to 1156 nm) and the first harmonic step (frequency conversion of 1156 nm to 578 nm) are carried out intra-cavity, where non-converted wavelengths are efficiently recycled.

The full details of the frequency-doubled Raman-shifted Nd:YAG laser used in this thesis have been reported in detail by Pask and Piper (Pask and Piper 3-6 Feb. 2002; Pask and Piper 1999). A basic description of the Macquarie yellow laser is also given here for convenience. Briefly, the laser is pumped by 18 W from a fibre-coupled diode laser at 808 nm. The fundamental output at 1064 nm from a Nd:YAG laser crystal was acousto-optically Q-switched with a repetition rate of 10 kHz. Intra-cavity stimulated Raman shifting (SRS) of 1064 nm in a $LiIO_3$ crystal generated a first Stokes wavelength of 1156 nm. The 1156 nm Raman output was then frequency-doubled intra-cavity, using LBO, to generate up to 1.4 W of 578 nm yellow output at 10 kHz. The pulse duration of the yellow output was ~12 ns. Because the fundamental and infrared powers were recycled intra-cavity, the overall efficiency of the yellow laser source was high (~7%) with respect to the diode pump power. The folded nature of the cavity used in the Raman laser, resulted in a particularly compact pump system, with an overall cavity length of ~25cm. The M^2 of this laser was measured by the author to be approx 2.5. The cavity configuration of the Raman laser is shown schematically in Figure 1.16.

The UV part of the setup is included in the schematic Ce:LiLuF laser cavity diagram in Figure 6.1 but described in detail here. A Keplerian mirror telescope was used to collimate the yellow output of the Raman laser and double the spot-size to be ~1.5 mm in diameter. A Berek polarization compensator was then used to convert the horizontally-polarised yellow light into vertically-polarised yellow light to match the 4^{th} harmonic generation geometry. The 4^{th} harmonic geometry used to double the 578 nm Raman laser output was identical to that used to double the 578 nm CVL output described in §1.3.1.2. To reiterate, an f = 50 mm

cylindrical lens was used to line focus the yellow beam into the 8 mm long BBO crystal. The resulting UV beam was re-collimated using another f = 50 mm cylindrical lens. The UV light was separated from the unconverted yellow light using a Pellin-Broca prism. The frequency-doubling of the yellow laser from 578 nm to 289 nm using the BBO crystal had an efficiency of ~26%. This compares favourably with previous 23% conversion efficiency obtained with a CVL (McGonigle *et al.* 1999a) and the 11% conversion efficiency found for the UV-CVL (§1.3.1.2) used in Chapters 3, 4 and 5. The good conversion efficiency obtained in the 4th harmonic generation of the Raman-shifted Nd:YAG laser was thought to be due to the high beam quality and high peak power of the yellow laser. The 289 nm pump laser was measured to have an M^2 value of 2.8.

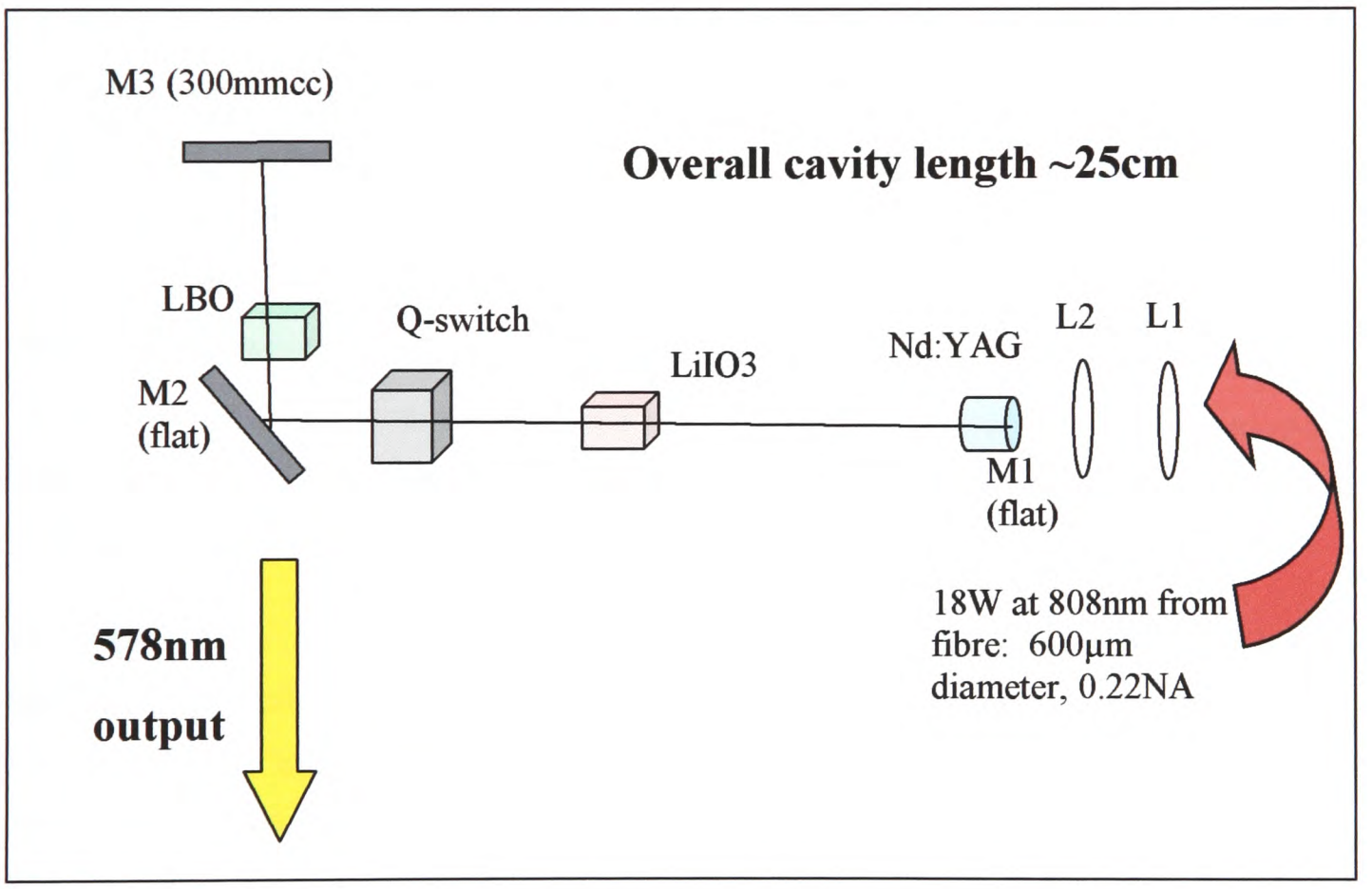


Figure 1.16 shows a schematic diagram of the frequency-doubled Raman-shifted Nd:YAG laser developed by Pask and Piper (Pask and Piper 3-6 Feb. 2002).

1.4 Thesis Outline

This thesis focuses on the use of Ce:LiLuF as a tunable UV laser crystal. The investigations reported here concentrate specifically on three main areas of Ce:LiLuF laser development. Firstly, experiments were carried out with the aim of gaining an understanding of the anomalous lasing behaviour of Ce:LiLuF observed by McGonigle *et al.* (McGonigle *et al.* 1999a; McGonigle *et al.* 1999c; McGonigle *et al.* 2001b). These results are described in

Chapter 2 and Chapter 3. Secondly, the development of a narrow-bandwidth Ce:LiLuF laser for use in OH monitoring is described in Chapter 4. Finally in Chapter 5, the novel use of a frequency-quadrupled Raman-shifted all-solid-state Nd:YAG laser, as a pump source for Ce:LiLuF, is reported for the first time.

In Chapter 2, the polarised small-signal gain was measured for Ce:LiLuF across most of the laser emission spectrum of the crystal (where accessible with the dye laser available). The dependence on temperature and polarisation of the 327 nm and 309 nm small-signal gain was investigated fully (corresponding to the two emission peaks in Ce:LiLuF). Single-pass gains as high as 10±1 (equivalent to a gain coefficient 30±3 cm^{-1}) were measured in Ce:LiLuF with an absorbed pump fluence of 0.46 J/cm^2. Further, the excited-state absorption was measured at 261 nm and 349 nm. The polarisation dependence of GSA, ESA and colour centre formation was proposed to arise from the mixed nature of the lowest *5d* level wave-function. With the aid of a finite-difference numerical simulation, the polarised excited-state absorption cross-sections at 309 nm, 327 nm, 261 nm and 349 nm were determined. Using the gain and ESA measurements, the presence of a broad ESA band (<261 nm to >349 nm) was identified and its origin was proposed to arise from a transition between the lowest *5d* state and the conduction band. A narrow, temperature dependent absorption band was also observed, between ~300-340 nm. This narrow absorption band was tentatively assigned to absorption by colour centres.

In Chapter 3, the results of investigations in which the affect of the colour centre absorption and ESA on Ce:LiLuF lasing behaviour are reported. Three main areas of Ce:LiLuF lasing are reported: firstly, the dominant 309 nm laser emission was investigated; secondly, 327 nm lasing was investigated in which a wavelength selective output coupler was used to force 327 nm lasing to occur in preference to 309 nm lasing; finally the tunability of the laser output was investigated thoroughly. In both the latter laser cavity configurations, the output was found to be made up of multiple polarisation and wavelength components. The effect of temperature on Ce:LiLuF lasing in each of these three cases was investigated and is reported in detail. The effect of a polarisation selection element in the laser cavity is presented including the observation of a 330% increase in 327 nm laser output power.

Using a simplified Ce:LiLuF laser model, simulations of the various laser cavity configurations were performed enabling an understanding of the competing gain, ESA and loss effects in the various laser cavity configurations to be achieved. The presence of multiple wavelength and polarisation components in the laser outputs are thought to arise from the gain-switched nature of lasing in Ce:LiLuF when pumped with a UV-CVL. Overall the

presence of σ-polarised lasing in Ce:LiLuF was found to be detrimental to the laser efficiency due to the dominance of σ-polarised ESA at the laser wavelengths in Ce:LiLuF.

In Chapter 4, two main laser cavity designs used, in the pursuit of narrow-bandwidth lasing in Ce:LiLuF, are described and the resulting laser bandwidths are reported. A number of the different wavelength selection elements used in these two cavities are described. The narrowest 308 nm bandwidth of 0.7 cm^{-1} was achieved using a telescope laser cavity with a single AR coated prism expander and a blazed UV diffraction grating in Littrow configuration.

In Chapter 5, using the new frequency-quadrupled Raman-shifted Nd:YAG pump at 289 nm, a slope efficiency of 62±3% with respect to absorbed pump power was obtained for Ce:LiLuF with lasing at 309 nm. This slope efficiency is the highest reported slope efficiency for Ce:LiLuF to date. The IR-to-UV total conversion efficiency of the laser was 0.41%. These experimental results provide evidence of highly efficient Ce:LiLuF lasing with an ideal all-solid-state pump source, in the absence of which has, until now, limited the development of Ce:LiLuF as a highly efficient commercial tunable UV laser.

Chapter 6 summarises the results presented in this thesis and discusses the implications of this work. Proposed avenues for future research on cerium lasers are also discussed.

[2] Detailed Spectroscopic Characterisation of $Ce:LiLuF_4$

Prior to the present work, emission and absorption spectra had been measured for Ce:LiLuF but the key cross-sections had not been determined. In this chapter, emission, ground state absorption (GSA) and excited-state absorption (ESA) cross-sections are determined using both experimental and theoretically simulated results. Using the determined cross-sections a number of proposals are presented explaining the possible origin of the polarisation and temperature dependence of the small-signal gain and excited-state absorption behaviour displayed by Ce:LiLuF.

2.1 Emission cross-section measurement and calculation

In Chapter 1, the *4f – 5d* emission and absorption characteristics of Ce:LiLuF are described. These are well known and mostly understood, however the detailed cross-sections of the *4f→5d* radiative absorption and the *5d→4f* radiative emission have not yet been determined. In this section the emission cross-sections for the fluorescence emission spectrum of Ce:LiLuF are determined and the absorption cross-section for 289 nm, π-polarised light, namely the pump wavelength used throughout this thesis, is approximated.

2.1.1 Experimental Configuration

In the determination of the emission cross-sections for Ce:LiLuF, the crystal studied was grown using the Czochralski technique at the Université de Maine, in France. This crystal was 0.78 (±0.05) mm long giving ~77% absorption of the π-polarised, 289nm pump. The Ce^{3+} doping was known to have a value somewhere between 0.4 mol% and 0.04 mol % (see §2.2.2). This crystal was cut from the same boule as the crystal used by McGonigle *et al.* (McGonigle *et al.* 1999a), however, the crystal used by McGonigle *et al.* was 2mm long, thus giving 95% pump absorption at 289 nm. The crystal was cut such that the crystallographic c-axis was contained within the horizontal plane of the end faces and the crystal faces were uncoated. The crystal was mounted on a brass water-cooled mount, such that good thermal contact was made between the crystal and the mount. The temperature of the crystal could be varied, using a Melcor solid state thermoelectric recirculating chiller, between room temperature (~25°) and -3°C.

Excitation of Ce:LiLuF was obtained by focussing the 4 mm diameter beam from a 10 kHz, UV-KE-CVL laser, described in §1.3.1.2, into the Ce:LiLuF crystal, using a 100 mm focussing lens, giving a pump spot diameter in the crystal of ~ 74 μm. The fluorescence was detected using a SPEX Minimate spectrometer with an attached SWH-04 Thorn EMI photo multiplier. The two polarizations in the fluorescence were separated using a broadband UV polarizing beam-splitter cube. A second polarizing cube, aligned at 45^0, was inserted in front of the detection set-up to eliminate the need to correct for the polarization-dependence of the spectrometer. The emission intensity results were adjusted to take into account the wavelength dependent response of the photomultiplier.

2.1.2 Results

The absolute emission cross sections were determined by the numerical integration of the polarized fluorescence emission spectrum of Ce:LiLuF using Equation 2.1 (Marshall *et al.* 1994),

$$\sigma_i(\bar{\nu}) = \frac{3\lambda^2 I_i(\bar{\nu})}{8\pi c n^2 \tau \int \left[2I_\sigma(\bar{\nu}) + I_\pi(\bar{\nu})\right] d\bar{\nu}} \qquad 2.1$$

where $I_i(\bar{\nu})$ is the relative intensity expressed in photons per wavenumber, with i denoting polarisation, namely σ or π. λ and c are the wavelength and the speed of light respectively, n, the refractive index was approximated for LiLuF from those measured for LiYF to be 1.47 for

σ-polarised light and 1.49 for π-polarised light (Weber 1986) and τ, the radiative emission lifetime of Ce:LiLuF used was 39 ns. The measured lifetime was found to be 37.7± 0.4ns (Figure 2.1), which is in good agreement with previously reported emission lifetimes for Ce:LiLuF of 40±2 ns (Sarukura *et al.* 1995b) thus 39 ns, the average of the measured and previously reported lifetime, was used in the determination of the emission cross-sections.

The σ- and π- polarised emission cross sections for Ce:LiLuF thus calculated are shown in Figure 2.1. Figure 2.1 shows that both the σ- and π-polarised emissions have two emission peaks, corresponding to the $F_{5/2}$ and $F_{7/2}$ splitting in the 4f level of Ce^{3+}. The σ-polarised emission peaks were at 307 nm and 327 nm with respective emission cross sections of $4.2x10^{-18}$ cm^2 and $6.9x10^{-18}$ cm^2. The π-polarised emission peaks were at 309 nm and 330 nm, with emission cross-sections of $6.7x10^{-18}$ cm^2 and $4x10^{-18}$ cm^2 respectively. The emission spectrum and lifetime of Ce:LiLuF were found to be independent of temperature in the range of -5 ^{0}C to 30 ^{0}C.

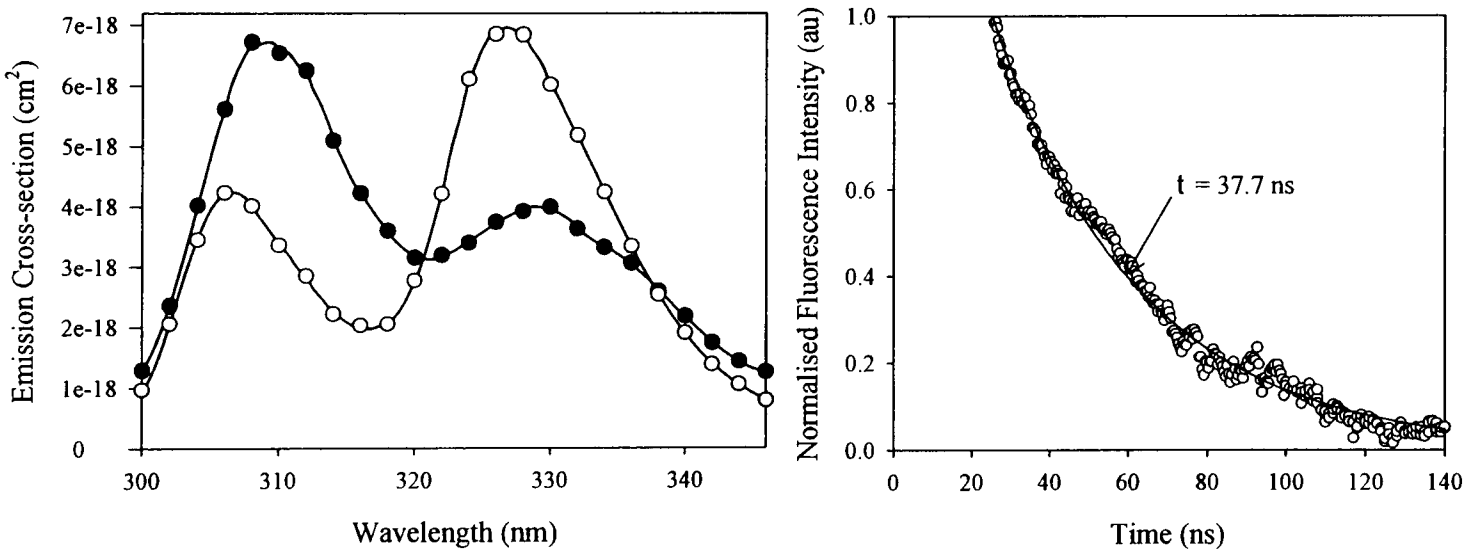


Figure 2.1 shows the polarised fluorescence emission spectrum of Ce:LiLuF. The fluorescence lifetime is depicted in the right-hand figure.

2.2 Absorption coefficient determination at 289 nm for π-polarised light.

2.2.1 Experimental Configuration

The UV-KE-CVL described in §1.3.1.2 was used as the pump source in these experiments providing pump powers up to ~800mW of 289 nm radiation. The transmission of an unfocussed π-polarised 289 nm pump beam, through the Maine grown 0.78 mm Ce:LiLuF

crystal, was determined. A photodiode and Tektronix TDS 3034 oscilloscope were used to detect the transmitted pump pulse both with the crystal in the light path and with no crystal present. The pump power used was 650 mW. The unfocussed pump was used so as to obtain the transmission of π-polarised, 289 nm light when no saturation of the absorption from the *4f level* to the *5d level* was present.

The transmission of the pump when focussed was also determined in order to assess the saturation of the lower 4f laser level at these pump powers. A focussing lens of 100 mm was used giving a calculated pump spot diameter of ~74 μm. This transmission was measured in the same manner as that used for the unfocussed pump.

2.2.2 Results

Using the detected pump pulses, the simple ratio of the pump pulse with the crystal in the light path, I_{out}, over the pump pulse with no crystal in place, I_{in}, gave the transmission, T, of π-polarised, 289 nm light through Ce:LiLuF. This transmission was found to be ~ 22±1% for the unfocussed pump beam. Taking into account the reflection losses at the air-crystal interfaces determined using Equation 2.2

$$R = \left(\frac{n_{crystal} - n_{air}}{n_{crystal} + n_{air}} \right)^2 \qquad 2.2$$

where n is the refractive index, giving reflection losses of $R \sim 4\%$ per interface gives an effective incident intensity, I_{0eff}, of $0.92I_0$ where I_0 is the actual incident intensity. Using the relationship in Equation 2.3

$$I = I_{0eff} e^{-\alpha_{ABS} l} \qquad 2.3$$

in which I/I_{0eff} is the transmission of the unfocussed pump beam and l is the length of the crystal, the absorption coefficient, α_{ABS}, for Ce:LiLuF was determined to be 18.3 ± 4cm^{-1} for π-polarised 289 nm light. Further analysis using the measured absorption coefficient measured here and the relationship in Equation 2.4, the number density, N_{4f}, of Ce:LiLuF could be determined.

$$\alpha_{ABS} = \sigma_{ABS} . N_{4f} \qquad 2.4$$

Due to near identical Ce^{3+} crystal field splitting of the Ce^{3+} ions in Ce:LiYF and Ce:LiLuF (Sarukura *et al.* 1995a) an estimate of the π-polarised absorption cross-section at 289 nm was

made using the previously determined Ce:LiYF absorption cross sections determined by M. Laroche, from the University of Caen in France, with cerium concentrations measured at the Laboratory of Vernaison, in France (see Figure 2.2). Using the π-polarised absorption cross-section of Ce:LiYF at 289 nm of $3.35 \times 10^{-18} cm^2$ and the absorption coefficient of $18.3 cm^{-1}$, determined from the transmission measurements, the Ce^{3+} number density was found to be $(5 \pm 1) \times 10^{18}$ cm^{-3}. This number density corresponds to a molecular percentage of Ce^{3+} in this Ce:LiLuF crystal of (0.04±0.01) mol%, calculated using the density of Ce:LiLuF as found by Combes *et al.* (Combes *et al.* 1997) of 5.96 gcm^{-3} ($5.96 \times 10^3 kgm^{-3}$). The 289 nm absorption cross-section of Ce:LiLuF measured here using the absorption coefficient is in agreement with independent 290 nm absorption cross-section calculations made at the University of Caen for the 2 mm Ce:LiLuF crystal cut from the same Ce:LiLuF boule (mentioned in section §2.1.1). The method used at Caen was similar to the method of number density determination used here.

The concentration of cerium in the Maine Ce:LiLuF crystal was also determined by Inductively Coupled Plasma – Mass Spectroscopy (ICP-MS) at Macquarie University in the Geochemistry Department and was found to be 0.413±0.066 mol% of cerium (equivalent to a number density of $5.6 \times 10^{19} cm^{-3}$). This concentration of cerium is 10 times that determined using the absorption coefficient just discussed. This discrepancy is thought to be due to the fact that ICP-MS determines the overall cerium concentration in the Ce:LiLuF crystal as opposed to the active Ce^{3+} concentration.

The measured absorption coefficient is representative of the Ce^{3+} in the crystal, thus the number density determined using the absorption coefficient method is possibly more accurate for the Ce^{3+} concentration determination. The reproducibility of the number density calculations for the two different crystals from the same boule implies that the difference in the number densities measured using the ICP-MS and absorption coefficient method is not due to an inhomogeneous distribution of the cerium doping within the LiLuF crystal. The former value determined using the absorption coefficient will be used in the calculations made in this thesis, the reasoning for which is discussed further in §2.5.1.

A comparison of the unfocussed and focussed pump transmissions showed an increase in the transmission at 289 nm with focussing, from T = 22±1% to T = 31±1%. This implies that there was some saturation of the lower *4f* population resulting in a decreasing absorption with increasing pump intensity.

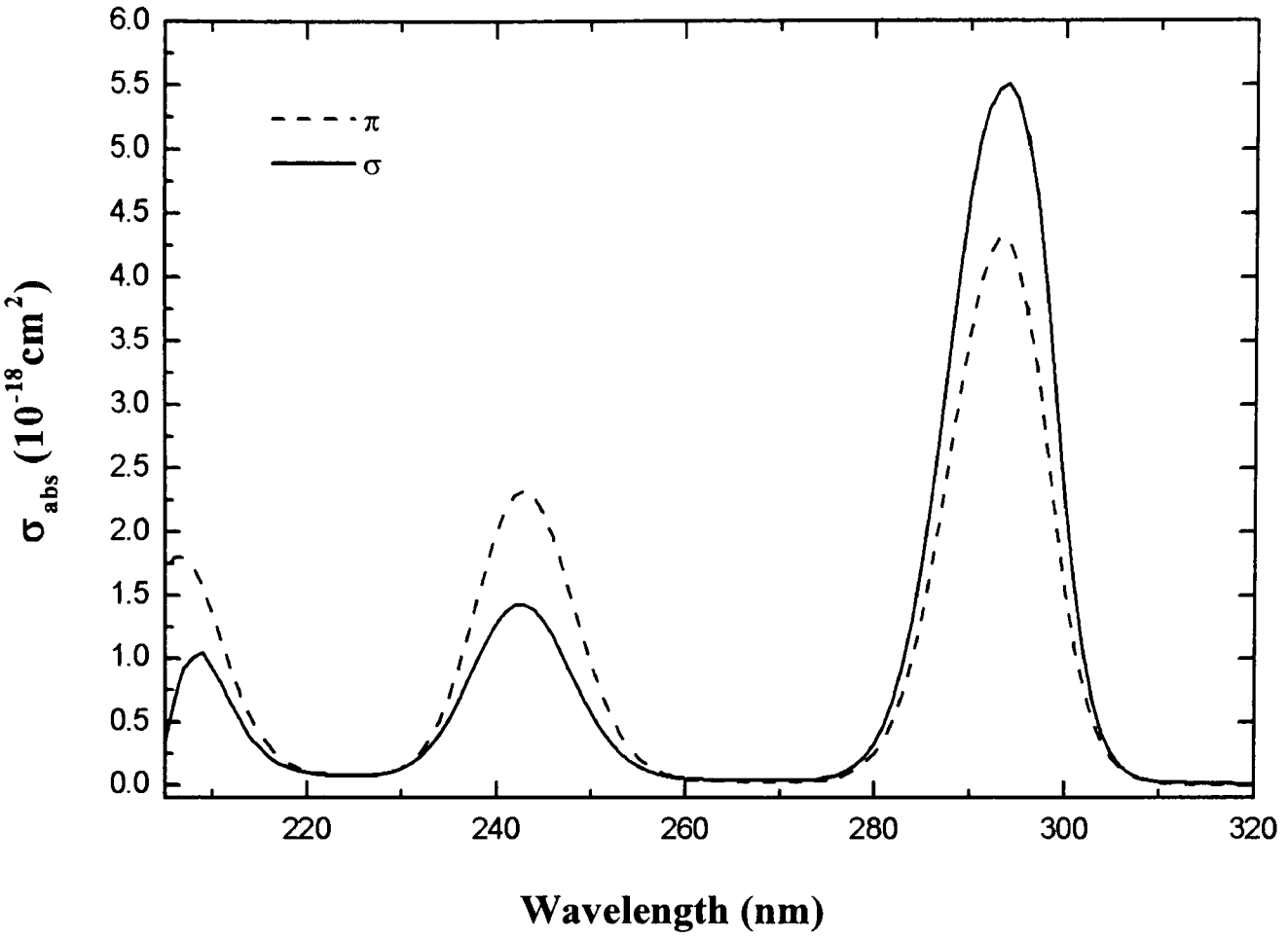


Figure 2.2 Absorption cross-section for Ce:LiYF determined at the University of Caen, France.

2.3 Small signal Gain Measurements for Ce:LiLuF

A thorough study of the small-signal single-pass gain in Ce:LiLuF is presented in this section in order to understand more fully the laser behaviour of Ce:LiLuF seen by McGonigle *et al.* as described in Chapter 1. McGonigle *et al.* (McGonigle *et al.* 2001b) found the laser output of the Ce:LiLuF laser to increase with decreasing temperature over all of the tuning curve of Ce:LiLuF, except at the 327 nm peak, where there is actually a decrease in laser output and a "flipping" of polarisation from π- to σ-polarised 327 nm emission. In order to investigate this behaviour the small-signal gain was measured across most of the tuning band of Ce:LiLuF. Further measurements were then made concentrating on the emission and gain peaks at 309 nm and 327 nm. At both wavelengths, both the σ- and π-polarised gain was investigated such that the anomalous 327 nm lasing observed by McGonigle *et al.* could possibly be explained. The temperature dependence of the small signal gain was also investigated in the hope of gaining more insight into the effect crystal temperature has on lasing.

2.3.1 Experimental Configuration

In the determination of the small signal gain of Ce:LiLuF, two Ce:LiLuF crystals from different origins were used. The first crystal studied was the Maine crystal described in

§2.1.1. As mentioned, this crystal was 0.78 mm long giving ~77% absorption of the π-polarised 289nm pump. The second crystal used was a Ce:LiLuF crystal grown using the Bridgman-Stockbarger technique at the former Kazan State University (0.8 wt% = 1.5mol% Ce^{3+} doping). The crystal was 2 mm long giving ~95% absorption of the π-polarised, 289 nm pump. This crystal was the same crystal for which results have been published by Coutts *et al.* (Coutts *et al.* 1996) and McGonigle *et al.* (McGonigle *et al.* 1999a). Both crystals were cut such that the crystallographic *c*-axis was contained within the horizontal plane of the end faces and in both cases, the crystal faces were uncoated. Again, the crystals were mounted on a brass water-cooled mount and the temperature of the crystal could be varied between room ~25 °C and -3 °C.

The pump source used to excite the CeLiLuF crystal was the UV-CVL (non-kinetically enhanced) described in §1.3.1.2. The probe laser used in these gain measurements was a 10kHz Q-switched, frequency-doubled, Q-peak Nd:YLF pumped LAS Intra-dye II laser. The dye used was Rhodamine 640 in ethanol (0.15 mM) giving a tuning range from 595 nm to 655 nm as shown in Figure 2.3, and a bandwidth of ~0.002 nm when doubled to the UV (measured by McGonigle (McGonigle 2000)).

Frequency-doubling of the dye laser was achieved by line focussing the laser into a 3 x 5 x 8 mm BBO crystal cut such that the central phase-match angle was 39°, which was then tuned to double the specific output of the dye laser being used. The tuning range of the frequency-doubled dye laser was 300-327 nm, and the output was σ-polarised. The polarisation of the probe was controlled using a ½ wave plate and polarising cube combination. The pulse length (FWHM) of the UV probe was approximately 16 ns. A telescope was used to collimate the frequency-doubled dye laser output before it was aligned with the pump beam. The intensity of the probe was controlled to be <1 mW by the use of neutral density UV filters. This minimal probe intensity ensured the gain was not saturated (50 nJ probe pulse energy compared to pump pulse energies of the order 10 μJ).

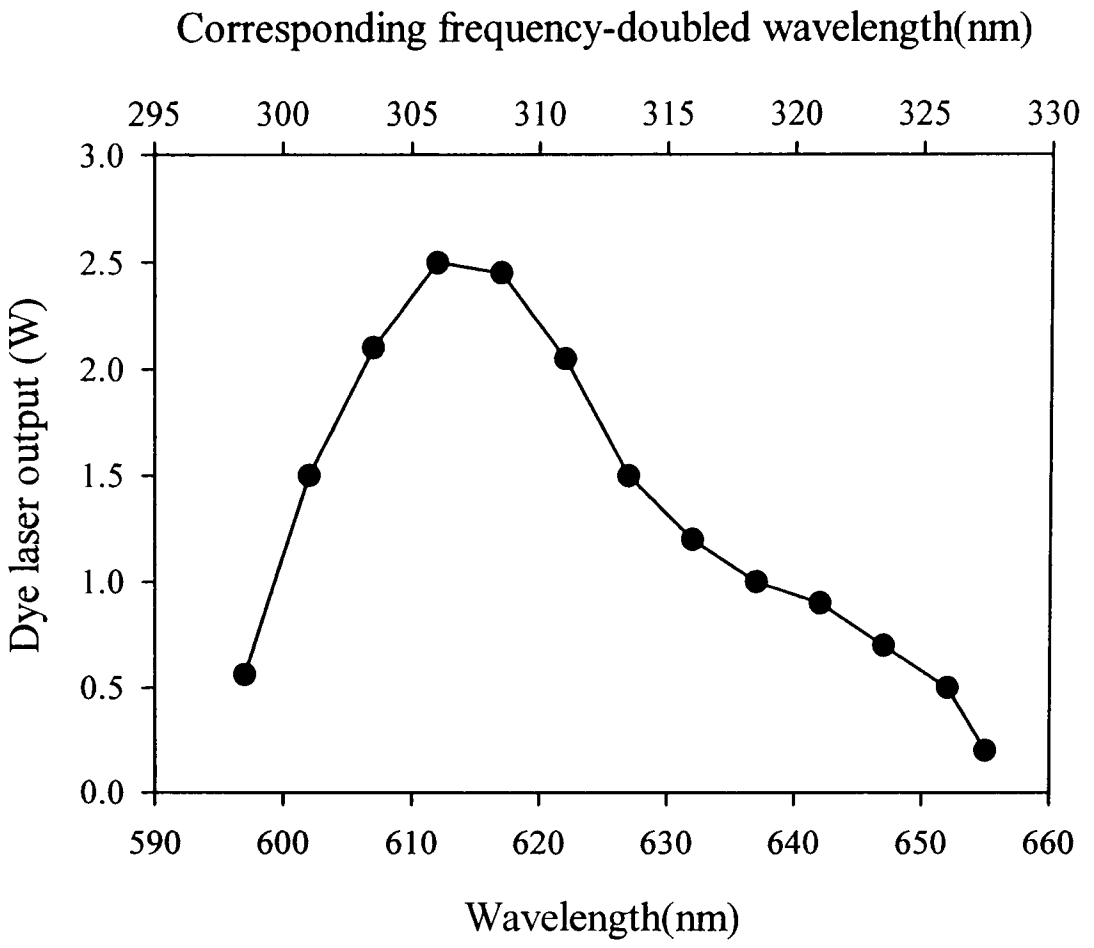


Figure 2.3 Tuning curve of the frequency doubled Nd:YLF pumped LAS dye laser

The pump and π-polarised probe beams were combined at a 45° dichroic mirror as shown in Figure 2.4. The alignment of the pump with the probe was verified in both the near field (~5 cm) and far field (~12 m) for each measurement. For the measurements with the σ-polarised probe, the same arrangement was used as with the π-polarised probe, however, the angle of the 45° mirror was increased such that the angle between the probe and the normal of the dichroic was between 65° and 75°. This was done so that more σ-polarised probe passed through the mirror, as with the dichroic mirror at 45° most of the σ-polarised probe was reflected. In order for the pump to reflect off the mirror at the correct angle, with the mirror at 65°-75°, a 45° prism was placed in the pump beam such that the beam was bent at an angle allowing alignment of the pump beam with the probe beam at the dichroic mirror, as with the π-polarised probe.

The probe beam size was ~2 mm in diameter compared to the ~6 mm pump beam size. The overlapping probe and pump beams were focussed using a 200 mm focussing lens into the Ce:LiLuF crystal (as opposed to the 100 mm lens used in emission cross-section determination) giving pump and probe spot diameters of 110 μm (M^2~9) and 39 μm (determined assuming an M^2=1) respectively. The position of the focus in the crystal was determined using the focal position resulting in maximum transmission of the pump through

the crystal. The small probe spot size meant the more uniform central region of the pump beam was being probed and consequently it was not necessary to take the spatial pump pulse shape into account when analysing the gain results.

The timing of the pump and probe pulses were adjusted for maximum gain using a Stanford DG535 digital delay generator triggered off the Q-switch signal from the frequency-doubled Nd:YLF pump laser. The CVL was triggered, via the digital delay generator, off the Q-switch signal of the Nd:YLF laser, with a jitter of 10-20 ns between the Q-switch and CVL pulses. The delay between the pump and probe pulses required to achieve maximum gain was ~10ns corresponding to the peak fluorescence, hence coinciding with the peak population inversion as expected.

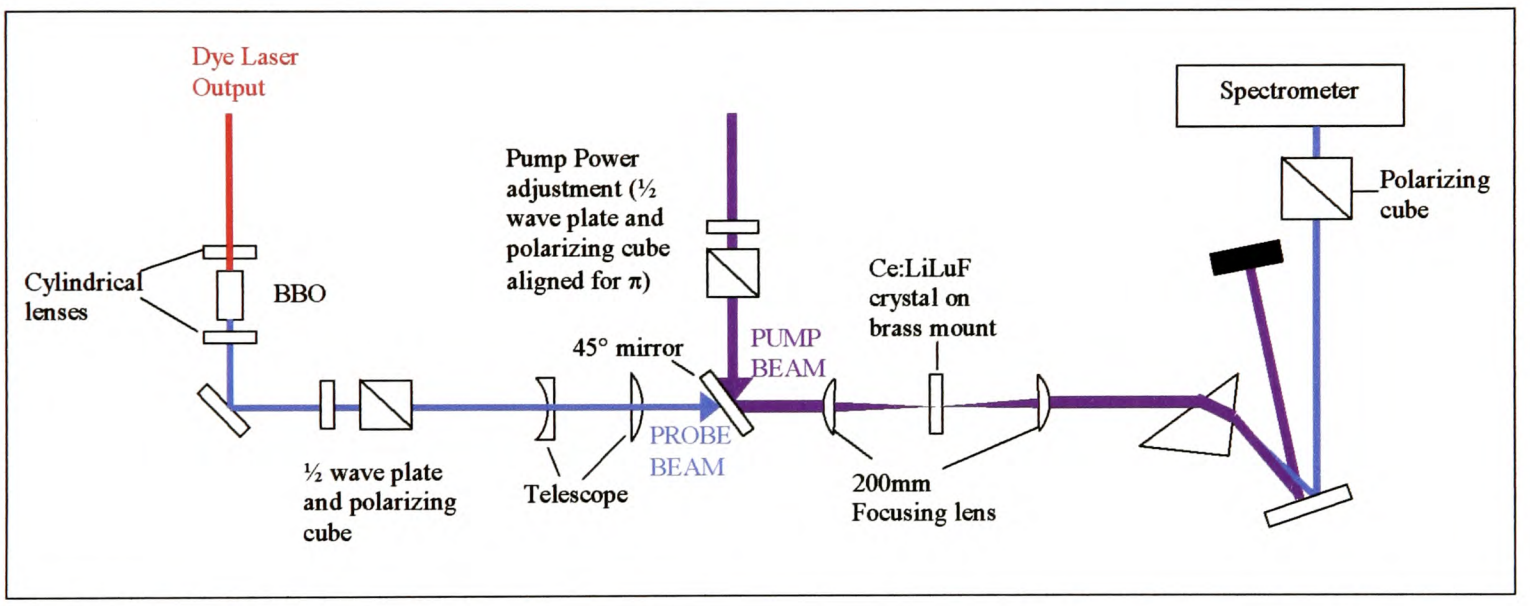


Figure 2.4 Schematic diagram of the experimental configuration used in the determination the small-signal single-pass gain for Ce:LiLuF.

After the Ce:LiLuF crystal, the pump and probe beams were split using a prism, the pump beam was blocked and the probe was sent into a 0.22 m SPEX Minimate spectrometer and detected on a photomultiplier tube as described in the emission cross-section measurements in §2.1.1. In each gain measurement, a reference probe pulse was recorded with the probe pulse shifted forward 100 ns, so as to arrive before the pump pulse, and thus it experienced no amplification. The timing was then adjusted back 100ns to coincide with maximum gain and the amplified probe was recorded in exactly the same way as the reference probe, thus it was not necessary to take into account the wavelength dependence of the photodiode and no other systematic errors were introduced. The oscilloscope was triggered off the fluorescence using a separate photodiode. A background subtraction was made, subtracting the fluorescence emission from the amplified probe pulses, as the fluorescence intensity reaching the photomultiplier was large enough to introduce errors at the low probe powers. In order to

negate the effects of the pump-probe jitter the oscilloscope was set such that it averaged 256 pulses for each reading.

2.3.2 Results

The small-signal single-pass gain was determined with variation of temperature, pump power, wavelength and polarisation.

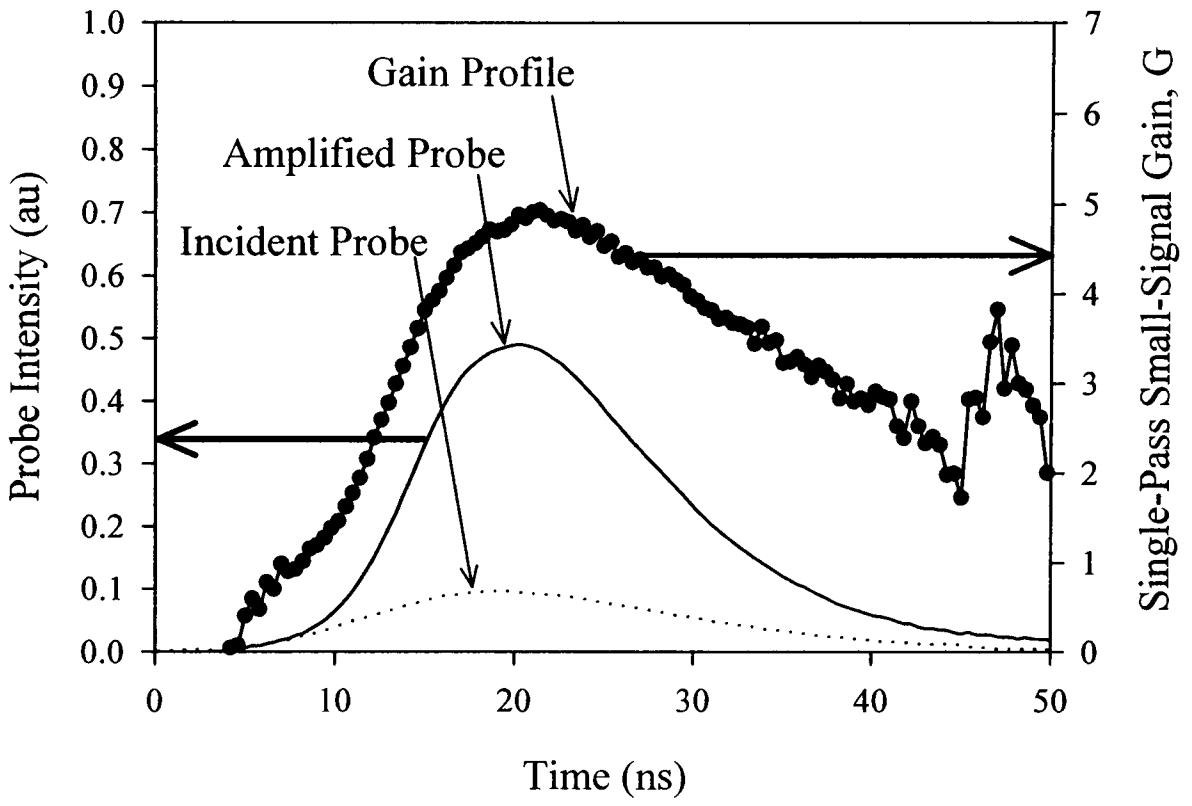


Figure 2.5 shows the 327 nm, σ-polarised incident probe pulse intensities, shown shifted backwards by 100ns in this figure, coincident with the amplified probe pulse. The corresponding small-signal gain profile for the σ-polarised 327 nm probe with 400mW pump power is also shown.

The polarised small-signal gain was measured with a pump power of 300mW (0.35 J/cm^2 incident pump fluence) over the tuning range of the frequency-doubled dye laser output. In the determination of the small signal gain a simple ratio of amplified probe, I_{out}, and incident probe, I_{in}, was taken such that G, the single-pass small-signal gain was given by Equation 2.5.

$$G = I_{out} / I_{in} \qquad 2.5$$

The probe pulse amplification is shown in Figure 2.5. The noise on the end of the gain profile (>45 ns) is due to the very low signal intensity after 40 ns and corresponding large error due

to these low intensities at these extremes of the probe pulse. The small signal gain measurement was taken at the peak of the gain profile.

The small-signal gain coefficient is described by equation 2.6 where G is the small-signal single-pass gain, α_G is the gain coefficient and l is the length of the crystal.

$$G = e^{\alpha_G l} \qquad 2.6$$

The measured small-signal gain coefficient, α_G, versus wavelength is shown in Figure 2.6 along with the polarised emission spectrum for Ce:LiLuF (from §2.1.2). The peak π-polarised gain appears at ~309 nm, with a peak gain coefficient value of 22±2cm^{-1}.

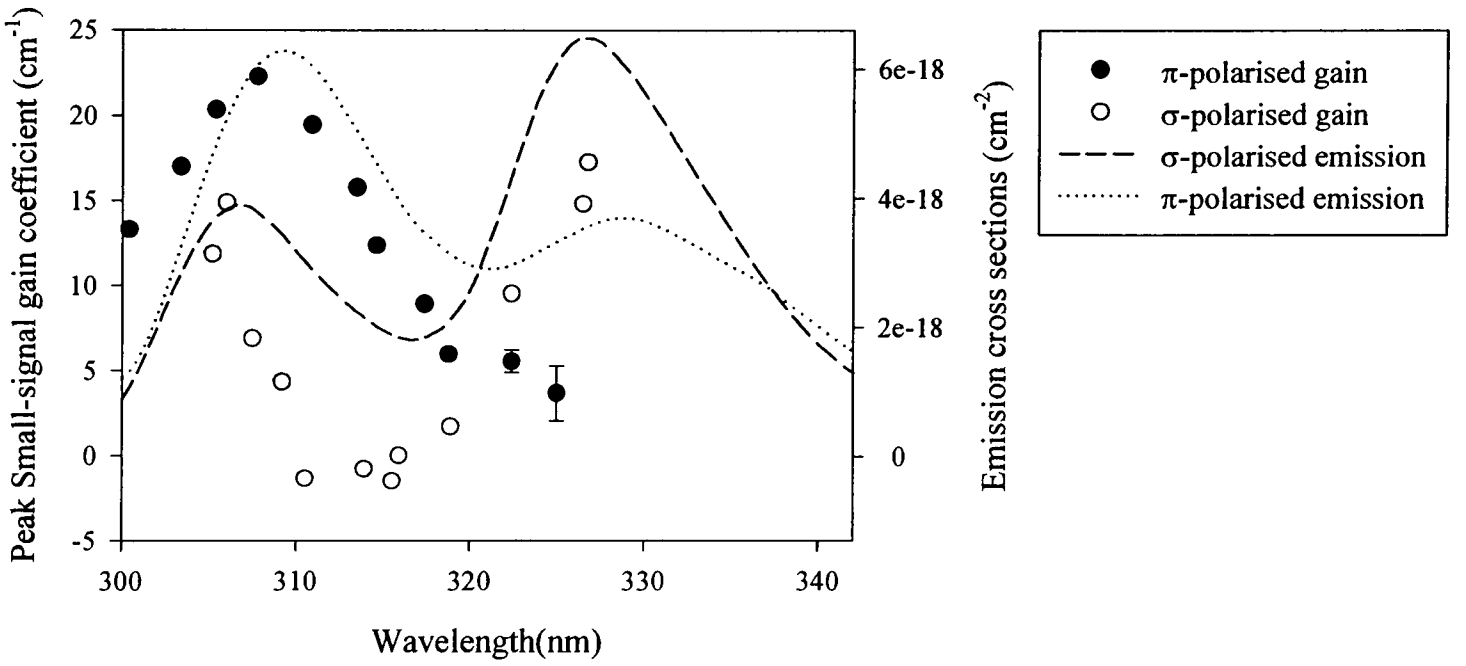


Figure 2.6 shows the σ- and π-polarised small-signal gain coefficient variation with wavelength of Ce:LiLuF measured with 300mW pump power (0.35 J/cm^2 incident pump fluence). The σ-polarised gain was measured at -3°C, whereas the π-polarised gain was measured at ~25°C. Also shown is the polarised emission spectrum of Ce:LiLuF.

Comparison of the gain and emission curves shows the gain spectrum follows the emission spectrum reasonably closely. The 309 nm, π-polarised gain peak was shifted to a slightly shorter wavelength (blue-shifted) in comparison to the 309 nm emission peak. This may have been the effect of a wavelength dependent excited state absorption, since the effective gain cross-section, σ_{EFF}, is dependent on the difference in emission cross-section, σ_{EM}, and excited state absorption cross-section, σ_{ESA}, as shown in Equation 2.7.

$$\sigma_{EFF} = \sigma_{EM} - \sigma_{ESA} \qquad 2.7$$

If the excited state absorption was dependent on wavelength such that the ESA at the shorter wavelengths was less than that at the longer wavelengths, the gain at the shorter wavelengths would be larger than the gain at the longer wavelengths, resulting in a blue-shift in the gain curve relative to the emission curve as seen experimentally here.

It is worth noting that the 327 nm, π-polarised gain was very small and the probe intensity very low at 326 nm hence the errors at 326 nm were significant. It is difficult to make any comments on the position of the longer wavelength π-polarised peak without further measurements.

The σ-polarised gain was determined at -3°C as the gain was more pronounced at the lower temperatures, and so the variation of σ-polarised gain with wavelength was shown more clearly. The π-polarised gain was sufficiently large at room temperature to show the variation with wavelength. For the 327 nm peak, the gain measurements are incomplete due to the limitations of the tuning range of the frequency-doubled dye laser; however, it did appear that the position of the σ-polarised gain peak lay at a similar wavelength to that of the σ-polarised, 327 nm emission peak, with the gain coefficient of 17±2 cm^{-1}. The shorter wavelength peak of the σ-polarised gain was at ~306nm, with a gain coefficient of ~15±2 cm^{-1}. This peak was also slightly blue-shifted from the σ-polarised emission peak. Between 310 nm and 316 nm the σ-polarised gain coefficient was negative implying no gain at these wavelengths. In fact, between 314 nm and 316 nm there was absorption, possibly resulting from the fact that the σ_{ESA} in this region of the tuning curve was greater than σ_{EM}, resulting in a negative σ_{EFF}, thus the overall absorption at these wavelengths for the σ-polarisation. σ-polarised lasing between 314 nm and 316 nm in Ce:LiLuF has not been reported to date in agreement with the lack of σ-polarised gain in this region.

The behaviour of the small-signal, single-pass gain at the emission peaks of 309 nm and 327 nm for both σ- and π-polarised probes was studied more fully, as well as the absorption at 316 nm of the σ-polarised probe. The gain with incident pump power was investigated first with the crystal at room temperature (~25°C). The temperature of the Ce:LiLuF crystal was then cooled to -3°. The results of these experiments are shown in Figure 2.7 and Figure 2.8.

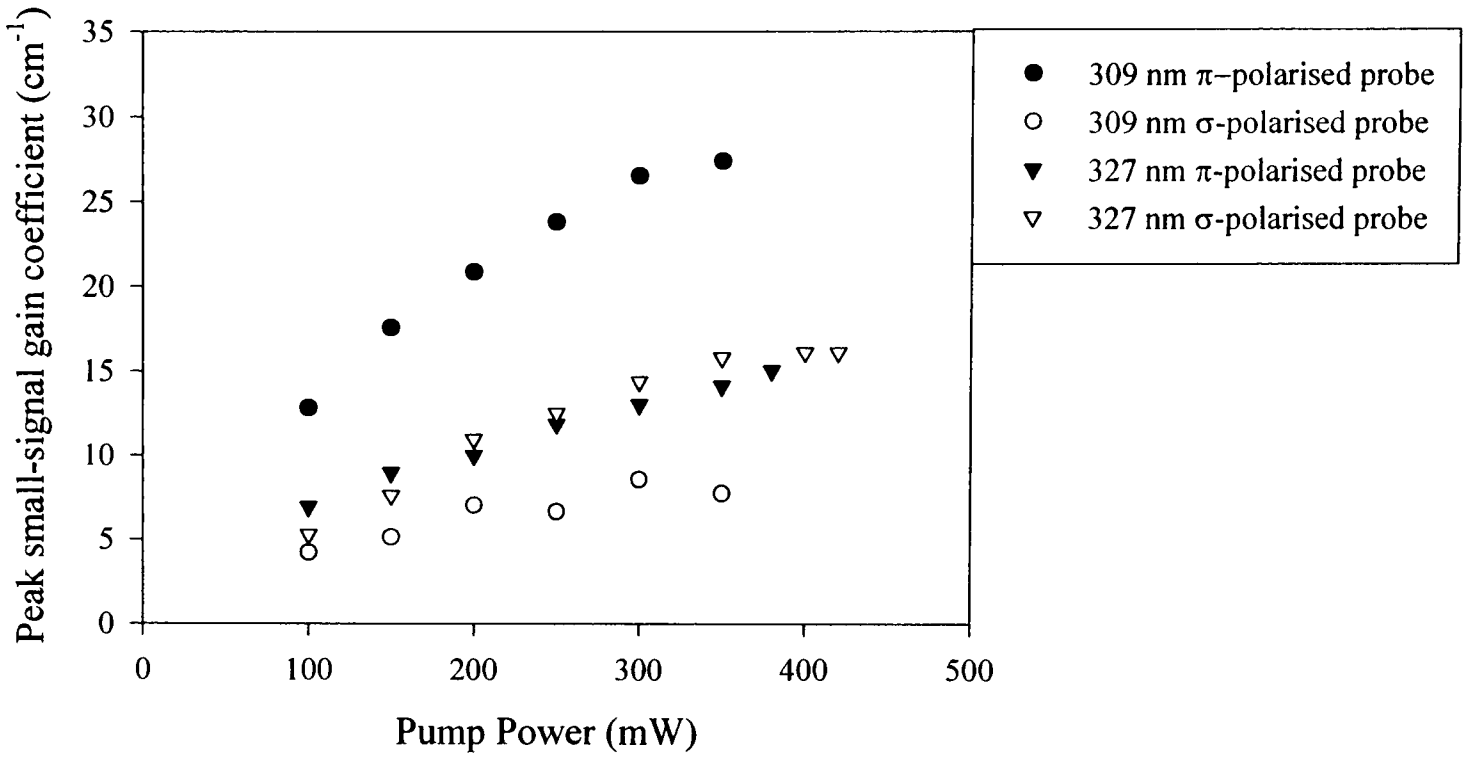


Figure 2.7 shows the variation of the small-signal gain coefficient with pump power in Ce:LiLuF with the crystal at room temperature. The pump fluence with 400 mW was ~0.46 J/cm^2.

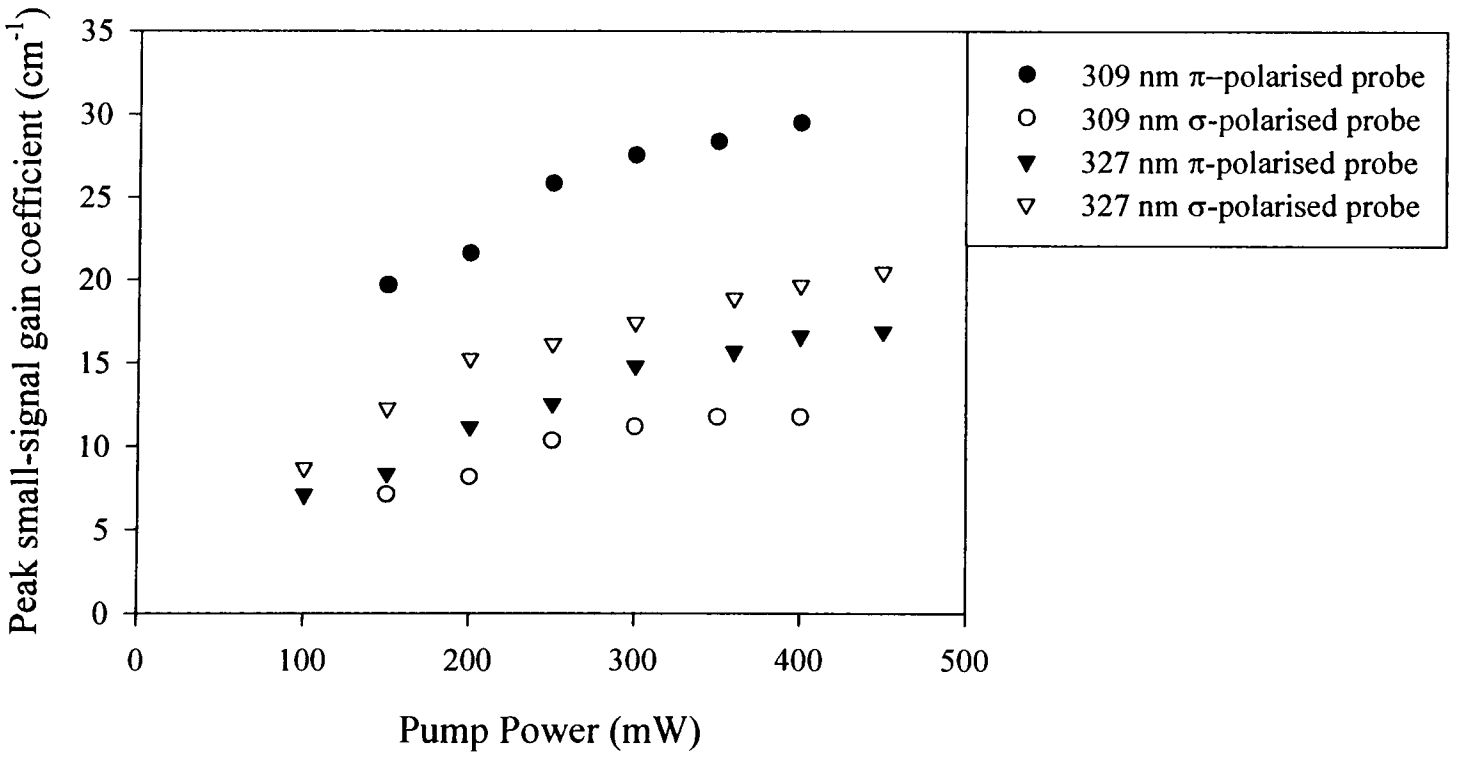


Figure 2.8 shows the variation of the small-signal gain coefficient with pump power in Ce:LiLuF with the crystal cooled to -3°C. The pump fluence with 400 mW was ~0.46J/cm^2.

The small-signal gain varied approximately linearly with pump power for both 309 nm and 327 nm, at the low pump powers for both polarisations. There was a very slight rolling over

of the gains at the higher pump powers, which is likely to be due to the depletion of the lower *4f* population as a result of the high pump powers (as seen in the transmission measurements,) rather than a saturation of the gain.

The effect of temperature on the gain was most noticeable for the experiments in which the σ-polarised, 327 nm probe was used, where the gain coefficient increased from 16±2 cm^{-1} to 20±2 cm^{-1} with the ~28 °C change in temperature. The next most notable change in gain was for the σ-polarised, 309 nm probe where the gain coefficient increased from 8±1 cm^{-1} to 12±1 cm^{-1} with the ~28 °C decrease in temperature. The π-polarised gain appeared to be less sensitive to temperature, in that, the change in gain coefficient with the ~28 °C change in temperature was only 2 cm^{-1} at 309 nm and ~0.5 cm^{-1} at 327 nm.

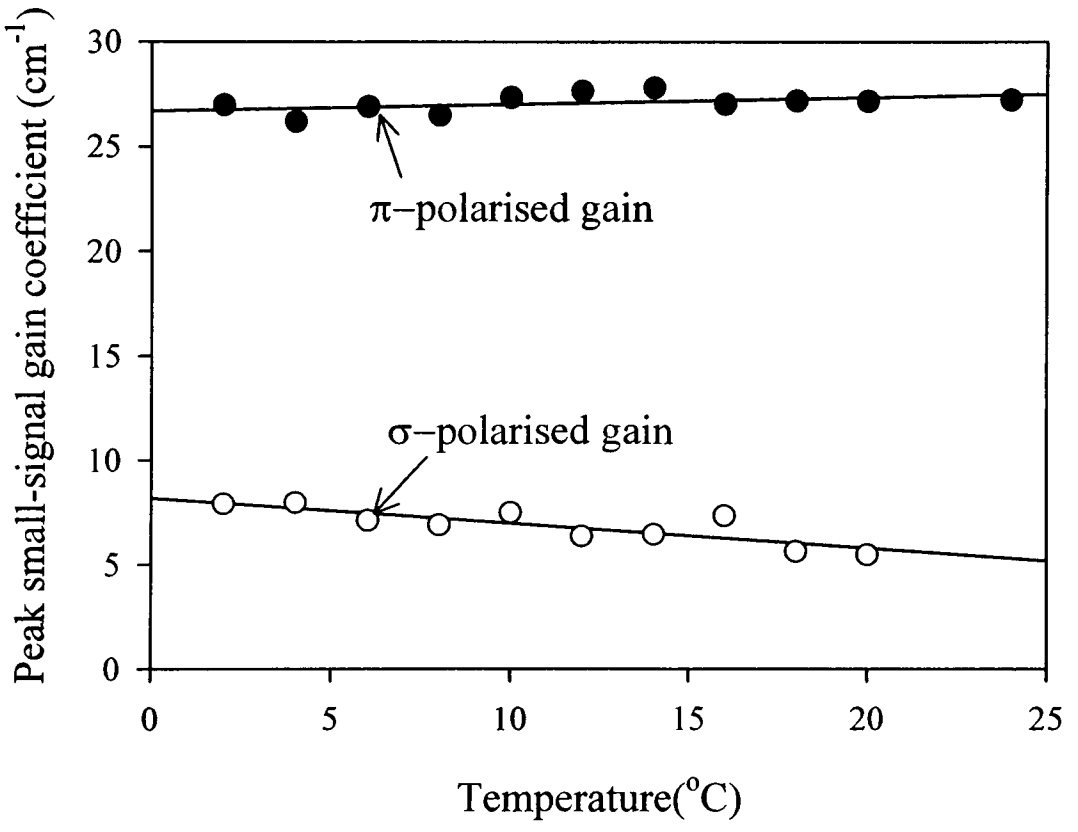


Figure 2.9 shows the temperature dependence of the polarised small signal gain at 309 nm with 360mW (equivalent to a pump fluence of 0.42 J/cm^2) of pump power in Ce:LiLuF.

The variation of gain with temperature was investigated more closely at 309 nm using 360mW pump power (0.42 J/cm^2); the results are shown in Figure 2.9. The σ-polarised gain had 40% increase in small-signal gain with decrease in temperature whereas the π-polarised gain had little to no variation with temperature. The small-signal gain variation with temperature at 327 nm for this Ce:LiLuF crystal was not measured at this time due to problems encountered with the dye laser at the longer wavelengths.

Most of the experiments were done on the Maine crystal due to the superior quality of this crystal as demonstrated by McGonigle *et al.* (McGonigle *et al.* 1999a). Small signal gain measurements have been made on the Kazan State crystal previously (Cashmore 1995), thus were not repeated in depth here. The small-signal gain variation with temperature of the Kazan State crystal was however determined here in order to verify that the temperature dependence of small signal gain was present in Ce:LiLuF crystals from different origins and grown using different techniques.

Figure 2.10 shows the variation of small signal gain in the Kazan State crystal with temperature, with 500mW of pump power. As can be seen, the dependence of small-signal gain with temperature was similar in the Kazan State crystal to that observed in the Maine crystal. In the Kazan crystal, a more pronounced increase in σ-polarised gain (-8%/°C) was observed compared to the increase in π-polarised gain with temperature (-0.5%/°C). The temperature effects were notably smaller in the Maine crystal than the Kazan State crystal with a percentage change in the σ-polarised gain of -2%/°C for the Maine crystal and -8%/°C for the Kazan State crystal. These results therefore suggest this temperature dependence of gain, particularly the σ-polarised gain, is inherent to Ce:LiLuF regardless of origin or growth technique, however the extent to which gain is affected by temperature is dependent on the particular crystal used.

It is also worth noting the ratios of the π-polarised gain to σ-polarised gain in both crystals are similar with the Maine crystal having a ratio π/σ of 3.4 and the Kazan State crystal having a ratio of 3.8. This ratio may be indicative of the similarity of the energy level purity in both crystals, more of which will be discussed in §2.6. The gain coefficient, displayed by the Maine crystal (~27±3 cm^{-1}) is larger than the Kazan State crystal (~20±2 cm^{-1}) even with the higher pump powers used for the Kazan State crystal measurements. This higher gain coefficient in the Maine crystal and the smaller dependence of gain on temperature may be symptomatic of the superior quality of the Maine crystal compared with the Kazan State crystal. This superior quality of the Maine crystal is thought to arise mainly from the presence of fewer impurities in the Maine crystal compared to the Kazan State crystal. Some of the superiority of the Maine crystal however may arise as a result of the smaller cerium concentrations in the Maine crystal which had a maximum of 0.4 mol% cerium compared to 1.5 mol% for the Kazan State Crystal. This would interfere less with the LiLuF crystal structure resulting in fewer defects within the crystal.

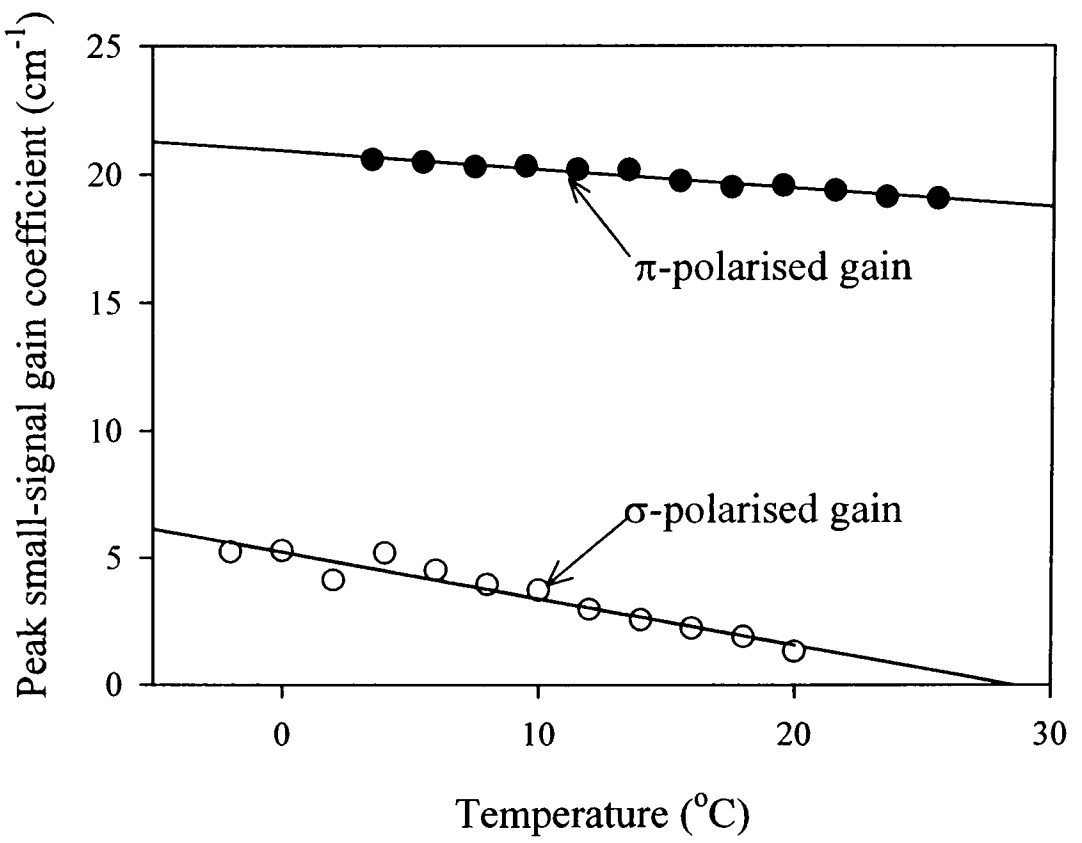


Figure 2.10 shows the variation with temperature of small-signal single-pass gain at 310 nm using the Kazan State crystal.

Further analysis of the absorption at 316 nm with a σ-polarised probe was undertaken in the hope of aiding an explanation of the temperature dependence of the gain seen at the emission peaks. Figure 2.11 shows how the absorption varied with time for two temperatures; -3°C (measurements made with 500 mW pump power) and 25°C (measurements made with 450 mW pump power). It is interesting to note that the 316 nm absorption coefficient is higher at -3°C (~6±1 cm^{-1}) than at 25°C (~4±1 cm^{-1}). This is in disagreement with what is implied by the temperature dependence of the σ-polarised gain discussed earlier. This higher absorption at -3°C is in part due to the 50mW difference in pump powers between the two measurements and is also thought to be the result of a variation of the pump-probe alignment between measurements. The fitted exponential lifetime of the absorption coefficient, thus the implied lifetime of absorbing species are shown, implying a low temperature lifetime of 34±4 ns. This is much shorter than the room temperature lifetime of 63±7 ns. This difference in lifetime may in fact be what is causing the temperature dependence of the gain. The limited amount of data taken in these lifetime measurements does limit the accuracy of these lifetimes and as such further investigation is required to provide more insight into this as a possible reasoning behind the temperature dependence of gain in Ce:LiLuF. This will be discussed in more detail in §2.6

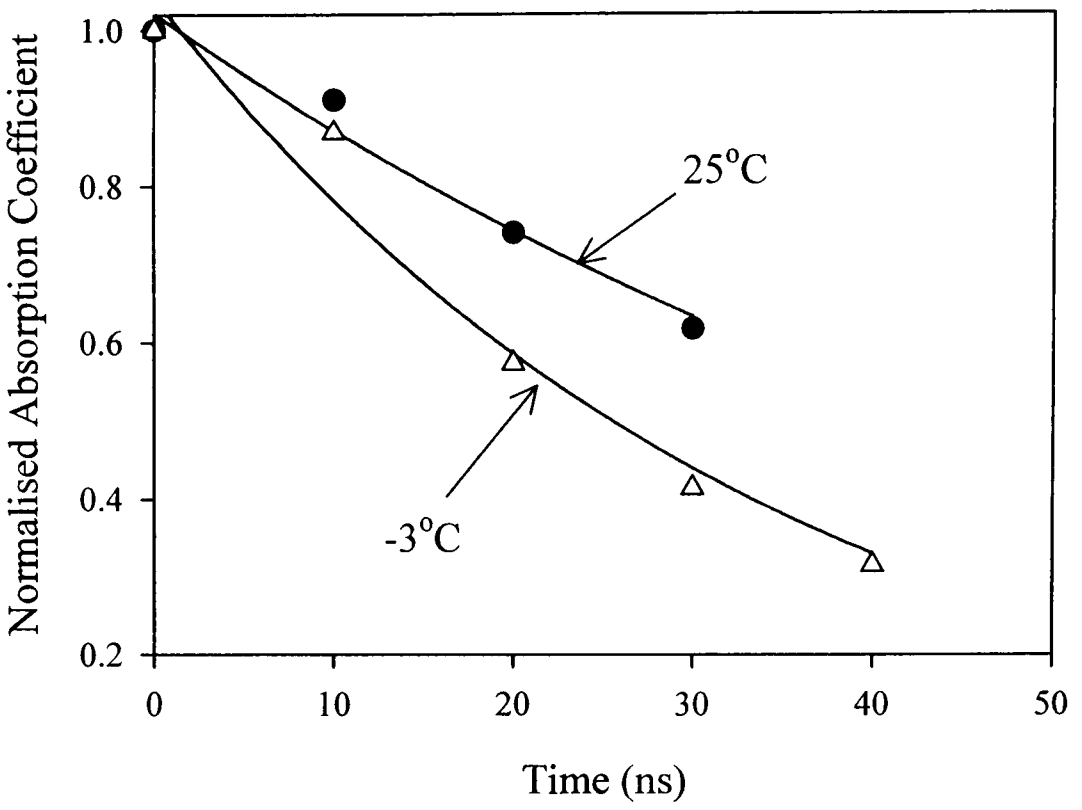


Figure 2.11 shows the lifetime of the absorption of the σ-polarised probe at 316 nm in Ce:LiLuF at -3°C (500 mW pump power) and ~25°C (450 mW pump power).

2.4 *Excited State Absorption Measurements for Ce:LiLuF at 261 nm and 349 nm.*

It has been suggested that excited-state absorption is present in Ce:LiLuF and is the reason for the polarisation "flipping" and tuning dip at 327 nm at low temperatures seen in Ce:LiLuF. In pursuit of proving this explanation, the excited state absorptions at 261 nm (frequency quadrupled Nd:YLF laser) and 349 nm (frequency tripled Nd:YLF laser), were measured, thus probing the ESA on either side of the emission spectrum of Ce:LiLuF.

The former wavelength, 261 nm, was chosen as it lies between the two lowest energy absorption bands in Ce:LiLuF thus this wavelength is not affected by any ground state absorption (GSA) from the lowest *4f* state to *5d* states. The results of experiments in which the variation of excited state absorption with pump intensity and probe intensity are reported.

The latter probe wavelength, 349 nm, lies at the longer wavelength extreme of the emission spectrum of Ce:LiLuF. The emission cross-section is small at 349 nm and a good approximation of this can be made by extrapolating the determined emission cross-section at 346 nm to 349 nm. These 349 nm ESA measurements, together with the 261 nm ESA measurements give some idea of the shape of the ESA spectrum in Ce:LiLuF.

2.4.1 Experimental Configuration

For the excited state absorption measurements only the Maine crystal was used. The UV-CVL was used to excite the Ce:LiLuF in these experiments, as described in §1.3.1.2. The probe alignment configuration through the 45° mirror used for the measurement of the excited state absorption in Ce:LiLuF was also identical to that used in the gain measurements described in §2.3.1.

The 261 nm probe used for ESA measurements was the fourth harmonic of a Q-switched 10 kHz Nd:YLF laser. The 523.5 nm output of the Nd:YLF laser had a pulse length of ~40 ns and a timing jitter between the Q-switch pulse and the laser pulse of 13 ns. The green, 523.5 nm Nd:YLF output was frequency-doubled using a 4 mm x 6 mm x 8 mm BBO crystal cut for second harmonic generation of the CVL 511 nm and 578 nm outputs, thus suitable for doubling 523.5 nm. The green Nd:YLF output was of sufficient intensity that no focussing into the doubling crystal was required, giving outputs of up to 225mW of 261.75 nm from ~7 W of 523.5 nm. The σ-polarised 261 nm probe was used either directly or converted to a π-polarised probe using two polarising cubes in succession, the first being at 45°, thus converting the σ-polarised probe into linearly polarised light at 45° to the horizontal, the second polarising cube was then used to select the desired π-polarised light. Only a few milliwatts of UV output were required to probe the excited state absorption at 261 nm so the losses induced by this method of polarisation conversion were not a concern.

The 349 nm probe used was from the third harmonic generation of the Nd:YLF laser using the unconverted 1047 nm together with the 523.5 nm to produce 349 nm using a 4 mm x 4 mm x 10 mm Type I LBO frequency-doubling crystal. The polarisation of the 1047 nm was orthogonal to the 523.5 nm polarisation, thus for simplicity, the doubling crystal was aligned at 45° to both green and infra-red input beams, giving an output at 349 nm with linearly polarised light at 45° to the horizontal, thus a polarising cube in the probe was arranged so as to select the desired σ- or π-polarisation.

For both the 261 nm and 349 nm probes, neutral density UV filters were used to reduce the probes to <1 mW. The reflection losses of the σ-polarised probe at the 45° mirror was counteracted in the same manner as described for the gain measurements in §2.3.1.

Timing, alignment and measurement of the pump and probe were also conducted using the same method used in the gain measurements described in §2.3.1, with absorption being maximised as opposed to gain. The pulse length of the 261 nm probe was ~100ns and that of the 349 nm pulse was ~70 ns. In the pulse length measurements an average of 256 pulses was

taken for the 261 nm measurements and an average of 64 pulses was taken for the 349 nm measurements, with the probes being triggered off the 289 nm pump pulse. These pulse lengths thus includes the jitter from both the Q-switch-Nd:YLF timing and the Q-switch-CVL timing. Since the absorption readings were averaged, the absorptions recorded were not affected the pump-probe jitter. The maximum absorption was found to coincide with the peak of the fluorescence, as was found in the gain measurements. Due to the long probe pulses at 261 nm and 349 nm, the maximum absorption was found to be relatively insensitive to pump-probe timing, with similar peak absorptions obtainable with probe timed such that the peak of the probe occurred between 10 ns and 60 ns after the pump pulse. The long probe pulse lengths enable the lifetime of the absorption coefficients to be determined relatively easily compared to those determined at 316 nm.

2.4.2 Results

The ground state absorption at 261 nm, measured with no pump, was found to be negligible as expected, since 261 nm lies between the 244 nm and 292 nm *4f* to *5d* absorption bands. Figure 2.12 shows the σ-polarised excited-state absorption measurements at 261 nm. The reference probe and absorbed probe are shown for comparison. The ESA at 261 nm resulted in a peak probe absorption of ~60% and an obvious lifetime dependence of the excited state absorption was seen. An exponential was fit to the 261 nm ESA absorption data, using only the absorption data starting ~10 ns after the peak absorption, to allow for the presence of the tail end of the pump pulse which could have distorted the time dependence of the absorption. The decay lifetime for the ESA was found to be 32±1 ns, which is in reasonable agreement with the determined fluorescence lifetime of Ce:LiLuF, namely 38 ns. This lifetime suggests the excited state absorption initiates in the lowest 5d level.

The variation of the 261 nm, σ-polarised and π-polarised absorption coefficients with pump power is shown in Figure 2.13. An approximately linear relationship between the excited state absorption and pump power was seen. This linear relationship implies that only one pump photon was absorbed per excited-state transition, suggesting that no pump photons were involved in the ESA transition from the lowest *5d* state to the terminal ESA state. There was no obvious saturation of the *5d* population occurring at the pump powers investigated.

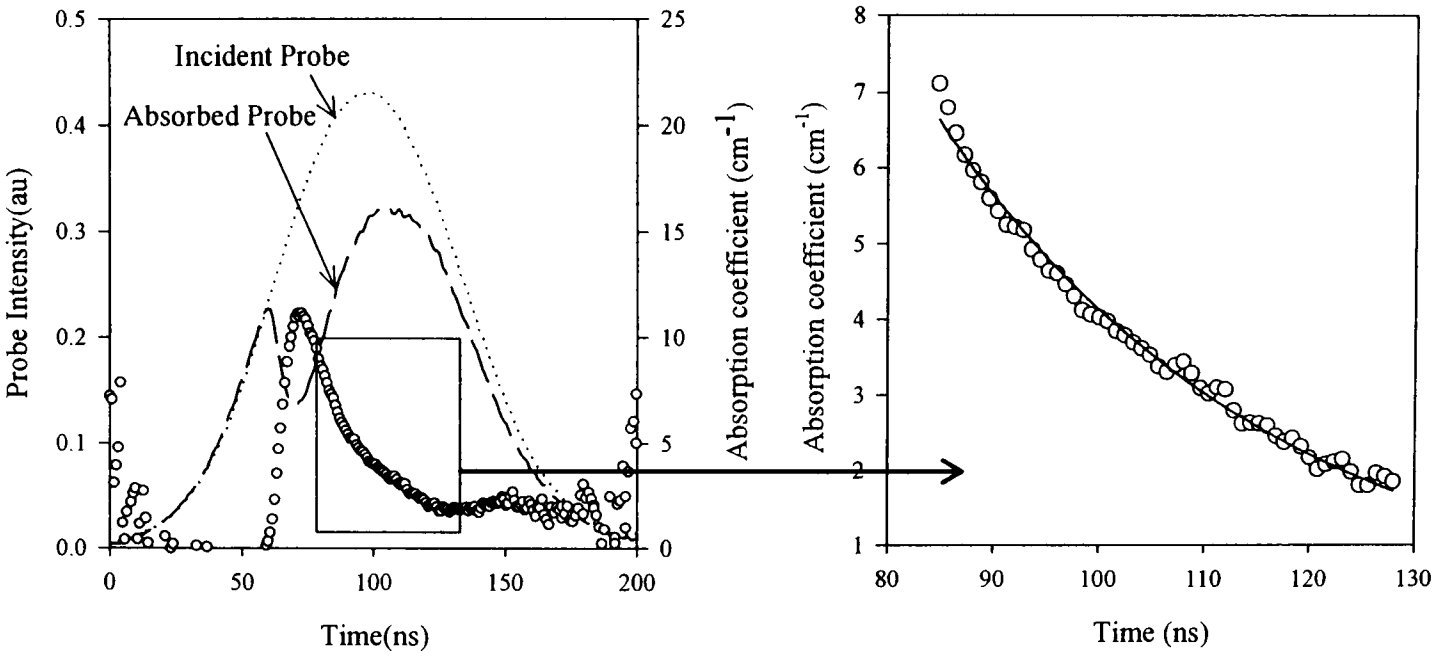


Figure 2.12 shows the 261 nm, σ-polarised probe pulses with the incident probe, I_{in} and absorbed probe pulse, I_{out}. The circles show the 261 nm ESA coefficient variation with time when pumped with 500mW of pump power (~0.6J/cm^2 pump fluence). The expanded insert shows the evolution of the ESA coefficient with time with the line showing the exponential decay fit giving a decay lifetime of ~32ns.

The excited state absorption at 261 nm did not show any variation with temperature. There was, however, an obvious polarisation dependence of the excited-state absorption with the σ-polarised absorption coefficient of 10±1 cm^{-1} being more than three times the π-polarised absorption coefficient of 3±1 cm^{-1}, with 400 mW of pump power (~0.46J/cm^2). The fluorescence emission data from §2.1.2 suggested similar gains should be expected for σ-polarised 327 nm and for π-polarised, 309 nm due to the similar σ_{EM} values at the emission peaks. What was seen, however, was that the 309 nm, π-polarised gain coefficient (26±3 cm^{-1}) was larger than the 327 nm, σ-polarised gain coefficient (15±2 cm^{-1}). The polarisation dependence of ESA shown by these ESA results is in excellent agreement with these gain results, in that the σ-polarised ESA was found to be larger than the π-polarised ESA which would in turn result in a more dramatic decrease in the σ-polarised σ_{EFF} than the π-polarised σ_{EFF} as a result of ESA.

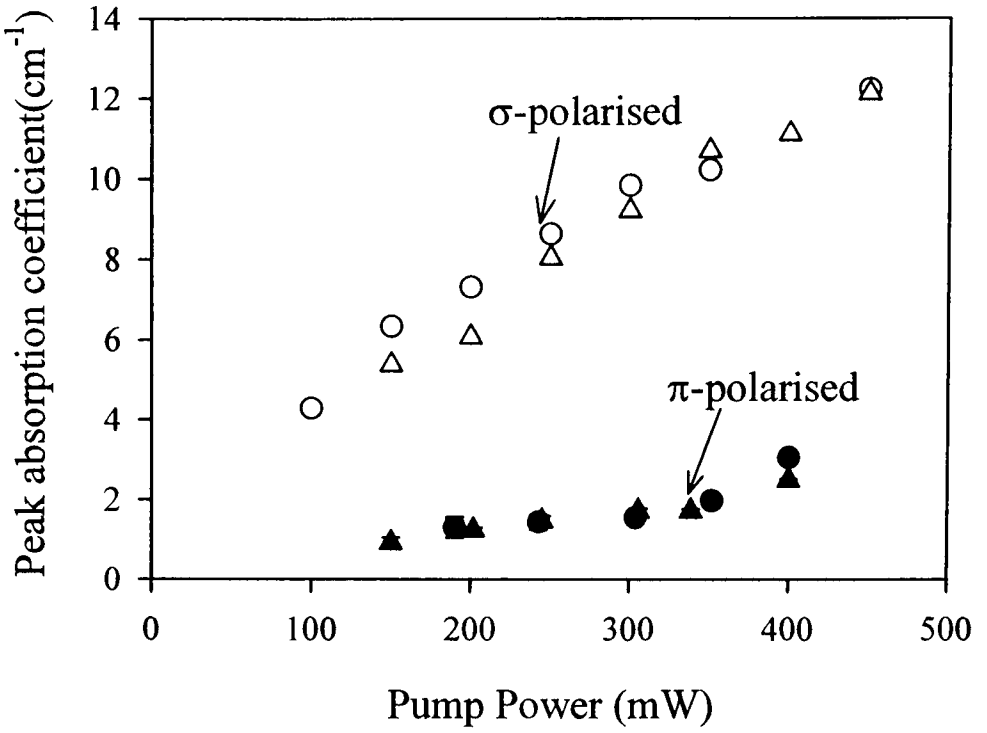


Figure 2.13 shows the variation of excited state absorption at 261 nm for both σ-polarised and π-polarised probes with incident pump power. The absorption coefficients at ~22°C (circles) and 2°C(triangles) are shown. The pump fluence with 400 mW was ~0.46 J/cm^2.

Further investigation into the temperature dependence of ESA confirmed the lack of temperature dependence observed in the ESA versus pump power results. The absorption of the probe in Ce:LiLuF was found not to vary significantly with probe intensity as shown in Figure 2.14. The slight variations seen in the figure were within the fluctuations expected due to fluctuations in the pump intensity or change in the probe intensity between the recording of the reference and absorbed probes. The lack of any structure to the probe absorption with probe intensity implies that the excited-state absorption at 261 nm was neither saturated nor the result of a multi-photon process. If two photons were required per excited-state transition then one could expect the absorption to be linearly proportional to the probe intensity. These results therefore ruled out the possibility that the absorption was due to probe induced colour centres which absorbed at the probe or pump wavelength, as these would result in an increase in absorption with increase probe intensity until colour centre formation saturated, as was seen in Ce:CaF_2 (see §1.2.3).

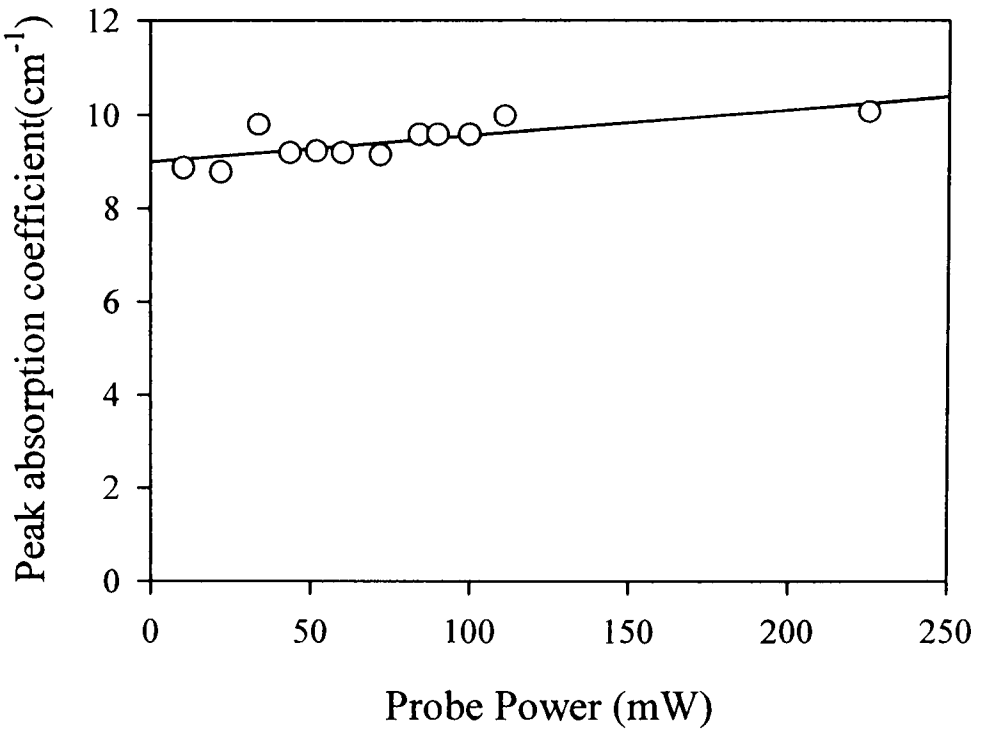


Figure 2.14 shows the σ-polarised excited state absorption at 261 nm variation with probe power when pumped with 460mW of pump power (pump fluence ~0.5J/cm^2).

The fluorescence, representative of the lowest *5d* population was monitored whilst probing with the 225 mW of 261 nm, σ-polarised probe in order to monitor the depletion of the *5d* population due to ESA. Less than 5% depletion was seen whilst this relatively high intensity probe was aligned and timed for maximum probe absorption. The little change that was seen may have been a figment of changes in the fluorescence due to changes in the pump pulse over this time. This lack of depletion is mostly likely to be because the probe-induced decrease in *5d* population due to ESA was small compared to the population inversion created by the high pump power used (460 mW), thus was not observable. If, however, this lack of depletion was real, it may indicate that the lifetime of the return of the electrons from the terminal state of the ESA transition to the lowest *5d* state is very short (<<20 ns).

The variation of the σ-polarised ESA coefficient at 349 nm with pump power is shown in Figure 2.15. The σ-polarised ESA at 349 nm was found to be smaller than the absorption at 261 nm with the σ-polarised probe. Like the 261 nm ESA results, there was a marked difference between σ- and π-polarised ESA but at 349 nm the π-polarised ESA was found to be negligible. As was seen at 261 nm the variation of 349 nm with pump power had a linear dependence suggesting this ESA was a single-photon absorption mechanism. The variation of absorption with temperature was also found to be negligible at 349 nm, as was seen at 261 nm. The relatively low absorption at 349 nm compared to that at 261 nm does indicate the presence of a wavelength dependence of the ESA.

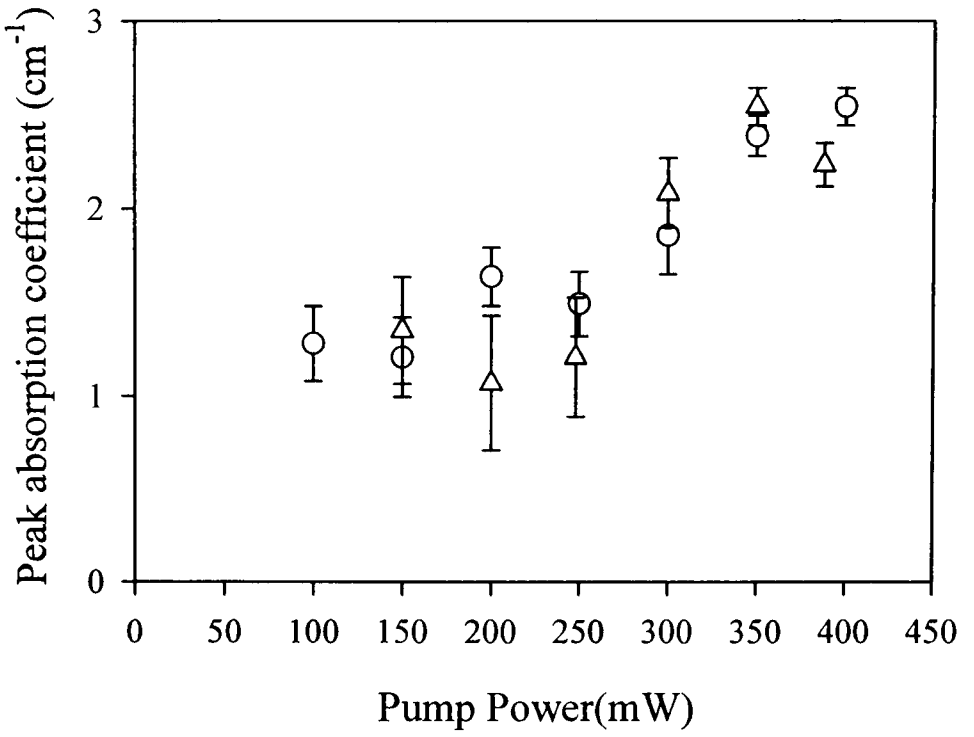


Figure 2.15 shows the 349 nm σ-polarised excited state absorption coefficient variation with pump power in Ce:LiLuF at ~22°C (circles) and -3°C(triangles). The pump fluence with 400 mW was ~0.46 J/cm^2.

2.5 Simulated small-signal gain and ESA cross-section determination.

Using a computer-based, finite-difference model of Ce:LiLuF, the dependence of the various energy level populations on pumping and the consequent interaction with radiation of the Ce^{3+} ion was simulated. In simulating the excited-state absorption and small-signal gain measured experimentally, the excited-state absorption cross-sections was determined, both within and outside the emission spectrum of Ce:LiLuF. The ESA cross-sections at 261 nm, 309 nm, 327 nm and 349 nm are presented in this section. Using the combination of these results, the ESA cross-section at 289 nm for the π-polarisation was estimated and hence the extent to which ESA is detrimental to pumping at 289 nm is discussed.

2.5.1 Program Description

The simulations undertaken in this thesis were conducted in a similar manner as that used by Marshall *et al.* (Marshall *et al.* 1994).

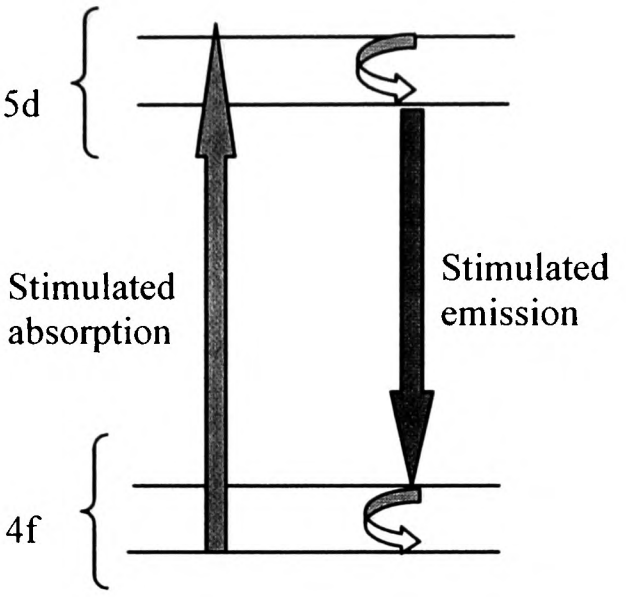


Figure 2.16 shows a simplified Ce^{3+} four-level laser energy level diagram.

Assuming an ideal four-level laser system, as shown in Figure 2.16, the effect of pumping on the *4f* and *5d* populations in Ce:LiLuF, in the absence of lasing, can be described with a set of relatively simple rate equations shown below in equations 2.8, 2.9 and 2.10,

$$\frac{dN_{4f}(z,t)}{dt} = \frac{-\sigma_{ABS}(\omega)N_{4f}(z,t)I(\omega,z,t)}{\mathrm{h}\omega} + \frac{N_{5d}(z,t)}{\tau_{5d}} \qquad 2.8$$

$$\frac{dN_{5d}(z,t)}{dt} = \frac{+\sigma_{ABS}(\omega)N_{4f}(z,t)I(\omega,z,t)}{\mathrm{h}\omega} - \frac{N_{5d}(z,t)}{\tau_{5d}} \qquad 2.9$$

$$\frac{dI(\omega,z,t)}{dz} = -\left[\sigma_{ABS}(\omega)N_{4f}(z,t) + \sigma_{ESA}(\omega)N_{5d}(z,t)\right] \times I(\omega,z,t) \qquad 2.10$$

where I, N_{5d} and N_{4f} are the intensity (Wm^{-2}), the upper *5d* population density (m^{-3}) and the lower *4f* population density (m^{-3}) respectively. σ_{ABS} and σ_{ESA} were the absorption and ESA cross sections respectively. ω was the pump frequency, z was the distance through the Ce:LiLuF crystal and t was time. The time increment, δt, was related to the distance increment, δz, such that $\delta t = \delta z/c$, where c was the speed of light. In this program δz was defined to be 1/100th of the crystal length, l. The value of δz was confirmed to be small enough that dN/dt and dI/dz could be approximated by $\delta N/\delta t$ and $\delta I/\delta z$ respectively by comparing the gain calculated using $\delta z = 0.01l$ and $\delta z = 0.005l$. The difference between the gains simulated using each δz increment was found to be negligible, thus confirming the validity of the δz value used.

The thermal population of the *upper 4f level* ($F_{7/2}$) was considered to be negligible as discussed in §1.1.3. The lifetime of the transition from the top of the 4f band ($F_{7/2}$) to the bottom of the *4f* band ($F_{5/2}$) was assumed to be very short in Ce^{3+} (such that the $F_{7/2} \rightarrow F_{5/2}$ transition was instantaneous). Thus the population difference (N_{5d}-$N_{F\ 7/2}$) was replaced the with just the upper 5d level population, N_{5d}. The corresponding rate equation describing the amplification of a probe is shown in equation 2.11, in which $I(\omega_{probe}, z, t)$ was the probe intensity and σ_{EFF} was the effective cross section described by equation 2.7.

$$\frac{dI(\omega_{probe}, z, t)}{dz} = I(\omega_{probe}, z, t)\sigma_{EFF}(\omega_{probe})N_{5d}(z, t) \qquad 2.11$$

The small signal gain, G, could also be obtained from the integral form of equation 2.11 rewritten as equation 2.12.

$$G = \exp\left\{\int_0^l \left[N_{5d}(z).\sigma_{EFF}(\omega_{probe})\right]dz\right\} \qquad 2.12$$

Using equation 2.11 the small-signal gain was simulated. As mentioned in §2.2.2, the cerium number density in the Ce:LiLuF crystal, determined using ICP-MS, was approximately 10 times the cerium number density implied by the absorption coefficient and the previously measured absorption cross-section for Ce:LiYF. Also as mentioned in §2.2.2 the cerium density derived from the absorption coefficient was likely to be a better indication of the active Ce^{3+} density than the cerium number density measured using ICP-MS which was thought to be indicative more of the total cerium density in the crystal rather than the *active* Ce^{3+} density in the crystal. Further, it was found, when comparing the simulated gain measurements and experimental gain measurements, the simulations using the cerium number density determined using the measured absorption coefficient showed a similar saturation of the gain at high pump powers as was seen experimentally, whereas the simulated results using the cerium number density, determined using the ICP-MS, did not show any saturation effects. The absorption cross section for Ce:LiLuF used in all the simulations described in this thesis, was 3.35×10^{-18} cm^2, for π-polarized light at 289nm, determined as described in §2.2.2. The corresponding number density of Ce^{3+} in the Ce:LiLuF crystal used, determined from the measured absorption coefficient of the crystal, was 5.47×10^{18}cm^{-3}. The emission cross sections for Ce:LiLuF, σ_{EM}, used in the model were those determined from the fluorescence measurements described in §2.1.2. A summary of the absorption and emission cross-sections used in this gain model is given in Table 2.1

Table 2.1 shows the fixed emission and absorption cross-section values used in the gain model.

Constant	Value
N_{4F}(Initial)	5.47×10^{18} cm^{-3}
σ_{ABS} (289 nm, π-polarised)	3.35×10^{-18} cm^2
σ_{EM} (309 nm, π-polarised)	6.72×10^{-18} cm^2
σ_{EM} (309 nm, σ-polarised)	4.01×10^{-18} cm^2
σ_{EM} (327 nm, π-polarised)	3.74×10^{-18} cm^2
σ_{EM} (327 nm, σ-polarised)	6.85×10^{-18} cm^2
σ_{ESA} (309 nm, π-polarised)	Set to 0 cm^2

The pump intensity used in the simulations was an appropriately scaled, experimentally measured, pump pulse, detected using a Thorlabs DET 200 photodiode and a Tektronix TDS 3034 oscilloscope. A very low intensity (<1 mW) continuous probe was simulated. The virtual crystal was made up of 100 spatial slices, of thickness δz =8 μm, making up the total crystal length of 0.8 mm. The pump and probe intensities were the shifted through the virtual crystal in time steps such that $\delta t = \delta z / c$. The changes in populations and intensities were calculated using equations 2.8, 2.9, 2.10 and 2.11. For each step the populations and intensities were then recalculated and updated accordingly. The duration of this virtual experiment was 50 ns.

Various assumptions were made when conducting these simulations, the grounding for which is discussed here. In the simulation, the model used was one dimensional in space, thus the

first assumption made was that the spatial shape of the pump and probe would not affect the peak small-signal gain coefficients or peak excited state absorption coefficients simulated. Experimentally, the spatial shape of the pump, with the pumping configuration used, was approximately top hat. The simulation of the pumping of crystal using this one-dimensional program was a good approximation. The spatial profile of the probe was of little consequence since it was the peak gain and absorption being determined. The probe used experimentally was very low intensity thus the probe did not perturb the gain and consequently a linear relationship between the probe intensity and gain (or absorption) existed.

The presence of non-radiative decay from the lowest *5d* level to the *4f* level was assumed to be negligible. The pumping efficiency was assumed to be 88% (Sarukura *et al.* 1995a). As will be described in §2.5, using this gain model, the 289 nm, π-polarised ESA cross-section was estimated from the ESA cross-sections determined at 261 nm, 309 nm and 349 nm. The ESA cross-section at the pump wavelength determined was not large enough to solely be the cause of the 88% quantum efficiency, thus other effects were possibly present. For this gain model, the 88% pumping efficiency was taken into account by decreasing pump area by a factor of 1.14 whenever it is quoted.

The lifetime of the terminal-ESA-state to *5d* level relaxation was unknown, however for the very low intensity probes used and the fact that there was negligible ESA at the pump wavelength, the population in the terminal-ESA-state was considered to be very small. Thus in the case of modelling the small-signal gain, the lifetime of the terminal-ESA-state was not required.

The experimental results showed the 309 nm, π-polarised small-signal gain to vary very little with temperature (Figure 2.9); however there was some variation as shown by the comparison of Figure 2.7 and Figure 2.8. The 309 nm, π-polarised laser output was found to increase with decreasing temperature until ~0°C, below which the temperature had little effect on the laser output power (shown in Figure 3.8 and Figure 3.24). For this gain model it was assumed, using the laser results described, that below 0°C the ESA cross-section at 309 nm for π-polarised light was negligible compared to the σ_{EM} at 309 nm for π-polarised light. Thus σ_{ESA}(309 nm,π) was set to be zero below 0°C. With this approximation the low temperature, π-polarised, 309 nm gain measurements could be used as a reference to obtain the pump intensity and hence the corresponding idealised top-hat pump spot-size required to simulate the experimentally measured small-signal gain at 309 nm for a π-polarised probe.

The pump intensity required to simulate the π-polarised, 309 nm small-signal gain equivalent to that found experimentally, meant that the pump mode had a spot diameter of ~70 μm, (taking into account the estimated 88% pumping efficiency in Maine Ce:LiLuF crystal). This implied the difference in pump intensity required by the gain model was approximately 2.5 times that thought to be used experimentally. The pump diameter used experimentally was calculated to be ~110 μm. Although the experimental pump diameter was never measured directly, the beam quality was measured, thus the experimental pump spot diameter was considered to be a reasonable estimate.

The discrepancies between the experimental and simulated pump intensities and corresponding pump spot sizes may have been the result of the uncertainty in the estimated Ce^{3+} number density. Any uncertainty in the Ce^{3+} number density would scale the pump intensity required by the gain model to simulate the correct population inversion and gain. As such, with the pump intensity discrepancy in mind, the gain simulated by the gain model was still thought to be accurate, giving a good description of the gain behaviour in Ce:LiLuF. The pump intensities and population inversion densities simulated by the gain model however were thought to less accurate and as such were viewed as indicative of only the order of magnitude.

Once the pump spot size was established, using the fixed emission cross-sections the 327 nm (σ- and π-polarised probes) and the 309 nm (σ-polarised probe) ESA cross-section could be deduced, and hence the effective gain cross-section changed, until the simulated small-signal gain was equivalent to the experimentally determined small-signal gain for these probe wavelengths and polarisations. In this manner the ESA cross-sections for σ-polarised 309 nm, σ-polarised 327 nm and π-polarised 327 nm were determined.

The ESA cross-sections at 261 nm and 349 nm are determined in a similar manner as the gain simulations, using the same spot size as used in the small-signal gain simulations, since the pumping configuration used in the ESA measurements was identical to that used in the gain measurements. The σ- and π-polarised emission cross-sections at 261 nm are zero since 261 nm lies between the lowest and second lowest *4f* to *5d* absorption bands, as can be seen in Figure 2.23. The σ-polarised emission cross-section at 349 nm was taken to be 0.5×10^{-18} cm^2, determined by extrapolating the emission data from 346 nm ($\sim 1 \times 10^{-18}$ cm^2) to 349 nm. The experimental absorption of the 261 nm and 349 nm probes was simulated by fitting the ESA cross-sections such that the simulated absorptions matched the observed absorptions. In this manner the polarised ESA cross-sections for 261 nm and 349 nm were determined.

2.5.2 Transmission simulation results

The transmission of the unfocussed pump pulse was simulated to be 23.6%. This was in good agreement with the experimentally determined transmission of 22±1%. The average transmission of the focussed pump beam was simulated by the model to be ~85%. This was much larger than the experimentally determined average transmission of 31%. Thus the unfocussed transmission is in good agreement with the experimental value, however the focussed transmission was not, suggesting that the population inversion simulated in the gain model as a result of pumping was the cause of this discrepancy.

As mentioned in the previous subsection, there was some uncertainty in the Ce^{3+} number density used in the laser model and as such the pump intensities and population inversions were thought to be only accurate within an order of magnitude. Thus this discrepancy in the transmission was to some extent expected. Underestimating the Ce^{3+} number density in the gain model would cause the simulated depletion of the lower laser level to be too high. This in turn would cause the simulated transmission to be too high, as was found of the transmission simulated in this gain model. The good agreement between the saturation of the gain simulated (see §2.3.2) and the experimentally determined gain however contradicts the possibility that the Ce^{3+} number density used was too low.

On the other hand it was possible that the saturation of the gain arose from saturation of the upper population by the probe. In order to confirm that the saturation of the simulated gain did in fact arise from a saturation of the pump absorption, a small-signal gain simulation was run with 400 mW of pump power and a small probe intensity (of the order of 10 W/m^2) and then again, with a more realistic probe intensity corresponding to ~1 mW average power (thus the intensity was of the order of 10^8 W/m^2). The small-signal gains determined in each case were found to be identical, and as such, the saturation of the gain was confirmed to originate from the saturation of the pump absorption and not from saturation of the gain by the probe.

The difference between the simulated and experimental transmissions could also have been a result of the assumption in the model that, spatially, the pump was a perfect top-hat where in reality it is not quite. Therefore assuming the pump had a Gaussian spatial profile, a spatially averaged transmission of 70% was determined, which was still much higher than the experimental focussed transmission of 31%. Thus the spatial profile of the pump spot was not the cause of the large difference in focussed simulated and experimental transmissions.

A variation in beam quality across the 289 nm pump pulse may also have resulted in the transmission discrepancy. In Chapter 1, the composition of the CVL laser pulse is described. To reiterate, the CVL pump pulse is composed of three or more roundtrip components, the

latter of which have a better beam quality than the first roundtrip component. With this pump pulse composition one could expect an increase in absorption towards the back end of the pump pulse, however the saturation of the absorption from the lower laser level would also cause an increase in transmission towards the back of the pump pulse. Figure 2.17(a) and (b) show the unfocussed and focussed pump transmissions determined experimentally. The unfocussed pump transmission is flat across the pump pulse as expected, since there is no noticeable depletion of the lower population at these low pump intensities. The simulated transmission of the unfocussed pump pulse was also found to be constant across the pump pulse as shown in Figure 2.17 (c). The focussed pump transmission increases from ~18% to ~37% towards the back end of the pump pulse. This increase in transmission towards the back end of the pump pulse was also seen in the simulated transmission, with the transmission changing from 27% to 94% over the pump pulse. The presence of a variation in transmission over the pump pulse in the simulated results suggested that change in transmission over the pump pulse seen experimentally was not a result of the variation in beam quality over the pump pulse but rather a result of the saturation of the lower level, since the beam quality in the gain model was assumed to be constant over the pump pulse.

Finally, it is also possible that experimentally the spatial UV-CVL pump profile had low intensity wings, contributing significantly towards the overall pump pulse intensity. These wings would, due to their low intensity, have a low transmission, resulting in an underestimation of the high intensity pump pulse transmission which was measured experimentally. This underestimation of the experimental transmission may have caused the difference in simulated and experimental transmission. Unfortunately the spatial profile of the pump spot was not measured so this cannot be confirmed.

Overall the gain model appears to show that the absorption is saturating quicker than seen experimentally, however in general the actual behaviour of the simulated transmission over the pump pulse was similar to that seen experimentally, seen by comparing Figure 2.17 (b) and (c). Thus, as mentioned earlier, the pump intensities required by, and the population inversions simulated by the gain model, are limited in their accuracy and as such are taken to reflect only the order of magnitude in the results.

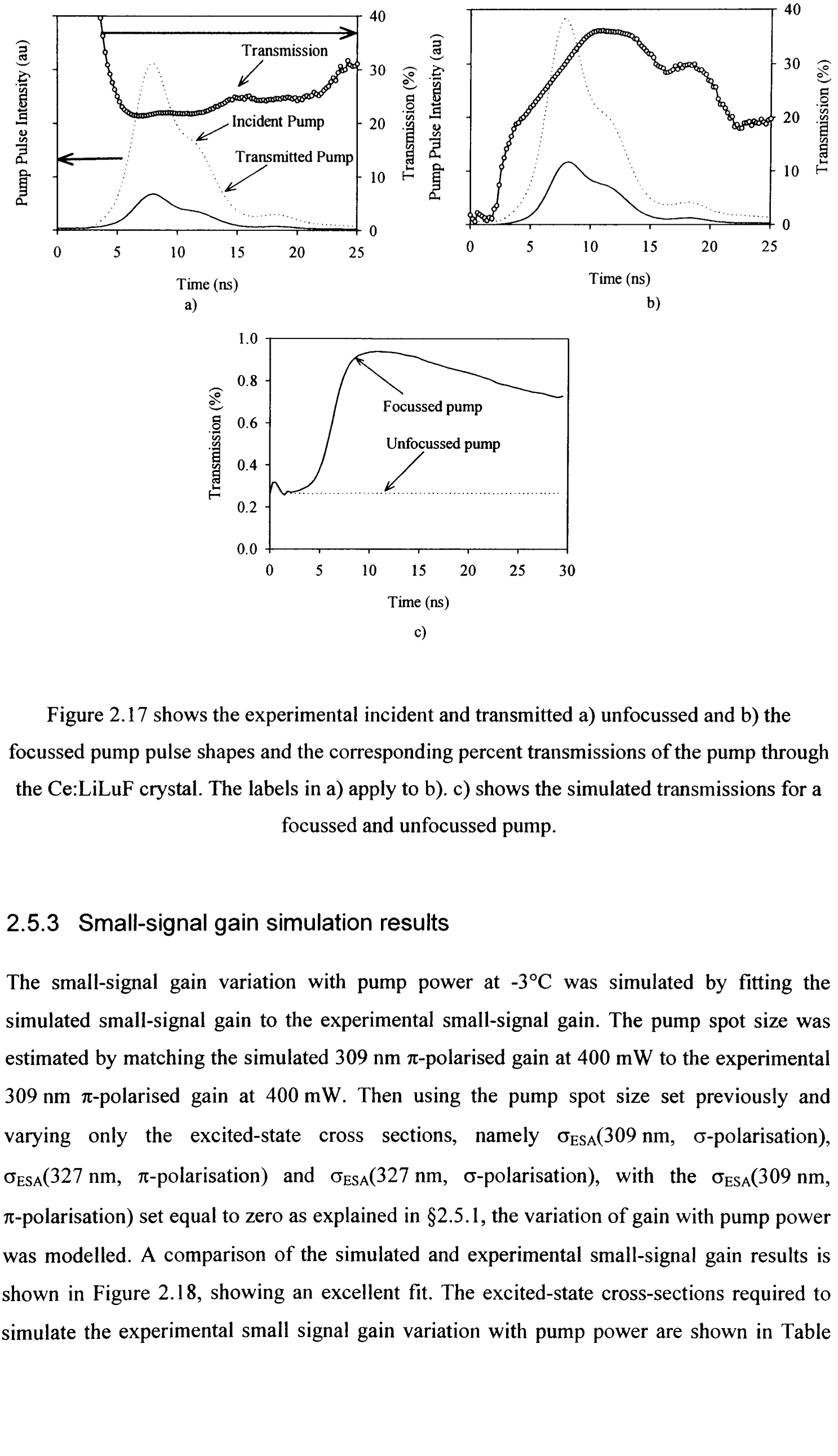


Figure 2.17 shows the experimental incident and transmitted a) unfocussed and b) the focussed pump pulse shapes and the corresponding percent transmissions of the pump through the Ce:LiLuF crystal. The labels in a) apply to b). c) shows the simulated transmissions for a focussed and unfocussed pump.

2.5.3 Small-signal gain simulation results

The small-signal gain variation with pump power at -3°C was simulated by fitting the simulated small-signal gain to the experimental small-signal gain. The pump spot size was estimated by matching the simulated 309 nm π-polarised gain at 400 mW to the experimental 309 nm π-polarised gain at 400 mW. Then using the pump spot size set previously and varying only the excited-state cross sections, namely σ_{ESA}(309 nm, σ-polarisation), σ_{ESA}(327 nm, π-polarisation) and σ_{ESA}(327 nm, σ-polarisation), with the σ_{ESA}(309 nm, π-polarisation) set equal to zero as explained in §2.5.1, the variation of gain with pump power was modelled. A comparison of the simulated and experimental small-signal gain results is shown in Figure 2.18, showing an excellent fit. The excited-state cross-sections required to simulate the experimental small signal gain variation with pump power are shown in Table

2.2. As can be seen there was negligible π-polarised ESA at these low temperatures, the σ-polarised ESA was however more significant with ESA cross-sections of the same order of magnitude as the emission cross-sections. The effective gain cross-sections were positive in all these cases as the overall the losses due to ESA were not enough to prevent gain from being seen for the wavelengths simulated, for both polarisations. The similarity between the effective cross-sections of both the 327 nm polarisations is very likely to be the origin of some of the interesting behaviour seen by McGonigle *et al.* (McGonigle *et al.* 2001b) described in Chapter 1. The actual resulting lasing behaviour will be discussed further in Chapter 3.

Although the ESA measurements at 261 nm and 349 nm showed no dependence on temperature, the small-signal gain variations with temperature at 309 nm and 327 nm are consistent with a temperature dependence of the ESA. Accordingly, the possibility of temperature dependent excited-state absorption, if not outside the emission spectrum of Ce:LiLuF (such as at 261 nm and 349 nm), but within the emission spectrum was taken into consideration and hence further simulations were undertaken for gain at 25°C, varying only the excited-state absorption cross-section at 309 nm and 327 nm, for each polarisation. These simulations suggested that, in all cases an increase in the ESA cross-section, with the 28°C increase in temperature, was required to mimic the experimental small-signal gain coefficients. Again an excellent fit was achieved as shown in Figure 2.19.

Table 2.2 Determined effective gain and excited state absorption cross-sections for Ce:LiLuF at -3°C.

Wavelength	309 nm	309 nm	327 nm	327 nm
Polarisation	π	σ	π	σ
σ_{EM} **(x10^{-18}cm^2)**	6.7	4.0	3.7	6.8
σ_{ESA}**(x10^{-18}cm^2)**	0	1.3	0	2.4
σ_{EFF}**(x10^{-18}cm^2)**	+6.7	+2.7	+3.7	+4.4

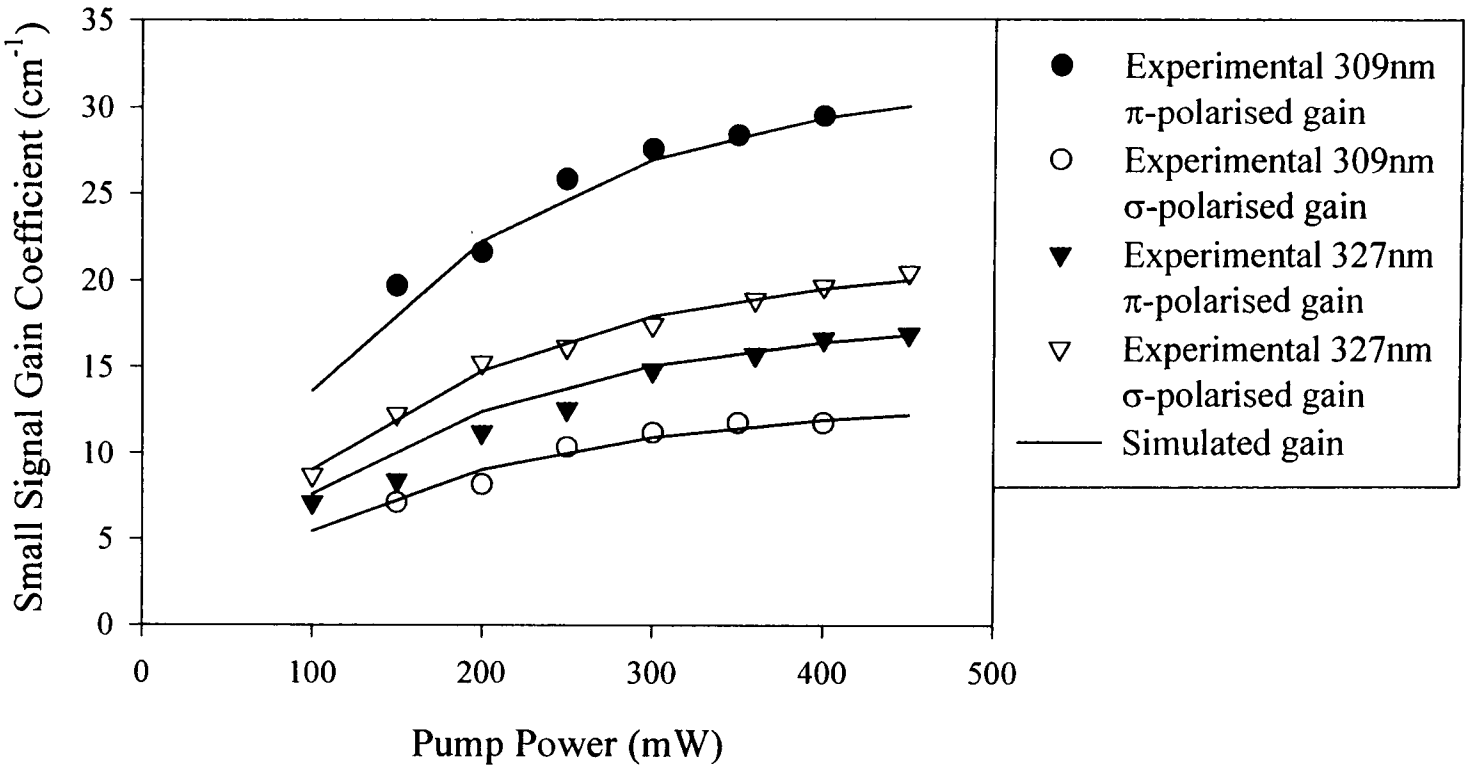


Figure 2.18 shows a comparison of the simulated small-signal gain coefficients and the experimentally determined small signal gain coefficients at -3°C. The lines show the simulated data and the symbols show the experimental data.

The new ESA cross-sections required to achieve the change in small-signal gain seen with temperature are shown in Table 2.3 along with a summary of the change in ESA with temperature. The increase in ESA cross-section for 309 nm, σ-polarised and both 327 nm polarisations was between 0.5×10^{-18} cm^2 and 0.6×10^{-18} cm^2. The change in ESA cross-section at 309 nm for the π-polarised gain required to simulate the change in gain with temperature was 0.15×10^{-18} cm^2, which is significantly smaller than for the other probe-polarisation combinations.

These simulations suggest that the presence of a temperature dependent excited state absorption would indeed result in the increase in small-signal gain with a decrease in temperature. The change in σ_{ESA} in all but the 309 nm, π-polarised, are of a similar extent, thus suggesting the change in ESA with temperature may be independent of polarisation and wavelength within the emission spectrum of Ce:LiLuF.

Table 2.3 show a comparison of the change in ESA cross-section required to simulate the change in small-signal gain in Ce:LiLuF with a 28°C temperature change.

Wavelength	309 nm	309 nm	327 nm	327 nm
Polarisation	π	σ	π	σ
σ_{ESA}(x10^{-18} cm^2) at -3°C	0	1.3	0	2.4
σ_{ESA}(x10^{-18} cm^2) at 25°C	0.15	1.8	0.55	3.2
$\Delta\sigma_{ESA}$(x10^{-18} cm^2/°C)	+0.15	+0.5	+0.55	+0.6

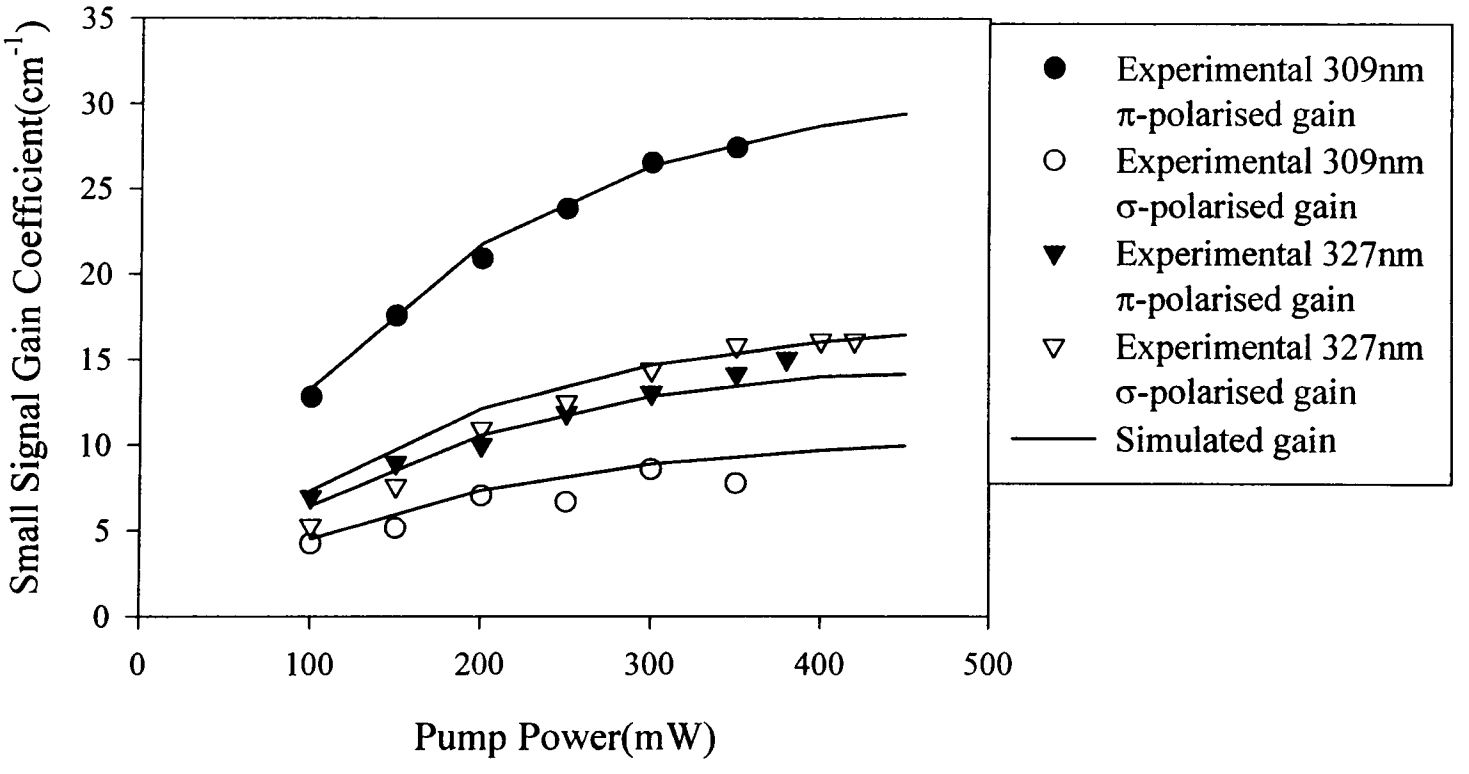


Figure 2.19 shows a comparison of the simulated small-signal gain coefficients and the experimentally determined small signal gain coefficients at 25°C. Excited-state absorption simulation results at 261 nm and 349 nm.

In order to determine the ESA cross-sections at 261 nm and 349 nm, the excited state absorption at these wavelengths was simulated. The ESA absorption cross-sections required

to achieve the experimentally measured ESA are shown in Table 2.4. It can be seen that good agreement between the experimental data and the simulated absorptions is obtained (Figure 2.20). The effective cross-sections at 261 nm and 349 nm imply absorption will be seen rather than gain, as expected, depicted by the negative sign of σ_{EFF}.

Table 2.4 Determined excited state absorption cross-sections for 261 nm and 349 nm the resulting effective gain cross-sections in Ce:LiLuF.

Wavelength and polarisation	261 nm; σ-polarisation	261 nm; π-polarisation	349 nm; σ-polarisation
σ_{EM} (x10^{-18} cm^2)	0	0	0.5
σ_{ESA}(x10^{-18} cm^2)	2.4	0.4	1.0
σ_{EFF}(x10^{-18} cm^2)	-2.4	-0.4	-0.5

A summary of the excited state absorption cross-sections, determined using the Ce:LiLuF model, is shown in Figure 2.21. As can be seen there is a definite broad excited-state feature in Ce:LiLuF between 261 nm and 349 nm, in which the σ-polarised absorption is dominant (shown by the extrapolation from 261 nm in the figure). A broad, π-polarised ESA feature also exists, however the π-polarised ESA cross-sections (between 0 and 0.5 x 10^{-18} cm^2) were much smaller than the σ-polarised ESA cross-sections (greater than 1 x 10^{-18} cm^2) in this wavelength region. On this ESA cross-section versus wavelength plot, the presence of a narrow absorbing feature both in the σ- and π-polarised absorption spectra can be seen, the peak of which lies between 320 nm and 340 nm. Again, as with the broad ESA spectrum, the σ-polarised absorption dominates the narrower absorption band, with only a small peak in the π-polarised ESA spectrum.

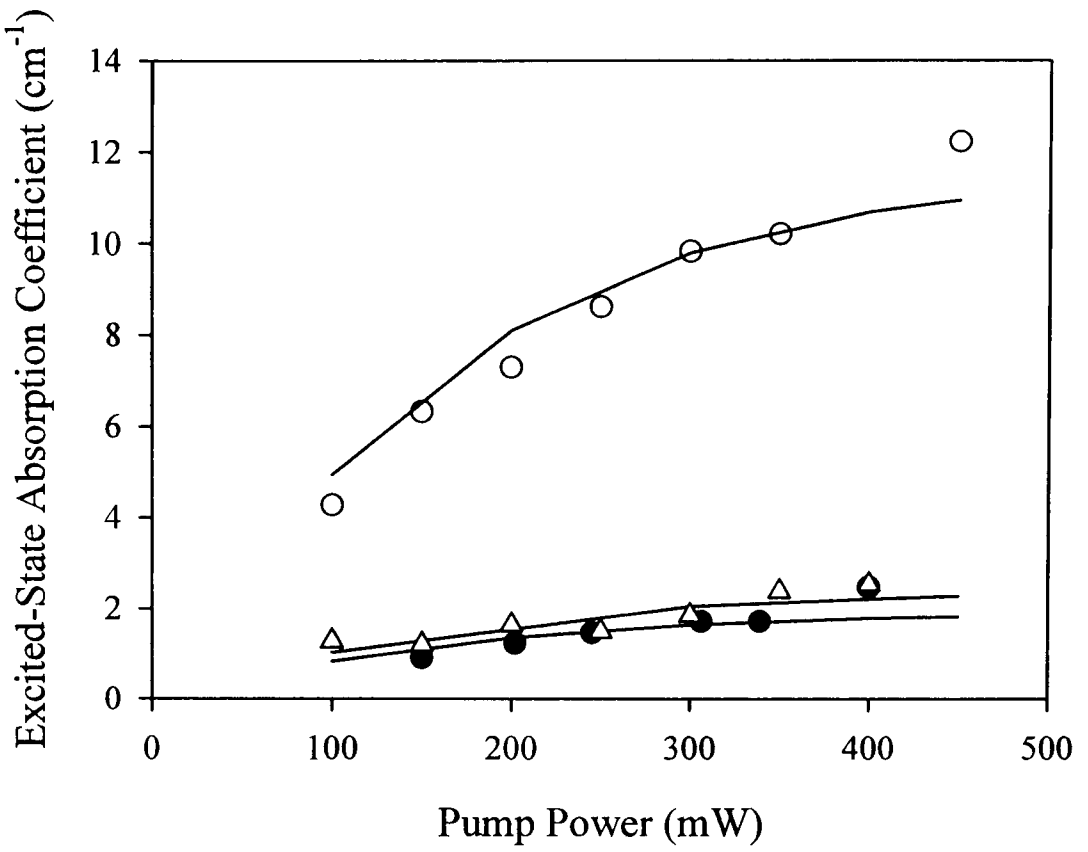


Figure 2.20 Comparison of the simulated and experimental ESA coefficients variation with pump power in Ce:LiLuF. The circles represent 261 nm and the triangles represent the 349 nm absorption (hollow - σ-polarised absorption, solid - π-polarised absorption).

The ESA cross-section at 316 nm was determined using the gain model to be $2.8\pm0.3 \times 10^{-18}$cm^2. The determined σ-polarised, 316 nm ESA cross-section is considered to only be approximate since the absorption at 316 nm was measured with a single pump power (500 mW pump power) and as such only one absorption value was used to obtained the ESA cross-section, unlike the ESA cross-sections determined at 349 nm in which the variation of absorption with pump power was simulated.

The addition of the 316 nm, σ-polarised ESA cross-section on the ESA versus wavelength chart results in a broader absorption band, than was estimated without this value, thus further data is essential in order to obtain an accurate idea of the shape of this narrow band feature.

The ESA spectrum provided by the simulations of the ESA and small signal gains between 261 nm and 349 nm gives evidence pointing to the presence of a broad ESA band in Ce:LiLuF between 261 nm and 349 nm on top of which appears to a narrower, temperature dependent absorption band peaking at ~330 nm. If this is in fact the case, the lack of temperature dependence of the absorption at 261 nm and 349 nm, and presence of temperature dependence between ~305 nm and 333 nm may be the result of the creation of pump-induced

colour centres which absorb strongly in between 305 nm and 333 nm. The validity of this proposal along with other possible explanations will be discussed in the next section, §2.6.

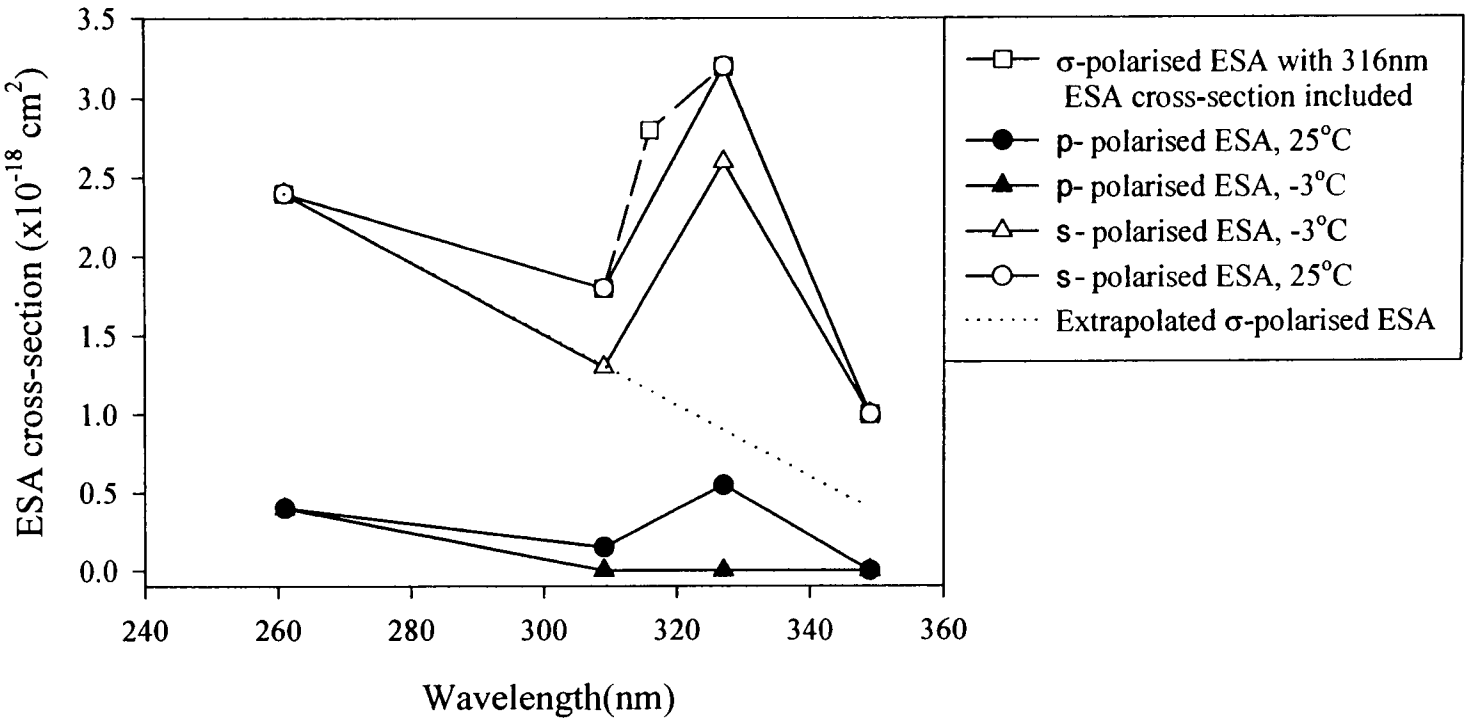


Figure 2.21 Summary of the wavelength dependence of the ESA cross-sections determined using the Ce:LiLuF model described in 2.5.1

Finally the ESA cross-section at 289 nm pump wavelength, in particular the π-polarised ESA cross-section, was estimated to be ~0.2 x 10^{-18} cm^2, which is small compared the 3.35 x 10^{-18} cm^2 ground-state absorption cross-section for π-polarised 289 nm radiation. The σ-polarised, 289 nm ESA cross-section was approximately 1.7x10^{-18} cm^2. The introduction of ESA at the pump wavelength into the program caused the small-signal gain to change by <5%, in fact only the gain at 309 nm with the σ-polarised probe was affected by more than 2%, with the small-signal gain decreasing by less than 2% for 327 nm probes and 309 nm, π-polarised probes in the presence of ESA at the pump wavelength. Thus the assumption made in §2.5.1 in which the ESA at the pump wavelength was neglected was a reasonable assumption.

The cross-sections determined by the numerical model described in this section gave an excellent replication of the experimental gain and ESA behaviour with pump power as shown in Figure 2.18, Figure 2.19 and Figure 2.20. The accuracies of the determined cross-sections however are limited by the accuracy of the trivalent cerium number density used in the gain model and pump mode size. The pump mode size required by the model was 70 μm compared to the calculated pump mode size of 110 μm, thus the pump mode size was accurate to within ~40% of the experimental spot size. The accuracy of the absorption cross-section determined

by Laroche is not known, hence the accuracy of the Ce^{3+} number density cannot be quantified. The discrimination between Ce^{3+} and other cerium species (eg Ce atoms, Ce^{2+} and Ce^{+}) in a crystal, in general, is very difficult. Measuring the absorption characteristics of the spectroscopically active Ce^{3+}, as was done in this thesis, is possibly the most accurate method of Ce^{3+} ion determination. Thus the Ce^{3+} number density determined in this thesis is considered to be a good approximation, and as such, the cross-sections determined here can be also regarded as good approximations to the true ESA cross-sections. Since the same Ce^{3+} number density was used throughout the modelling, the ESA cross-sections determined are considered to be correct to within a common scale factor, hence the behaviour displayed remains true despite any scaling of the cross-sections.

2.6 Discussion

The small-signal gains over most the Ce:LiLuF emission spectrum have been presented, giving the most detailed small-signal gain determinations for Ce:LiLuF to date. High gain coefficients of up to 30 cm^{-1} (equivalent to a single pass gain of 10) were achieved at 309 nm for a π-polarised probe in Ce:LiLuF with a pump fluence of 0.46J/cm^2. The temperature dependence of the small-signal gain in Ce:LiLuF has also been presented for the first time showing an increase in small-signal gain with decreasing temperature. The temperature dependence was found to be more explicit for the σ-polarised gain than the π-polarised gain. The temperature dependence of gain in Ce:LiLuF was shown to be inherent to Ce:LiLuF, with the extent of the temperature dependence varying according to the origin and growth procedure of the Ce:LiLuF laser crystal .

The results presented in this chapter give the most detailed analysis of the excited-state behaviour in Ce^{3+} in LiLuF to date. Understanding the excited-state behaviour in Ce:LiLuF provides the insight into the origin of the unusual lasing behaviour displayed by Ce:LiLuF, reported by McGonigle *et al.* (McGonigle *et al.* 1999a; McGonigle *et al.* 1999c; McGonigle *et al.* 2001b) and Cashmore *et al.* (Cashmore 1995), which has not been possible until now. The ESA in Ce:LiLuF was found to be anisotropic in nature with the σ-polarised absorption being dominant. The ESA outside the Ce:LiLuF emission spectrum was found to have a lifetime similar to that of the *lowest 5d* level and this absorption was also found to be independent of temperature.

Simulations of the small-signal gain and ESA in Ce:LiLuF enabled the ESA cross-sections to be determined at 309 nm, 327 nm, 261 nm and 349 nm to be determined, and the ESA cross-sections at 316 nm and 289 nm to be estimated. A temperature dependence of the ESA at 309 nm and 327 nm was shown as a possible origin of the temperature dependence of the

small-signal gain in Ce:LiLuF. There were various limitations of the gain model used in this chapter. The most prominent limitation was the uncertainty in the Ce^{3+} number density. This uncertainty in turn resulted in a large uncertainty in the pump intensities required by and population inversions simulated by the gain model. However even with these limitations the gain model still proved an extremely useful tool in understanding the gain behaviour in Ce:LiLuF.

There are two interesting features of the excited-state absorption determined in this chapter namely the polarisation dependence and the presence of what appears to be a temperature dependent narrow excited-state absorption band superimposed on top of a broad excited state absorption band. In the next section, a proposition is put forward and discussed as to the origins of these two features.

2.6.1 Origin of ESA in Ce:LiLuF

In general the ESA cross-sections determined for Ce:LiLuF in this thesis, are between 3.2×10^{-18} cm^2 and $<10^{-19}$ cm^2, and are therefore similar in magnitude to the ESA cross-sections in Ce:YAG (10×10^{-18} cm^2 at 700 nm (Hamilton *et al.* 1989)), Ce:LiCAF ($\sim 4.6 \times 10^{-18}$ cm^2 at 290 nm, σ-polarised) and Ce:LiSAF ($\sim 2.2 \times 10^{-18}$ cm^2 at 290 nm, σ-polarised) (Marshall *et al.* 1994). The large ESA cross-sections determined for Ce:LiLuF in this work suggest the transition to which they correspond is parity allowed, since these cross-sections are very similar in magnitude to the emission cross-sections for the $4f \rightarrow 5d$ which is known to be parity allowed (Hamilton *et al.* 1989).

The ESA in Ce:YAG has been shown to arise from the *lowest 5d* level (Jacobs *et al.* 1978; Miniscalco *et al.* 1978; Owen *et al.* 1981; Hamilton *et al.* 1989). Owen *et al.* (Owen *et al.* 1981) found the energy of the transition from the *lowest 5d* to the 3^{rd} *5d* level in Ce:YAG to be in good agreement with the energy of the absorbed photons. However the magnitude of the ESA cross-section in Ce:YAG ($\sim 10^{-18}$ cm^2) suggested that it was unlikely for the ESA to be a result of a $5d \rightarrow 5d$ transition since this is a very disallowed optical dipole transition, thus the corresponding cross-section would be much smaller than was determined. However Owen *et al.* did suggest that should the purity of the *upper 5d* levels be reduced due to the close proximity of the conduction band, this may reduce the disallowed nature of the transition enough to account for the larger emission cross-section. It has been since more or less accepted that in the case of Ce:YAG the ESA transition terminates in the conduction band and that, the higher *5d* levels lie within, or with comparative energy to the conduction band as indicated by photoconductivity results and ground state absorption measurements by Hamilton *et al.* (Hamilton *et al.* 1989). The GSA spectrum of Ce:YAG is shown in Figure

2.22. This spectrum shows an obvious overlap of the broad *4f→ CB* transition and the *4f → upper 5d* level transitions below 280 nm.

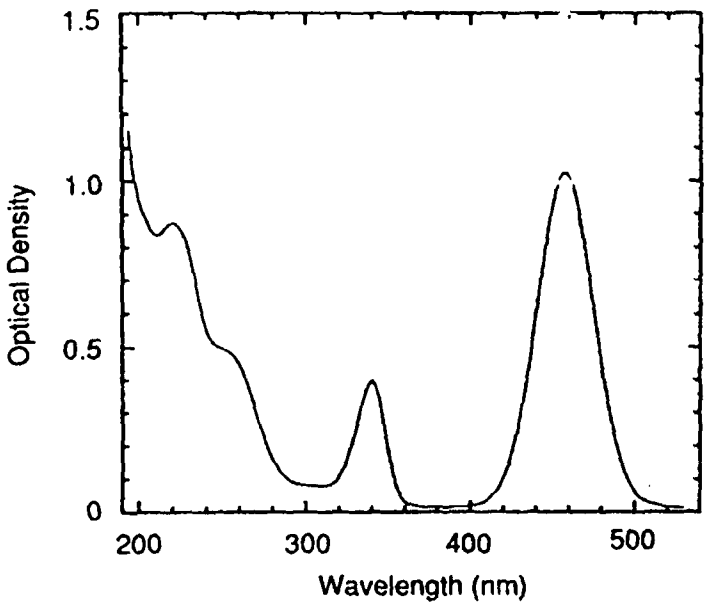


Figure 2.22 Ground state absorption spectra of Ce:YAG as measured by Hamilton *et al.* (Hamilton *et al.* 1989).

In Ce:LiCAF and Ce:LiSAF, the conduction band is also thought to be the terminal state of the ESA, but unlike Ce:YAG the upper *5d* levels are not known to overlap the conduction band and as such the loss due to ESA is much less and high gains have been observed (Marshall *et al.* 1994). In the same manner as seen in Ce:YAG, the magnitude of the ESA cross-sections in Ce:LiLuF are of the same order as the Ce:LiLuF emission cross-sections. However in Ce:LiLuF, the ground-state absorption bands of the higher lying *5d* levels are distinguishable from the rising background absorption as shown in Figure 2.23, indicating their discrete nature.

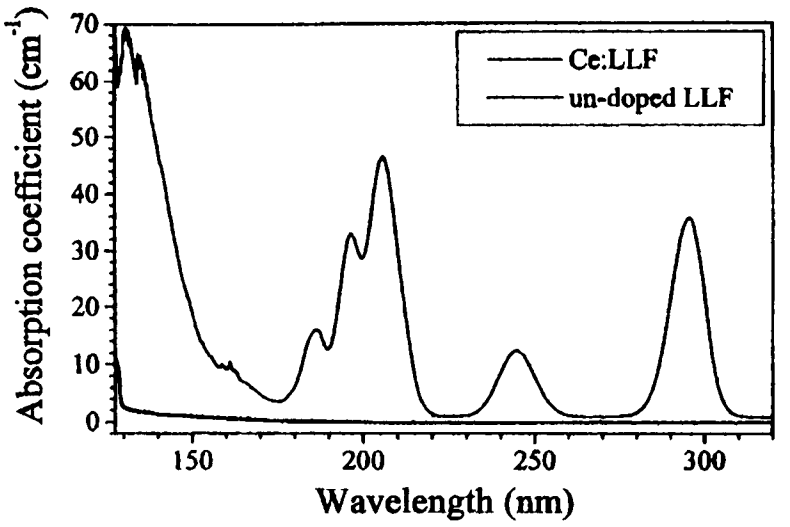


Figure 2.23 Ground-state absorption spectrum for Ce:LiLuF as measured by Ranieri *et al.* (Ranieri *et al.* 2000).

The ESA results determined in this chapter suggest that, firstly a broad ESA band from <261 nm to >349 nm exists which has no discernible temperature dependence. Secondly, there is a narrow ESA band from ~300 nm to 340 nm superimposed on the broad ESA band, present for both polarisations, which appears to be very sensitive to temperature, resulting in a decrease in the absorption with decreasing temperature. Assuming the lowest *4f* level corresponds to an energy of 0 cm^{-1}, the absorption band starting at ~ 170 nm (59000 cm^{-1}) and peaking at ~130 nm (77000 cm^{-1}) in Figure 2.23 is thought originate from a *4f*→*CB* transition. The undoped LiLuF absorption corresponding to the *valence band* → *conduction band* (photo-ionisation) transition starts at ~130 nm, as seen in Figure 2.23, supporting this assignment. Figure 1.9 in Chapter 1 shows explicitly the energy levels of the Ce^{3+} derived from Figure 2.23.

It is proposed that the broad excited-state absorption band observed in Ce:LiLuF is the result of a lowest *5d* level → *CB* transition. The lifetime of the 261 nm excited-state absorption indicates that the initial state for the broad ESA band was the lowest *5d* level. The lowest *5d* level is at ~ 34000cm^{-1}, thus the energy corresponding the lowest *5d*→ *CB* transition is ~25000 cm^{-1}; from this, the wavelength of light required to cause the excitation of an electron from the lowest *5d* state to the conduction band would be at most 400 nm. In order to reach the apparent peak of the conduction band (shown in Figure 2.23) from the lowest *5d* level a wavelength of ~230 nm would be required. This wavelength range is in excellent agreement with the extrapolation of the σ-polarised ESA spectrum shown in Figure 2.21. Further, should the shape of the *4f*→*CB* ground-state absorption band in Figure 2.22 be taken to give an indication of *5d*→*CB* ESA cross-section variation with wavelength, this too would be in

excellent agreement with the increasing ESA cross-sections with decreasing wavelength shown in Figure 2.21. Similarly, the wavelength dependence of pump induced absorption in Ce:LiLuF seen by Laroche *et al.* (Laroche *et al.* 10 -15 September 2000) also resembles the broad ESA band shown in Figure 2.21 for Ce:LiLuF. Ce:LiCAF and Ce:LiSAF have also been found to have a larger σ_{ESA} at shorter wavelengths (266 nm) compared to longer wavelengths (290 nm) (Marshall *et al.* 1994).

The single-photon mechanism implied by the linear relationship between the pump intensity and the induced absorption at 261 nm and 349 nm, (representative of the broad ESA band), is in concurrence with this simple excited–state absorption from the lowest *5d→CB*. The decay of the broad band ESA is assumed to be non-radiative as, so far, evidence of the decay from the conduction band is scarce. With the intense probe (~half the pump intensity) at 261 nm there was no noticeable fluorescence or phosphorescence from the conduction band.

Figure 2.21 shows that Ce:LiLuF has a narrower ESA band superimposed on top of the broad ESA band. The shape of the narrow band seen in Ce:LiLuF implies that between approximately 300 nm and 330 nm a positive slope of ESA with wavelength exists, for which the absorption at longer wavelengths is greater than that at shorter wavelengths. The blue-shift of the shorter wavelength peak in the small-signal gain spectrum when compared to emission spectrum is also suggestive of such a positive slope between 300 nm and 330 nm. Thus the position of the narrow band suggested by the ESA cross-sections determined using the gain simulations is in good agreement with the small-signal gain spectrum determined experimentally.

As to the origin of the narrower excited-state absorption band, it is proposed that it is due to a transition between the lowest *5d* level and a more discrete structure, such as a colour centre, lying within the conduction band. A closer look at the 130 nm absorption band shown in Figure 2.23 shows structure at ~160 nm (62500cm^{-1}) as well as near the peak of the absorption band. The variation in absorptivity in the GSA spectrum, giving the conduction band what appears to be structure, may arise from the presence of regions within the conduction band to which a transition from the *4f* level has different parity conditions. This may indicate an inhomogeneity of the conduction band arising from more discrete centres, possibly colour centres, embedded in the conduction band. Interestingly, should the structure in the GSA spectrum of Ce:LiLuF at 160 nm represent such a discrete centre within the conduction band, the energy difference of ~30000 cm^{-1} between this discrete centre (62500 cm^{-1}) and the bottom of the lowest *5d* level (~32600 cm^{-1}) corresponds very closely, in energy, to the transition resulting in the narrow ESA absorption band in Figure 2.21 (29000-33000 cm^{-1}). Furthermore it is conceivable that this structure, which is small in the GSA

spectrum, is larger in the ESA spectrum and shifted in wavelength due to the different parity conditions of the *4f→ discrete centre* transition compared to the lowest *5d→ discrete centre* transition.

Due to the prominence of colour centres in cerium lasers previously reported, the absorption structure seen at 160 nm in the GSA spectrum of Ce:LiLuF and the narrow-band absorption between 300 nm and 340 nm, may indeed have originated from colour-centres. Colour centres in cerium lasers have been thought to originate from a variety of impurities, including divalent cerium in O_h sites as well as the $F^{'}$ centres in a <111> site next to a Ce^{3+} ion (Pogatshnik and Hamilton 1987). Previously in both Ce:LiYF (Lim and Hamilton 1989; Sarukura *et al.* 1995a) and Ce:LiLuF (Sarukura *et al.* 1995a), a narrow band pump-induced absorption feature has been observed between ~310 nm and 400 nm. Lim *et al.* (Lim and Hamilton 1989) suggested colour centres arising from fluorine vacancies were responsible for this narrow absorption band. The position of the Ce:LiYF and Ce:LiLuF narrow absorption bands are very similar. The isomorphic nature of Ce:LiLuF and Ce:LiYF and the similarity in wavelength of these narrow absorption bands does suggest the origin of the narrow ESA band in Ce:LiLuF is also due to such fluorine vacancies colour-centre absorption, as was found to be the case in Ce:LiYF. One must keep in mind that Ce^{2+} is well known to cause the colour centres resulting in the red/ brown colouration of Ce:CaF_2 crystals (Pogatshnik and Hamilton 1987). No colouration of the Ce:LiLuF crystal used in this thesis has been observed, but in §2.2.2 a discrepancy was found between the measured cerium concentration and the implied Ce^{3+} concentration. This discrepancy suggested that a majority (~ten times the Ce^{3+} concentration) of cerium atoms and ions within the LiLuF crystal used were not in the useful form of Ce^{3+} and may have been in the form of Ce^{2+} ions. Results reported by Staebler and Schnatterly (Staebler and Schnatterly 1971) on ionised photo-chromic centres related to Ce^{2+} ions in CaF_2, show a well-defined absorption peaks at ~750 nm, ~300 nm and ~250 nm. The 300 nm peak was found to be more intense for exposure to σ-polarised 330 nm light. It is possible that similar Ce^{2+} photo-chromic centres are present in Ce:LiLuF with UV irradiation giving rise to the narrowband absorption seen in Ce:LiLuF. Colour-centres can be identified by a characteristic decay lifetime or the colour centres may be bleached by certain wavelengths, such details are required to identify the type of colour centre present in Ce:LiLuF.

Figure 2.24 shows a diagram of the ESA model in which a colour-centre is embedded in the conduction band. The energy of the colour centre (or other discrete absorbing centre) implied by the narrow ESA band wavelength places the colour centre between 64000 cm^{-1} and 68000 cm^{-1}, which is well inside the conduction band.

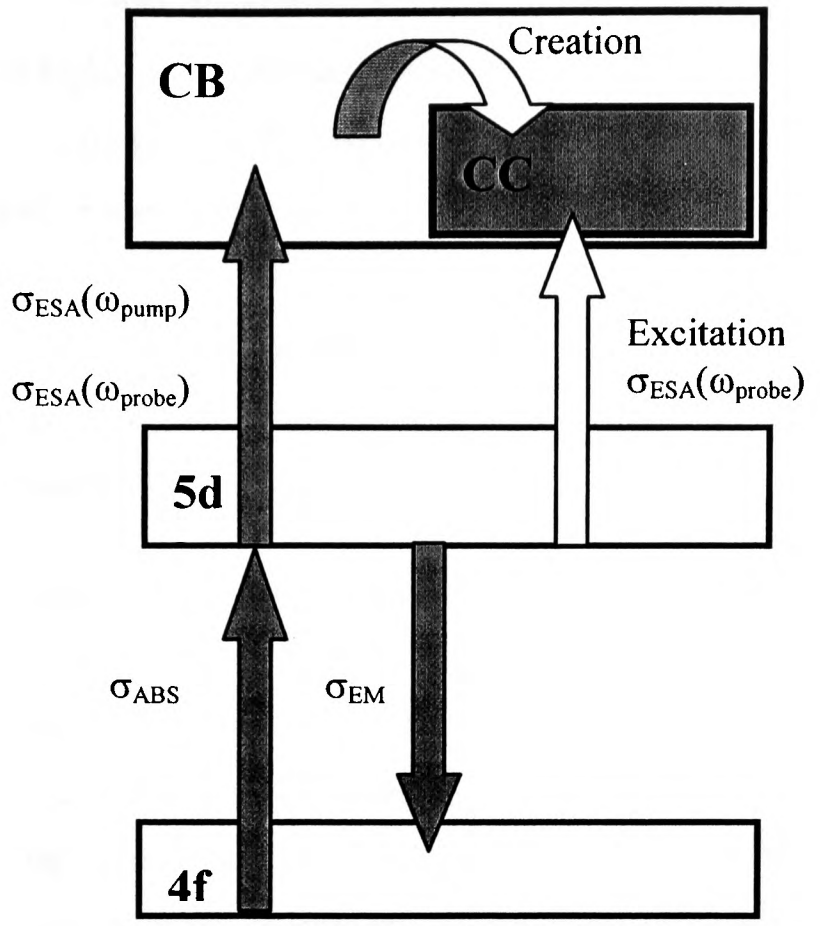


Figure 2.24 shows a schematic diagram of the creation and excitation of a colour centre which is embedded in the conduction band. The curved arrows represent non-radiative processes and the straight arrows represent radiative transitions.

2.6.2 Creation, dissociation and relaxation of colour centres and the origin of the temperature dependence of ESA and small-signal gain in Ce:LiLuF.

Possibly the most interesting feature of the lasing and gain experiments undertaken on Ce:LiLuF is the apparent temperature dependence of the ESA and consequent dependence of small signal gain and lasing on temperature. Understanding the mechanism leading to the temperature dependence may lead the way to obtaining even higher gains and more efficient lasing than already seen, either purely through further cooling, bleaching, or further improvements in growth methods as a result of understanding why and where the absorptive losses arise in the crystal structure.

The explicit temperature dependence of lasing in Ce:LiLuF is unique amongst the cerium doped laser crystals, however various spectroscopic properties of other cerium doped crystals have been found to be dependent on temperature. Firstly, one of the original papers on Ce:YAG by Weber (Weber 1973) reports the temperature dependence of the fluorescence lifetime in Ce:YAG. This lifetime is found to decrease rapidly due to an increase in non-radiative decay at temperatures above a threshold temperature specific to the doped crystal.

The threshold for Ce:YAG was found to be at ~600K, ~300K higher than that for Pr^{3+}:YAG. It was thought that this higher threshold temperature in Ce:YAG arises from the larger *4f→5d* band gap in Ce:YAG, compared to Pr:YAG, thus higher energy phonons were required to achieve phonon-assisted non-radiative decay. Also in Ce:YAG, Jacobs *et al.* (Jacobs *et al.* 1978) showed that by cooling the Ce:YAG crystal by ~40°C the excited-state absorption disappeared almost completely, in a similar manner to what has been shown in this chapter for the π-polarised ESA in Ce:LiLuF. Unfortunately this temperature dependence of ESA in Ce:YAG was not investigated further.

More recently, investigations into the formation of transient and stable colour centres by 308 nm pumping in Ce:LiYF showed that the stable colour centres were bleached as well as created by the 308 nm photons (Lim and Hamilton 1989). The lifetimes of the transient colour centres were found to be strongly temperature dependent and hence it was thought that the colour centres decay was phonon-assisted. The photo-bleaching of the stable colour centres was also found to be temperature dependent arising from the reduction, with decreasing temperature, of the ground-state absorption cross-section at 308 nm. This is thought to be due to the narrowing of the *4f→5d* absorption band with decreasing temperature. Thus there was less *4f→5d* absorption at 308 nm, hence more photons were then available for photo-bleaching of the colour centres, resulting in more efficient photo-bleaching.

Finally McGonigle *et al.*, aside from the reported temperature dependence in the lasing in Ce:LiLuF, have also reported an increase in spontaneous emission with decreasing temperature (McGonigle *et al.* 2001b). This increase in fluorescence with decreasing temperature was found to be independent of the pump intensity, in that the same increase was found with a focussed and unfocussed pump beam. The lifetime of the emission was found to be independent of temperature. McGonigle *et al.* proposed that these temperature effects were mediated by a one-photon absorption process involving the fluorescence photons. The unchanging emission lifetime indicated that the crystal heating did not provide an alternative *5d* relaxation mechanism. The fluorescence intensity is directly related to the *lowest 5d* population thus the increase in fluorescence intensity with decreasing temperature can possibly indicate an increase in the pumping efficiency, resulting in a higher average population inversion. The reason behind such an increase in pumping efficiency is not known. The increase in *5d* population with decreasing temperature however cannot be related to pump-induced effects (such as ESA), as if this was the case, the increase in *5d* population with decreasing temperature would be dependent on pump intensity, and as such, decreasing the temperature would have more of an effect with the focussed pump compared to the effect with the unfocussed pump and this is not what was seen.

On an aside, Combes *et al* (Combes *et al.* 1997) have investigated the temperature dependence of X-ray induced emission in Ce:LiYF and have proposed a model to describe the variation in colour centre emission intensity and Ce^{3+} luminescence intensity with temperature. The X-ray induced Ce^{3+} luminescence was found to increase with increasing temperature and it is thought that this arose from the increase in F_2^- centre mobility with increasing temperature. This increase in mobility of the F centres was thought to result in an increased probability of the F centres decaying non-radiatively or being trapped at a Ce^{3+} site as opposed to forming colour centres. The increase in F centres being trapped in the Ce^{3+} site resulted in the increased luminescence. X-ray induced emission observations may not be directly relevant to UV induced emission however, it may provide insight into the possible decay mechanisms of UV induced colour centres in Ce:LiYF.

With the variety of effects temperature has on emission, non-radiative decay probabilities, colour centre bleaching and lifetimes as well as impurity movements in cerium doped crystals, the overall mechanism describing the temperature dependence of the excited state absorption in Ce:LiLuF is not expected to be a simple one. Consequently, using the observations of Ce:LiLuF temperature dependence described in this chapter together with previously reported evidence regarding excited state absorption in Ce:LiLuF, one simplified origin of the temperature dependence in Ce:LiLuF is proposed here and its validity is discussed.

Assuming the 300-340 nm absorption does arise from a colour centre lying within the conduction band as proposed in the previous section then the temperature dependence of only the narrow-band absorption rather than the whole ESA absorption spectrum is conceivable. What is known about the temperature dependence of the narrow band absorption is that a decrease in temperature results in a decrease in absorption between 300 nm and 340 nm. This temperature dependence will arise from either a decrease in the number of absorbing colour-centres with decreasing temperature or a decrease in the absorption efficiency with decreasing temperature.

It can be surmised that the colour centres in Ce:LiLuF are created by excited-state absorption of the pump wavelength from the *lowest 5d* $\rightarrow$ *CB*, followed by migration of electrons through the conduction band to impurities (as shown in Figure 2.24). The independence of the probe absorption on the probe intensity described in § 2.4.2 does give some evidence of such a mechanism, as opposed to radiatively induced colour centre formation via probe ESA photons. Further evidence supporting this creation mechanism is given by the absorption measurement made by Laroche *et al.* (Laroche *et al.* 10 -15 September 2000). Laroche *et al.* measured the excited-state absorption between 300 nm to 700 nm with σ-polarised and

π-polarised pumping at 290 nm. The ESA resulting from σ- polarised pumping was found to be ~2 times greater than that with π-polarised pumping. The magnitude of the ESA observed with the σ- or π-polarised pumps may be indicative of the colour centre density induced by that pump polarisation. This is in turn perhaps results in the higher colour-centre creation efficiency when using a σ-polarised pump than a π-polarised pump caused by the higher σ-polarised lowest $5d \rightarrow CB$ ESA cross-section compared to the π-polarised lowest $5d \rightarrow CB$ ESA cross-section at 290 nm. A colour centre creation mechanism dependent on the migration of electrons through the conduction band is inclined to be highly sensitive to temperature since the mobility of electrons within the conduction band will be dependent on temperature. The mobility of the electrons will increase with increased temperature thus the probability of an electron being trapped and creating a colour centre, will also increase and subsequently, the colour centre density and resulting colour centre absorption will increase with increasing temperature. This mechanism would result in the temperature dependence seen experimentally.

This temperature dependence of colour centre formation supports the effect of temperature on bleaching in Ce:LiLuF reported by McGonigle *et al.* (McGonigle *et al.* 2001b). At room temperature the 633 nm absorption was found to be 0.5% and cooling of the crystal virtually eliminated this 633 nm absorption. If indeed this 633 nm absorption was due to bleaching of colour centres, a decrease in colour centre density with decreasing temperature would decrease the amount of absorption at the bleaching wavelengths.

The temperature dependence of fluorescence intensity in Ce:LiLuF observed by McGonigle *et al.* (McGonigle *et al.* 2001b) could also arise from such a decrease in colour-centre creation rate. As a decrease in temperature would induce a decrease in the absorption of the 300 nm to 340 nm photons and consequently would result in an increase in fluorescence intensity. However this is unlikely to be the case since the creation rate of colour centres is dependent on pump intensity and McGonigle *et al.* found the temperature dependence of the fluorescence intensity to be independent of pump intensity. McGonigle *et al* (McGonigle *et al.* 1999a) also showed that anti-solarant pumping at 578 nm during Ce:LiLuF lasing resulted in a 30% increase in the laser output of Ce:LiLuF, which is also perhaps indicative of a decrease in absorption at the laser wavelength that would result from a reduction in colour centre density due to bleaching.

$$CC_{Precursor} \underset{\text{Dissociation}}{\overset{\text{Formation by acceptance or loss of an electron via the conduction band}}{\rightleftharpoons}} CC \qquad 2.13$$

$$CC \underset{\text{Non-radiative relaxation}}{\overset{\text{Excitation by laser and pump photons}}{\rightleftarrows}} CC^* \qquad 2.14$$

In a similar manner to the non-radiative creation mechanism just described, the non-radiative dissociation of the colour centres to colour centre precursors shown in equation 2.13, as well as the non-radiative decay of excited colour centres to unexcited colour centres shown in equation 2.14, arising from the overlap in the energy of the colour centre with that of the conduction band, is also inclined to be sensitive to temperature. If the mobility of electrons was to increase with increasing temperature, one would expect the decay lifetime to be shorter at higher temperatures. The thermally activated decay of colour centres seen in Ce:LiYF (Lim and Hamilton 1989) could be the result of such a temperature dependence. The possible decay mechanisms for a colour centre in the conduction band are shown schematically in Figure 2.24.

The temperature dependence of the absorption lifetimes observed for the pump-induced σ-polarised, 316 nm absorption in Ce:LiLuF showed the lifetime of the absorption to be smaller at low temperatures than at high temperature. This opposes the electron mobility model just described. With a cold crystal, the lifetime of the absorption was found to ~34 ns, which was similar to the 261 nm ESA lifetime shown in Figure 2.12, which is perhaps indicative that the cold crystal absorption was pure *5d→CB* ESA. The hot crystal had a longer lifetime of ~63 ns. This hot crystal absorption may be a combination of *5d→CB* and colour centre absorption. The lifetime of this type of absorption would be a combination of the *5d* lifetime and the colour centre lifetime. Thus the increase in lifetime seen experimentally in the hot crystal may be indicative of both ESA and subsequent colour centre absorption, where the latter were longer lived, giving the longer apparent lifetime.

Other possible decay mechanisms of colour centres in Ce:LiLuF include non-radiative decay to the upper and lower *5d* levels and then either fluorescence or further non-radiative decay to the *4f* level as shown in Figure 2.25. Of particular interest is the fact that McGonigle *et al.* (McGonigle *et al.* 2001b) did see visible fluorescence at a range of wavelengths between ~500 nm and ~700 nm, during lasing. The fluorescence wavelength was found to depend on the wavelength to which the laser was tuned, between 315.5 nm and 332 nm. The crystal used in these experiments was the 2 mm Maine Ce:LiLuF crystal. This visible fluorescence was not present with the cavity misaligned, even though the pump was still present; suggesting the creation of the radiating species was due to the presence of the laser photons of between 315-332 nm. Although, this fluorescence has not been detected in recent experiments using the 0.78 mm Maine crystal, the fluorescence does suggest a radiative decay pathway from the conduction band is present, if not dominant. It also suggests that the emitting species are

excited by photons at laser wavelengths. Should the visible fluorescence arise from the decay of the narrow-band absorbing feature, as suggested by the tuning region in which it is seen, this would be in reasonably good agreement with the decay from the narrow-band absorbing feature in Figure 2.23 to the highest *5d* state as the wavelength would be between ~350 nm and ~1.2 μm, thus encompassing the range of visible fluorescence seen.

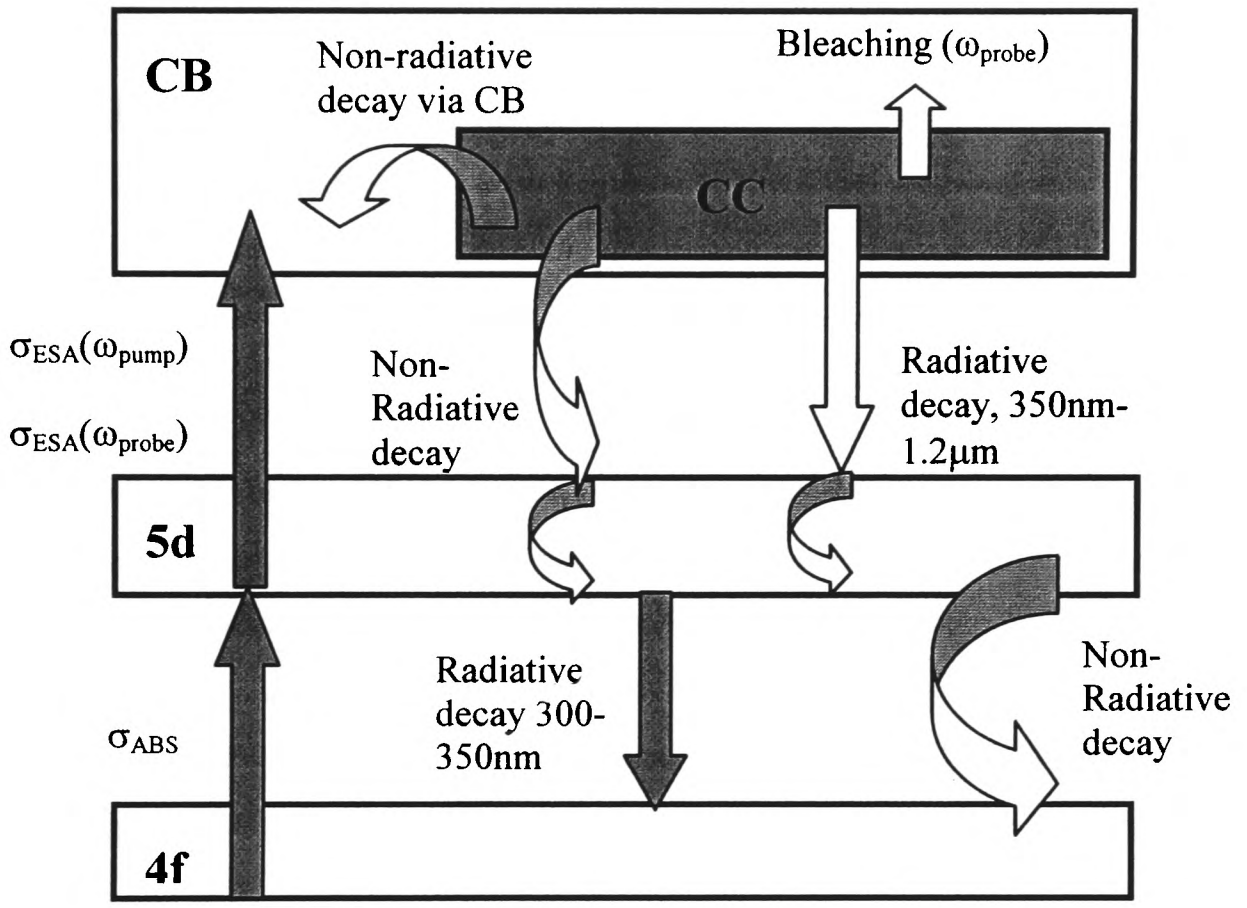


Figure 2.25 shows a schematic diagram of the decay pathways possible for a colour centre in the conduction band.

2.6.3 Polarisation of the ESA Cross-sections in Ce:LiLuF

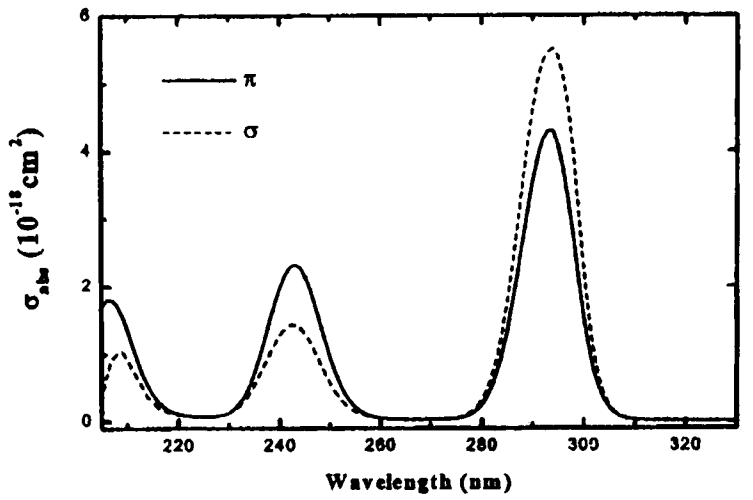
The extent to which the polarisation dependence of the excited-state absorption influences the small-signal gain in Ce:LiLuF reported here is similar to that found in Ce:LiCAF and Ce:LiSAF (Marshall *et al.* 1994) where the ESA cross-sections were in general larger for the σ-polarisation than the π-polarisation. Most notably, at the pump wavelength used for Ce:LiSAF (266 nm), the σ-polarised σ_{ESA} was found to be 3.5 times larger than the π-polarised σ_{ESA} at this wavelength, thus explaining the notable difference in the gain achieved using the π-polarised pump ($G \cong 11$) compared to the σ-polarised pump ($G<2$). Marshall *et al.* (Marshall *et al.* 1994) suggested the variation in magnitude of the σ- and π-polarised ESA cross-sections was due to the layered nature of LiSAF and LiCAF. The conduction band is generally thought to be made up of the cation (+ve ion) wave functions.

From the crystal structure of LiSAF, Marshall *et al.* deduced that parallel (π) to the *c*-axis of the crystal, the Ce^{3+} ions interact mostly with Li^{+} and Al^{3+} ions, whereas perpendicular (σ) to the *c*-axis, the Ce^{3+} ions interact mostly with Sr^{2+} ions. As a result of the different interaction strengths between Ce^{3+} ions with Li^{+} and Al^{3+} ions compared to the interaction strength of Ce^{3+} ions with Sr^{2+} ions, the energy of the conduction band perpendicular to the *c*-axis was thought to be lower than the energy of the conduction band parallel with the *c*-axis. As such, it was proposed that since the position of the π-polarised conduction band is higher in energy than the σ-polarised conduction band, the σ-polarised ESA occurs more easily than the π-polarised ESA, hence the larger σ_{ESA} for σ-polarised ESA.

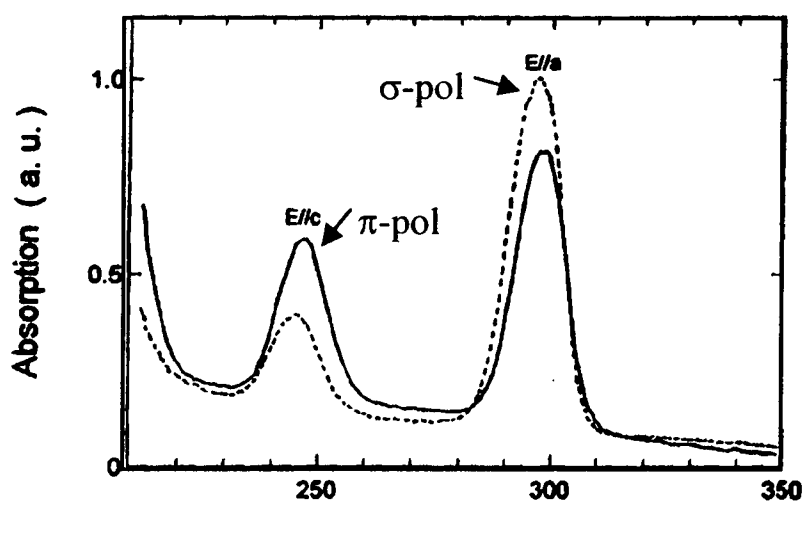
Based on the same overall idea used by Marshall *et al.*, using evidence provided by electron spin resonance (ESR) in Ce:LiCAF, Yamaga *et al.* (Yamaga *et al.* 1998) further substantiated the basis of Marshall *et al.*'s explanation. They found the eigenfunction of the lowest *5d* state to extend in the direction perpendicular to the *c*-axis, thus implying the lowest *5d* interacted more with σ-polarised light than π-polarised light, thus the lowest *5d*→*CB* transition occurred more readily when driven by σ-polarised light. Where Marshall *et al.* proposed it was the energy of the conduction band that varies for the two polarisations, Yamaga *et al* proposed it was rather the strength with which σ-polarised light interacts with the lowest *5d* level compared to the strength with which the π-polarised light interacts with the lowest *5d* level that is different.

The layered nature characteristic of LiCAF and LiSAF is to some extent valid for LiYF and LiLuF, in that these crystals are also layered (Yosida *et al.* 1997). The layers in LiLuF are interlaced in a scheelite structure such that the overall environment perpendicular to and parallel to the Ce^{3+} ions (replacing the Lu^{3+} ions) can be approximated as being similar (see scheelite structure of Ce:LiYF in Chapter 1). Thus the explanations put forward by Marshall *et al.* and Yamaga *et al.* toward understanding the polarisation dependence of the ESA in Ce:LiCAF are not transferable to Ce:LiLuF. However, using ESR results from Yosida *et al.* (Yosida *et al.* 1997) and Yamaga *et al.* (Yamaga *et al.* 2002) a better understanding of the polarisation dependence of Ce:LiLuF can be achieved. As described by Yosida *et al.*, the polarised (GSA) spectrum of Ce:LiYF shows a mixture of both σ- and π-polarised absorption at 245 nm and 292 nm. This mixture of polarization in the absorption was suggested to be due mixing of the $|x^2\text{-}y^2\rangle$ E_g state and $|2z^2\text{-}x^2\text{-}y^2\rangle$ E_g state in the *5d* level. Since Ce:LiLuF is isomorphic to Ce:LiYF, using the similarity of electronic configuration between these two crystals, a similar mixing of the excited 5d (E_g) $|x^2\text{-}y^2\rangle$ and $|2z^2\text{-}x^2\text{-}y^2\rangle$ states can be used to explain the analogous GSA behaviour seen in Ce:LiLuF. The similarity of the GSA spectra

can be seen by comparing the absorption spectra for Ce:LiLuF to that for the Ce:LiYF both shown in Figure 2.26.



a)



b)

Figure 2.26 Polarised GSA spectra for a) Ce:LiLuF (Laroche *et al.* 2003) and b) Ce:LiYF (Yosida *et al.* 1997).

The GSA at 292 nm corresponds to the *4f*→ lowest *5d* state transition, the terminal state of which is the lowest *5d* level, from which the ESA is believed to originate. The GSA is found to be larger for σ-polarised radiation than for π-polarized radiation at 292 nm, suggesting the lowest *5d* level interacts more strongly with σ-polarized light than with π-polarized light. This GSA polarisation dependence is very reminiscent of the polarisation dependence of the measured ESA in Ce:LiLuF. Since the lowest *5d* level is common to the 292 nm GSA transition and the ESA transition in Ce:LiLuF, it is possible that the polarisation dependence of the ESA arises from the mixed nature of the lowest *5d* level, like the GSA. If the wave function of the conduction band is approximated by an *s*-orbital, which interacts equally with

the σ- and π-polarisations, then the polarisation dependence of the ESA will arise from the lowest *5d* level.

The initial state of the GSA cannot be approximated as an *s*-orbital, thus the polarisation dependence of the *4f* → lowest *5d* transition is a result of the interaction of both the *4f* and *5d* wave-functions and is not purely due to the mixed nature of the lowest *5d* level. As such, unfortunately comparing the ratio of σ- to π- polarised GSA and ESA cross-sections, cannot be used to confirm the origin of polarisation dependence in GSA and ESA is the same. However the resemblance of the polarisation dependence of the ESA to the GSA in Ce:LiLuF does suggest the polarisation dependence arises from the mixed nature of the lowest *5d*, ^2E_g states.

Continuing in a related area, the close resemblance of the σ : π ratio of the small-signal gain (determined in §2.3.2) for the relatively poor quality Kazan State crystal (1 : 3.8) when compared to that of the higher quality Maine crystal (1 : 3.4) may be indicative of the fact that the use of different growth methods and starting materials in the preparation of the Ce:LiLuF crystals does not affect the general purity of the *4f* and *5d* states and thus the way in which Ce^{3+} ions interact with polarised light. The different growth methods and starting materials, (in particular the purity of the starting materials) do however contribute significantly to the number and behaviour of defect/impurity sites in the crystal matrix, and hence play an important part in determining the severity of colour centre effects in the crystals. The better lasing efficiency found with the Maine crystal (McGonigle *et al.* 1999a) compared to the Kazan State crystal (McGonigle *et al.* 1999c) is evidence of this.

In summary, this chapter provides the first detailed evidence of the presence of excited-state absorption in Ce:LiLuF, with the ESA cross-sections of equal order of magnitude to the emission cross-sections. These results have allowed some understanding of the laser behaviour seen in Ce:LiLuF to be achieved. The most significant result is the dominance of σ-polarised ESA in Ce:LiLuF both at the lasing wavelengths and the pump wavelengths. Another significant result is some evidence suggesting that ESA coincident with the longer wavelength GSA peak is less severe than that coincident with the shorter wavelength GSA peaks. This means that pumping into the longer wavelength GSA band, in particular with π-polarised pump light is beneficial to the pumping efficiency of Ce:LiLuF. Evidence suggesting that the π-polarised lasing can be expected to be more efficient than σ-polarised lasing is also given, again resulting from the dominant σ-polarised ESA. The effect of polarised ESA on Ce:LiLuF lasing, in particular, is discussed in detail in the next chapter.

Thus although much can be learnt about the effects of ESA on lasing in Ce:LiLuF from the results presented in this chapter, many more questions are posed by the results. Proposed answers to some of these questions were presented in this subsection, but more substantial evidence is required to back them up fully.

[3] Lasing in $Ce:LiLuF_4$

3.1 Introduction

In this chapter, a report is made of the investigations undertaken which were directed towards a better understanding of the unusual lasing behaviour observed by McGonigle *et al.* (McGonigle *et al.* 2001b) in Ce:LiLuF. The unusual lasing behaviour observed by McGonigle *et al.* is described in detail in Chapter 1. A brief recap of this behaviour is given here. The efficiency of the Ce:LiLuF laser, when pumped by the 10 kHz frequency doubled yellow output of a copper vapour laser (CVL), was found to be very temperature dependent, with the laser output increasing noticeably with decreasing temperature. The temperature dependence of lasing over the tuning curve of Ce:LiLuF observed by McGonigle *et al.* was of particular interest. At room temperature, continuously tunable output was obtained between 305 nm and 335 nm. The laser output was found to be π-polarised over the whole laser tuning range. Cooling the Ce:LiLuF crystal down to -3°C, resulted in an increase in the laser output between 305-324 nm and 330-335 nm. As at room temperature, in these tuning regions, the laser output was all π-polarised. Between 324 nm and 330 nm, the laser output was found to increase with decreasing temperature until ~10° C. Below 10°C the laser output was found to decrease. The laser output in this region was also found to become increasingly σ-polarised as well as increasingly unstable as the crystal was cooled below 10°C. In the previous chapter the temperature dependence of the gain was shown to arise possibly from a temperature dependence of the excited-state absorption. This temperature dependence of the small-signal gain would cause an increase in laser efficiency with decreasing temperature such as that observed by McGonigle *et al.* The decrease in laser output at 327 nm with decreasing

temperature is, however, not in agreement with the temperature dependence of the small-signal gain measured in Chapter 2.

The mechanism behind this unusual lasing behaviour was the central interest, motivating the laser experiments described in this chapter. To investigate the overall lasing behaviour in Ce:LiLuF more fully, various experiments were conducted. In §3.2, the π-polarised, 309 nm lasing was the focus. In these experimental investigations, the laser cavity used had non-wavelength selective output couplers which resulted in pure 309 nm, π-polarised lasing. In this section, firstly the dependence of the 309 nm lasing thresholds and efficiencies with two different laser cavity designs was investigated. Secondly the temperature dependence of 309 nm, π-polarised Ce:LiLuF lasing was measured.

In §3.3, the 327 nm lasing was the focus of investigation. In these experiments output couplers biased towards 327 nm lasing were used, allowing the lasing behaviour at 327 nm, in particular, to be investigated more fully. In §3.4, a detailed investigation of the temperature dependence of the prism-tuned laser output was undertaken, particularly in the neighbourhood of 327 nm. Finally in §3.5, the results of simulations of the lasing in Ce:LiLuF (using a simplified laser model) are reported. These simulations were run to aid an understanding of the complex competitive effects present in Ce:LiLuF lasers. §3.6 collates all the simulated and experimental data and the understanding of the Ce:LiLuF lasing gained from the previous sections is discussed.

3.2 Ce:LiLuF Lasing with Non-Wavelength Specific Output Couplers.

3.2.1 Experimental Configuration

In these experiments, both the KE-UV-CVL (in the Rigrod-analysis experiments) and non-kinetically enhanced UV-CVL (in all the other experiments described in this section) were used, giving 289 nm, 10kHz output which was used to pump the 0.78 mm Maine Ce:LiLuF crystal. In all the lasing experiments described in this chapter the pump configuration used was that described in §1.3.1.2. The 0.78 mm long crystal gives ~77% absorption of the pump light. As in the previous chapter the crystal was uncoated and cut such that the *c*-axis corresponded to the horizontal axis of the crystal end face. The Ce:LiLuF crystal was found to be slightly wedged, both perpendicular and parallel to the c-axis. As described in §2.1.1, the crystal temperature was controlled using a Melcor chiller. A quasi-longitudinal pumping configuration was used in which the ~5 mm (in the case of the KE-UV-CVL) and the 6 mm (in the case of the UV-CVL) pump beam was focussed into the crystal using a 100 mm focussing lens, giving pump spot diameters in the crystal of ~66 μm

and ~55 μm respectively. By adjusting the lens-crystal distance for maximum transmission, the focus was confirmed to be optimally positioned in the Ce:LiLuF crystal.

The laser cavities used in the lasing experiments described in this section consisted of a flat output coupler and a curved high reflector. Two high reflectors were used, one with radius of curvature (ROC) of 0.1 m and the other with ROC = 0.25 m. The reflectivities of the high reflectors were >99.9% between 300 and 330 nm. Output couplers of 90%, 80%, 50% and 30% reflectivity were used. The 90%, 50% and 30% output couplers used in this section had approximately equal reflectivities (equivalent to within ~2%) at 309 nm and at 327 nm, the 80% output coupler on the other hand had a reflectivity of 78% at 309 nm and a reflectivity of 65% at 327 nm (this will be specified where necessary).

A simple near-hemispherical cavity arrangement was used, with a small angle (<10°) between the pump beam and laser mode, as shown in Figure 3.1. The cavity was aligned using a He-Ne laser. The cavity length with the 0.1 m ROC high reflector was ~9 cm and that with the 0.25 m ROC high reflector was 4.5 cm (as was used by McGonigle *et al.* (McGonigle *et al.* 1999a)). In both cavities the output coupler was placed 1-3 mm from the Ce:LiLuF laser crystal. The crystal was aligned such that one face was normal to the laser mode and located near the waist on the plain mirror such that the reflection loss for one face could be neglected.

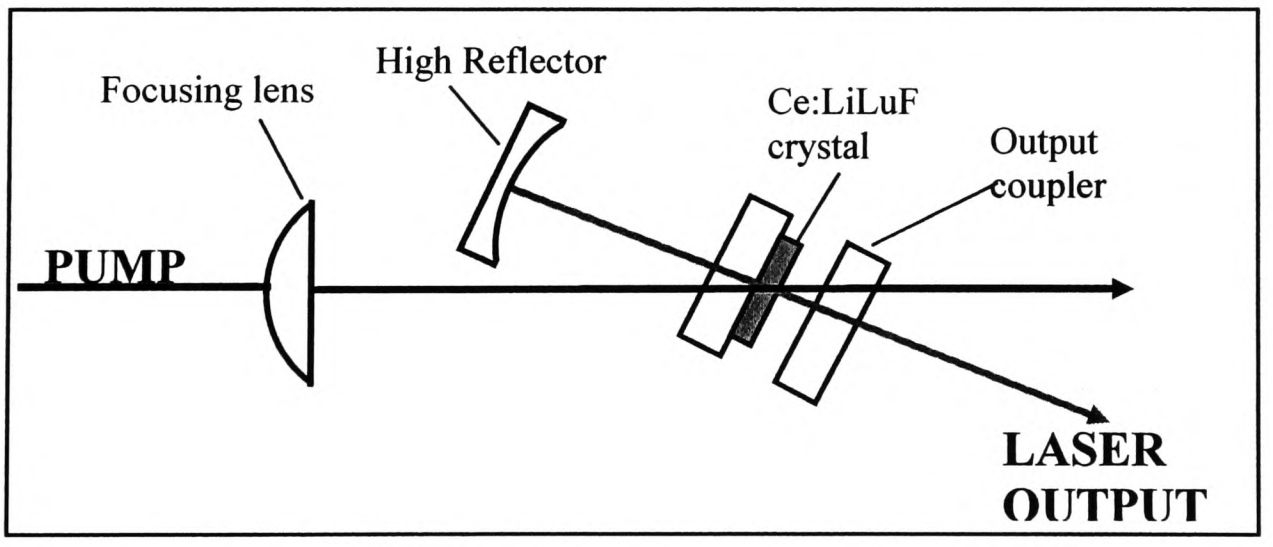


Figure 3.1 shows a schematic diagram of the near-hemispherical cavity and quasi-longitudinal pumping configuration used in the Ce:LiLuF laser.

The laser output was found to be very sensitive to the output coupler position as well as to both the vertical and horizontal laser crystal alignment. The sensitivity of the crystal-output coupler distance is discussed further in the §3.2.2. The origin of the sensitivity of the crystal alignment was not clear, however it may have been due to the wedged shape of the crystal, requiring a balance between the gain length and c-axis alignment for maximum output.

In all the experiments described in this section, the fluorescence and laser pulse measurements were made using a Thorlabs DET 200 photodiode (<1ns rise time) connected to a Tektronix TDS 3034 500 MHz oscilloscope.

3.2.2 Results 1 - Cavity dependence of Ce:LiLuF lasing.

In this investigation, firstly a Rigrod analysis of the Ce:LiLuF 309 nm lasing was conducted. The cavity used was the 9 cm long cavity with the 0.1 m ROC high reflector. The laser output was measured with varying pump powers with each of the four output couplers available, namely output couplers with reflectivities of 30%, 50%, 80% and 90%. In these experiments the Ce:LiLuF crystal was cooled to ~ -1°C. In order to maintain the exact cavity length and intrinsic cavity losses, when changing output coupler, only the output coupler mirror was removed leaving the mirror mount unchanged. Small adjustments were then made only to the angle of the output coupler mirror to achieve maximum laser output. The laser output and slope efficiencies measured in these experiments are shown in Figure 3.2 and a summary of the lasing behaviour is given in Table 3.1.

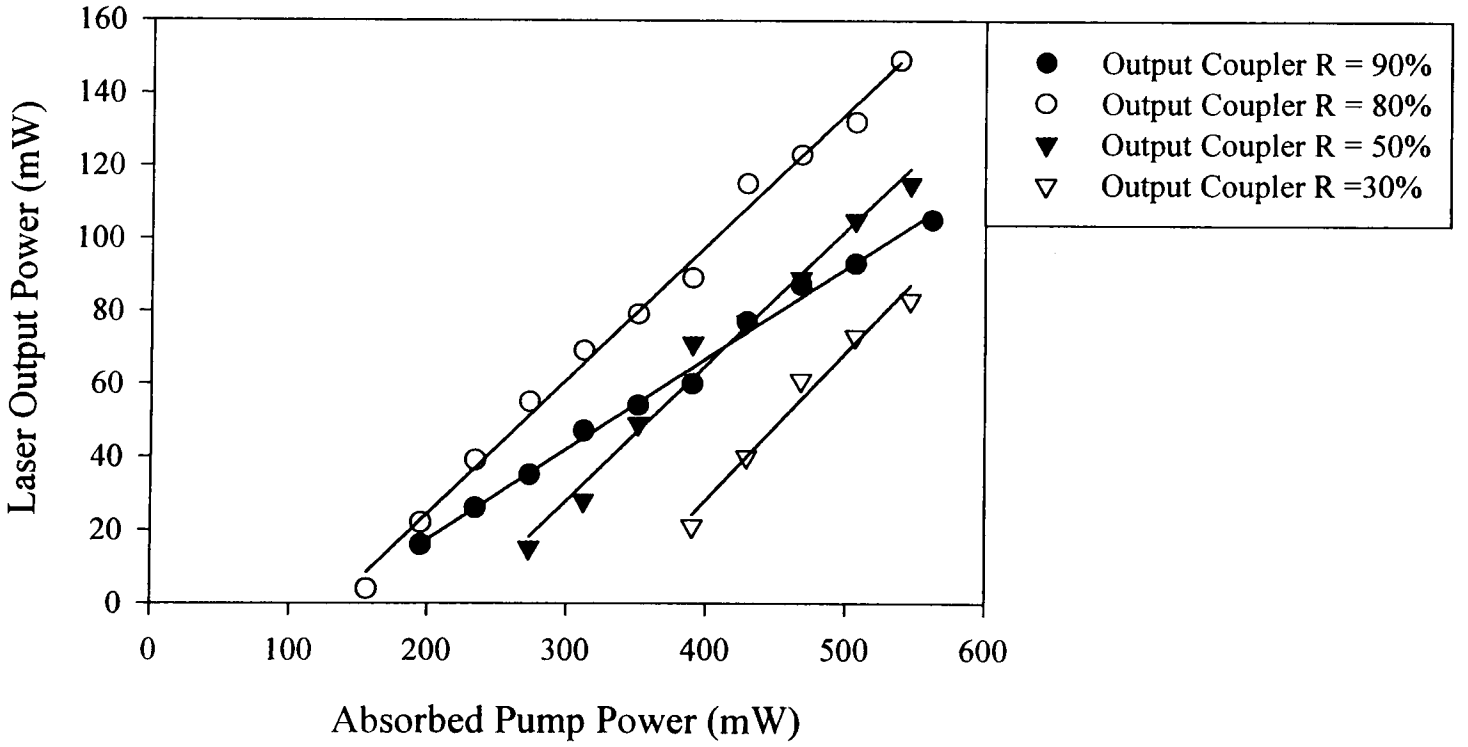


Figure 3.2 shows the laser-pump characteristics for Ce:LiLuF with four different output couplers with the crystal temperature held at ~ -1°C.

The wavelength of the laser output, with all four output couplers, was found to be at 309 nm and was completely π-polarised. The maximum output obtained was with the 80% output coupler (R=78% at 309 nm), with a laser output of 150mW from an incident pump power of 690mW, (corresponding to an absorbed pump power of 530 mW). As can be seen in Figure

3.2, there is very little difference in slope efficiencies of the 30%, 50% and 80% output coupler cavities with the slope efficiencies of 40%, 37% and 36% respectively. The slope efficiency of the laser output from the 90% output coupler cavity was 25%. The laser output powers with 30% and 50% output couplers can be seen to saturate slightly at the higher pump powers reducing the overall slope efficiencies.

The main difference caused by varying the output coupler reflectivity is the change in the laser threshold. The lasing threshold with the 90% and 80% reflectivity output couplers was as low as 130 mW (13 μJ per pulse), increasing up to 225 mW and 330 mW with the 50% and 30% reflectivity output couplers respectively. This increase in threshold with decreasing output coupler reflectivity is expected since the cavity loss is larger, thus a higher gain, hence more pump power was required to overcome this increased loss.

The build up time of the laser pulse, measured from the start of the pump pulse to the start of the laser pulse, was found to be 9±1 ns, 9±1 ns and 12±1 ns for the 90%, 80% and 50% output couplers respectively. The pulse shapes for the 30% output coupler were not measured at this time. Figure 3.3 shows the timing of the pump and laser pulses together with the depletion of the fluorescence, for lasing with the 50% output coupler. It is interesting to note that these build up times correspond to a relatively small portion of the 40 ns fluorescence decay lifetime.

The depletion of the upper laser level, reflected in the difference in fluorescence with and without lasing (laser cavity blocked) was found to be ~62%, 56% and 41% for the 90%, 80% and 50% output coupler reflectivities. It is interesting to note that the threshold inversion indicated by the fluorescence intensity after the initial depletion (>10 ns) varies with pump power. This suggests that the remaining inversion should be independent of pump power; in fact it increases with increasing pump power. This suggests that the laser and pump mode-matching is not particularly good and that some of the pump mode is not depleted. Figure 3.4 shows the variation of depleted fluorescence with pump power.

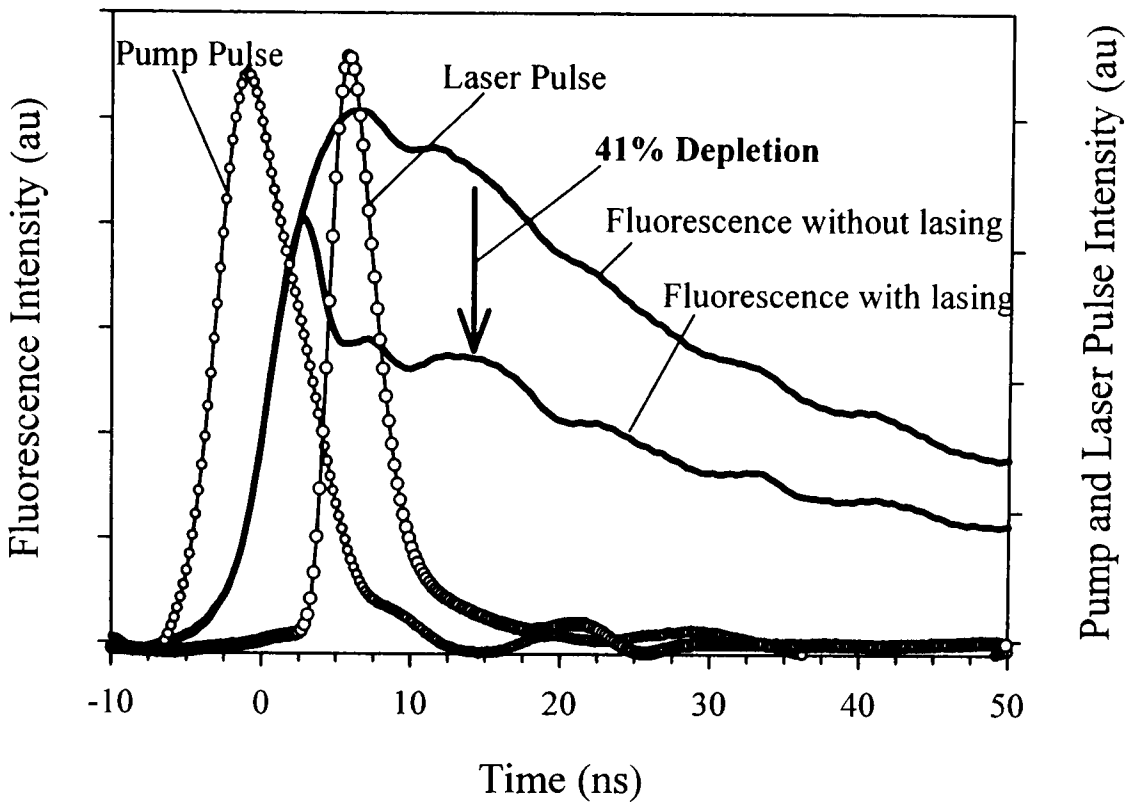


Figure 3.3 shows the fluorescence depletion and laser pulses measured for Ce:LiLuF lasing, with the crystal cooled to ~-1°C, with a 50% reflectivity output coupler cavity with 600 mW pump power.

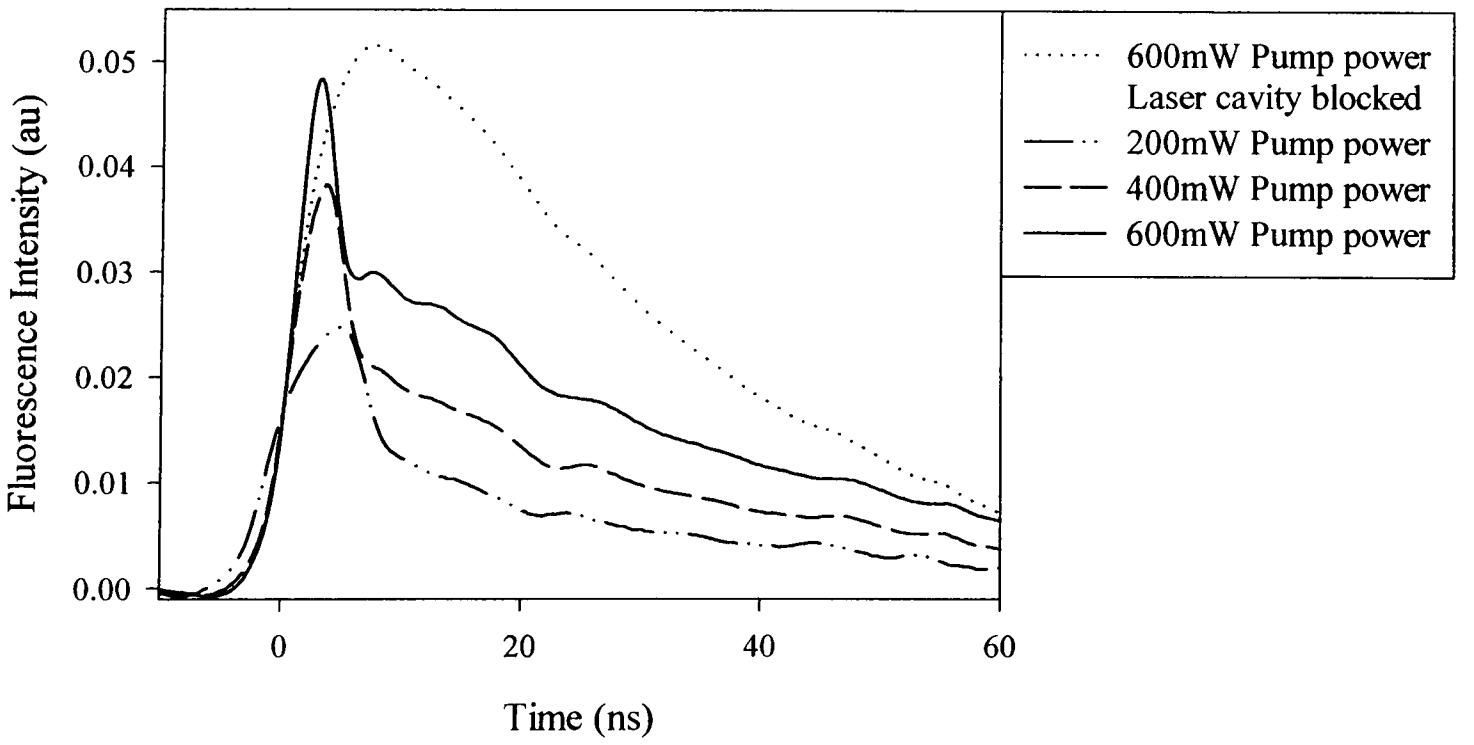


Figure 3.4 shows the change in depleted fluorescence with pump power. In the cavity used for these results, the 90% output coupler was used.

Table 3.1 shows a summary of the 309 nm laser results for Ce:LiLuF with the laser crystal cooled to -1°C.

Output Coupler Reflectivity	R = 90%	R = 80%	R = 50%	R = 30%
Maximum Output (mW)	105±5	149±5	115±5	83±5
Threshold (mW)	130±10	130±10	225±10	330±10
Slope Efficiency (%)	24.7 ± 1	36.6 ± 1	37.0 ± 2	40.3 ± 4
Depletion (%) with 600mW Pump	62	49	41	n/a
Depletion (%) with 200mW Pump	59	40	22	n/a
Build up time (ns)	9±1	9±1	12±1	n/a

Using a "Caird plot" (Caird *et al.* 1988) described by equation 3.1, the passive loss and intrinsic slope efficiency of a laser cavity can be determined. In the Caird plot, the inverted slope efficiency, $1/\eta_{sl}$, is plotted against $1/T$, where T is the transmission of the output coupler. L_d, the round trip passive loss and η_o, the intrinsic slope efficiency can be determined from the slope and intercept of the Caird plot.

$$\frac{1}{\eta_{sl}} = \frac{L_d}{\eta_o}\frac{1}{T} + \frac{1}{\eta_o} \qquad 3.1$$

Equation 3.2 shows the relationship between the intrinsic slope efficiency, pumping efficiency η_p, and quantum defect λ_p/λ.

$$\eta_o = \frac{\lambda_p . \eta_p}{\lambda} \qquad 3.2$$

The Caird plot of the output coupler results, displayed in Figure 3.2, is shown in Figure 3.5. From this plot, the passive loss of the 0.1 m ROC high reflector cavity used for these measurements was determined to be ~8% and the intrinsic slope efficiency was found to be ~45%, which implied a pumping efficiency of ~50% (using equation 3.2). The passive loss of this cavity so determined is very low which is very encouraging, since this is inclusive of the round trip reflection loss of one crystal face due to the wedged nature of the crystal (~8%).

The determined pumping efficiency of 50% is low compared to the quantum efficiency determined by Sarukura *et al.* of 88±8% (Sarukura *et al.* 1995a), by comparison of the detected yield with the yield of a standard. It is plausible that, due to the method used by Sarakura *et al.*, the uncertainty in the 88% quantum yield is higher than quoted and the 50% pumping efficiency determined here is not unreasonable. The poor pump and laser mode overlap, suggested by the variation in the remaining inversion with pump power, could be the origin of the relatively low pumping efficiency determined using the Caird plot.

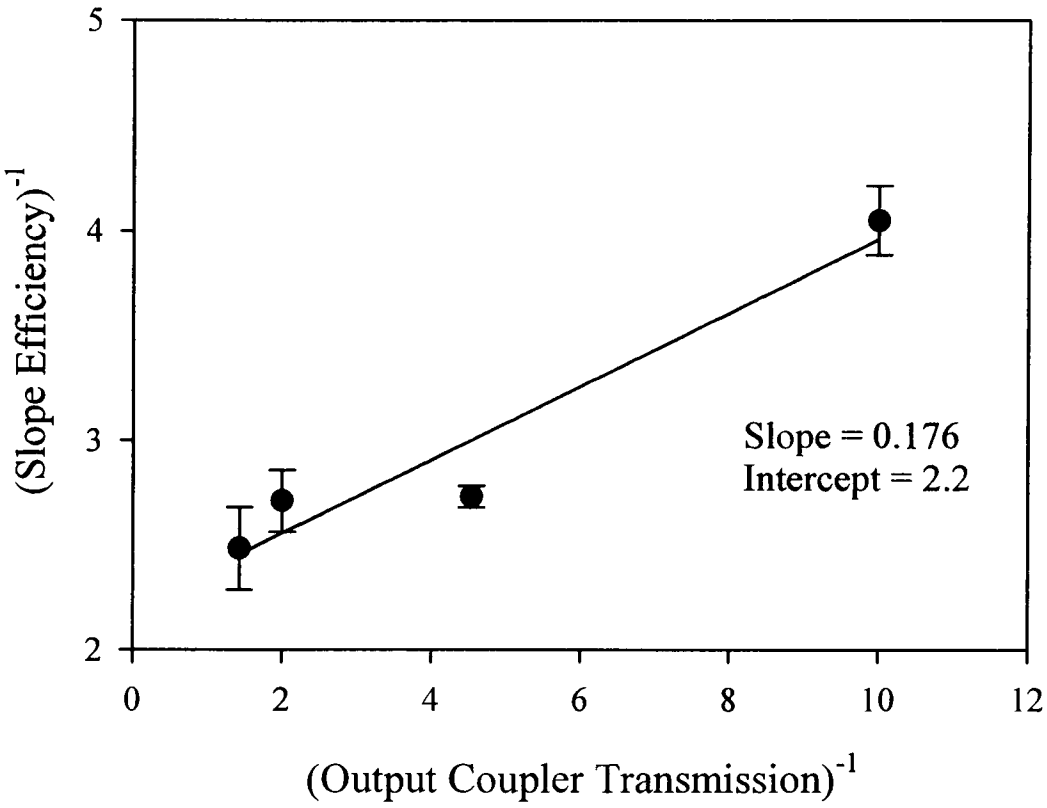


Figure 3.5 shows a Caird Plot for 309 nm lasing in Ce:LiLuF

In the course of the experiments conducted on 309 nm lasing in Ce:LiLuF, two laser cavities were investigated. The first investigations were carried out with the same cavity used by McGonigle *et al.* (McGonigle *et al.* 1999a), which was the 0.25 m ROC cavity described in §3.2.1. In the latter experiments, the 0.1 m ROC cavity was used. Even though some difference in the laser behaviour of each cavity can be expected comparisons can still be made. These comparisons of the laser characteristics of both cavities are described next.

As was mentioned in §3.2.1, the lasing threshold of the hemispherical cavity was found to be very sensitive to the output coupler-crystal distance, with an obvious decrease in the threshold as the output coupler-crystal distance was decreased. To explore the dependence of the threshold on the cavity used and, in particular, on the output coupler-crystal distance, two cavities were investigated, the first of which was that used by McGonigle e*t al.* (McGonigle *et al.* 1999a) which consisted of the 0.25 m ROC high reflector and a 4.5 cm long cavity. The

second cavity consisted of a 0.1 m ROC high reflector and 9 cm long cavity. In both cases the output coupler-crystal distance was small (~1 mm). Using the 80% output coupler in both cavities the laser output with pump power was determined. Then with the 0.25 m ROC high reflector cavity, the output coupler-crystal distance was adjusted such that in the first case the output coupler was virtually touching the crystal and in the second case the output coupler–crystal distance was a little larger (~3 mm). These measurements were carried out at 30°C and -4°C and the results are shown in Figure 3.6.

As can be seen the slope efficiency of the laser is relatively insensitive to the laser cavity configuration at both temperatures, however the threshold is very dependent on the cavity used, and is, in particular, dependent on the output coupler-crystal distance. The threshold for lasing, with the crystal at low temperatures, was found to be lowest for the 0.1 m ROC cavity where the threshold was ~50 mW. The threshold for lasing with the 0.25 m ROC high reflector cavity was ~300 mW with the output coupler very close to the Ce:LiLuF crystal (giving a total cavity length of ~4.5 cm) and 400 mW with the output coupler a little further from the Ce:LiLuF crystal (giving a total cavity length of 4.8 cm). The difference in laser mode diameter corresponding to the 4.5 cm long cavity and 4.8 cm cavity was only I μm. A roll-off of the laser output was present at the higher pump power when the 0.25 m ROC high reflector cavity was used. The 0.1 m ROC high reflector cavity laser output did not show any noticeable roll-off at the higher pump powers.

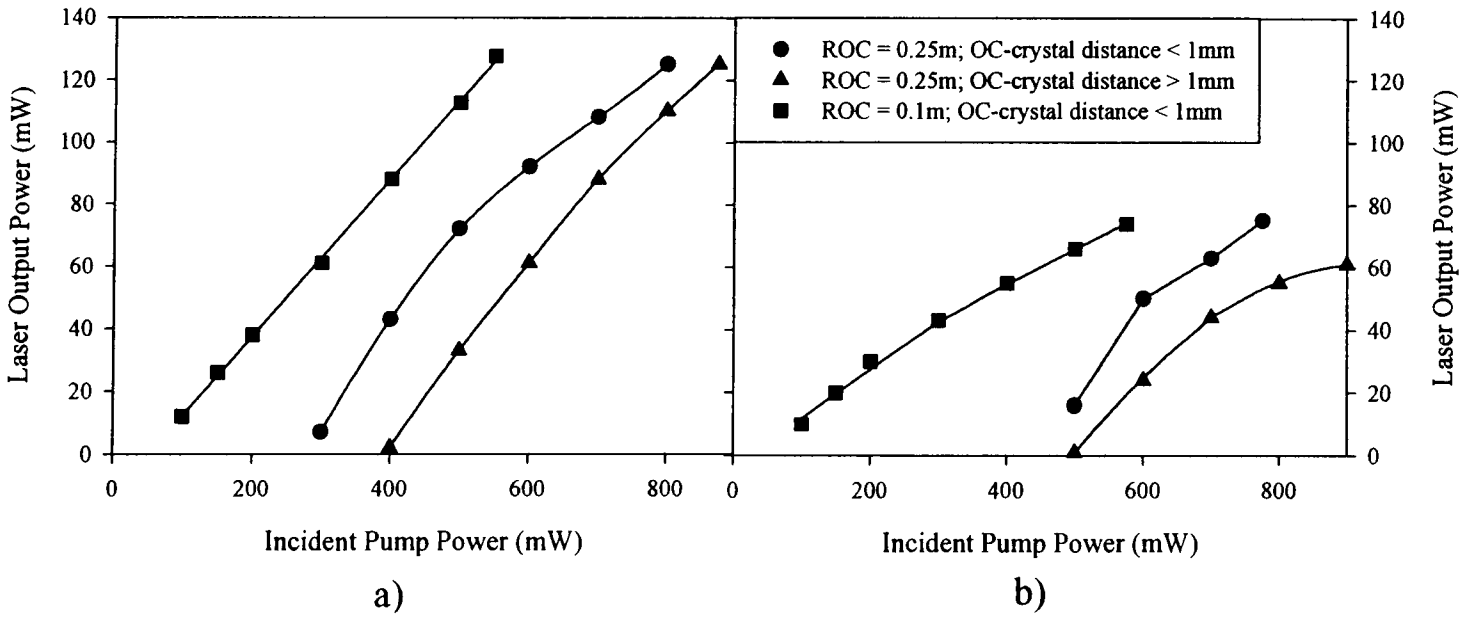


Figure 3.6 shows the comparison of three different laser cavities with varying high reflector ROC, and output coupler (OC) – crystal distance, at a) -4°C and b) 30°C.

Only two curved high reflectors were available for the Ce:LiLuF laser experiments, namely the 0.25 m and 0.1 m ROC UV high reflectors. In the case of the experiments conducted by

McGonigle *et al.* (McGonigle *et al.* 1999a), a 200 mm lens was used to focus the pump beam, giving a beam diameter of ~132 μm. The cavity used by McGonigle *et al.* was the 0.25 m ROC cavity with a laser mode diameter of 194 μm on the flat output coupler. The 0.1 m laser cavity had a mode diameter, on the flat output coupler, of 110 μm. The use of a 200 mm lens in the experiments described in this chapter would have given better mode-matching of the pump (132 μm) and laser (110 μm) modes in both laser cavities. Attempts were made to get lasing with the 200 mm lens used to focus the pump beam, however better lasing efficiency was achieved with the 100 mm lens (with a corresponding pump mode diameter of 66 μm). This was possibly due to the combination of the lower pump intensity in the crystal with the longer focussing lens and the short laser crystal (0.78 mm) used in these experiments compared to that used by McGonigle *et al.*(2 mm). The short laser crystal meant that the overall absorption of the pump was less than experienced by McGonigle *et al.* and hence a more intense pump was required to achieve a high enough gain to get high laser output powers.

3.2.3 Results 2 -Temperature dependence of 309 nm lasing in Ce:LiLuF

In the next experiment the laser output was monitored while the temperature was decreased from 22°C to -3°C. The 0.1 m ROC high reflector cavity was used with the 80% reflectivity output coupler.

In Figure 3.7, one can see that the 309 nm laser output increased by ~70% when the laser crystal temperature was decreased from 22°C to -3°C. The slope efficiency at room temperature was found to be 17% (with respect to absorbed pump power) and a slight roll-off of the output at higher pump powers was observed. The slope efficiency at -3°C was found to be almost twice that at room temperature with an efficiency of 32% (with respect to absorbed pump power), and there was no noticeable roll-off of the laser output at the higher pump powers. The threshold of lasing in both cases was found to be ~50 mW. This low threshold (compared to those in §3.2.2) is thought to be due to a better optimization of the laser cavity.

Figure 3.8 shows the actual dependence of the laser output on temperature. In this experiment, the ROC = 0.25 m high reflector cavity and an 80% output coupler was used. The cavity length was approximately 4.5 cm and the output coupler was less than 1 mm from the crystal. As can be seen, the laser output increased by ~40% with the ~25°C decrease in temperature.

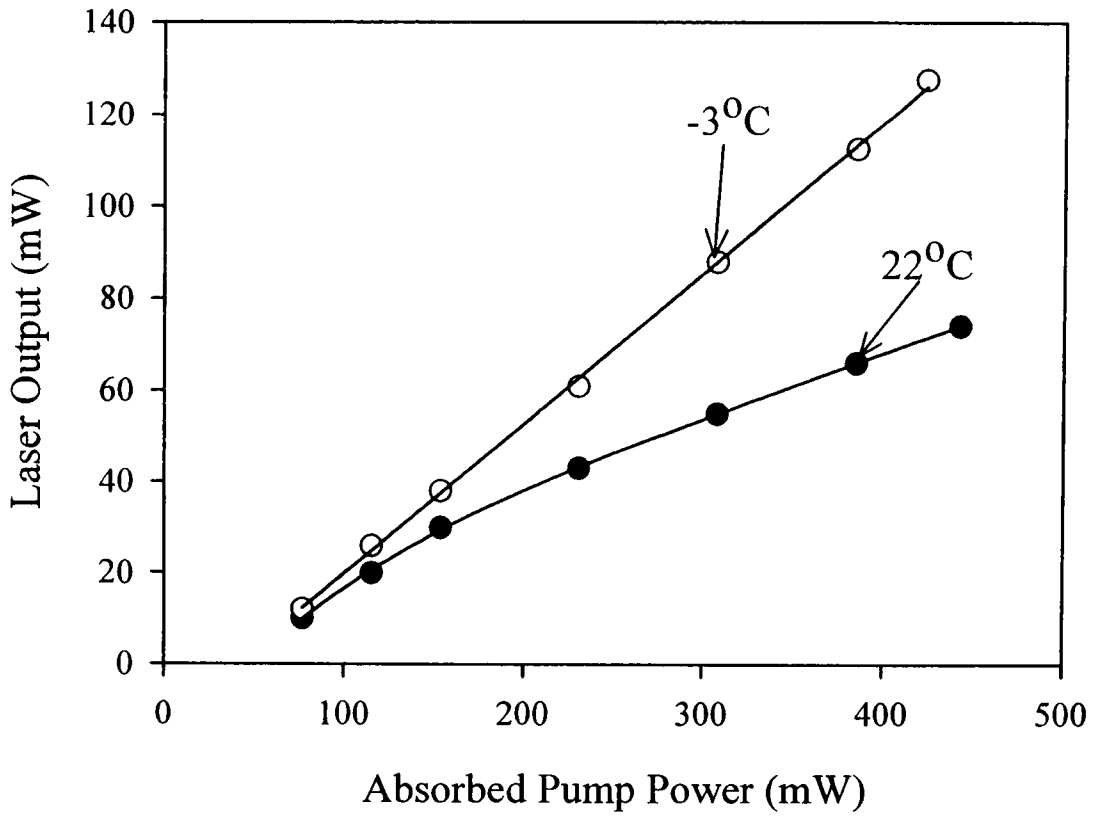


Figure 3.7 is a graph showing the temperature dependence of the slope efficiency using an 80% reflectivity output coupler with the 0.1 m ROC high reflector cavity.

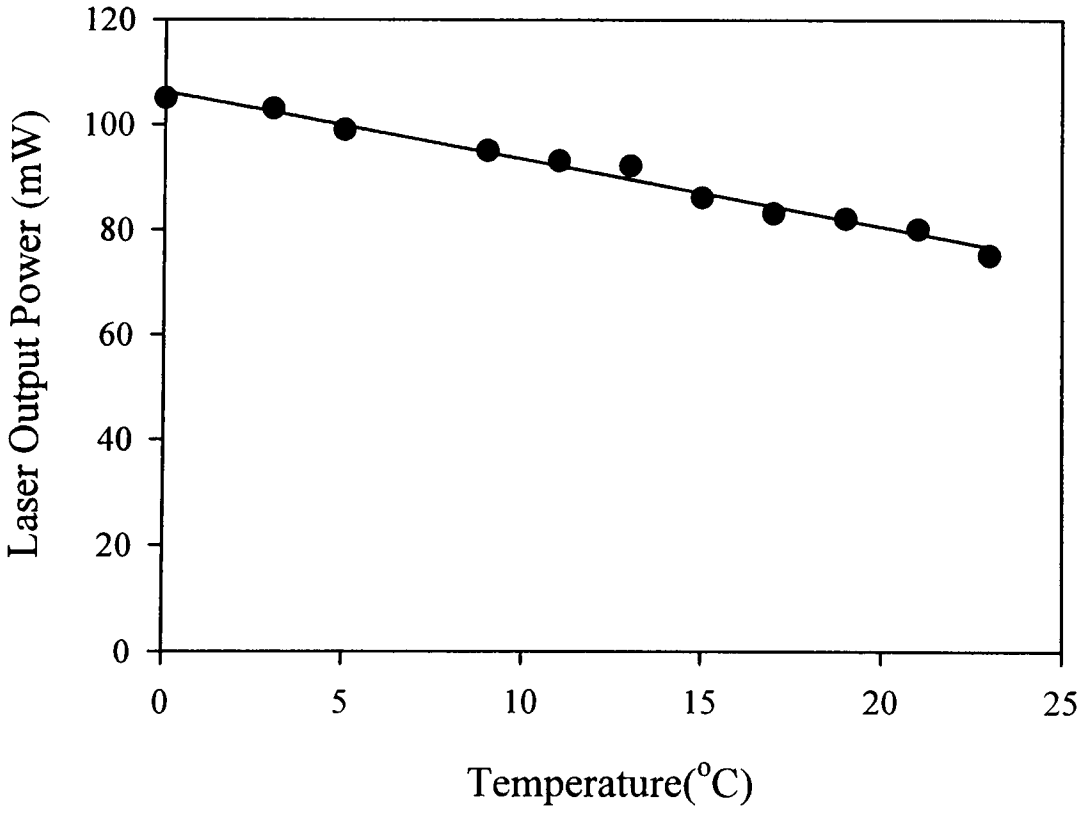


Figure 3.8 shows the temperature dependence of Ce:LiLuF laser output at 309 nm with the 0.25 m ROC high reflector and 80% output coupler with 750mW pump power.

Figure 3.9 shows the change in fluorescence depletion with decreasing temperature. The depletion was found to increase slightly with decreasing temperature from 60% at 20°C to

67% at -2.5°C. The fluorescence intensity has been scaled such that the peak intensities were similar. There was no obvious trend in the fluorescence peak intensity with temperature unlike the increase in fluorescence intensity with decreasing temperature observed by McGonigle *et al.* (McGonigle *et al.* 2001b). The earlier build up times for the cooled Ce:LiLuF crystal indicated by the earlier onset of depletion shown in Figure 3.9 suggests an increase in the effective gain cross-section or a decrease in cavity loss with temperature. The remaining inversion indicated by the fluorescence intensity remaining after the initial depletion was also found to vary with temperature. This change in the remaining inversion does suggest it is the effective gain cross-section or cavity loss which is changing, as opposed to a change in the pumping efficiency.

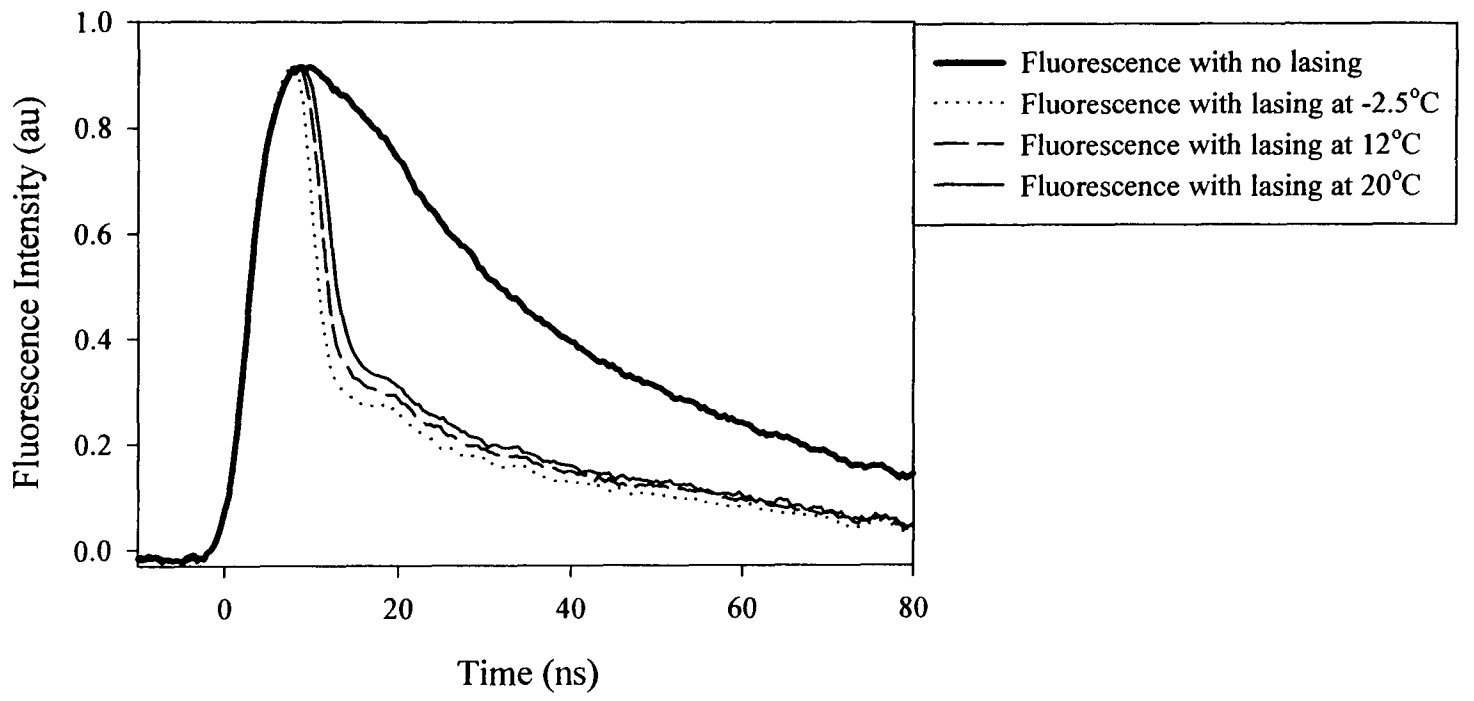


Figure 3.9 shows the temperature dependence of the fluorescence depletion for lasing with the 0.25 m ROC high reflector, 80% output coupler laser cavity. Note the fluorescence intensities have been scaled such that the peaks have similar intensities.

3.3 Lasing of Ce:LiLuF with wavelength-dependent output coupling reflectivities.

3.3.1 Experimental configuration

In the following experiments the pump source used was the non-kinetically-enhanced UV-CVL laser and the pumping configuration used, as before, was that described in §1.3.1.2. The pump was focussed into the laser crystal using a 100 mm focussing lens, giving a pump mode diameter of 55 μm. The near hemi-spherical laser cavity used in the following

experiments consisted of a 0.1 m ROC high reflector and a flat output coupler. As in the previous section the output coupler was placed very close to the 0.78 mm, Maine Ce:LiLuF crystal and the high reflector placed such the cavity length was ~9 cm giving a calculated laser mode diameter of ~110 μm. The output couplers used in this set of experiments had, in both cases, a higher reflectivity at 327 nm than at 309 nm. The first output coupler, M302, had reflectivities of 54% at 309 nm and 92% at 327 nm. The second output coupler used, M303, had reflectivities of 9% and 70% at 309 nm and 327 nm respectively. These output couplers were specifically used to force 327 nm lasing, however as will be described in the results section below, some 309 nm lasing does take place, the amount of which is governed by the reflectivities at 309 nm of the output coupler being used.

In most of these results the polarisation and wavelength of the laser output was determined qualitatively. A calcite crystal was used to separate the polarisations of the output, and a diffraction grating was used to separate the 309 nm and 327 nm components of the laser output. In the qualitative measurements the laser pulses and fluorescence were detected using a DET 200 photodiode and Tektronix TDS 3034 oscilloscope. The laser pulses were scattered off a black surface and this scatter was detected using the photodiode.

When quantitative measurements were made, a Spex Minimate spectrometer was used with a SWH-04 Thorn EMI photo multiplier as a detector. In these measurements the polarisations in the laser output were separated using a polarisation beam-splitting cube. The beam-splitting cube did not perfectly separate the polarisations and it was found that some σ-polarised emission reached in the π-polarisation detector and visa versa.

In order to force σ-polarised or π-polarised lasing, a polarisation dependent loss (Brewster plate) was introduced into the laser cavity in the form of an uncoated silica slide of 1mm thickness. This slide was placed between the high reflector and the Ce:LiLuF crystal. Figure 3.10 shows how the slide was arranged at Brewster's angle, θ_B, to either the π-polarised laser mode or the σ-polarised laser mode thus introducing into the cavity a σ-biased or π-biased loss respectively, this in turn forcing π-polarised lasing or σ-polarised lasing. The loss introduced to the polarisation for which the slide was set at Brewster's angle was considered negligible.

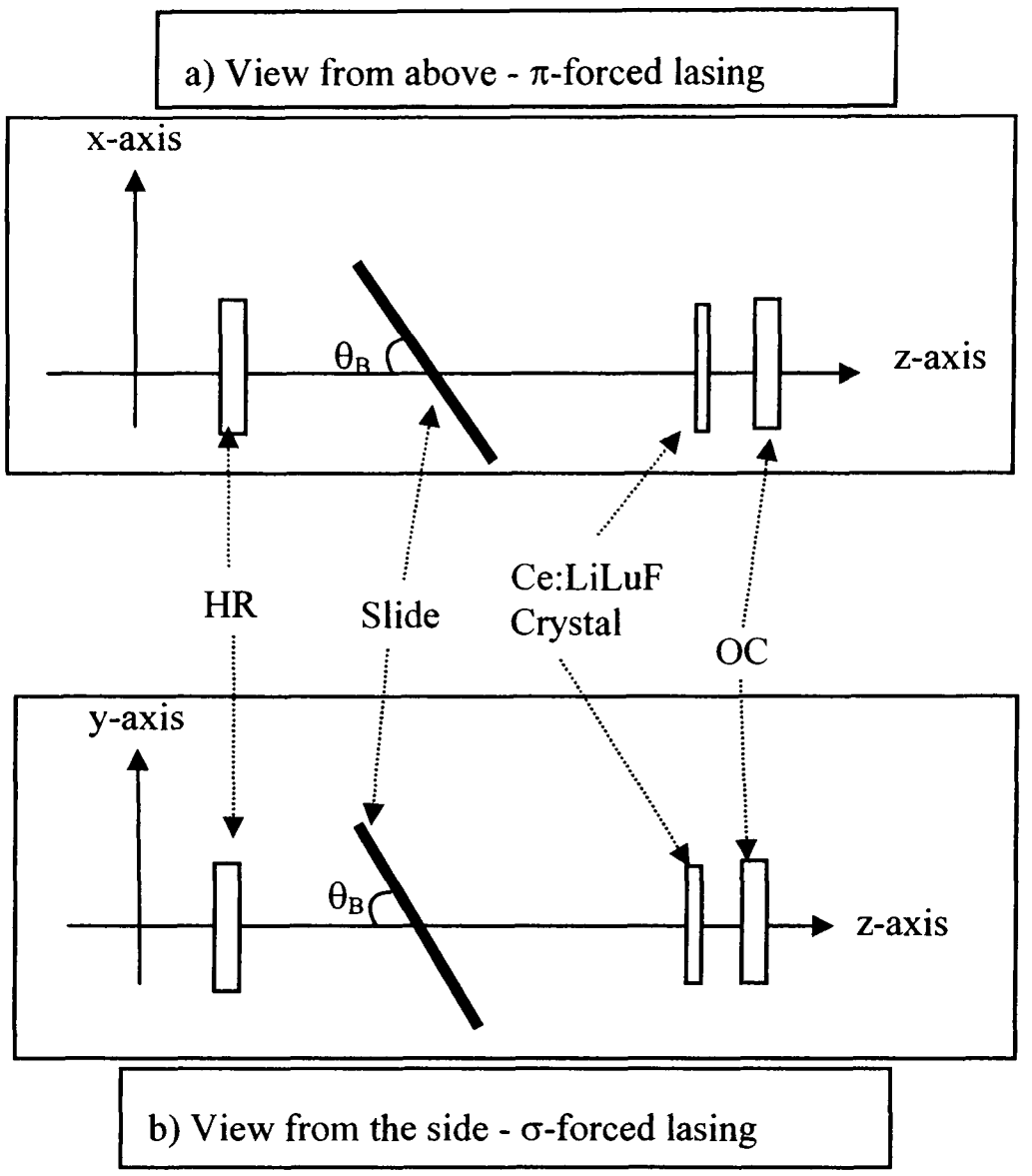


Figure 3.10 shows a schematic diagram of slide placed in cavity so as to introduce a) a σ-biased loss and b) a π-biased loss into the laser cavity. The c-axis of the crystal was parallel to the y axis.

3.3.2 Results 1: Lasing in Ce:LiLuF with the M302 output coupler (R=54% @ 309 nm and R=92% @ 327 nm).

The first experiments were carried out using the M302 output coupler (with no Brewster plate). The variation of laser output with pump power at room temperature and 4°C is shown in Figure 3.11. The influence temperature has on the lasing efficiency with the M302 output coupler is similar to what was seen with the 309 nm lasing in the previous section. Here, a 100% increase in the laser output power from 50 mW at room temperature to 100 mW at 4°C was observed, with 750 mW of pump power. It is obvious from the laser output versus pump power curves that there are two different slopes present, a low slope efficiency at low pump powers (~4% at 25°C and ~6% at 4°C) and a higher slope efficiency at the higher pump powers (~18% at 25°C and 31% at 4°C). An increase in slope efficiency with temperature was

seen at both high and low pump powers, thus a similar shape of the laser output versus pump power curve was seen at 4°C and 25°C.

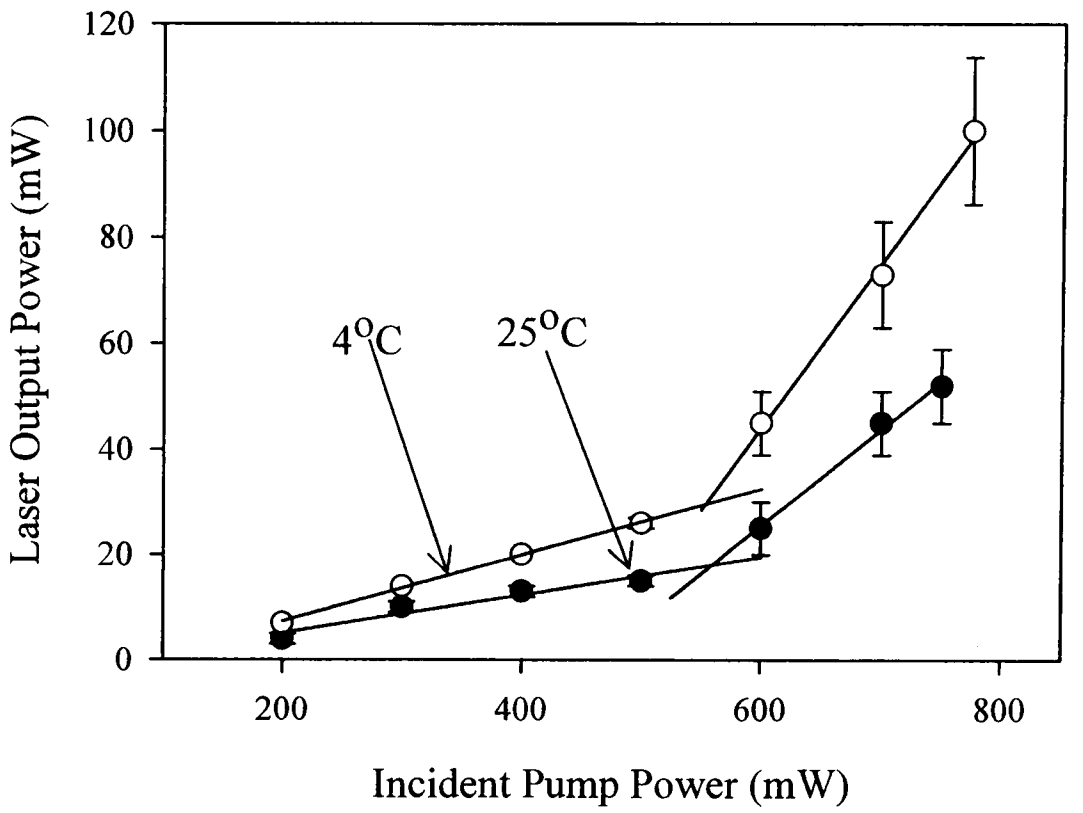


Figure 3.11 shows the variation of laser output with the M302 output coupler, with the Ce:LiLuF crystal temperature at 25°C and 4°C as indicated.

One should note that at the higher pump powers there was increasing fluctuation in the laser output. Looking more closely at the polarisation and wavelength of the output, with the crystal cooled to 4°C, it was found that output of this laser consisted of a combination of unstable 309.5 nm π-polarised laser output and relatively stable 327.5 nm, σ- and π-polarised, laser outputs.

With 450 mW of pump power an output power of 27 mW was achieved. Of this, ~24 mW was 327 nm, σ-polarised output, and ~3 mW was 327 nm, π-polarised output. No 309 nm lasing was present at this pump power. With 740 mW pump power, the output was found to fluctuate between ~76 mW and ~55 mW. When looking at the polarisation components of this laser output separately it was found that the σ-polarised output (327 nm) fluctuated only slightly between 22 mW and 25 mW (6%), whereas the π-polarised (327 nm + 309 nm) output fluctuated more dramatically between 30 mW and 50 mW (25%).

The wavelength components of the π-polarised laser output were separated and the laser peak intensity monitored using a photodiode. The 309 nm π-polarised laser output was found to fluctuate noticeably and there was negligible fluctuation of the 327 nm π-polarised output.

Figure 3.12 shows this variation of the laser peak intensity in the two polarisation components of the laser output at the high pump powers. As can be seen the σ-polarised output is much more stable than the π-polarised output, with a fluctuation of ~5% for the σ-polarised peak intensity and 14% for the π-polarised intensity. It is interesting to note that the presence of a very small increase (~8%) in the σ-polarised output coincides with a large decrease (80%) in the π-polarised output. This behaviour is suggestive of the coupled nature of the two polarisation laser modes.

Figure 3.13 shows the relative timing of the σ- and π-polarised laser pulses. These laser pulse measurements were taken as a single-shot measurement, confirming that both σ- and π-polarised laser modes exist simultaneously, as opposed to a flipping of the laser mode between σ-polarised and π-polarised laser oscillation between shots, as was originally thought to be the case by McGonigle *et al.* (McGonigle *et al.* 2001b). As can be seen, in this particular set of pulses, the π-polarised laser pulse is very short (~3 ns FWHM) compared to the σ-polarised laser pulse (8 ns FWHM). In actual fact, it is likely that the π-polarised FWHM pulse length measurement was shorter than 3 ns as a result of limitations of the photodiode used (1 ns rise time). The build up times of the π-polarised laser pulse and the σ-polarised laser pulse were very similar with build up times of 10±1 ns and 11±1 ns respectively. The depletion of the fluorescence shown in Figure 3.13 corresponds to ~57% depletion.

Next, the silica slide was placed in the cavity such that a large σ-polarised cavity loss was induced. In this experiment the Ce:LiLuF crystal was at room temperature. The results are shown in Figure 3.14. As can be seen the introduction of the slide into the cavity caused the laser output to increase by 130% from 52 mW to 120 mW with a pump power of 750 mW. The effect of the σ-biased intra-cavity loss on the slope of the laser output with pump power is also dramatic. There is no longer as obvious a change in slope efficiency with pump power as was seen without the slide in the cavity. The laser output was found to be relatively stable and to consist of π-polarised 327 nm (~ 30%) and 309 nm (~70%) components at the high pump powers. Minimal σ-polarised laser output was present. The bandwidth of the π-polarised, 309 nm and 327 nm outputs were found to be 2 nm and 3 nm respectively, suggesting that lower losses are experienced by the 327 nm, π-polarised laser mode. These bandwidths are therefore consistent with output coupler reflectivities.

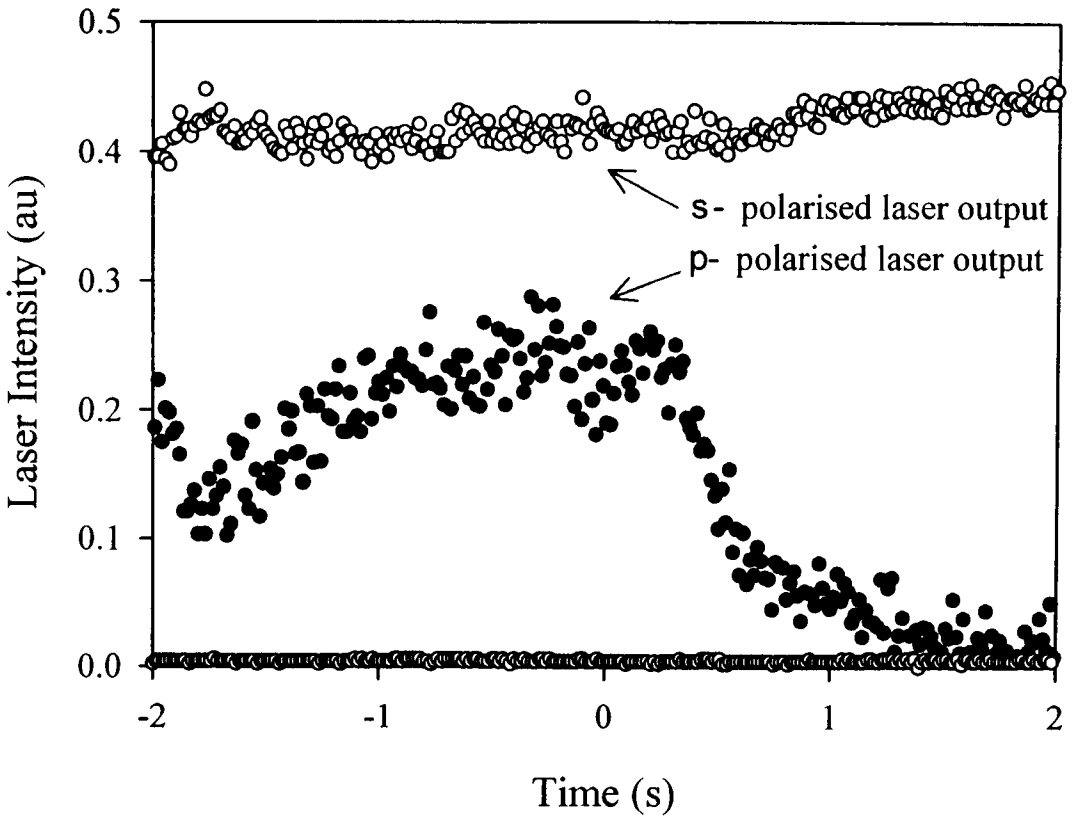


Figure 3.12 shows the shot-to-shot fluctuation of the π- and σ-polarised laser peak pulse intensity with 790 mW pump power using the M302 output coupler, with the laser crystal cooled to 4°C.

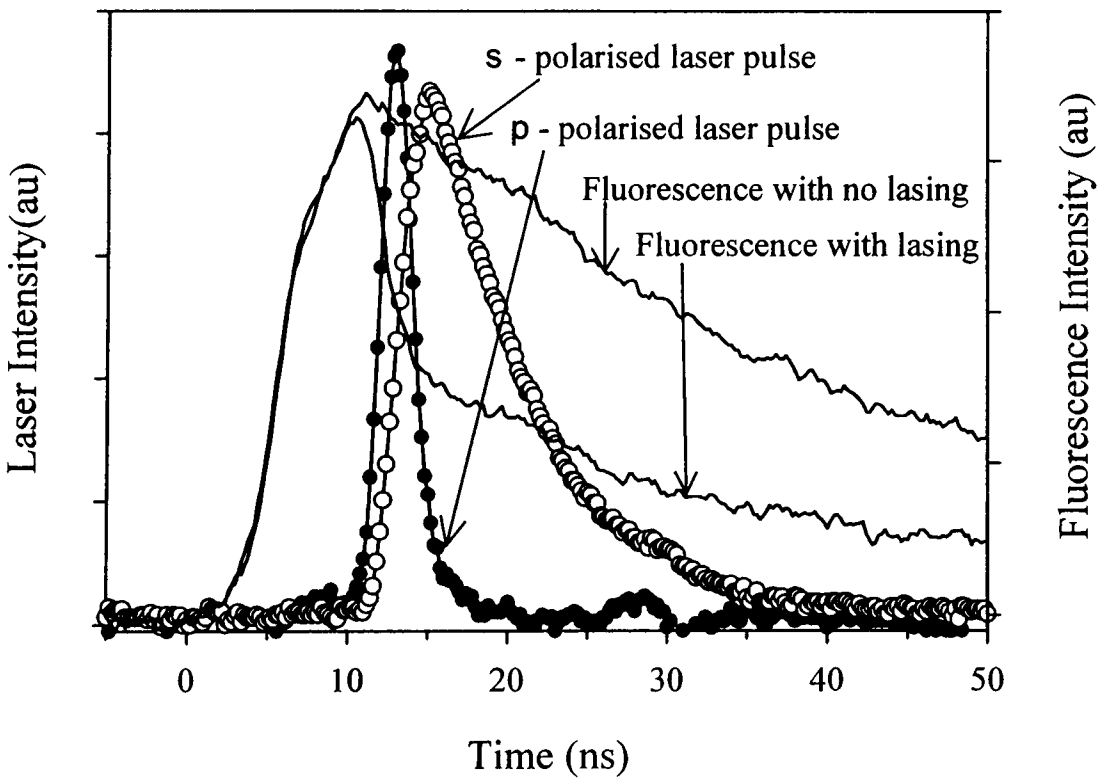


Figure 3.13 shows the Ce:LiLuF fluorescence depletion and timing of the laser pulses for the polarisation components of the laser output (not relative intensities) using the M302 cavity with 790 mW of pump power with the crystal cooled to 4°C. The pump pulse started at ~0 ns in these measurements.

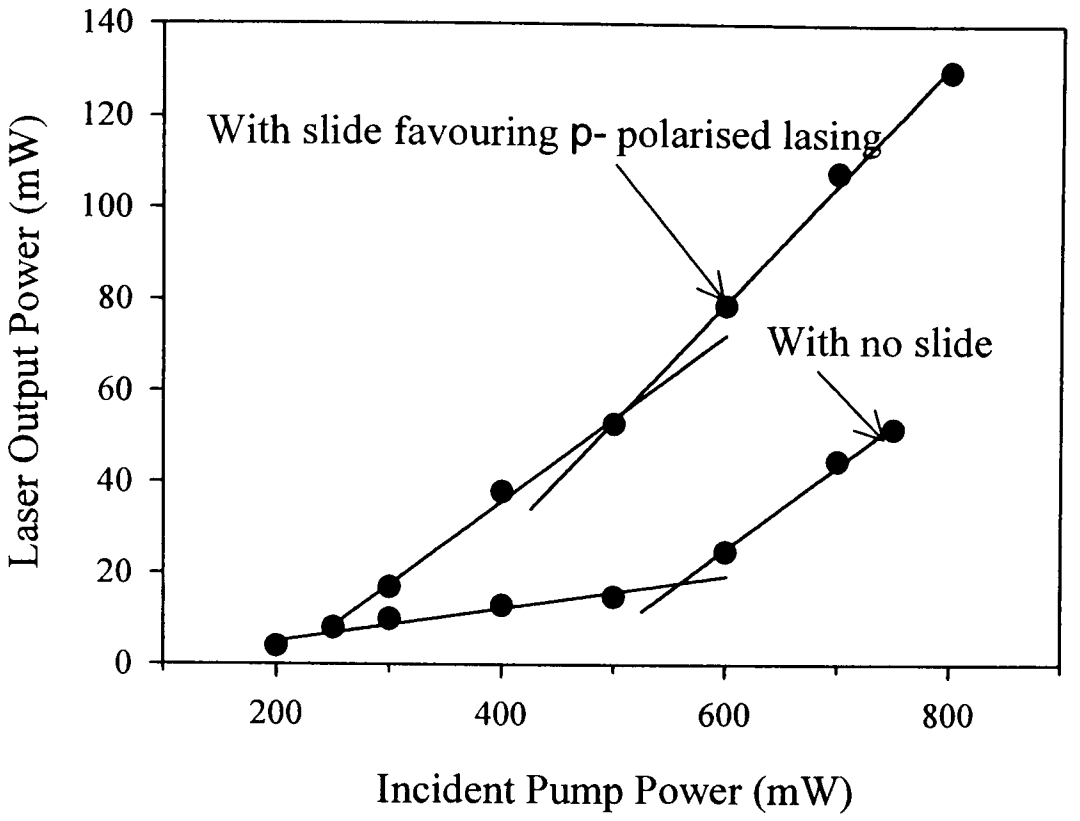


Figure 3.14 shows the variation of laser output power in Ce:LiLuF with the M302 output coupler at room temperature. Shown are the results both with and without a σ-biased loss, induced by the introduction of a silica slide into the laser cavity.

3.3.3 Results 2: Lasing in Ce:LiLuF with the M303 output coupler (R=9% @309 nm and R=70% @ 327 nm)

The M303 output coupler was used in the 0.1 m ROC high reflector laser cavity. This output coupler was more strongly biased towards 327 nm lasing. With this output coupler the effect of the introduction of σ- and π-polarisation biased losses into the cavity was investigated. At 1°C the laser output with no slide in the cavity was measured to be 34 mW with 775 mW of pump power, and the output was all at 327 nm, mostly σ-polarised, with only a very small amount of the output being π-polarised. When the slide was introduced such that the lasing was forced to be π-polarised, the laser output was measured to be 112 mW from 800 mW of pump power and the output was found to contain both 309 nm and 327 nm components. Next, the slide was placed such that the lasing was σ-forced. The σ-forced laser output was measured to be 27 mW from 775 mW of pump power and the output was found to be all at 327 nm and σ-polarised. These results show a 230% increase in laser output was caused by forcing lasing to be π-polarised. For the σ-forced lasing, the output was found to decrease by 20% compared to non-polarisation biased lasing. Since there was only a small amount of π-polarised 327 nm emission in the unbiased cavity it is thought that most of the 20% reduction in output power was the result of increased intra-cavity losses resulting, possibly,

from the imperfect alignment of the slide to Brewster's angle with respect to σ-polarised light.

Shown in Figure 3.15 are the laser output power variations with pump power for both the π-forced lasing (σ-biased intra-cavity loss) and σ-forced lasing (π-biased intra-cavity loss). The π-forced lasing had an output of 88mW compared to 25 mW from the σ-forced lasing, both with 750 mW of incident pump power. As in the M302 case, there were two distinguishable slopes seen in the π-forced lasing output. Similarly it was found that only at the higher pump powers was 309 nm lasing present. At lower pump powers, the lasing was predominantly at 327 nm and π-polarised. A small amount of the laser output at higher pump powers was found to be σ-polarised and at 327 nm, indicating that even with the high induced loss (>70%) seen by the σ-polarised laser field, σ-polarised lasing could still occur.

The σ-forced lasing does not show this pump power dependence of the slope efficiency, however this is expected since the σ-polarised output consists only of 327 nm lasing whereas the π-polarised laser output has 309 nm and 327 nm lasing components. The bandwidth of the 327 nm output with the π-forced cavity was found to be ~3 nm whereas with the σ-forced cavity the bandwidth of the 327 nm output was found to be ~2 nm. This suggests higher gains or lower losses are experienced by the π-polarised 327 nm emission compared to those experienced by the σ-polarised 327 nm emission.

The pulse shapes of the π-forced M303 laser output are shown in Figure 3.16. In this figure the start of the pump pulse coincides with the start of the fluorescence. As can be seen, at high pump powers there is an intense, short laser pulse is present starting ~10 ns after the pump pulse, coincident with a longer, less intense laser pulse. The intense narrow pulse is not present at the lower pump powers, enabling the assignment of this laser pulse to the π-polarised, 309 nm laser pulse. The broad, low intensity laser pulse can then be assigned to the π-polarised, 327 nm laser pulse, since it is present at low and high pump powers. The depletion associated with the narrow, intense 309 nm laser pulse is much sharper than that associated with the broader 327 nm laser pulse suggesting higher gains for the 309 nm laser field than the 327 nm laser field.

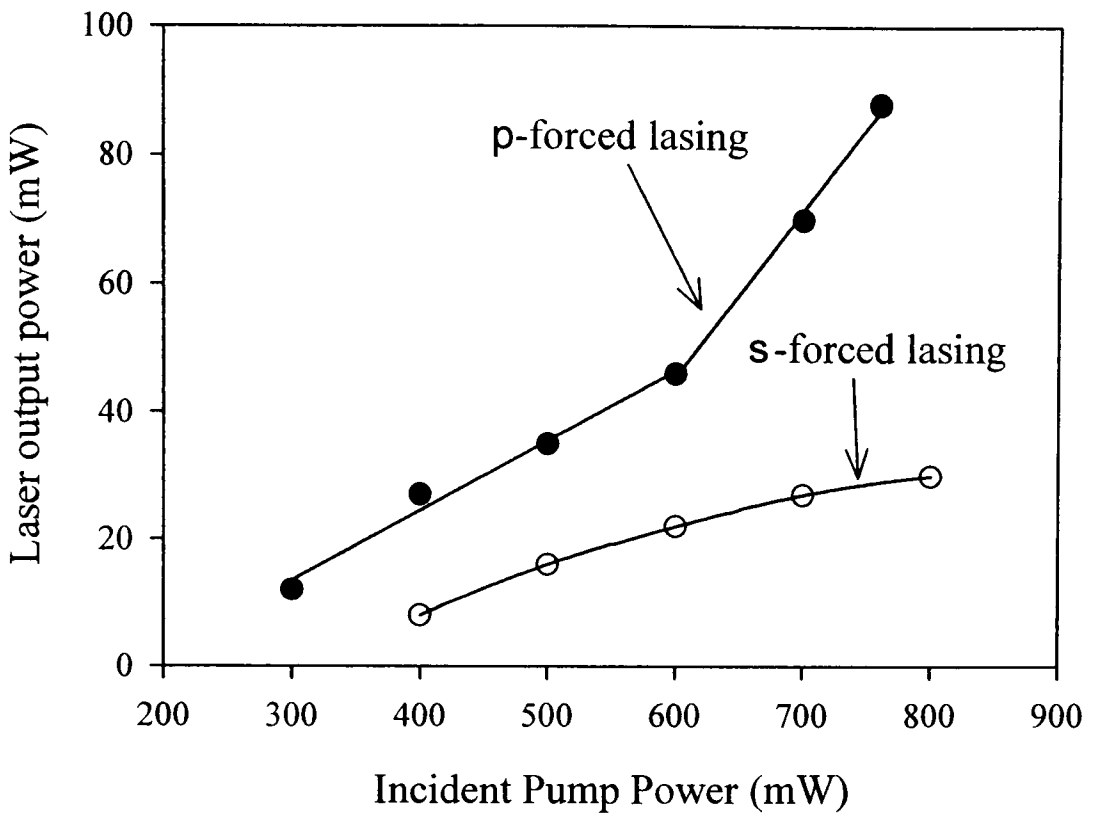


Figure 3.15 shows the variation of Ce:LiLuF laser output with pump power using the M303 output coupler with the crystal cooled to 2°C. The variation of the laser output both with a σ-biased intra-cavity loss (π-forced lasing) and a π-biased intra-cavity loss (σ-force lasing) introduced into the cavity is shown.

The temperature dependence of both the σ- and π-forced lasing was also investigated. These results are shown in Figure 3.17. A 20°C decrease in temperature resulted in a 200% increase in the σ-forced laser output and a 100% increase in the π-forced laser output. In the π-forced lasing case it was interesting to find, at room temperature, that there was no 309 nm laser output present only 327 nm output. As the temperature of the crystal was decreased the laser output was found to contain increasing amounts of 309 nm output. At low temperatures it was also interesting to note that some σ-polarised lasing was occurring even with the high σ-biased loss in the cavity.

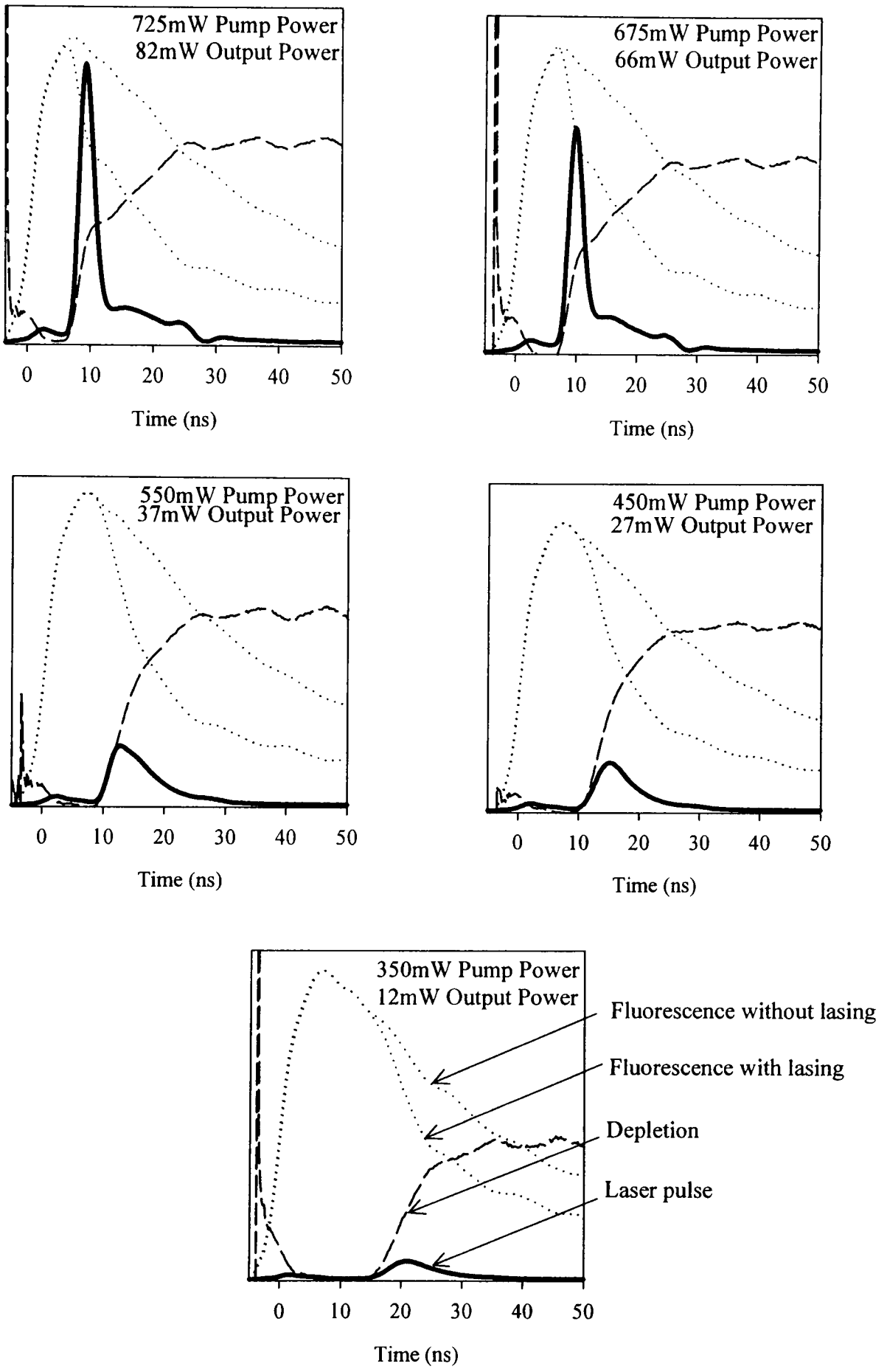


Figure 3.16 shows the laser and fluorescence pulses for decreasing pump powers for the Ce:LiLuF laser with the M303 output coupler. The lasing was π-forced and the crystal held at 4°C. The labels are shown in the bottom figure and apply to all the other figures.

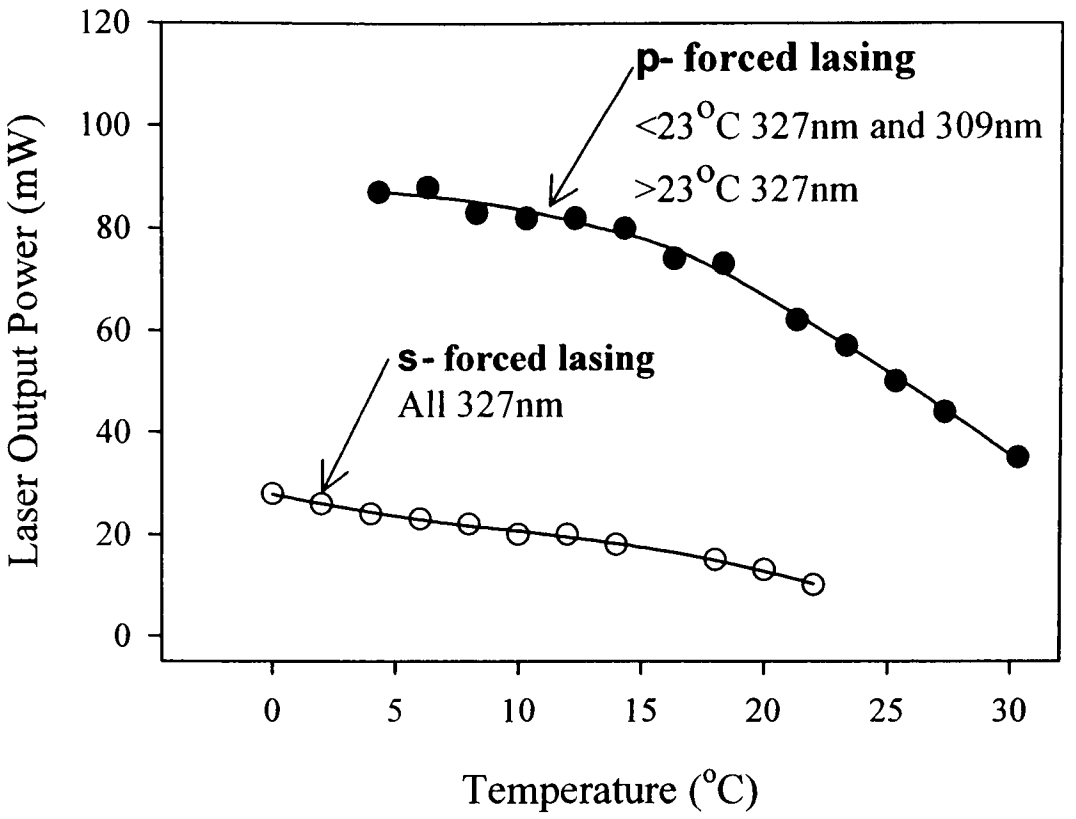


Figure 3.17 shows a comparison of the temperature dependence of σ- and π-forced Ce:LiLuF lasing with the M303 output coupler with 750 mW pump power.

The pulse shapes at 4°C, 18°C and 27°C are shown in Figure 3.18. As can be seen once again the presence of 309 nm lasing, in this case at the low temperatures, is characterised by an intense, narrow laser pulse (~3 ns FWHM) with a relatively short build up time of 10±1 ns, and the 327 nm laser pulse is characterised by the broader (~5 ns FWHM) less intense pulse. As the temperature is increased, the laser pulse, made up more of 327 nm and less of 309 nm, becomes broader and the build up time increases slightly to 12±1 ns.

For the π-forced M303 output coupler cavity, the composition of the laser output with increasing pump power was similar to that with decreasing temperature. Namely, at both low pump powers and high temperatures there was very little 309 nm in the output. As the pump power was increased or the temperature decreased, the 309 nm laser output increased until it was comparable with the 327 nm laser output. It was also found that by varying the vertical alignment of the output coupler, corresponding to an increase of the cavity losses, this behaviour could be duplicated, such that, with the output coupler well aligned for lasing, 309 nm lasing was present, whilst when the laser was increasingly misaligned the laser output became predominately 327 nm. Figure 3.19 shows the similarity between the laser pulses with varying pump powers and fixed output coupler alignment and varying output coupler alignment and fixed pump power. In both cases the presence of 309 nm lasing is characterised by the narrow intense laser pulse with short build up times as previously mentioned.

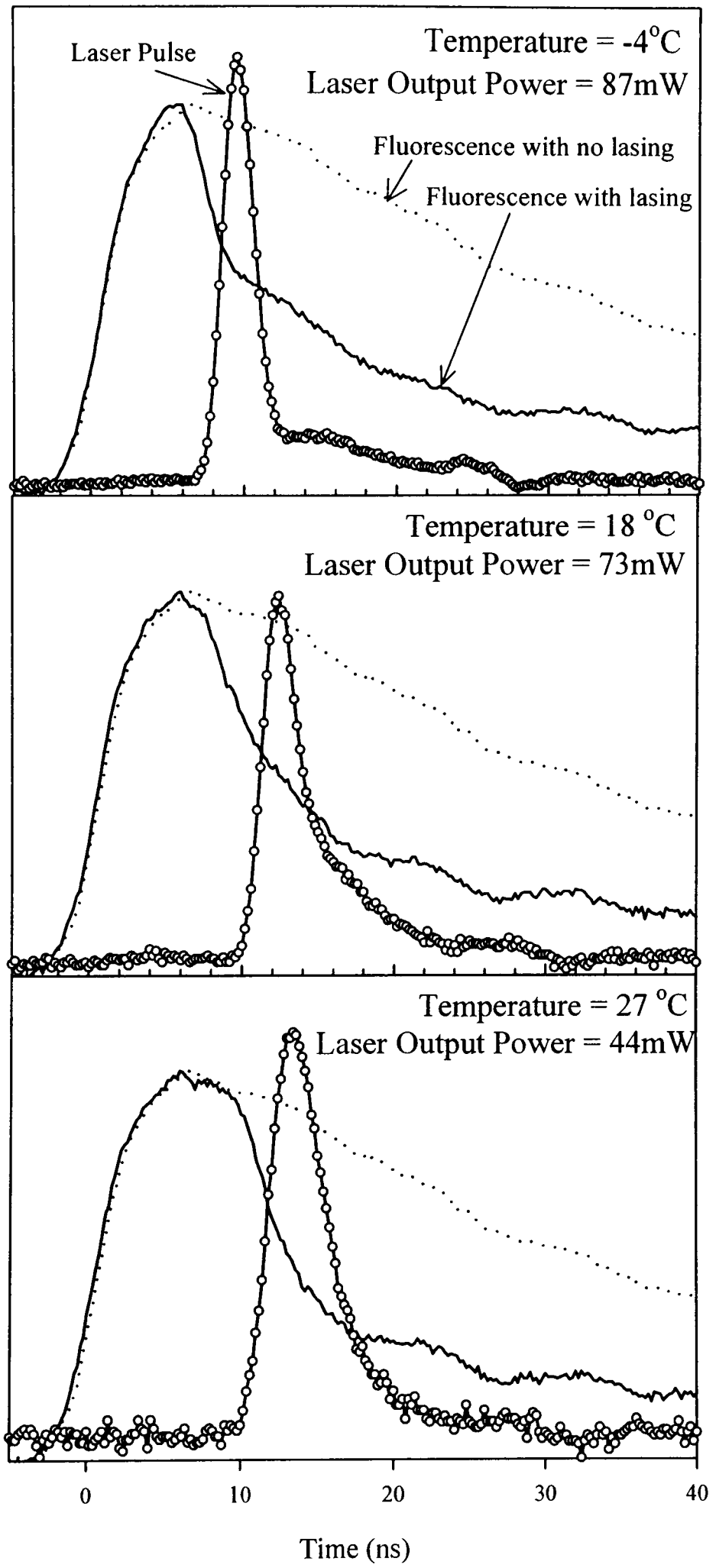


Figure 3.18 shows the laser and fluorescence pulses from the π-forced Ce:LiLuF laser with the M303 output coupler cavity, pumped using 750 mW pump power.

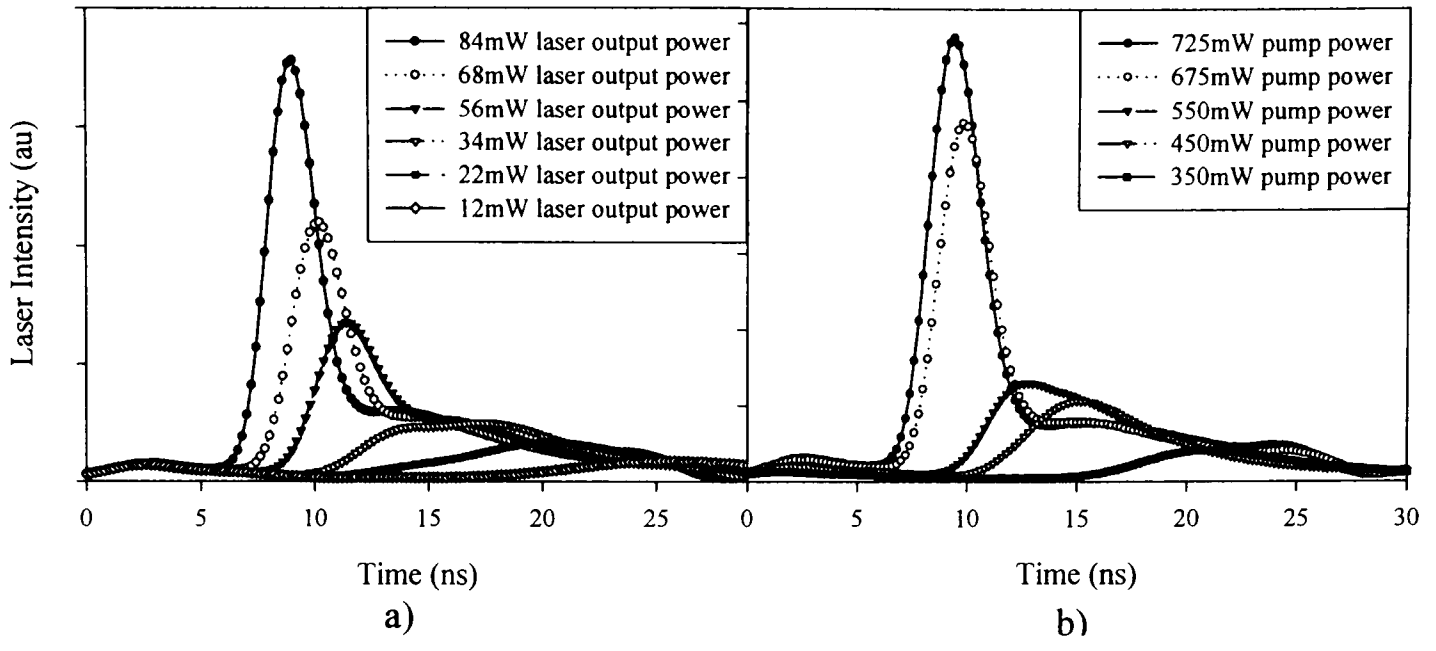


Figure 3.19 shows the Ce:LiLuF laser pulses with M303, π-forcing laser cavity a) with fixed 700 mW pump power and varying output coupler alignment and b) with fixed output coupler alignment and varying the pump power.

In summary, using the M303 output coupler, the composition of the laser output is similarly dependent on temperature, pump power and intra-cavity losses. The 309 nm component in the Ce:LiLuF laser output was coincident with low temperatures, high pump powers and low cavity loss.

3.4 Tunable Lasing in Ce:LiLuF

3.4.1 Experimental Configuration

The pump source used in this section was the KE-UV-CVL described in §1.3.1.2. A 100 mm focussing lens was used to focus the ~ 5 mm diameter pump beam into the crystal, giving a pump spot diameter of ~ 66 μm inside the crystal. The cavity used was a quasi-longitudinally pumped hemi-spherical cavity, consisting of a curved high reflector with ROC of 0.1 m and a flat 90% reflectivity output coupler placed close to the Ce:LiLuF laser crystal. A 60° quartz prism, placed in the cavity between the crystal and the high reflector, was used to enable tuning of the laser. A schematic diagram of this cavity is shown in Figure 3.20. As in the previous chapter the cavity length was ~9 cm. The wavelength of the laser was tuned by rotating the high reflector about the vertical axis. The prism was aligned to be at Brewster's angle to the laser mode which minimised loss for only the π-polarised laser mode, the σ-polarised laser mode on the other hand still experienced loss at the prism faces.

A calcite crystal was used to separate the σ- and π-polarised components of the laser output and, as in the previous section, the wavelength of the laser output was monitored using a SPEX Minimate spectrometer with photomultiplier attached.

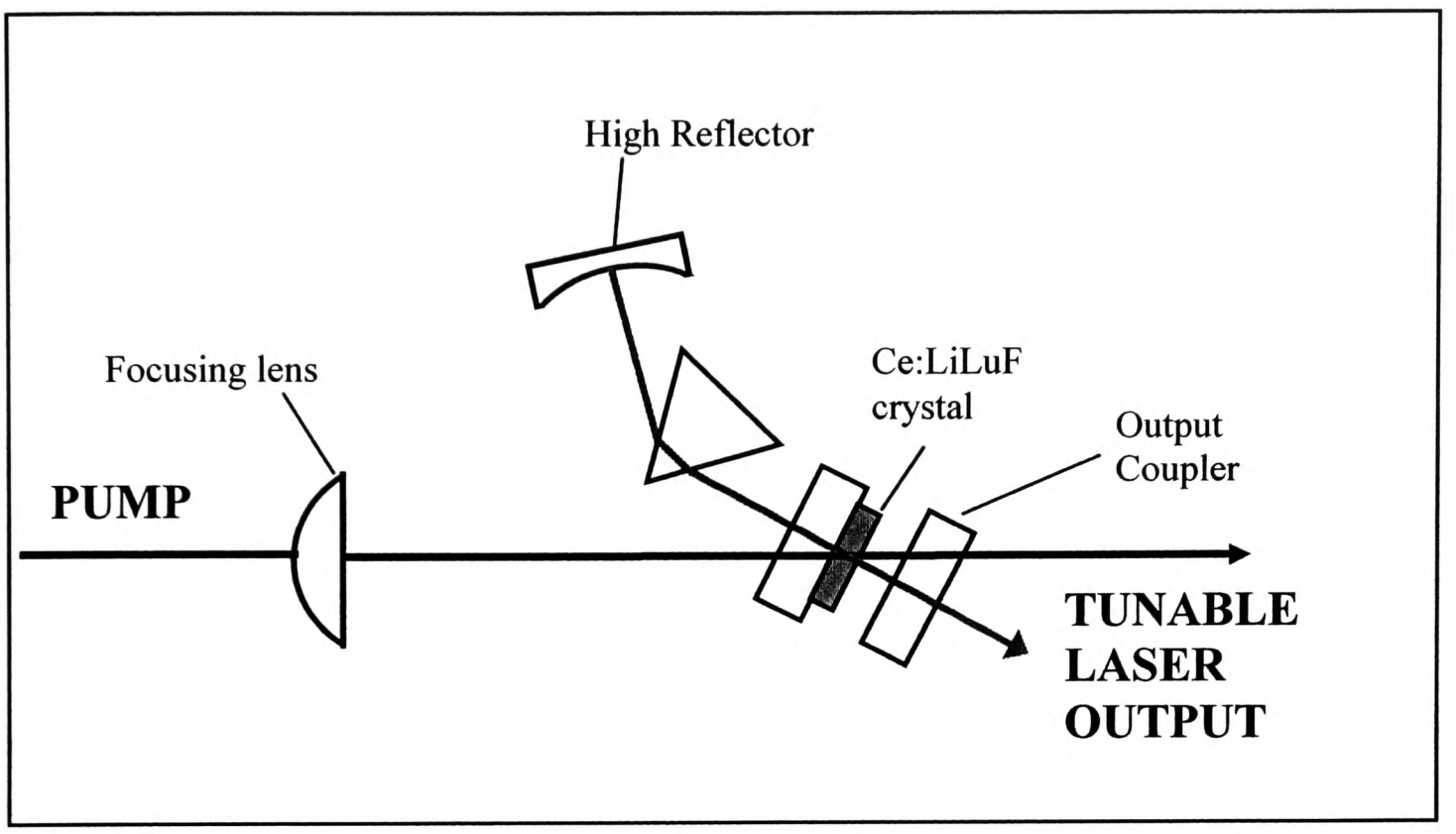


Figure 3.20 shows a schematic diagram of a prism tuned Ce:LiLuF laser.

3.4.2 Results of prism-tuned lasing in Ce:LiLuF

Continuous tunability between 305 nm and 335 nm was achieved using the prism-tuned cavity with the 90% output coupler. The effect of temperature on the tuning curve of Ce:LiLuF is shown in Figure 3.21. At room temperature the laser output was found to follow the π-polarised fluorescence emission spectrum closely. The laser output was found to be π-polarised across the whole tuning range. In a similar manner to the results presented by McGonigle *et al.* (McGonigle *et al.* 1999c), it was found that at low temperatures there was a dip in the laser output at 327 nm where in the room temperature curve there was a peak at 327 nm. At 327 nm the output was found to fluctuate more with decreasing temperature and the amount of σ-polarised 327 nm lasing was also found to increase with decreasing temperature. This is in agreement with the "flipping" behaviour previously reported (McGonigle *et al.* 2001b).

A closer look at the polarised 327 nm laser pulses revealed the presence of two distinguishable laser pulses as shown in Figure 3.22. The two figures show the two extremes of the fluctuating laser pulse. These pulses are each single shot measurements. The relatively

stable σ-polarised laser pulses were characterised by a short, relatively intense pulse with a ~10 ns build up time and a pulse length of ~5 ns. A low intensity tail lasting about 15 ns was also seen after the initial peak of the σ-polarised laser pulse. The fluorescence depletion coinciding with the σ-polarised laser pulse is distinctly dominant compared to the depletion due to the π-polarised pulse.

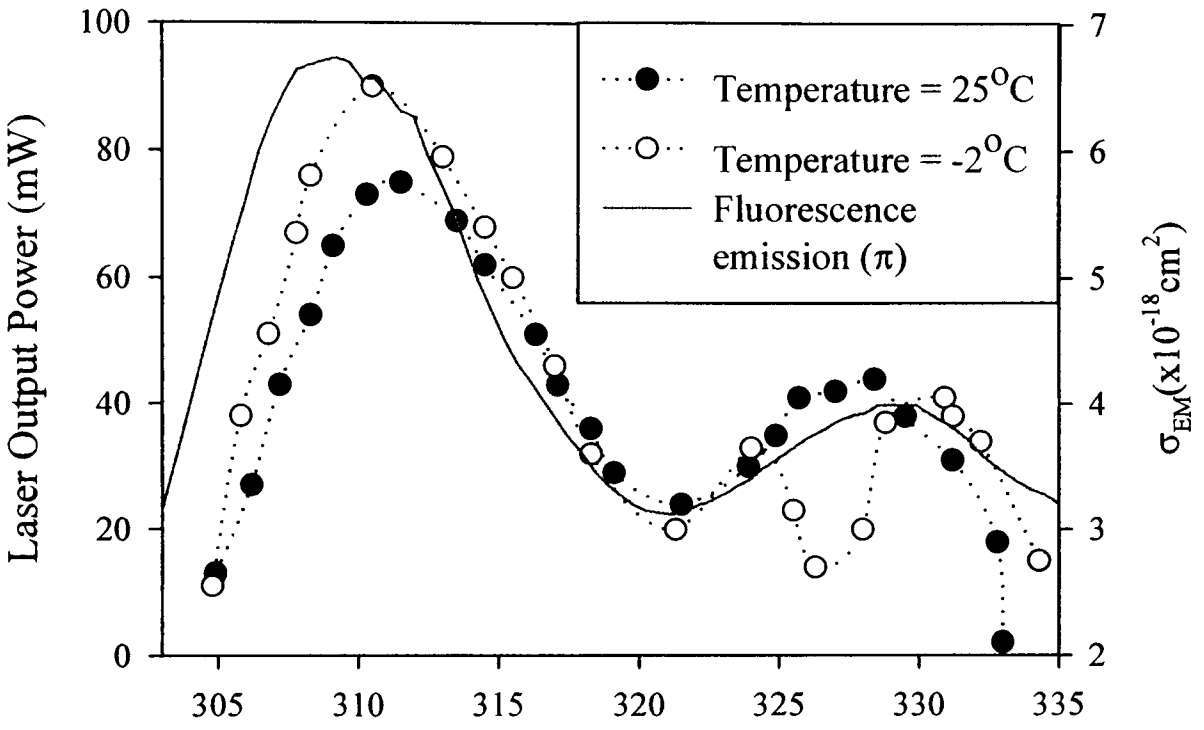


Figure 3.21 shows the tuning curve of Ce:LiLuF with the laser crystal at 25°C and -2°C with incident pump powers of 760 mW and 675 mW respectively.

The π-polarised laser pulse was characterised with a similar build up time to the σ-polarised laser pulse of 11±1 ns and the intensity of the pulse was found to be unstable. The π-polarised laser pulse was dramatically longer than the σ-polarised pulse with pulse length of ~12 ns. In Figure 3.22 a) the π-polarised laser pulse shows two peaks, an early small peak, followed by the more dominant later peak. The presence of the tail in the σ-polarised laser pulse and the early, π-polarised peak, coincident in time with the main σ-polarised laser peak, might suggest that the calcite crystal was not perfectly aligned with respect to the c-axis of the Ce:LiLuF crystal, thus some σ-polarised emission may have reached the π-polarised light detector and visa versa causing this peak. However, this pulse shape is proven to be a true feature of this laser pulse in §3.6.4.

It is interesting to note that for the laser pulse with low π-polarised content (Figure 3.22 (a)) the build up time of the σ-polarised laser pulse was 9±1 ns. This is 2 ns shorter than the build

up time for the σ-polarised laser pulse when there is a high π-polarised content in the laser output (Figure 3.22(b)). This difference in build up time may be related to the cause of the fluctuations in the π-polarised laser output.

The fluctuation in the π-polarised laser pulse intensity was also found to coincide with a variation in the average fluorescence depletion. For the high intensity π-polarised pulse shown in Figure 3.22(b), a depletion of 38% is seen, whereas the lower intensity π-polarised lasing in Figure 3.22(a) produces only 30% depletion. This is as would be expected, as the increase in the depletion is coincident with an increase in the total laser output

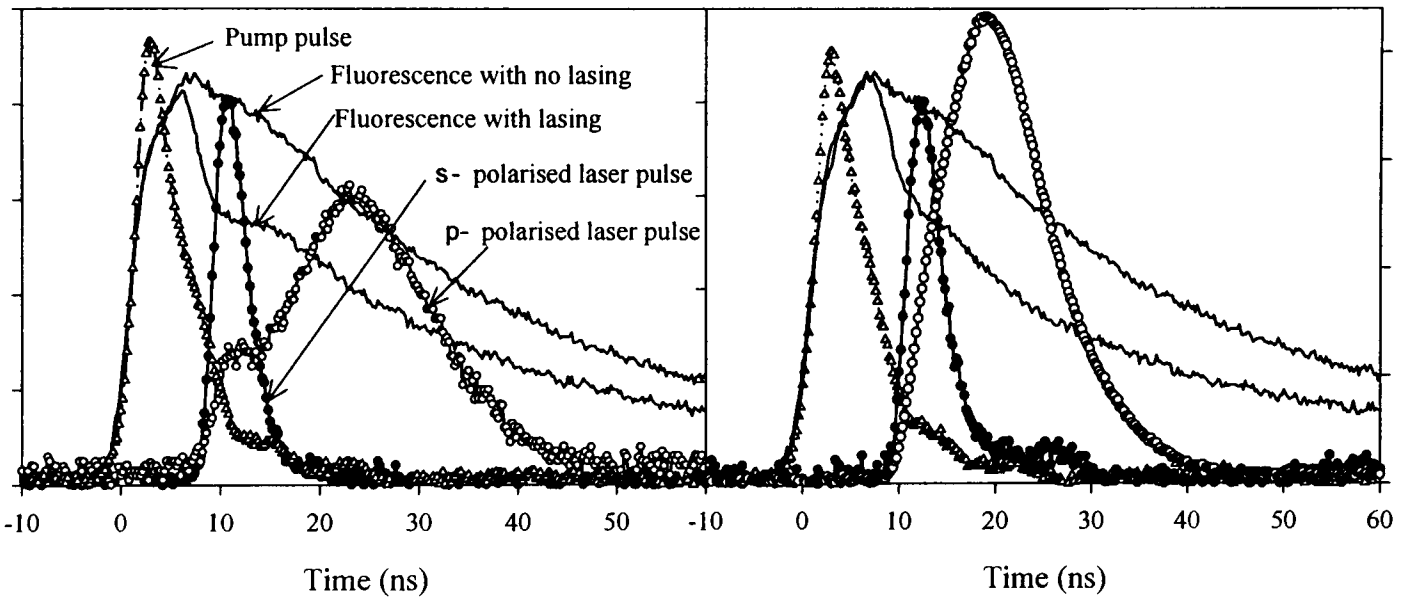


Figure 3.22 shows the pump pulse, fluorescence pulse both with and without lasing and the polarised laser pulses for lasing tuned to 327 nm in a prism tuned Ce:LiLuF laser at -2°C. Two extremes of the π-polarised fluctuations are shown (left) with low π-polarised content in output and (right) with high π-polarised content in the laser output.

The stability of the polarised laser pulses on a millisecond time scale is shown in Figure 3.23. As can be seen, the π-polarised laser output fluctuated by ~50% above and below the average π-polarised output intensity. The σ-polarised laser output was much more stable with only a 20% fluctuation above and below the average intensity. These results show that the laser output is not flipping in polarisation, as initially suggested by McGonigle *et al.* (McGonigle *et al.* 1999c) to be the cause of the fluctuations seen, but rather both σ- and π-polarised laser modes exist in the cavity simultaneously, and the π-polarised laser mode fluctuates in intensity.

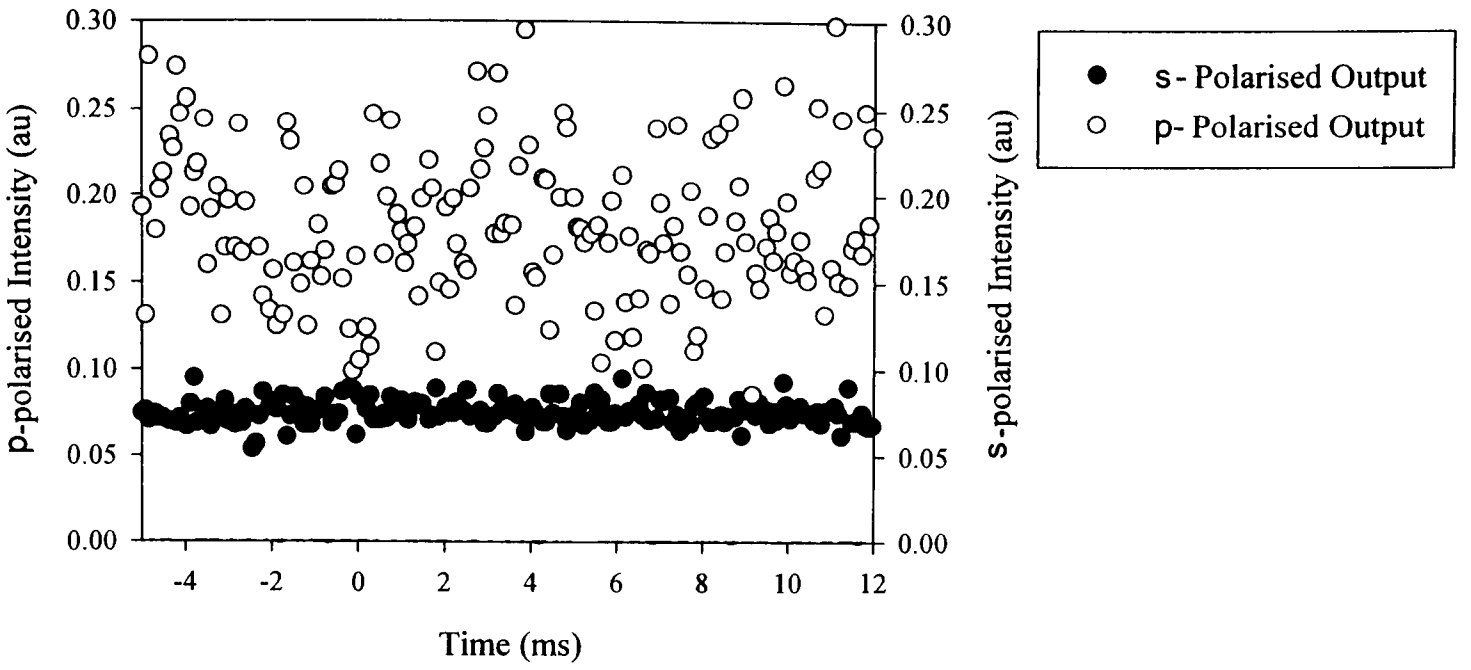


Figure 3.23 is a graph showing stability of the σ- and π-polarised components of the 327 nm laser output of the tunable Ce:LiLuF laser at -2°C.

The lasing of Ce:LiLuF when tuned to 311 nm and 327 nm was investigated further in order to gain a better understanding of the dip at 327 nm and the fluctuation of the π-polarised laser output at low temperatures. The variation of laser output power with temperature when tuned to 311 nm and 327 nm is shown in Figure 3.24. The 311 nm laser output was found to increase with decreasing temperature with a slight roll off of this increase below 4°C. A 65% increase in output power was evident with only a 30°C change in crystal temperature. The 327 nm laser output was found to increase with decreasing temperature until 10°C. Below 10°C the laser output decreased in power. The output below 10°C became predominantly σ-polarised and the laser output power fluctuated more as the temperature decreased. Unfortunately the magnitudes of these fluctuations were not recorded in detail and so are not represented on the 327 nm curve.

The slope efficiency of the laser was determined when tuned to ~311 nm and ~327 nm, with the crystal cooled to -3°C. These slopes are shown in Figure 3.25. The slope efficiency of lasing when the laser was tuned to 311 nm, with respect to incident pump power was found to be ~20%. When tuned to 327 nm, the slope efficiency was only ~1%.

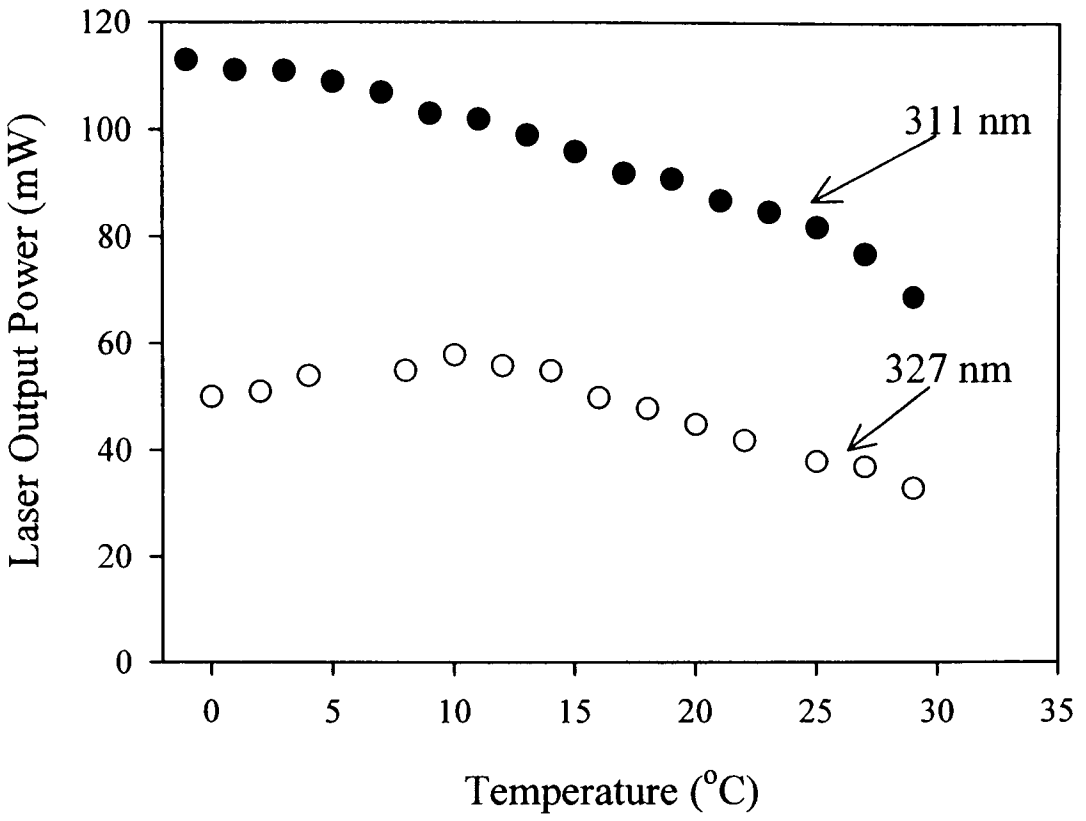


Figure 3.24 shows the variation of Ce:LiLuF laser output power with temperature when tuned to 311 nm and 327 nm, with 700 mW pump power.

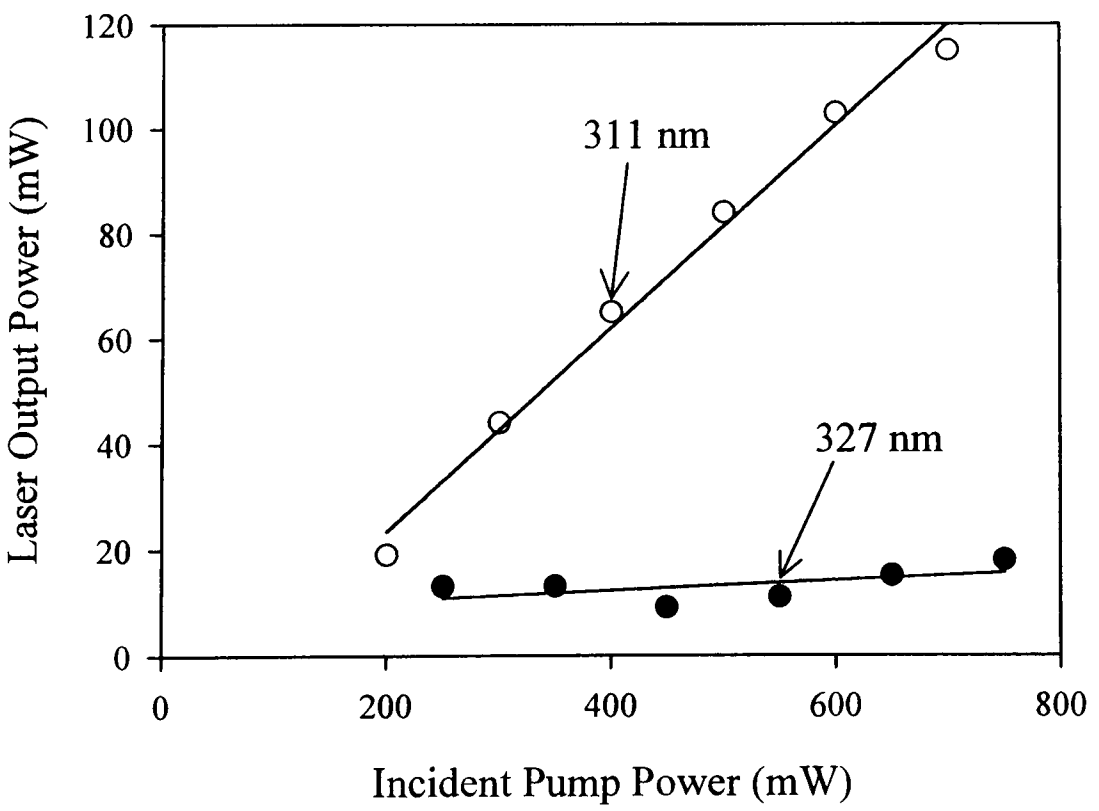


Figure 3.25 shows the variation of the output of a prism tuned Ce:LiLuF laser, cooled to -3°C and tuned to 311 nm and 327 nm.

The dip in laser output at 327 nm in the tuning curve shown in Figure 3.21 at low temperatures was coincident with the presence of σ-polarised lasing, in as much that the

lasing at room temperature was all π-polarised, and at low temperatures both π-polarised and σ-polarised output were present. In order to ascertain the effect of the presence of the σ-polarised laser mode a Brewster's angle silica slide was placed in the laser cavity such that it induced a σ-biased loss in the cavity thus forcing π-polarised lasing. The effect of this σ-biased loss in the cavity was dramatic. The tuning curve at low temperatures showed no dip at 327 nm with the σ-biased loss in the cavity, as shown in Figure 3.26. The introduction of the σ-biased loss into the cavity causes a 330% increase in the laser output at 327 nm. With the σ-biased loss in the cavity the output throughout the tuning curve was predominantly π-polarised with only a little σ-polarised output present at 327 nm. The overall output power with the σ-biased loss is in the cavity was higher than that without the σ-biased loss, though this is thought to be due solely to better alignment of the laser cavity compared to when the tuning curve was recorded with no loss introduced. Comparison of the π-polarised fluorescence emission curves shown in Chapter 2 show the correlation of the π-polarised laser output with the π-polarised emission cross-section is excellent

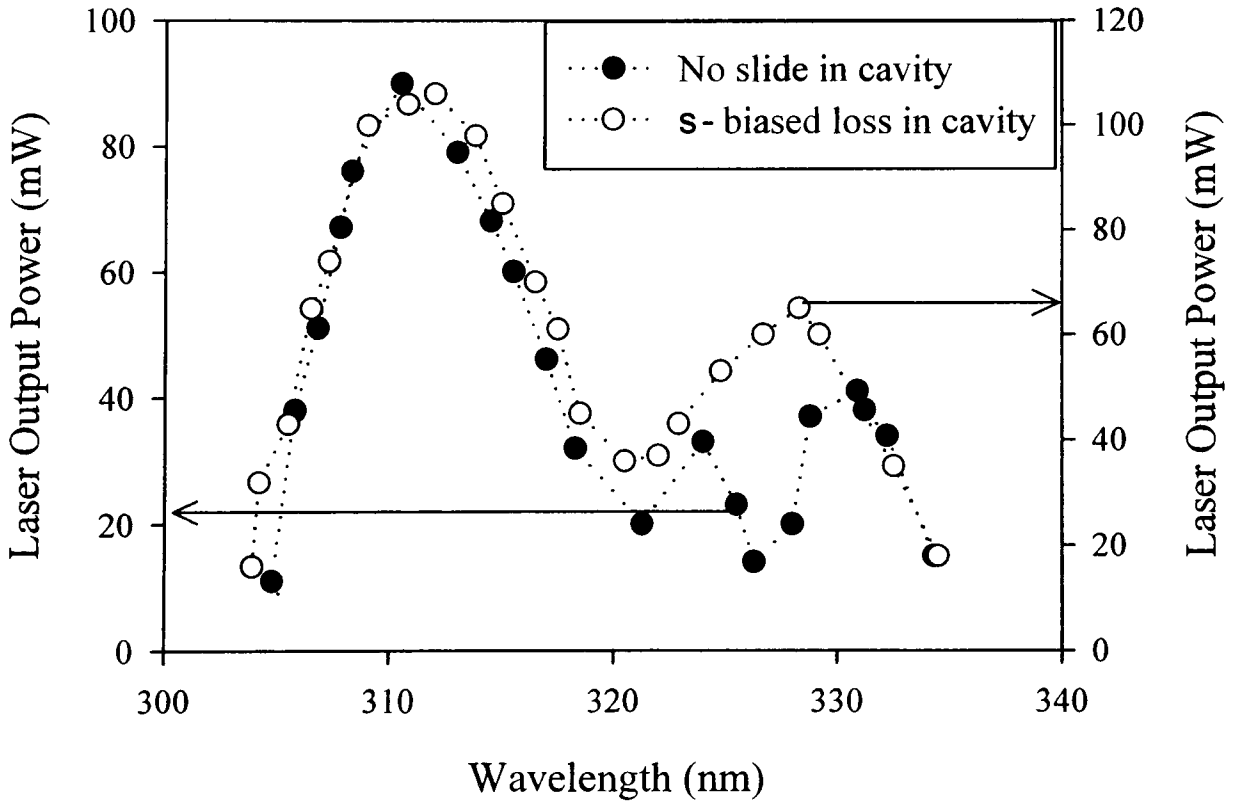


Figure 3.26 shows the tuning curves of Ce:LiLuF with ~600 mW pump power with the crystal cooled to -4°C both with and without a σ-biased loss introduced into the cavity.

Figure 3.27 shows the effect of the σ-biased slide on the output power at 327 nm for decreasing temperature. As can be seen, with the σ-biased loss in the cavity, the variation of the laser output at 327 nm with temperature is almost identical in behaviour to the 311 nm output in this experiment.

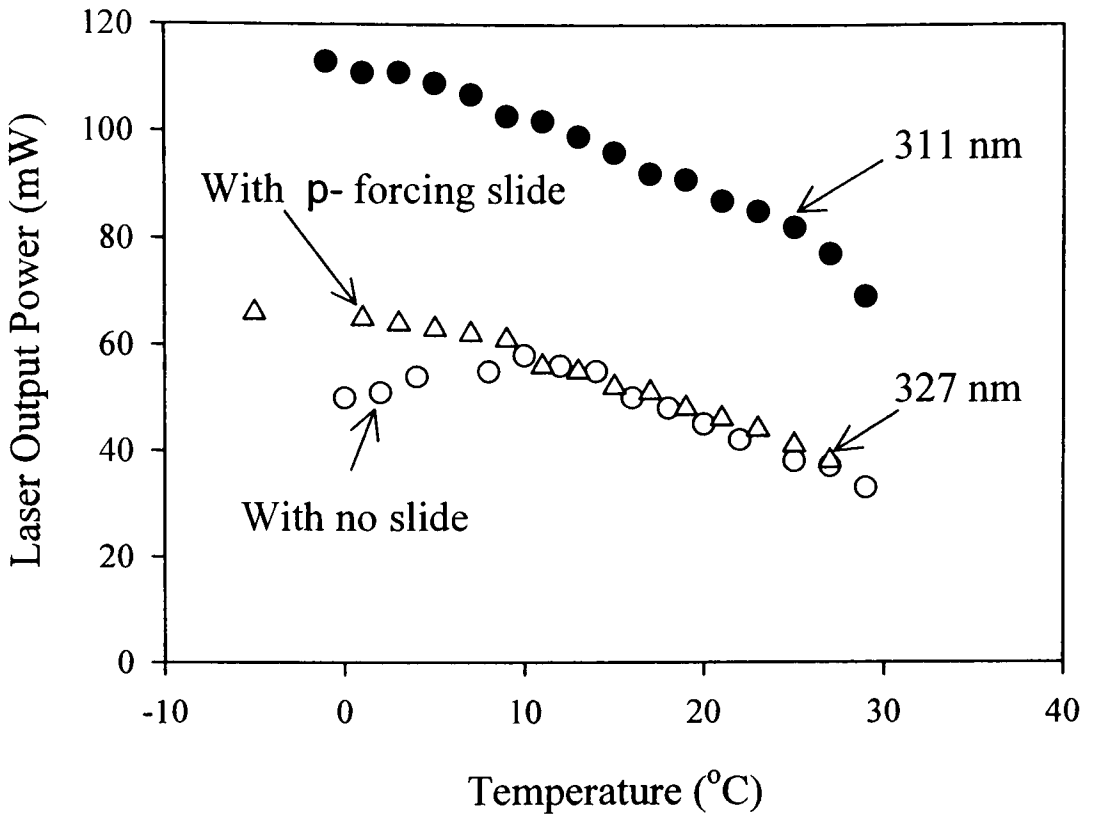


Figure 3.27 shows the dependence of Ce:LiLuF laser output power on temperature. For 327 nm the laser output was compared for a cavity both with and without a σ-biased loss introduced.

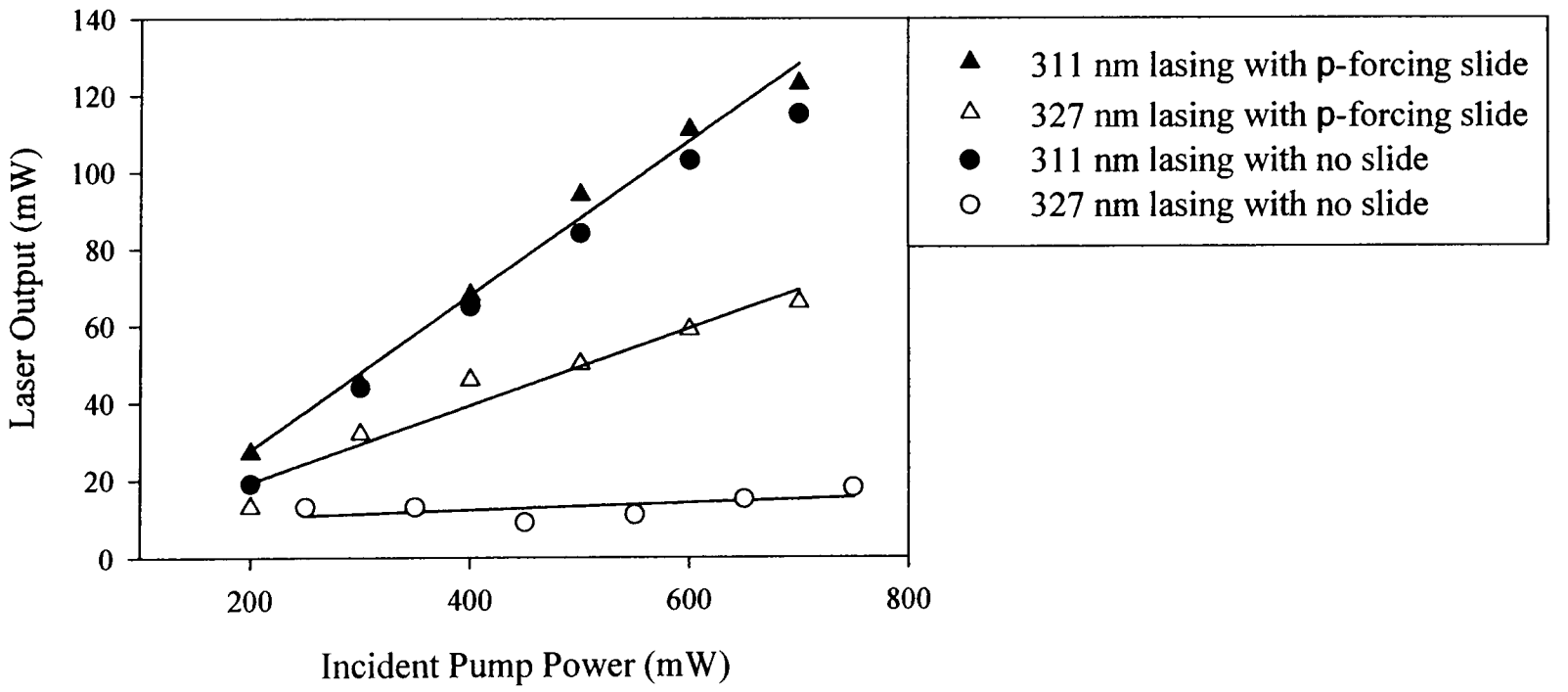


Figure 3.28 shows the dependence of the Ce:LiLuF laser output with incident pump power at 311 nm and 327 nm both with and without a σ-biased loss introduced into the cavity. The crystal was cooled to -2°C for these measurements.

A change in output power of 74% at 327 nm was observed for a 30°C change in temperature with the σ-biased loss in the cavity. This is comparable to that seen at 311 nm (65%) with a 30°C temperature decrease with no introduced loss.

The slope of the 327 nm lasing was found to also change dramatically with the σ-biased loss in the laser cavity. The slope efficiency at -2°C, increased from 1% at 327 nm to 10% with the introduction of the σ-biased loss. The σ-biased loss was found not to cause any change in the 311 nm output, as was expected.

3.5 Simulation of Lasing in Ce:LiLuF

There are three main areas of the experimental lasing results, reported in the earlier sections of this chapter, for which a better understanding of the results is required. In order to gain further insight into the Ce:LiLuF laser behaviour, the laser was simulated using a finite-difference numerical model. This model is described next in §3.5.1.

In order to ascertain the limitations of the laser model, the 309 nm lasing with the 30%, 50%, 80% and 90% output couplers was simulated. First, using the laser model, the temperature dependence of the output of a Ce:LiLuF laser was simulated. The temperature dependence of the Ce:LiLuF laser efficiency was thought to arise from the temperature dependence of σ_{ESA} in Ce:LiLuF as discussed in Chapter 2. This proposal was tested by simulating the temperature dependence of Ce:LiLuF lasing using the temperature dependence of σ_{ESA} determined in Chapter 2.

Second, the presence of multiple wavelength and polarisation components in the laser output with the M302, M303 and prism-tuned cavities required further understanding. The presence of these multiple components was shown to be temperature, pump power and intra-cavity loss dependent, which suggested a strong coupling and competition between the various possible laser modes in Ce:LiLuF lasers. In order to decipher the effects of the different mode controlling parameters, the laser behaviour, operating with the M302 and M303 output couplers or the prism-tuned cavity, was simulated. Since the laser model simulated only one laser pulse cycle, the presence of fluctuations in certain components of the laser output could not be simulated easily.

3.5.1 Program Description

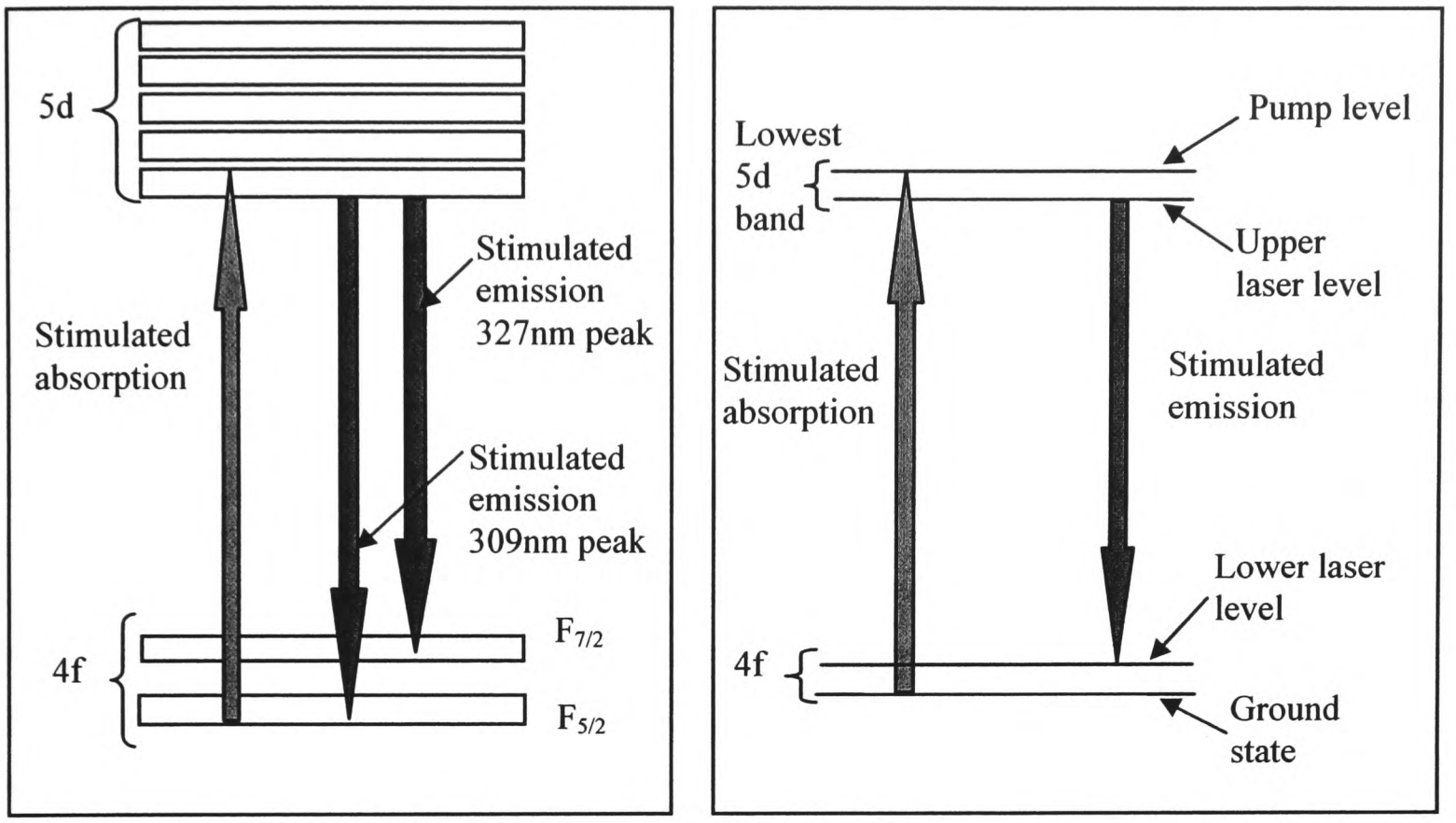


Figure 3.29 shows schematic diagrams of a four-level (left) and a simplified four-level laser system.

The Ce^{3+} energy configuration can be approximated by an ideal four-level laser system described in §2.5.1 and shown in Figure 3.29. In this ideal four-level laser model, the effects of excited-state absorption were also included. The pump wavelength (289 nm), used in the lasing experiments reported in this thesis, corresponds to the transition from the bottom of the *4f* band (ground-state) to the lower band of the *5d* manifold. Because of this, it was assumed that the lower *5d* band was both the terminal state of stimulated absorption at 289 nm as well as the initial state from which stimulated emission takes place (shown in Figure 3.29 (left)). In the simulations described in this section, the relaxation from the pump level to the upper laser level (see Figure 3.29 (right)) was assumed to be instantaneous. Lasing occurred between the upper laser level and the lower laser level, with the lower laser level corresponding to the whole *4f* level ($F_{7/2}$ for 327 nm lasing and $F_{5/2}$ for the 309 nm lasing). The transition between the lower laser level and the ground state was also assumed to be instantaneous, as such the population in the lower laser level was assumed to be negligible at all times and hence the spontaneous and stimulated emission, in effect, filled the ground state directly. Thus, with the lower laser level population being negligible, it was only the upper laser level population (N_{5d}) which influenced the spontaneous and stimulated emission processes (see equations 3.4, 3.5 and 3.6). This is represented mathematically in equation 3.3.

$$\text{Population Difference} = N_{\text{Upper laser level}} - N_{\text{Lower laser level}} \cong N_{5d}$$
$$\text{since } N_{\text{Lower laser level}} \cong 0 \qquad 3.3$$
$$\text{and } N_{\text{Upper laser level}} = N_{5d}$$

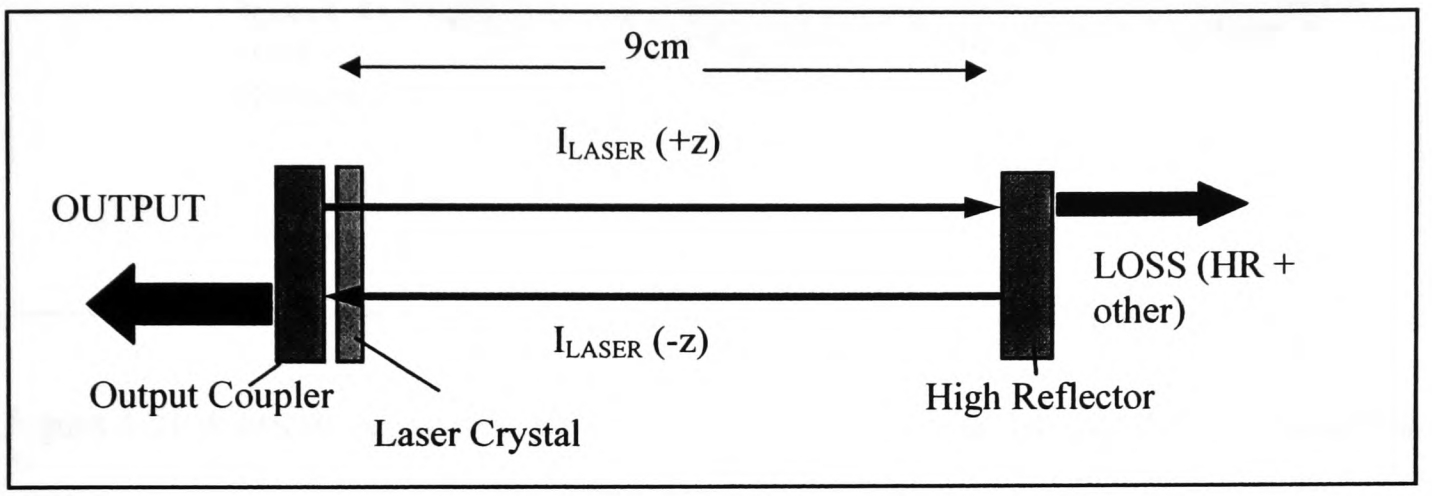


Figure 3.30 is a diagram of the laser cavity simulated in this section.

In the model describing a Ce:LiLuF laser, a simple 9 cm long laser cavity consisting of a high reflector, output coupler and laser crystal (shown schematically in Figure 3.30) was simulated. A finite difference simulation was run in which the crystal was pumped in an identical manner to that described in the gain simulations (see equations 2.8, 2.9 and 2.10 in §2.5.1). Similarly, the crystal was "cut" into 100 slices of length δz (=8 μm), such that the differential *dI/dz* could be approximated by $\delta I/\delta z$. The light propagating through the laser cavity in this model did so in time steps of duration δt, such that $\delta t = \delta z / c$, where c is the speed of light. The value of δz was confirmed to be a small enough increment in that by decreasing δz, there was negligible effect on the behaviour of the laser model.

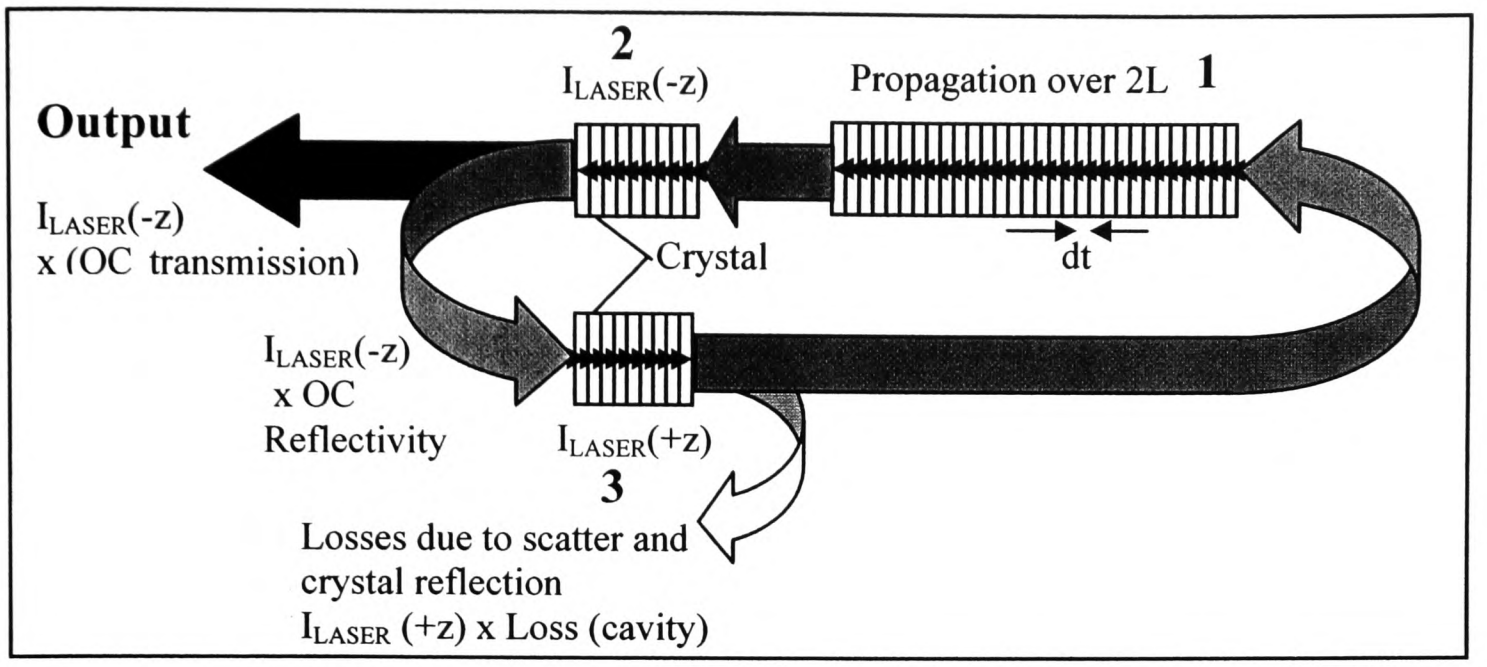


Figure 3.31 shows the equivalent schematic diagram of the laser cavity used to simulate the laser behaviour in Ce:LiLuF.

Each round trip of laser cavity was modelled such that it consisted of three sections as shown in Figure 3.31. The first section consisted of a propagation length of 18 cm corresponding to the crystal→high reflector→crystal experimental propagation length, in which there was no gain or loss. The second section of the laser cavity consisted of the laser crystal of length 0.8 mm, in which the laser and spontaneous emission travelled from right to left (-*z*). The intensity of the spontaneous emission was governed by equation 3.4, in which $I_{spontaneous}$, is the spontaneous emission intensity, N_{5d} is the upper *5d* laser level population, τ is the *5d* level lifetime, ω_{laser} is the laser frequency and $\Omega_{laser\ mode}$ (= $2.3\text{x}10^{-6}$srad) is the fraction of the solid angle into which photons are being emitted in the direction of the laser mode, (since only the photons travelling in the direction of laser oscillation contribute to the laser mode).

$$\frac{dI_{spontaneous}}{dz} = \frac{N_{5d}}{\tau}.\text{h}\omega_{laser}.\Omega_{lasermode} \qquad 3.4$$

The spontaneous emission was added to the left travelling laser mode, I_{laser}(-z), and the result was amplified according to equation 3.5 in which σ_{EM} and σ_{ESA} are the emission and excited-state absorption cross-sections respectively. As the light exited the crystal, the laser intensity was subject to the loss due to the output coupler transmission. This loss was in effect the laser output.

$$\frac{dI_{laser(-z)}}{dz} = (\sigma_{EM} - \sigma_{ESA}).N_{5d}.I_{laser(-z)} \qquad 3.5$$

The laser intensity that was not lost as laser output was "reflected" such that it was travelling through the crystal from left to right (+z), this corresponding to the third section of the laser cavity. As in the second section of the laser cavity the right travelling laser beam underwent amplification as described by equation 3.6 and the spontaneous emission as in equation 3.4 was added.

$$\frac{dI_{laser(+z)}}{dz} = (\sigma_{EM} - \sigma_{ESA}).N_{5d}.I_{laser(+z)} \qquad 3.6$$

On exiting the right side of the crystal, a loss corresponding to the reflection, scattering and other loss mechanisms was introduced. To approximate the intrinsic cavity losses due to scattering and crystal reflections within the cavity (with no prism or polarisation bias), the ~10% loss determined using the Caird Plot in §3.2.2 was used. In the case of the prism-tuned laser cavity or the laser cavities with the polarisation biased loss, these losses were introduced at this point in the program too. The actual loss values introduced will be specified when they are introduced. The remaining right travelling emission was emitted from the crystal and then re-circulated back into the first section of the laser cavity having completed one round trip.

The depletion of the upper *5d* population and the consequent filling of the lowest *4f* level caused by the combined +z and –z laser intensities were described by equations 3.7 and 3.8. Figure 3.32 shows a detailed flow diagram showing the calculations undertaken for each time step ($\delta t = \delta z / c$).

$$\frac{dN_{4f}}{dt} = \left[\sigma_{EM}(\omega_{laser}).N_{5d}.\left[I_{laser(+z)} + I_{laser(-z)}\right]\right] / \mathrm{h}\omega_{laser} \qquad 3.7$$

$$\frac{dN_{5d}}{dt} = -\left[\sigma_{EM}(\omega_{laser}).N_{5d}.\left[I_{laser(+z)} + I_{laser(-z)}\right]\right] / \mathrm{h}\omega_{laser} \qquad 3.8$$

In this laser model the π-polarised 289 nm absorption cross-section used was that used in the gain simulations in Chapter 2, as were the 309 nm and 327 nm σ- and π-polarised emission cross-sections. The polarised excited-state absorption cross-sections for 309 nm and 327 nm, determined in Chapter 2, were also included in the laser model.

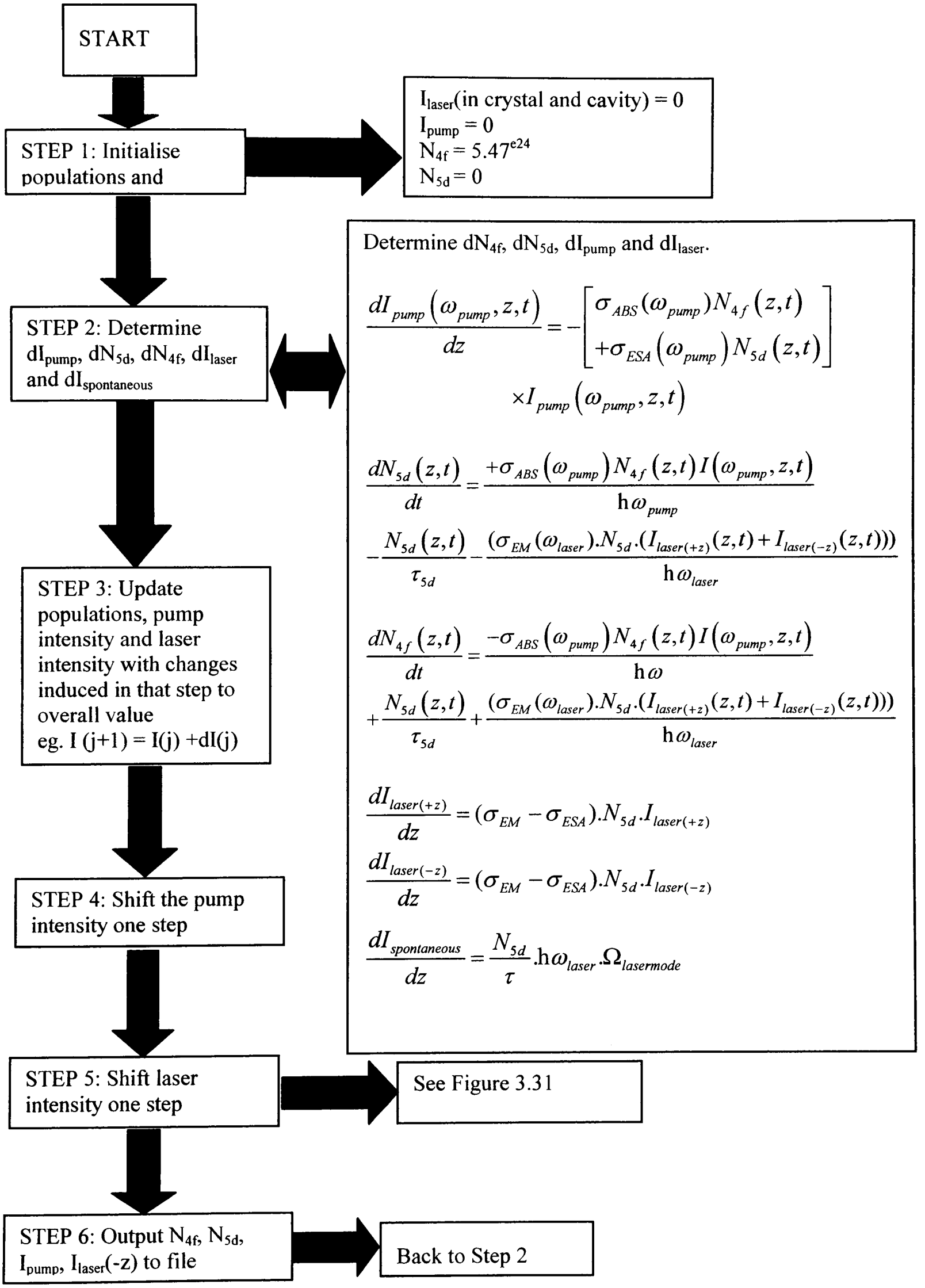


Figure 3.32 shows a flow diagram of calculations made for each time step in the laser simulation.

In the laser model, unlike the gain model, in addition to these ESA transitions due to laser photons, the ESA transitions due to the pump photons were also included. An ESA cross-section of 0.2×10^{-18} cm^{-2} was used for the 289 nm π-polarised pumping (from Chapter 2). By simulating emission at both 309 nm and 327 nm simultaneously for both σ- and π-polarisations, gain competition effects intrinsic to the laser were expressed automatically.

The relaxation rate of electrons that have been promoted to colour centres or the conduction band via ESA transitions, is not known. Initial experimental results were presented in §2.4.2, in which the effect of an intense probe on the fluorescence intensity was found to be negligible. This was suggestive of either a very fast relaxation rate or insufficient probe intensity for the fluorescence depletion to be noticeable. Thus two lifetime extremes were investigated. The one extreme was the instantaneous return of the electrons from colour centres and the conduction band to the *5d* state such that the *5d* population was unperturbed by the ESA transition. The second extreme was the infinitely slow relaxation rate of these transitions. In the latter case the electrons excited via ESA did not return to the *5d* level in the time of the virtual experiment (50 ns), thus modelling a lifetime of >>50 ns. In a test run, comparing the outcome of each relaxation scenario, some small differences were found in the pulse shapes. The overall lasing behaviour, however, was found not to vary noticeably. Since the variation arising from the different lifetime scenarios was only slight, only the very fast (instantaneous) relaxation simulations are presented in this thesis.

In the simulations, all the radiation was represented as intensity (in Wm^{-2}). The experimental pump spot size calculated was of limited accuracy due to the variation of the pump beam quality and the focal position of the pump in the crystal. Thus, in most of the cases studied using this laser model, small adjustments were made to the pump spot sizes such that the simulated thresholds matched the experimentally determined thresholds. This ensured that the laser model investigated was the same lasing regime as was investigated experimentally, and as such comparisons of the simulated and experimental lasing behaviour could be made. As derived from the Caird plot in §3.2.2 the pumping efficiency was assumed to be 50% in all the simulations run. This pumping efficiency was taken into account when matching the simulated and experimental lasing thresholds.

In a similar manner to the pump spot size, the laser spot size was not known to any significant accuracy either. In order to compare simulated and experimental laser output behaviour the laser intensity from the simulations was required in units of average power (W). Since the repetition rate, pulse length and simulated intensity were known to a good accuracy, in order to match experimental and simulated laser output powers small variations in the laser spot size were made to match the simulated results to the experimental laser outputs.

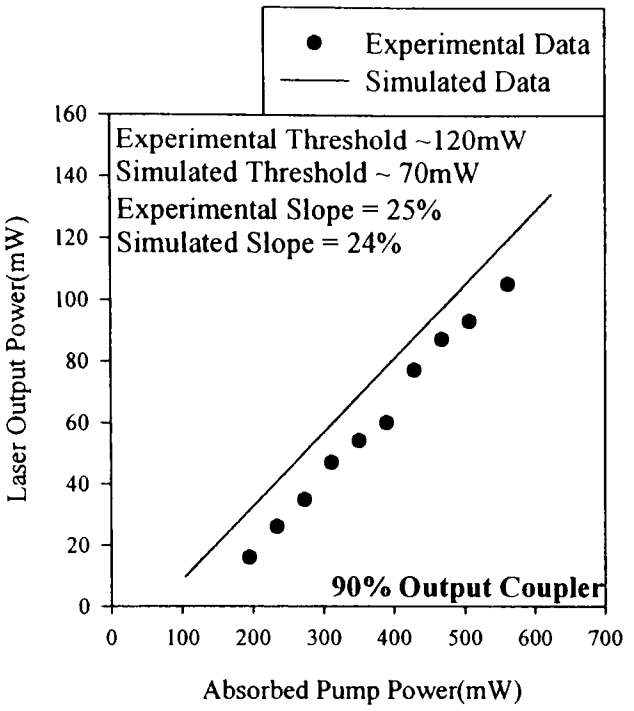
By varying the pump spot area, effectively the horizontal axis of a laser output versus pump power curve is scaled linearly, similarly by scaling the laser spot area the vertical axis is scaled linearly. The effect of scaling these axes is purely to make comparisons between simulated and experimental results easier and, since it is mainly the behaviour which is being investigated, the actual pump power and laser power values are of little significance. Some variation between the calculated experimental spot sizes and spot sizes used in the simulations was expected due to the fact that the laser model used in the simulations had only one spatial dimension, in reality modes are Gaussian or Gaussian-like. In all cases the pump and laser mode diameters are indicated in the figure captions or on the figures themselves for reference.

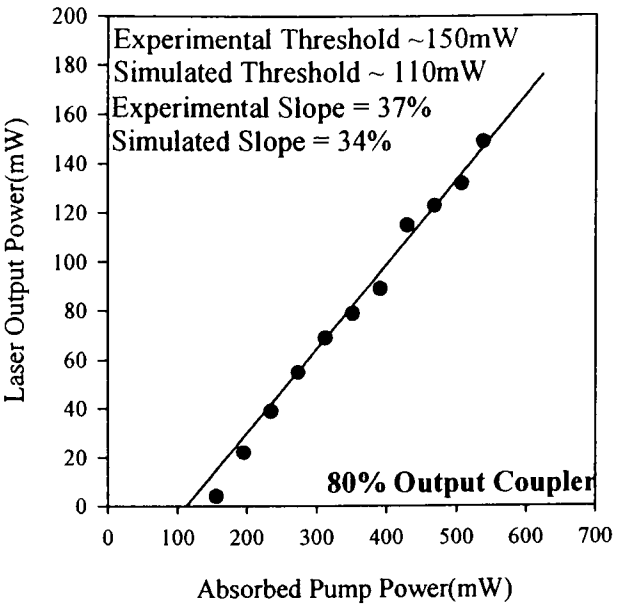
3.5.2 Modelling Results 1 - Simulations of Lasing in Ce:LiLuF with non-wavelength selective output couplers.

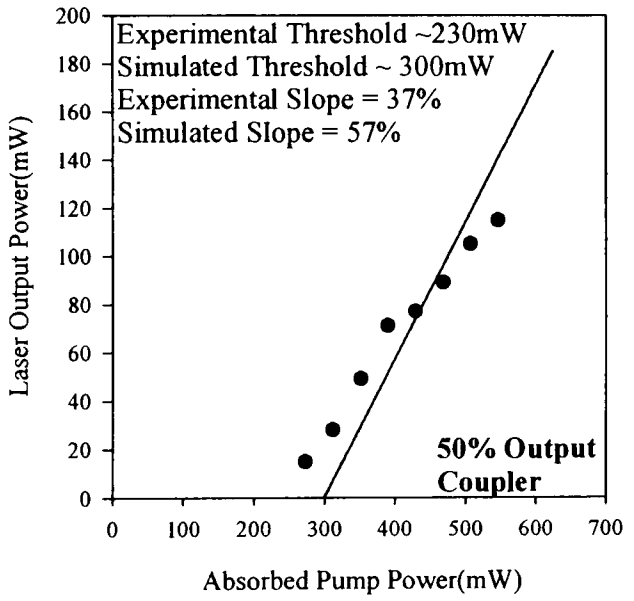
Firstly the dependence of the laser output on output coupler reflectivity was simulated with the crystal cooled to -3°C, using the low temperature ESA cross-sections determined in Chapter 2, namely $\sigma_{ESA}(309, \pi) = 0\text{x}10^{-18}$ cm^{-2}, $\sigma_{ESA}(309, \sigma) = 1.8\text{x}10^{-18}$ cm^{-2}, $\sigma_{ESA}(327, \pi) = 0\text{x}10^{-18}$ cm^{-2} and $\sigma_{ESA}(327, \sigma) = 2.6\text{x}10^{-18}$ cm^{-2}. These results allowed the performance of the laser model to be ascertained.

The diameter of the focussed pump spot required by the laser model to match the threshold of lasing simulated with the 80% output coupler to that measured experimentally was 160 μm. The laser spot diameter required was 170 μm. These values of pump and laser spot diameter give a threshold of 120 mW compared to the experimental threshold of 150 mW. The simulated slope efficiency was 34% compared with that obtained experimentally of 37%.

Using the pump and laser spot sizes required to match the simulated laser output and lasing threshold with the 80% output coupler, the lasing with the 90%, 50% and 30% reflectivity output couplers was simulated. The plots for the 90%, 80% 50% and 30% output couplers with these spot diameters are shown in Figure 3.33. As can be seen in Figure 3.33 the threshold for the 90%, 50% and 30% output couplers was not in very good agreement with the experimental results.







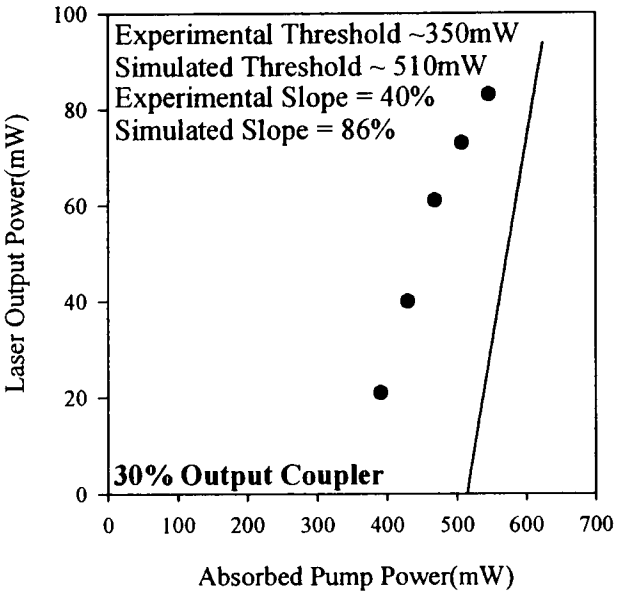


Figure 3.33 shows the comparison of simulated (lines) and experimental (points) Ce:LiLuF laser results for 90%, 80%, 50% and 30% reflectivity output coupler with the crystal cooled to -3°C. The simulations were carried out using a pump mode diameter in the crystal of 160 μm and a laser mode diameter of 170 μm in the crystal.

The simulated slope for the 90% output coupler was in good agreement with the experimental slope achieved with the 90% output coupler, but the simulated slopes for the 50% and 30% output couplers were much larger than those determined experimentally. The laser output of the simulations with the 90%, 80%, 50% and 30% output couplers was at 309 nm and π-polarised as was seen experimentally. The σ- and π-polarised 327 nm emission and σ-polarised 309 nm emission simulated was purely spontaneous emission with the characteristic 40 ns decay lifetime.

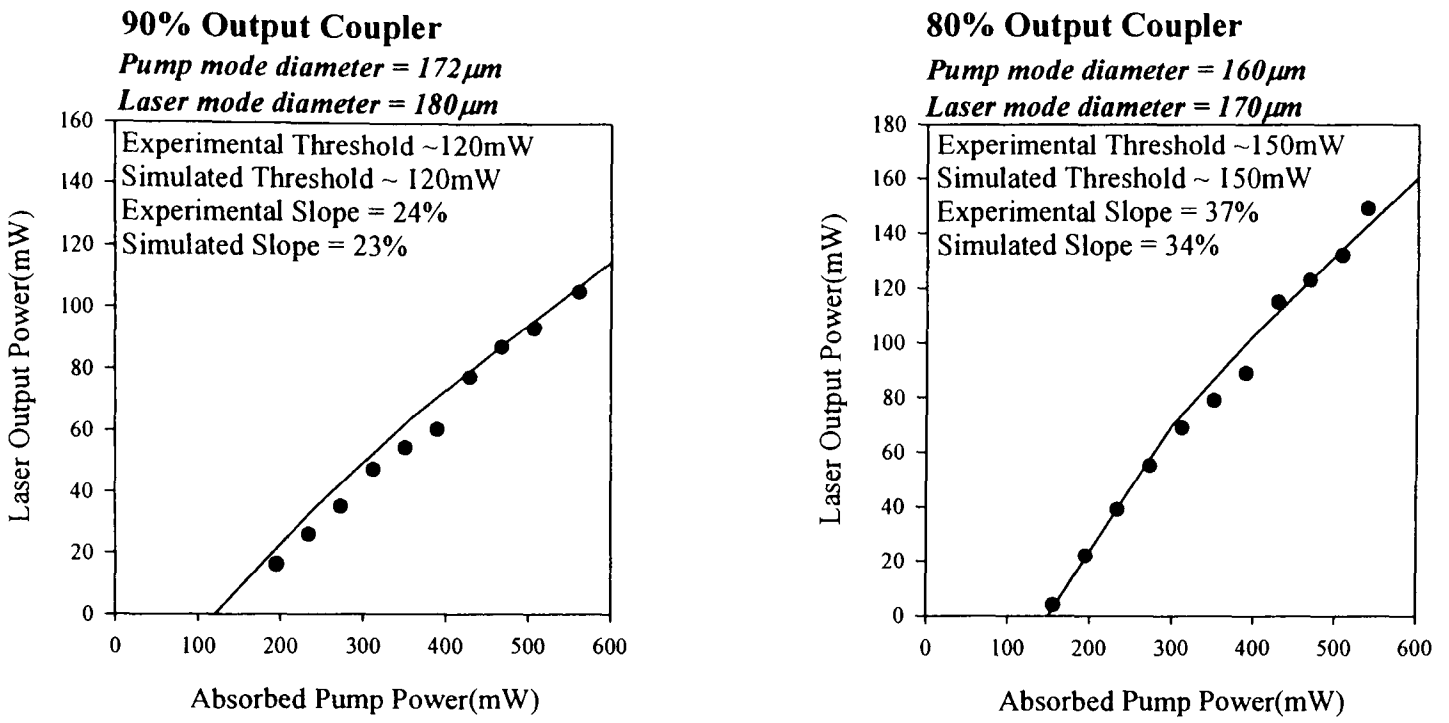


Figure 3.34 show a comparison of simulated (lines) and experimental (points) Ce:LiLuF laser results for 90%, 80%, 50% and 30% reflectivity output coupler with the crystal cooled to -3°C. The simulations were carried out using a pump mode and a laser mode diameter in the crystal as shown in italics above each plot.

Matching the pump and laser spot sizes for each of the output couplers individually, a much closer agreement between experimental and simulated thresholds, slopes and output powers could be obtained, as shown in Figure 3.34. In all four cases the simulated data showed a similar roll-off to the experimental data.

In general, the pump mode diameters required to match these 309 nm lasing characteristics (between 132 μm and 172 μm) were 2-3 times those used experimentally of 66 μm (calculated using a Gaussian approximation of the pump beam). The laser mode diameters used to simulated comparable laser output powers from the model (between 180 μm and 113 μm) were in general very similar to those calculated for the experimental laser mode diameters (~110 μm). The similarities of the required pump and laser mode diameters in the simulations are particularly encouraging as to the accuracy of the laser model.

The change in residual inversion, shown by the variation of depleted fluorescence with pump power in §3.2.2, was suggestive that the mode-matching was not particularly good in the experiments conducted. This was taken into account by using the 50% pumping efficiency determined in §3.2.2. In fact the variation in residual inversion suggested that the pump mode was larger than the laser mode throwing some doubt on the calculated experimental pump mode sizes. The discrepancies in the pump and laser mode sizes, particularly the former, are thus considered to be reasonable, taking into account the uncertainties of the Ce^{3+} number density (as described in Chapter 2).

The build up times, depletions and pulse lengths predicted by the laser model are summarised in Table 3.2. In general the build-up times and pulse lengths simulated are in good agreement with those determined experimentally. The pulse lengths measured experimentally are thought to be 1-2 ns shorter than reported due to the 1 ns rise-time of the detectors used. The depletions on the other hand are much larger than those determined experimentally. These very high simulated depletions imply that, in the laser model used, the stimulated emission had much larger extraction efficiency than was found in reality. This large simulation extraction efficiency would allow a much larger depletion of the upper level population than was found experimentally. However it is also possible that the discrepancy between the simulated and experimental depletions may be a result of the imperfect overlap of the experimental pump and laser modes. The un-depleted fluorescence, indicative of an un-depleted pumped region, would reduce the average depletion measured experimentally. Thus it is possible that the simulated depletion is a more accurate representation of the actual depletion. Such high depletions could be realistic, with perfect mode overlap and a quantum efficiency of unity.

The simulated pump and laser pulses and the simulated fluorescence resulting from lasing in Ce:LiLuF with a 50% output coupler and the crystal cooled to -3°C are shown in Figure 3.35. A comparison of Figure 3.3 and Figure 3.35 shows good agreement between the experimental

and simulated pulse shapes as well as the obvious disagreement between the experimental and simulated depletions.

Table 3.2 shows a comparison of the simulated and experimental build-up times, depletions and laser pulse lengths for Ce:LiLuF lasing at -3°C. Note the experimental pulse durations are all ~ 1-2 ns shorter in reality due to the rise time of the detector.

OC reflectivity	Experimental Results			Simulated Results		
	R=90%	R=80%	R=50%	R=90%	R=80%	R=50%
Build-up time (ns)	9	9	12	11	12	14
Pulse length (ns)	7	6	4	4	3	3
Depletion %	62	49	41	94	91	75

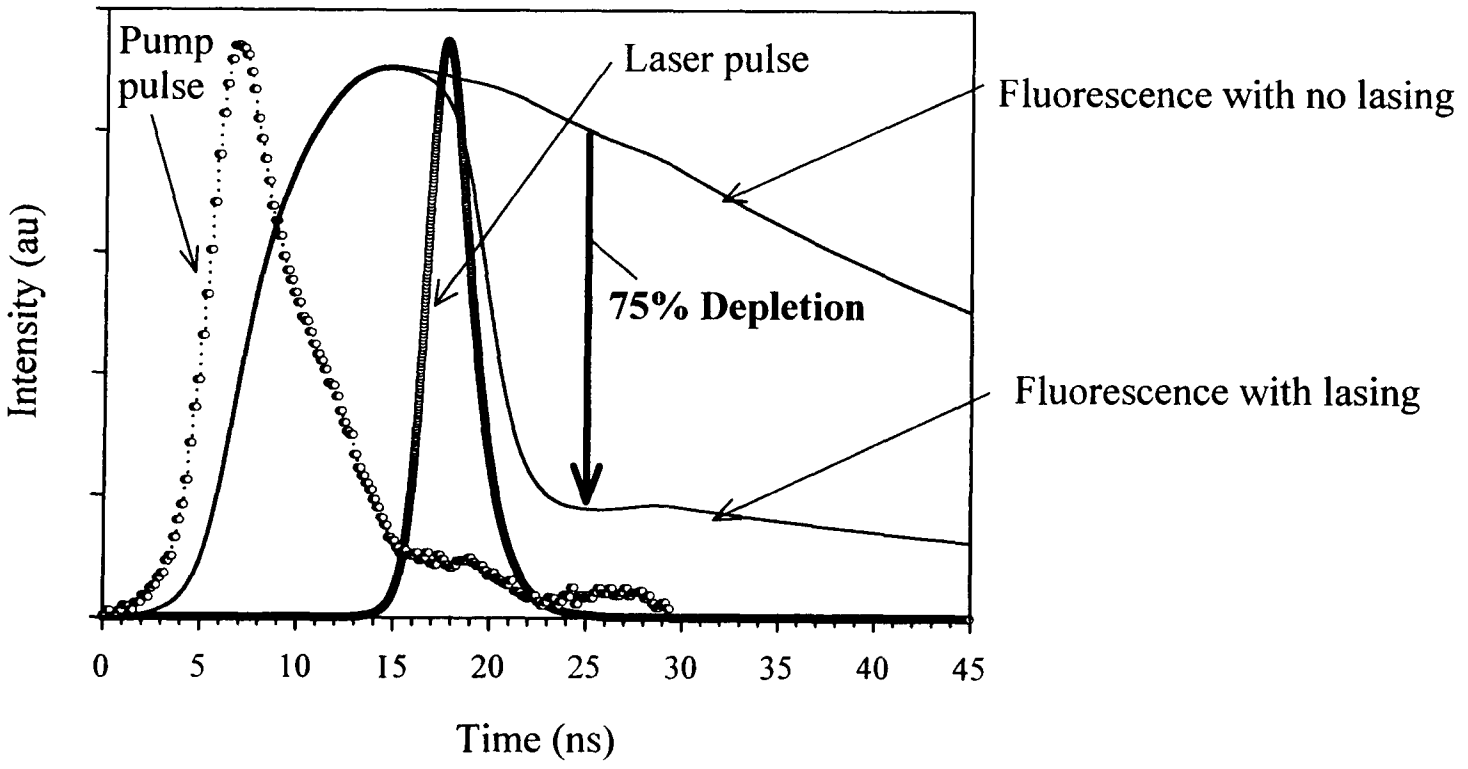


Figure 3.35 shows the simulated laser and pump pulses and depleted fluorescence for lasing Ce:LiLuF, with a 50% output coupler and a crystal temperature of -3°C.

The lasing behaviour simulated thus far shows, in general, that this laser model is a good approximation of the actual Ce:LiLuF laser and that keeping in mind the limitations imposed

on the laser model by the assumptions made, the laser model is overall a useful tool to understanding the lasing in Ce:LiLuF.

The temperature dependence of the laser output at 309 nm with the 80% output coupler (using the 0.1 m high reflector cavity) was also investigated using the ESA cross-sections at room temperature of 0.15×10^{-18} cm^{-2} and at -3°C of 0 cm^{-2}, as determined in Chapter 2. The change in σ_{ESA} of 0.15×10^{-18} cm^{-2} with the 28°C decrease in temperature, derived from the gain experiments in Chapter 2, was found to have very little effect on the laser output. This is shown in Figure 3.36. In fact a larger change in σ_{ESA} was required to model the change in behaviour. Maintaining the pump and laser mode sizes and adjusting only the σ_{ESA} for π-polarised light at 309 nm the experimental laser behaviour at room temperature could be reproduced using $\sigma_{ESA} = 2 \times 10^{-18}$ cm^{-2}.

This high sensitivity of lasing at 309 nm to temperature does suggest that the laser is much more temperature sensitive when a large laser field is present and/or saturation of the gain is occurring compared to the temperature sensitivity observed when the gain is not saturating and only a very low intensity probe beam is present. This sensitivity is discussed further in §3.6.

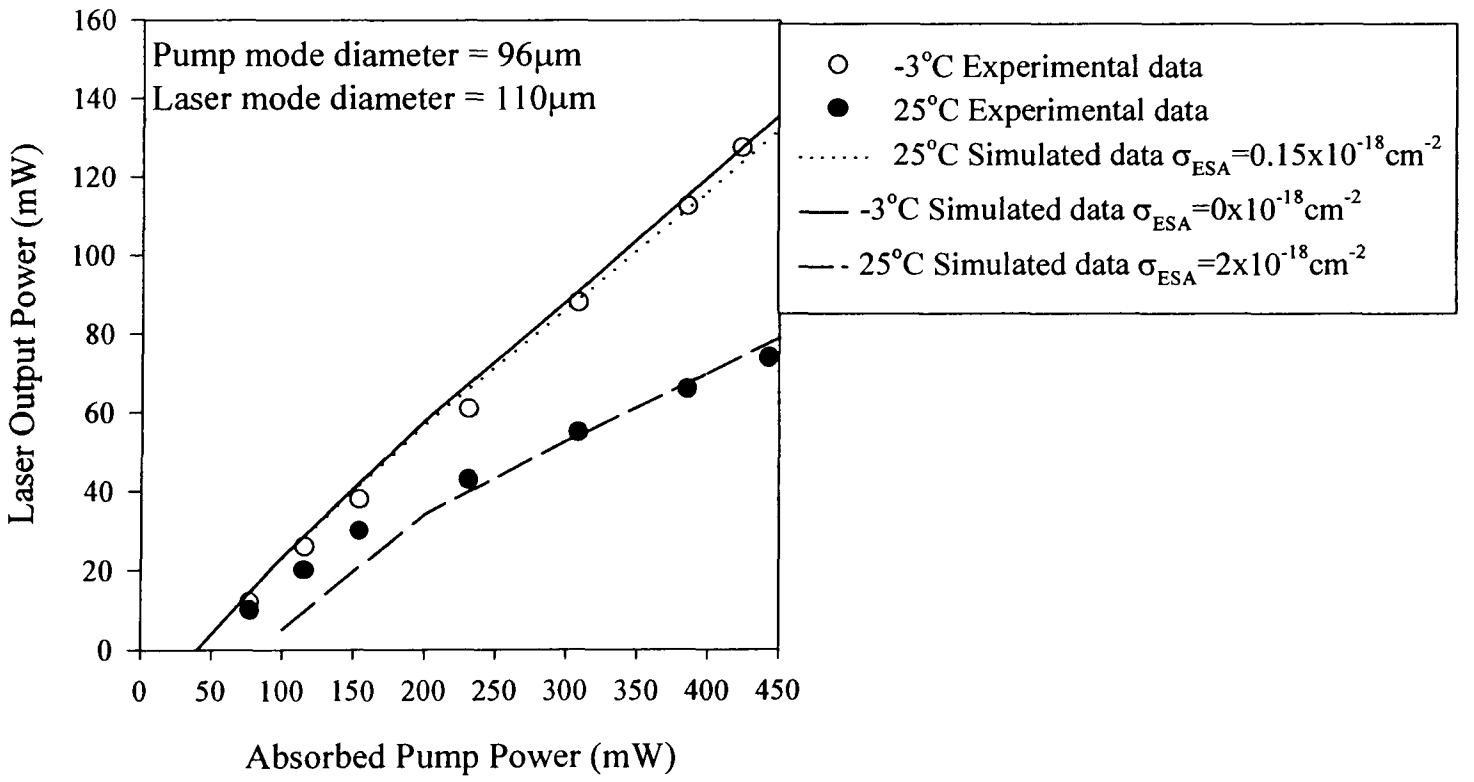


Figure 3.36 shows a comparison of the experimental and simulated Ce:LiLuF laser output with the laser crystal cooled to -3°C and 25°C using an 80% reflectivity output coupler, with a pump mode diameter and laser mode diameter of 96 μm and 110 μm respectively.

3.5.3 Modelling Results 2: Simulations of lasing in Ce:LiLuF with wavelength-selective output couplers

For clarity, the lasing behaviour of Ce:LiLuF with the M302 and M303 output coupler cavities observed experimentally is summarised in Table 3.3.

In order to gain some understanding of the behaviour of Ce:LiLuF laser when lasing at 327 nm, the lasing with the M302 and M303 output couplers at low temperatures was simulated. Since the room temperature σ_{ESA} (309 nm, π) determined using the gain simulations and the laser simulations disagree, the simulations conducted for lasing at 327 nm were all done at low temperatures and no further temperature comparisons were made. Both the very slow (infinite) and very fast (instantaneous) ESA relaxation lifetime extremes were investigated.

The laser behaviour for the M302 output coupler laser cavity was simulated at various pump powers. The results are shown in Figure 3.37. The simulated laser behaviour showed excellent agreement with the experimental behaviour. In particular, the slope efficiency was found to show some variation with pump power as was seen experimentally.

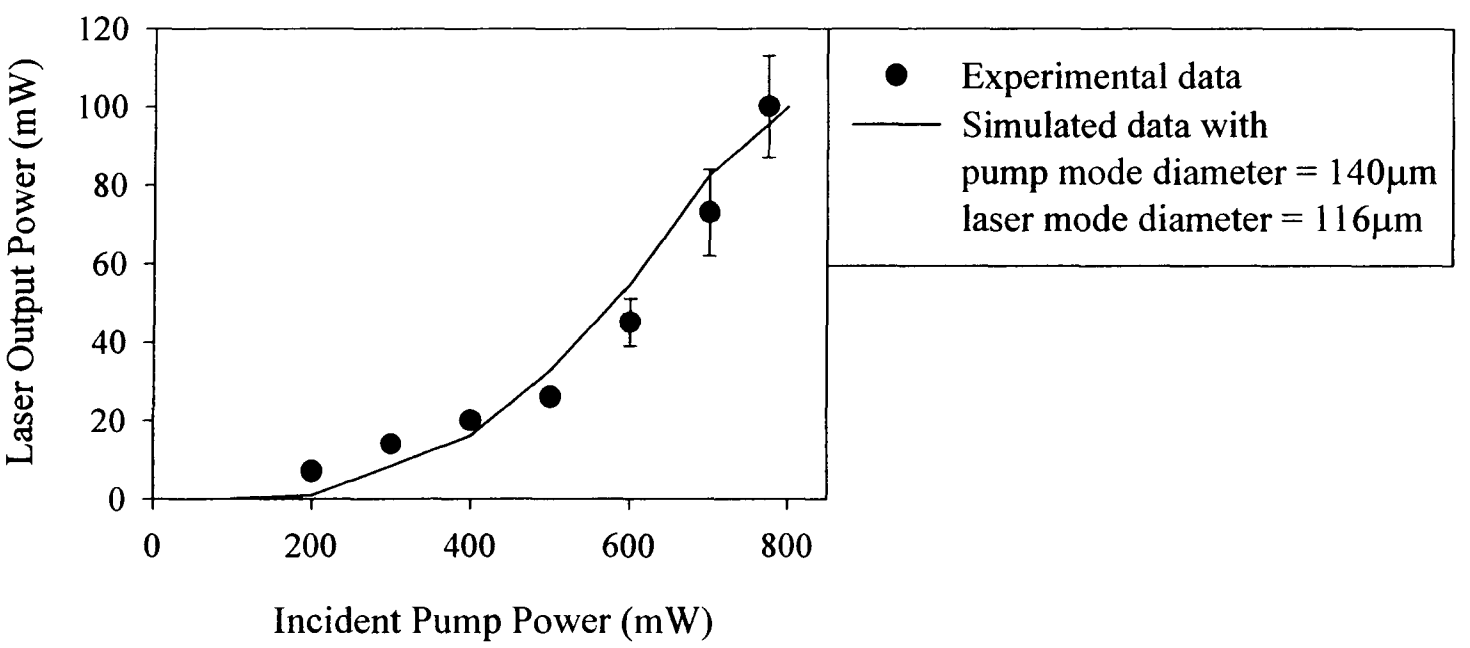


Figure 3.37 shows the lasing in Ce:LiLuF simulated with the M302 output coupler (see §3.3.1) at -3°C with a pump mode size of 140μm and a laser mode size of 116 μm.

Table 3.3 shows a summary of the experimental M302 and M303 laser output content for reference.

	M302 Output Coupler	M303 Output Coupler - π-forced lasing	M303 Output Coupler -σ-forced lasing
309 nm Reflectivity	54%	9%	9%
327 nm Reflectivity	92%	70%	70%
Total σ-polarised Intra-cavity loss	10%	~55%	10%
Total π-polarised Intra-cavity loss	10%	10%	~55%
Behaviour at Low Pump Powers	Output contained mostly σ-polarised 327 nm; a small amount of π-polarised 327 nm was present in the output.	Output contained mostly π-polarised 327 nm	Output was all σ-polarised 327 nm.
Behaviour at High Pump Powers	Above 450 mW the output was mostly σ-polarised 327 nm and π-polarised 309 nm; a small amount of π-polarised 327 nm was present in the output.	Above ~600 mW the output was mostly π-polarised 327 nm and π-polarised 309 nm; a small amount of σ-polarised 327 nm was present in the output.	Output was all σ-polarised 327 nm.

A closer look at the composition of the laser output simulated showed a similar dependence of the laser output composition on pump power as was found experimentally. The individual 327 nm, σ- and π-polarised and 309 nm, π-polarised components of the laser output are shown in Figure 3.38. There was no lasing at 309 nm for the σ-polarisation, as expected due to the very small 309 nm, σ-polarised effective emission cross-section. The 327 nm, σ-polarised and 309 nm, π-polarised lasing thresholds simulated are in excellent agreement with the experimental thresholds gained from the extrapolation of the low and high pump power slope efficiencies. Figure 3.38 shows the simulated 327 nm, σ-polarised laser output had a threshold power of ~150 mW. The simulated 327 nm, π-polarised lasing and 309 nm, π-polarised lasing both had a threshold of ~300 mW. The 327 nm, σ-polarised output was found to be dominant below 450 mW pump power with a maximum output power of 12 mW. Above 450 mW pump power, the 327 nm, σ-polarised laser output rolled off to a steady output power of ~8 mW at 800 mW. The 327 nm π-polarised output was less than 2 mW for all powers above threshold. This low 327 nm, π-polarised output power simulated would have been detectable experimentally by eye and using the photo-multiplier, thus its presence, even at very low levels, is in agreement with the experimental results. The 309 nm, π-polarised output dominated above 450 mW, showing a steep increase in output power with increasing pump power (22% slope efficiency).

The 309 nm π-polarised and the 327 nm, σ- and π-polarised laser pulses corresponding to the laser output composition for the M302 laser cavity are shown in Figure 3.39. Comparison of the experimental laser pulses shown in Figure 3.13 with these simulated pulses in Figure 3.39 shows excellent agreement. The build up times for the π-polarised and σ-polarised laser pulses determined experimentally were approximately 10 ns and 11 ns respectively. The build up times predicted using the laser model were ~8 ns for all 3 components of the laser output which is in excellent agreement with the experimental build up times. The π-polarised, 309 nm pulse simulated had a pulse length of ~3 ns which is identical to that found for the π-polarised component of the experimentally determined laser output. The σ-polarised laser pulse simulated had a pulse length of ~14 ns which is larger than that of 8 ns determined experimentally. Once again, as was found with the purely 309 nm lasing in §3.5.2, the depletion predicted by the laser model (98%) was much larger than that determined experimentally (57%). It is interesting to note that even when the *5d* population has been depleted by the 309 nm laser pulse, the population inversion appears to be high enough to sustain the 327 nm lasing, as the 327 nm laser pulse does not reach its peak until ~10 ns after the sharp depletion caused by the 309 nm laser pulse.

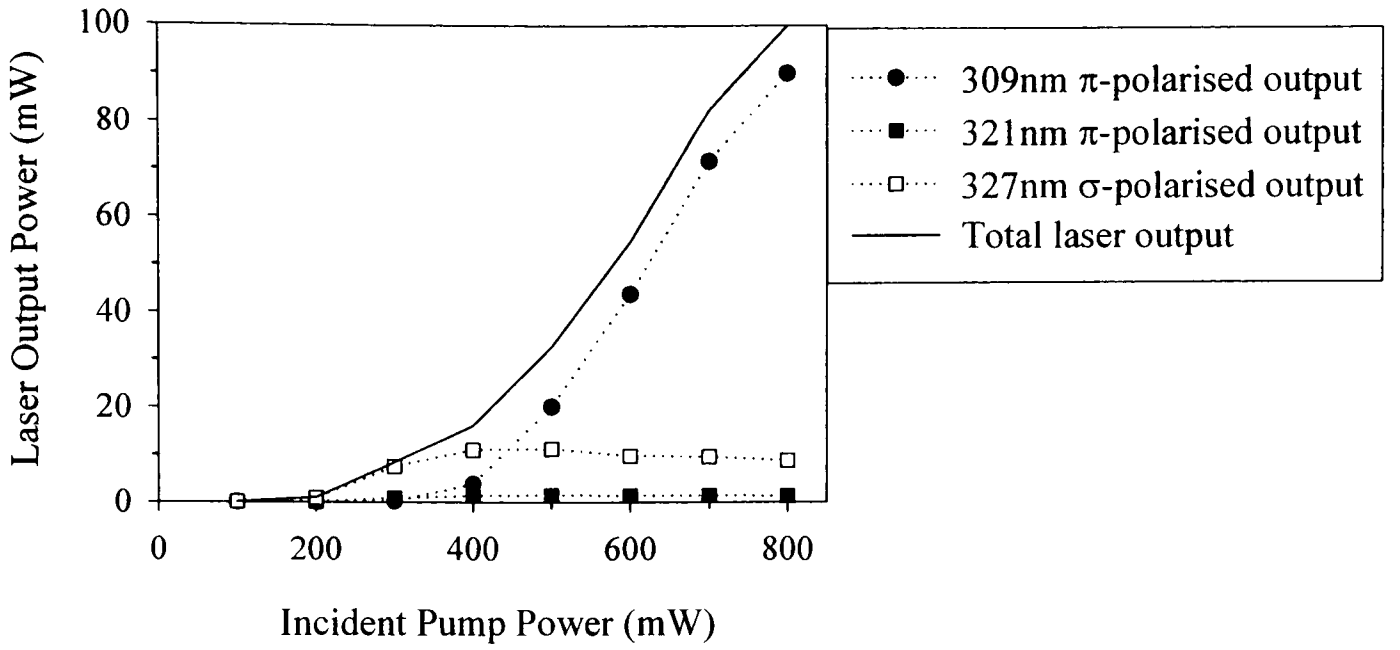


Figure 3.38 shows a detailed graph of the different components of the laser output for lasing in Ce:LiLuF simulated with the M302 output coupler at -3°C with the 140 μm pump mode diameter.

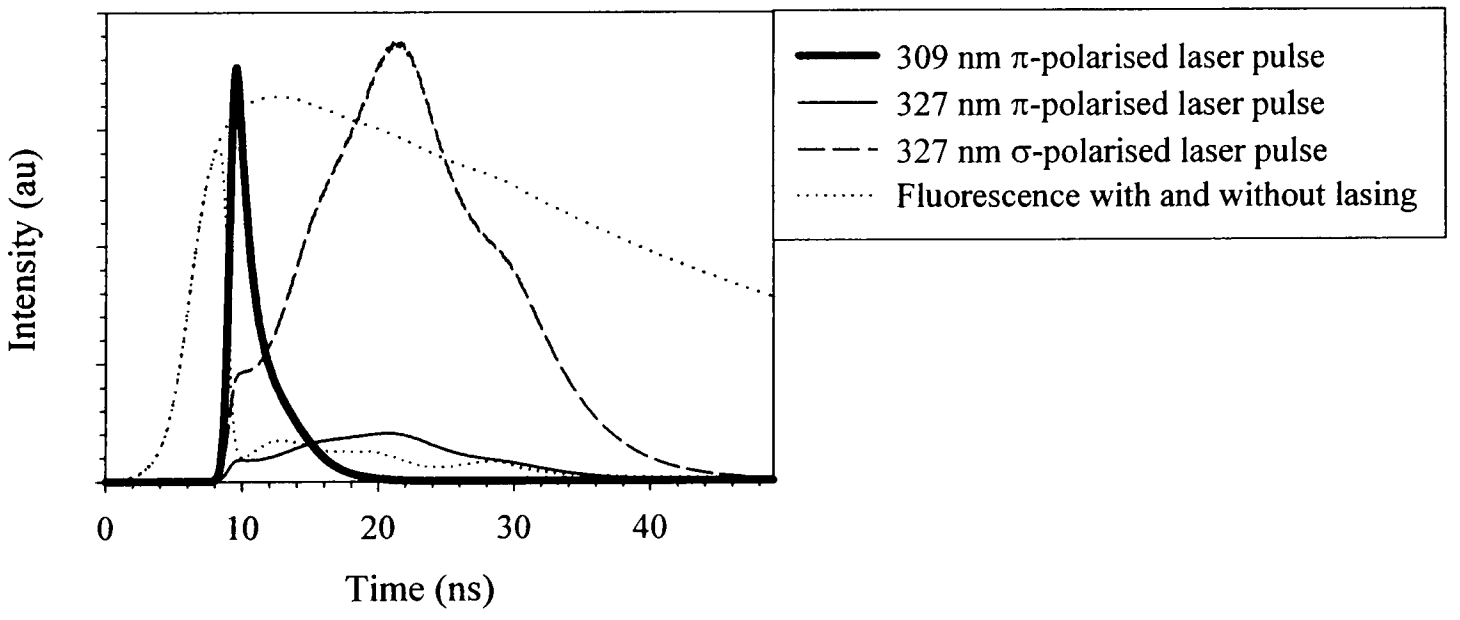


Figure 3.39 shows the wavelength and polarisation components of the Ce:LiLuF laser pulse simulated for lasing with the M302 output coupler, with 800 mW pump power and with the crystal held at ~ -3°C. The pulse intensities shown are not to scale.

The lasing with the M303 output coupler was simulated at low temperatures for both σ-forced lasing and π-forced lasing. The presence of the slide in the cavity was simulated by increasing the loss experienced by the π-polarised laser field for σ-forced lasing and σ-polarised laser field for π-forced lasing. The loss introduced experimentally by the slide was introduced into

the laser model at the same point as the scattering and crystal reflection losses were accounted for. Since the exact loss experienced due to the slide was not known, the slide induced round-trip loss was approximated to be 50% (assuming a 16% loss at each face of the slide). The lasing being forced (namely π-polarisation for π-forced lasing) was assumed to have no extra loss induced by the slide. The results of these simulations are shown in Figure 3.40.

In the case of the σ-forced lasing, the simulated behaviour is in excellent agreement with the experimental behaviour. A roll-off of the output power with pump power is seen in the simulated results as was seen in the experimental results and, as expected, the laser output simulated with the σ-forcing slide was all σ-polarised 327 nm output. For π-forced lasing at low pump powers the output simulated consisted only of π-polarised, 327 nm emission. At high powers the simulation deviated from the experimental behaviour in that the threshold of 309 nm lasing simulated was >800 mW and experimentally the 309 nm threshold was ~600 mW. A small amount of 327 nm, σ-polarised emission was observed in the simulation results at pump powers of ~800 mW. This π-forced lasing behaviour is close to that seen experimentally, particularly at the lower pump powers.

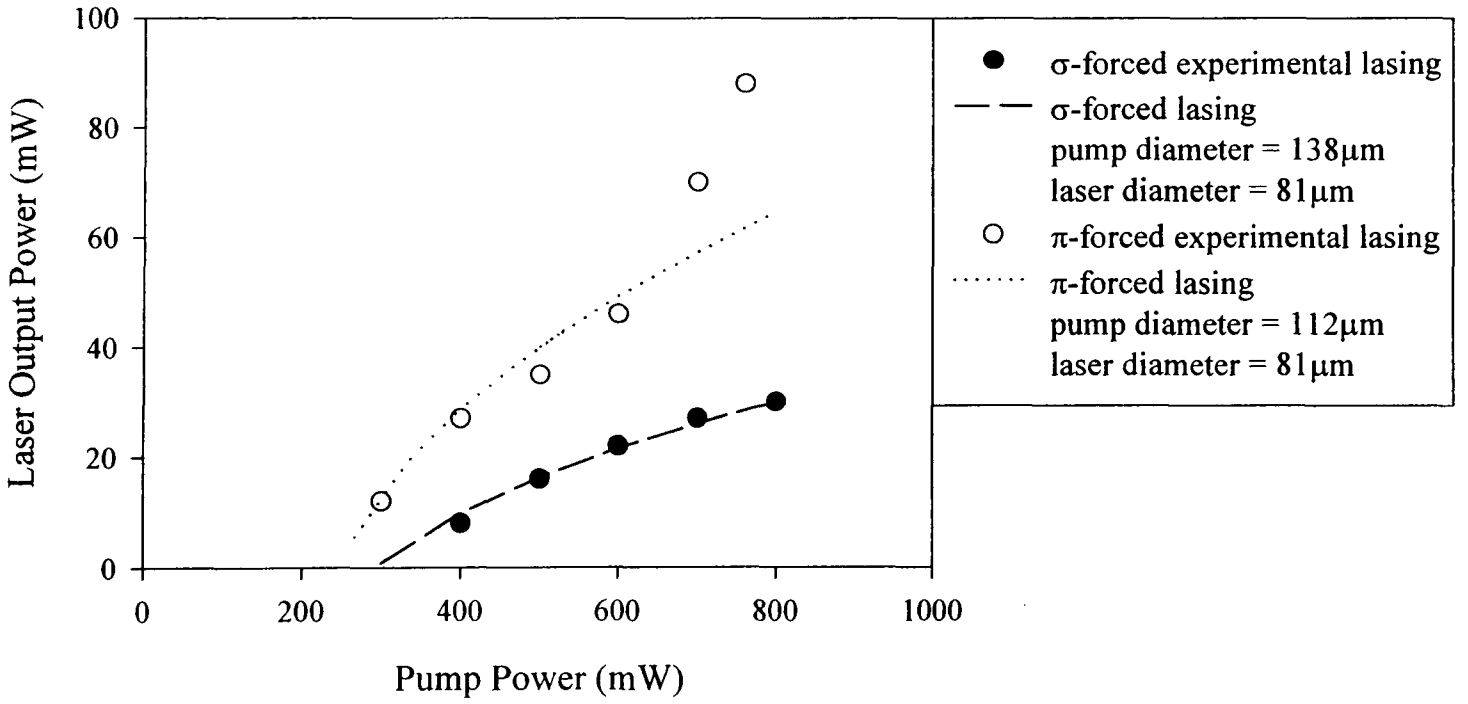


Figure 3.40 shows the simulated lasing in Ce:LiLuF using the M303 output coupler, with the crystal cooled to ~ -3°C. Both σ-forced and π-forced lasing is shown.

A closer look at the simulated laser pulses reinforces the similarities shown by the simulated π-forced lasing model. The pulse build up time for the 327 nm π-polarised laser pulse determined experimentally (shown in Figure 3.13) with 800 mW pump power was found to be ~13 ns, whereas that for the π-polarised 309 nm laser pulse was found to be ~10 ns. The

simulated build up times with 800 mW pump power were similar to these experimentally determined build up times, with the 327 nm π-polarised build up time being ~11 ns and the π-polarised 309 nm build up time being ~9 ns. The pulse lengths simulated are also in good agreement with the experimental pulse lengths with the simulated 327 nm laser pulse being ~4 ns compared the ~7 ns pulse length measured experimentally. The 309 nm pulse length simulated was ~2 ns compared to that measured experimentally of ~3 ns. These pulse lengths are actually in better agreement due to lengthening of the experimental pulses arising from the limited rise-time of the photodiode used.

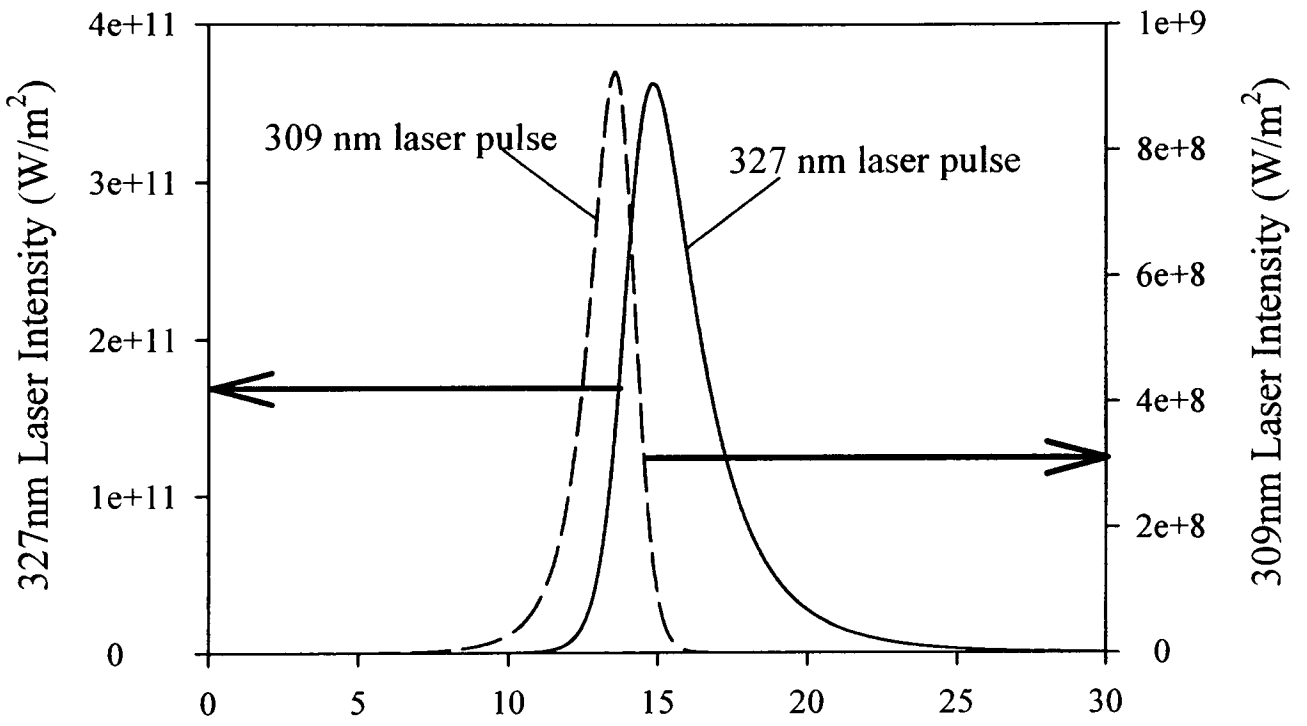


Figure 3.41 shows the simulated laser pulses for π-polarised forced lasing in Ce:LiLuF at -3°C using the M303 output coupler.

The reason for the differences in the experimental and simulated π-forced M303 lasing results is once again attributed to the affects of the excessive depletion predicted by the laser model. This large depletion simulated will shift the threshold of the 309 nm lasing to higher pump powers than was seen experimentally, thus these small differences between the simulated and experimental lasing behaviour is expected, keeping the limitations of the laser model in mind.

3.5.4 Modelled Results 3: Simulations of lasing in a prism-tuned cavity

In order to understand the presence of the dip seen in the tuning curve for Ce:LiLuF lasing at 0°C when tuned to 327 nm, as reported previously by McGonigle *et al.* (McGonigle *et al.* 1999c), the 327 nm lasing in a prism-tuned cavity, with the 90% output coupler was

simulated. The presence of the prism in the cavity was simulated by including a ~50% loss per round trip with the intra-cavity loss of the 10% loss, used in un-tuned lasing simulations. This loss was approximated assuming a ~16% reflection per AR coated face of the prism. The prism was aligned to Brewster's angle with respect to the π-polarised laser field, thus this 50% prism loss was simulated so that only the σ-polarised laser mode saw the prism-induced loss. The prism is wavelength selective, thus a wavelength biased loss of 100% at 309 nm was introduced into the simulation to take this into account, thus lasing at 309 nm could not occur. The prism-tuned lasing was simulated with and without the slide-induced σ-polarised loss in the cavity. An extra σ-polarised round trip loss of 50% was introduced into the cavity for the π-forced lasing case, as was used in the previous section. For the π-polarised laser field it was assumed that no extra losses were induced by the slide or the prism. A summary of these losses are shown in Table 3.4.

Table 3.4 shows a summary of the losses included in the prism-tuned, unbiased and π-forced cavity, tuned to 327 nm.

Cavity Component Loss	Loss for σ-polarised 327 nm with no slide in cavity	Loss for σ-polarised 327 nm with slide in cavity	Loss for π-polarised 327 nm with and without a slide in the cavity
Prism Loss	50%	50%	0%
Slide Loss	0%	50%	0%
Other Losses	10%	10%	10%
TOTAL ROUND TRIP LOSS	55%	77.5%	10%

The simulated behaviour displayed by the π-forced lasing in the prism-tuned cavity, tuned to 327 nm, was found to be similar to that seen experimentally. The laser slope efficiency simulated (10%) was in excellent agreement with the experimental slope efficiency (10%). The laser output was found to be all π-polarised and at 327 nm as was seen experimentally. The prism-tuned laser with no slide in the cavity was also simulated. The simulated output was found to be vary little from that with the π-forcing slide in the cavity, assuming the laser

mode size was unaffected by the removal of π-forcing slide. The slope efficiency obtained from the laser model (~9%) with no σ-bias in the cavity was larger than that achieved experimentally (~1%). In the unbiased laser cavity simulated, the output consisted of mostly π-polarised 327 nm laser emissions and with very little σ-polarised emission in the output. This was not in agreement with the experimental results. The laser output with pump power, both with an unbiased cavity (no slide present) and with a σ-biased loss in the cavity are shown in Figure 3.42.

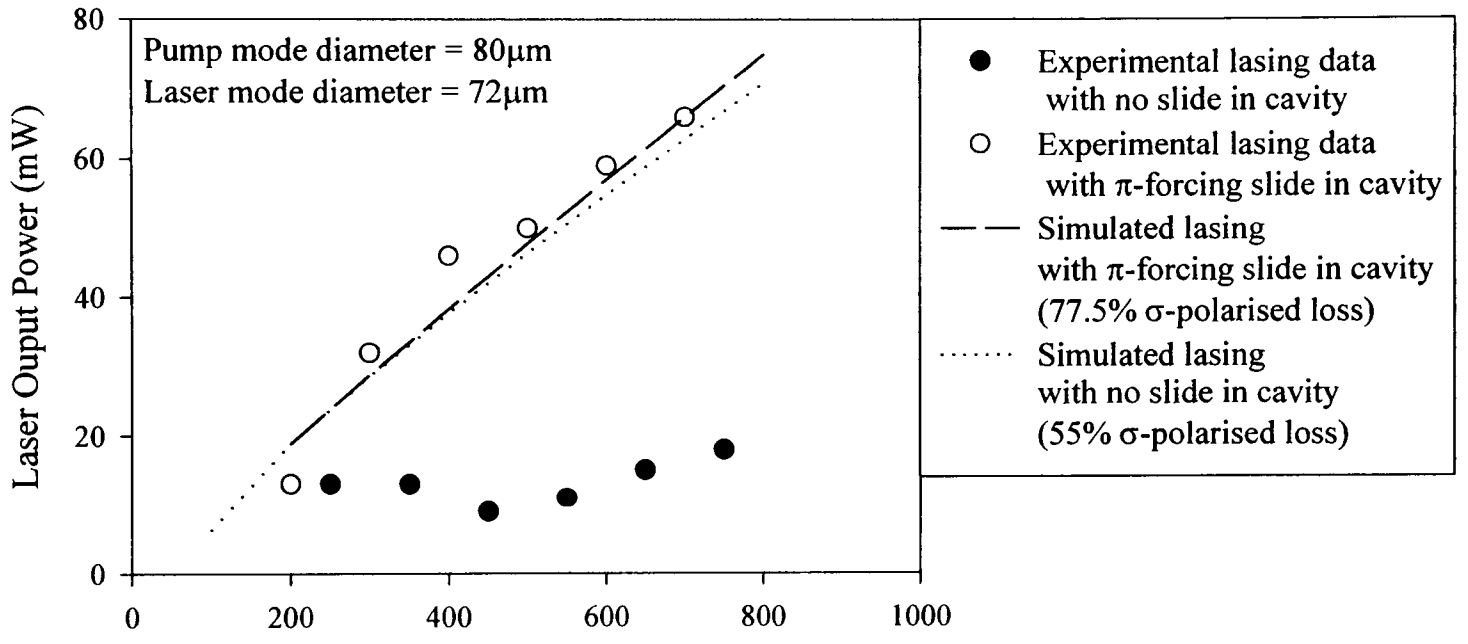


Figure 3.42 shows the simulated slope efficiencies for Ce:LiLuF lasing in a prism tuned cavity, tuned to 327 nm with 55% σ-biased loss and 77.5% σ-biased loss (representative of a slide in the cavity forcing π-polarised lasing). The crystal temperature was assumed to be ~0°C and the pump mode diameter used was 80 μm.

The laser pulses for the cavity with no polarisation biased loss and for the π-forced cavity are shown in Figure 3.43. The laser pulses predicted by the laser model, with no polarisation loss bias in the cavity, were similar to those measured experimentally (shown in Figure 3.22), with the build up times approximately equal (~10 ns) for both polarisations, as was seen in the experimental results, where the build up time was also ~10 ns. The σ-polarised, 327 nm laser pulse was found similar in pulse length to that seen experimentally whilst the π-polarised pulse was found to be shorter than the experimentally measured pulse length. The simulated π- and σ-polarised pulse lengths were 6 ns and 3 ns compared to the experimentally determined π- and σ-polarised laser pulse lengths of 12 ns and ~5 ns respectively. The right hand figure shows the laser pulse predicted by the laser model with a π-forcing slide placed in

the laser cavity. As can be seen, in this cavity there was no σ-polarised, 327 nm laser output present.

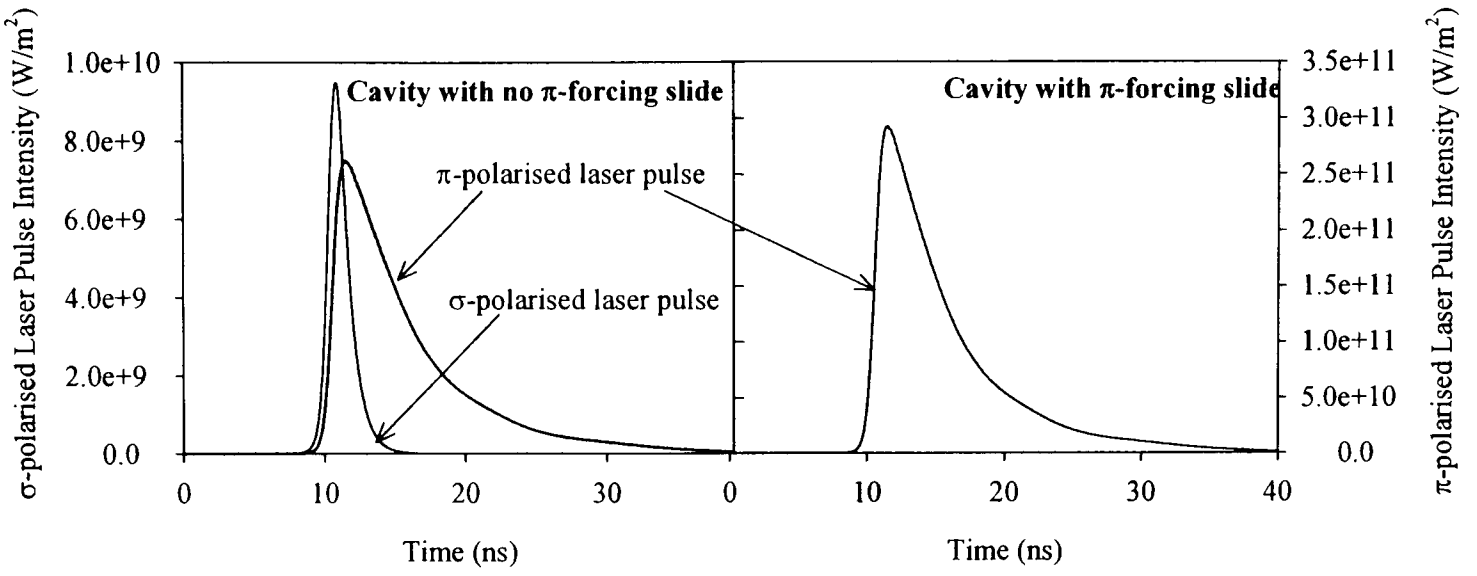


Figure 3.43 shows the simulated laser output pulses from the prism tuned Ce:LiLuF laser cavity, with a 90% output coupler and the crystal temperature of ~0°C. The cavity was tuned to 327 nm, with and without a σ-polarised biased loss introduced as specified.

In the simulated prism-tuned cavity lasing at 327 nm, the maximum percentage change induced by the presence of the π-forcing slide was only ~7%, corresponding to an increase from ~70 mW of output power with no slide in the laser cavity to 75 mW with the slide in the cavity. Experimentally the percentage change induced by the introduction of the π-forcing slide into the cavity was ~300%. Although the change in output power with the introduction of the σ-biased loss into the cavity was not as dramatic as was found experimentally, the behaviour does follow the experimental behaviour to a good extent. In order to check that the increase in σ-polarised loss induced by the slide was not under-estimated, resulting in the underestimation of the change in output power on addition of the σ-biased loss into the cavity, the change in laser output with σ-biased intra-cavity loss was simulated. These results are shown in Figure 3.44. These results show that, in the simulations described above, the amount of σ-biased loss introduced into the laser cavity did not coincide with the largest change in total output power possible from the system. In fact the maximum change in output power that could be induced by the π-forcing slide was 70% with a 43% increase in loss from 15% to >50% σ-polarised loss.

The presence of fluctuations in the laser output observed experimentally may contribute to the discrepancy between the experimentally determined increase in laser output and that determined using the laser model. If no fluctuations were present it is possible that the laser

output with no polarisation-bias in the cavity may have been higher in general. If the fluctuations in the laser output caused the overall output in the unbiased cavity to be lower experimentally than the simulated laser output, better agreement between the slope efficiency, laser output and induced increase in laser output with the introduced σ-biased loss could be expected.

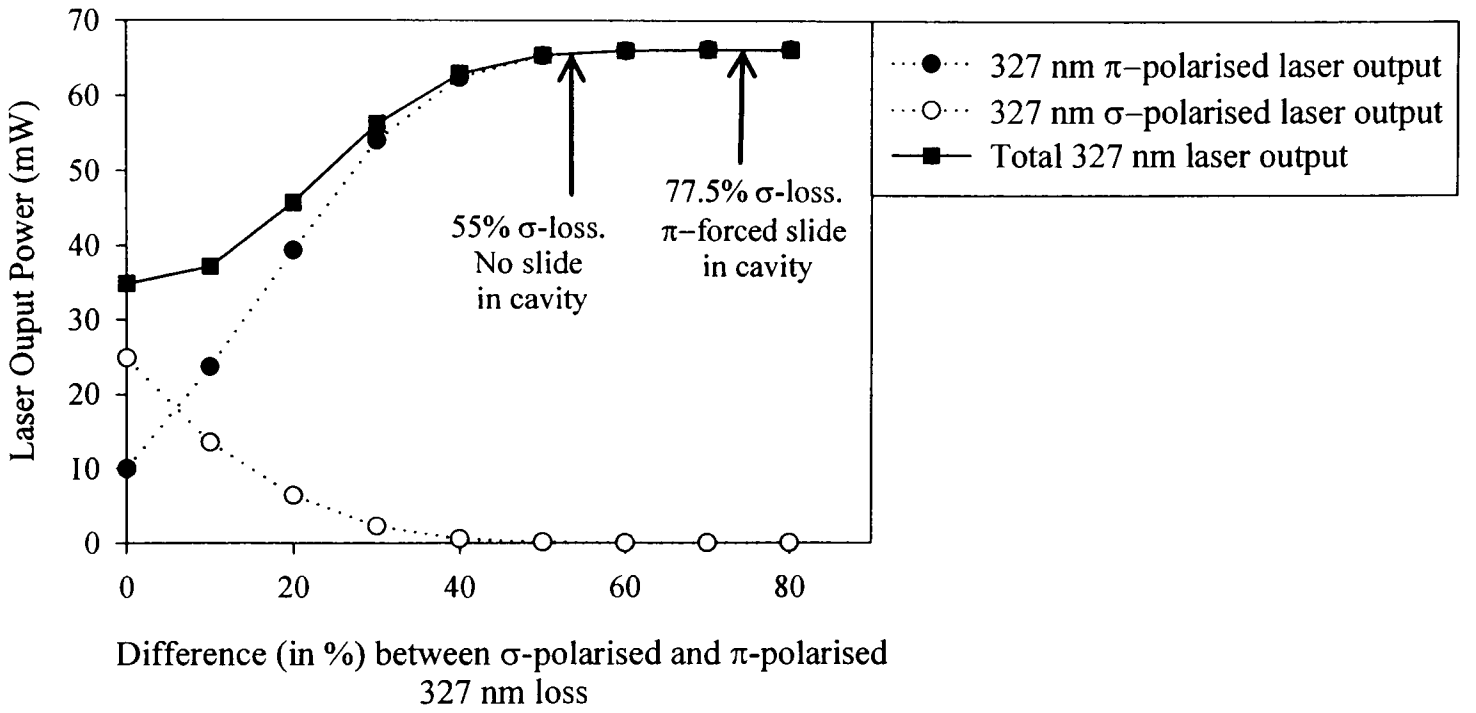


Figure 3.44 shows the simulated variation of laser output in Ce:LiLuF with σ-biased intra-cavity loss. The loss seen by the π-polarised 327 nm laser emission was 10%. The pump mode diameter and laser mode diameter used for these simulations was 80 μm and 68 μm respectively.

3.6 Discussion

This discussion is set out such that the various features of the laser experimental results from §3.2, §3.3, and §3.4 are explained as far as possible, with the aid of the simulated results from §3.5. There are four main sections in this discussion; first, the dependence of the lasing on the laser cavity used is discussed. Second, the temperature dependence of the laser efficiency of Ce:LiLuF is discussed. Third, the origin of the multi-component laser output of Ce:LiLuF with the M302, M303 and prism-tuned laser cavities is discussed. And finally the presence of the fluctuations in the laser output in certain conditions is discussed.

3.6.1 Dependence of Ce:LiLuF lasing characteristics on the laser cavity used

Recall that the threshold of lasing at 309 nm with the 80% output coupler was found to be much higher for the 4.5 cm long, 0.25 m ROC high reflector cavity (300 mW) than for the 9 cm long, 0.1 m ROC high reflector cavity (50 mW). The main difference between the two laser cavities used in §3.2.2 is that the laser mode size in the crystal, and hence the fraction of the laser mode that is interrogating the pumped volume, is different in each cavity. The position of the output coupler in both cases was close to the crystal, thus the laser mode size in the crystal was approximately equal to the laser mode size on the flat output coupler (using a half-symmetrical cavity Gaussian approximation). The ratio of the cavity length to ROC of the high reflector in the 0.25 m ROC cavity (0.18) was small compared to that of the 0.1 m ROC cavity (0.9). For the half-symmetric resonator cavity the spot size on the flat mirror is given by equation 3.9, where g is given by $g = 1 - L/R$, where L is the cavity length and R is the ROC.

$$\omega^2 = \frac{L\lambda}{\pi}\sqrt{\frac{g}{1-g}} \qquad 3.9$$

Using equation 3.9, the laser mode size on the output coupler of the 0.1 m ROC cavity was found to have a diameter of 110 μm, which is almost half that of the 0.25 m ROC cavity where the diameter was determined to be 194 μm. It is interesting to find that, in both cavities, the laser mode spot diameters inside the laser crystal predicted, using equation 3.9, are much larger than the estimated pump mode diameter in the crystal of 66 μm. This is most likely to be the origin of the 50% pumping efficiency.

From these theoretically determined spot sizes some insight into the laser threshold dependence on the cavity used can be gained. It can be inferred that in the 0.25 m ROC high reflector cavity, the laser mode size was much larger than the pump mode size in the crystal, thus only the central portion of the laser mode was amplified. Since the whole laser mode experiences loss at the output coupler and (in the 0.25 m ROC high reflector cavity) only a small central portion of the laser mode is amplified, the gain required to overcome the loss experienced by the whole laser mode is high. This would result in the higher lasing threshold seen experimentally for the 0.25 m ROC high reflector cavity. The 0.1 m ROC high reflector cavity on the other hand had better mode matching allowing more of the gain region to be interrogated by the laser mode, thus resulting in a much lower threshold.

When the output coupler was moved closer to the laser crystal in the 0.25 m ROC laser cavity, a decrease in the lasing threshold from 400 mW to 300 mW was observed. Initially the decrease in threshold was attributed to the decrease in laser mode size resulting from the movement of the output coupler, giving better mode matching. However the calculated change in laser mode size determined was too small to induce such a decrease in lasing threshold (<2% decrease in mode area). Another possible origin of the decrease in threshold may have arisen from the quasi-longitudinally pumped nature of the laser. In this cavity, the laser threshold would have been sensitive to the angle between the laser mode and the pump mode, but this sensitivity would have been reduced if the output coupler was placed close to the laser crystal, as alignment of the laser mode and pump mode was easier with the small output coupler-crystal distance. On the other hand, some double pass pumping may be occurring with the laser crystal close to the output coupler. Such double pass pumping would have a better overlap with the laser mode when the output coupler was closer to the laser crystal, possibly accounting for the lower threshold.

The roll off seen in the laser output with the 0.25 m ROC high reflector cavity in Figure 3.6 may be indicative of the saturation of the pump absorption at pump powers above 500 mW. Saturation is therefore more evident in the 0.25 m ROC high reflector cavity because the output power of 120 mW was achieved with >800 mW of pump power compared to the 0.1 m ROC high reflector cavity where only 500 mW was required to achieve 120 mW of output power. Had the 0.1 m ROC cavity laser output been monitored above 500 mW, it is suspected that saturation would be evident for this cavity too.

3.6.2 Temperature dependence of the laser output in Ce:LiLuF

In Chapter 2, the temperature dependence of small-signal gain in Ce:LiLuF was discussed in detail. The temperature dependence was proposed to arise from a decrease in excited-state absorption with decreasing temperature. This temperature dependent excited-state absorption was tentatively thought to arise from colour centres. For the lasing at 309 nm, with the 80% output coupler, a 70% increase in the laser output was found when the crystal temperature was decreased from 22°C to -3°C. The increase in percent depletion and decrease in build up time with decreasing temperature, shown by the fluorescence in Figure 3.9, does suggest the 309 nm, π-polarised σ_{EFF} increased with decreasing temperature, corresponding to a decrease in σ_{ESA} or σ_{EM}, or the intra-cavity loss decreased with decreasing temperature. The decrease in residual inversion during the laser pulse points specifically to an increase in σ_{EFF} or a decrease in intra-cavity loss as opposed to an increased pumping efficiency.

Neither the intra-cavity loss nor the spontaneous emission cross-sections (σ_{EM}) are thought to be temperature dependent, leaving only the ESA cross-section at the laser wavelengths to vary with temperature. (The spontaneous emission cross-sections were considered to be independent of temperature as the fluorescence lifetime has been found to have no dependence on temperature between -3°C and 40°C (McGonigle *et al.* 2001b)). Using the change in σ_{ESA} determined from the gain simulations for a decrease in temperature from room temperature to -3°C, in Chapter 2 ($\Delta\sigma_{ESA}=0.15 \times 10^{-18}$ cm^2), a change in laser output of only 3% was found (see Figure 3.36) as opposed to the 70% increase in laser output observed experimentally. In fact, in order to simulate the change in laser output with temperature, whilst maintaining the pump and laser mode sizes used to simulate the low temperature laser output, a $\Delta\sigma_{ESA}$ of 2×10^{-18} cm^2 was required. This gave excellent agreement between the experimental and simulated laser outputs as shown in Figure 3.36.

The origin of the discrepancy between the excited-state absorption cross-section determined using the gain simulations in Chapter 2 and that required to model the temperature dependence of the laser output at 309 nm is not known. There are various possibilities though, such as a temperature dependent excited-state absorption mechanism which is also dependent on the laser mode intensity. For instance, should colour centre formation be induced by ESA at the laser wavelengths and if these colour centres are absorbing at the laser wavelengths, extra losses will be incurred in the presence of lasing compared to when low probe intensities are present, such as during the gain measurements. This type of loss mechanism may not have been obvious in small-signal gain measurements, and as such the temperature induced $\Delta\sigma_{ESA}$ determined by the gain measurements would be smaller than that determined during lasing.

3.6.3 Presence of multiple polarisation and wavelength components in the laser output of Ce:LiLuF with M302, M303 and prism-tuned cavity

The lasing results seen in Ce:LiLuF with the M302, M303 and prism-tuned laser cavities are very unusual in several ways. Firstly, there is more than one emission wavelength and more than one emission polarisation in the laser output. Secondly, with certain output couplers (M302 and M303) the slope efficiencies appear to change with pump power. Thirdly there is a temperature dependence of the laser output powers as well as a temperature dependence of the composition of laser output. There are many different factors which govern the presence or absence of lasing at a specific wavelength, such as the effective gain cross-section, σ_{EFF}, the intra-cavity loss and the pump intensity. In each cavity investigated in this chapter these factors are different for the different wavelengths and polarisations, thus the coupled nature and competition effects between the laser modes are different in each cavity.

Using the laser model, the behaviour of lasing with the M302, M303 and prism-tuned cavities was simulated to a good accuracy. In these simulations the σ_{EM} and σ_{ESA} values determined in Chapter 2 were used, as shown in Table 3.5. The laser model included the different competition effects in the laser mode resulting from the different σ_{EFF} and cavity losses; thus, the similarities between the experimental and simulated laser behaviour add to the validation of the cross-sections determined in Chapter 2. Overall the unusual lasing behaviour of Ce:LiLuF reported in this chapter is thought to result from the similarity between the σ_{EFF} for the π- and σ-polarised 327 nm and π-polarised 309 nm lasing wavelengths. The actual origin of this behaviour is explicitly discussed in this section.

Table 3.5 shows a summary of the emission, excited-state absorption and effective cross-sections for Ce:LiLuF at low temperatures are shown for 327 nm (σ- and π-polarisations) and π-polarised 309 nm.

	309 nm; π-polarised	327 nm; π-polarised	327 nm; σ-polarised
σ_{EM} ($x10^{-18}$ cm^2)	6.7	3.7	6.8
σ_{ESA} ($x10^{-18}$ cm^2)	0	0	2.4
σ_{EFF} ($x10^{-18}$ cm^2)	6.7	3.7	4.4
Small-signal Gain Coefficient at low temperatures for a pump power of 400 mW (in cm^{-1})	29	17	20

Intuitively the lasing behaviour observed in Ce:LiLuF makes sense, except that, in the simplest case, one would expect only one laser mode to exist at one time. An example of the intuitive understanding of the laser behaviour in Ce:LiLuF is given by the variation of the slope efficiencies with pump power seen in the M302 laser cavity. To recap the lasing behaviour with the M302 output coupler cavity, found experimentally: the M302 output coupler had a very low transmission loss through the output coupler at 327 nm (8%) and a relatively large transmission loss though the output coupler at 309 nm (46%). At low pump powers 327 nm, σ-polarised and π-polarised components were present in the output. At pump powers greater than 450 mW in addition to both 327 nm components in the output, a 309 nm π-polarised component was also seen. The build up times of both σ-polarised and π-polarised

components of the laser output were very similar (~1 ns difference). At high powers this 309 nm component fluctuated in intensity and was characterised by a very short laser pulse (FWHM~3 ns). The 327 nm laser pulse at high pump powers was characterised by a much longer pulse length (FWHM~8 ns). At low temperatures the slope efficiency was found to increase noticeably above pump powers of ~450 mW from 6% to 31%.

Intuitively it is obvious from the composition of the laser output at low pump powers and high pump powers that the lasing at 309 nm has a much higher threshold than the 327 nm lasing. This is expected with the high reflectivity of the output coupler at 327 nm (92%) and the relatively low reflectivity of the output coupler at 309 nm (54%). The presence of both σ- and π-polarised 327 nm lasing at low pump powers is likely to be due to the similar gain cross-sections of 4.25×10^{-18} cm^{-2} and 3.74×10^{-18} cm^{-2} respectively. The variation in the slope efficiency with pump power is very likely to arise from the different thresholds for 327 nm lasing and 309 nm lasing, as the steeper slope above 500 mW coincides with the presence of 309 nm in the laser output. Thus above 500 mW both the 327 nm and 309 nm lasing contribute to the laser output causing an increase in laser efficiency.

Intuition however cannot explain the presence of the different polarisation and wavelength oscillations occurring simultaneously in the laser, nor can intuition explain the difference in the laser pulse shapes and timings. In fact an important clue to understanding the lasing with the M302, M303 and prism-tuned laser cavities lies in the laser pulse shapes. Remembering that in all three of these cavities which give mixed laser outputs, there was a short laser pulse coincident with a longer laser pulse component of the laser emission. The short laser pulse and long laser pulse in all situations have an almost identical build up time. These build up times suggest that early on there is a high enough gain to allow lasing at 327 nm (in both polarisations) as well as at 309 nm (π-polarised), in the case of the M302 and M303 output couplers for example, even though the losses seen by each polarisation and wavelength may be different. This behaviour is indicative of the gain switched nature of the lasing in Ce:LiLuF.

Using the experimental pump pulse to simulate lasing in Ce:LiLuF, the laser output was found to resemble the experimental output closely, including the presence of a broad and narrow laser pulses in the output, both of which had similar build up times. Thus in order to uncover what was taking place during lasing, the laser model, which is known to predict the laser behaviour very well, was used with a very basic simplification. A top-hat pump pulse was used to replace the experimental pump pulse in the laser model, with an intensity equal to the peak intensity of the pump pulse (~1×10^{12} Wm^{-2}) and a pulse length of ~30 ns.

For simplicity the M303 output coupler cavity (R=9% at 309 nm and R=70% at 327 nm) results are described first as these results show the lasing behaviour most clearly. The laser output pulses are shown in Figure 3.45, in which the laser output pulses are all on the same scale and the *5d* population and pump pulse have been adjusted for convenience. Figure 3.45a) clearly shows the gain switching behaviour. The gain switching can to be seen to be very damped in this laser, with only one main spike in the *5d* population followed by very small relaxation oscillations. The 327 nm, σ-polarised laser pulse shows an intense sharp peak at the beginning of the laser pulse which then dies down to a stable intensity after ~10 ns. The stable intensity of the laser output pulse coincides with a stable 5d population which is therefore the threshold 5d population for 327 nm, σ-polarised lasing. This threshold inversion population is ~5 times lower than the peak inversion population. Very low intensity 327 nm π-polarised and 309 nm π-polarised laser peaks can also be seen at ~10 ns showing that the gains resulting from the very high 5d population at the population spike were sufficient that these outputs were able to build up before the gain was quenched by the 327 nm, σ-polarised lasing. The relative pulse energies are shown under each figure for comparison. This π-polarised, 327 nm lasing would not occur without the *5d* population spike, as the 327 nm, π-polarised effective gain cross section is smaller than the 327 nm, σ-polarised effective gain cross-section, and the losses seen by both polarisations are equivalent. This means the threshold population inversion would be high enough to sustain the σ-polarised lasing but too low to sustain the π-polarised lasing. In a similar manner, the 309 nm, π-polarised effective gain cross-section is larger than the 327 nm, σ-polarised cross-section but the losses seen by the 309 nm emission are much larger due to the low reflectivity of the output coupler at 309 nm (R=9%) compared to 327 nm (R=70%). This means the threshold population inversion required to sustain lasing at 309 nm would be much higher than that required to sustain 327 nm, σ-polarised lasing.

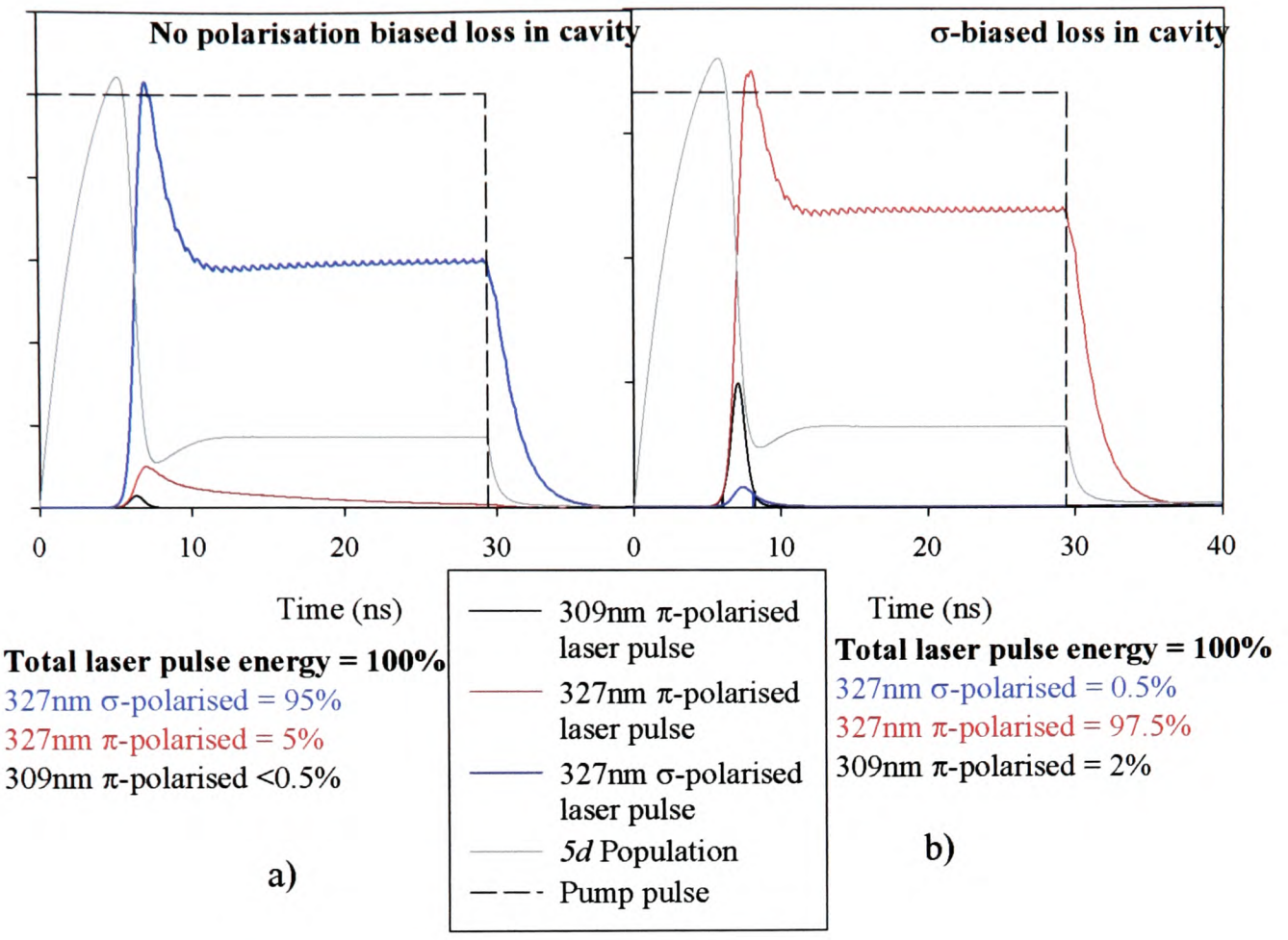


Figure 3.45 shows the simulated output of the M303 output coupler cavity with a top hat pump pulse with a pump power of $1x10^{12}$ Wm^{-2} with a) no polarisation-biased loss in the cavity and b) with a loss in the cavity such that π-lasing is forced. The crystal simulated was cooled to ~0°C.

Simulation results from the π-forced, M303 laser cavity are shown in Figure 3.44 b). In this cavity the 327 nm, π-polarised loss is much less than the 327 nm, σ-polarised loss (due to the slide in the cavity) and 309 nm, π-polarised loss (due to the low reflectivity of the output coupler at 309 nm). Therefore although the effective gain cross-section at 327 nm is smaller for the π-polarisation than the σ-polarisation and also smaller than the 309 nm, π-polarisation effective gain cross-sections, the lasing is predominantly at 327 nm and π-polarised.

Figure 3.46 shows in more detail the lasing behaviour with the M303 π-forced laser cavity. Shown in the figure, by the vertical lines, are the peaks of the laser output pulse, which represents the point at which the net round-trip gain is equal to one, in other words where the gain is equivalent to the intra-cavity loss. The horizontal lines show the actual *5d* population existing when the net round-trip gain is unity for 309 nm and 327 nm. The 309 nm threshold *5d* population is much higher than the π-polarised, 327 nm threshold *5d* population and it is thus obvious that the 309 nm lasing threshold is only reached because of the presence of the *5d* population spike. It is also worth noting that the threshold *5d* population causing the roll

over of the 327 nm, π-polarised laser pulse at its peak is the same as that required to sustain the laser pulse after 10 ns, as expected.

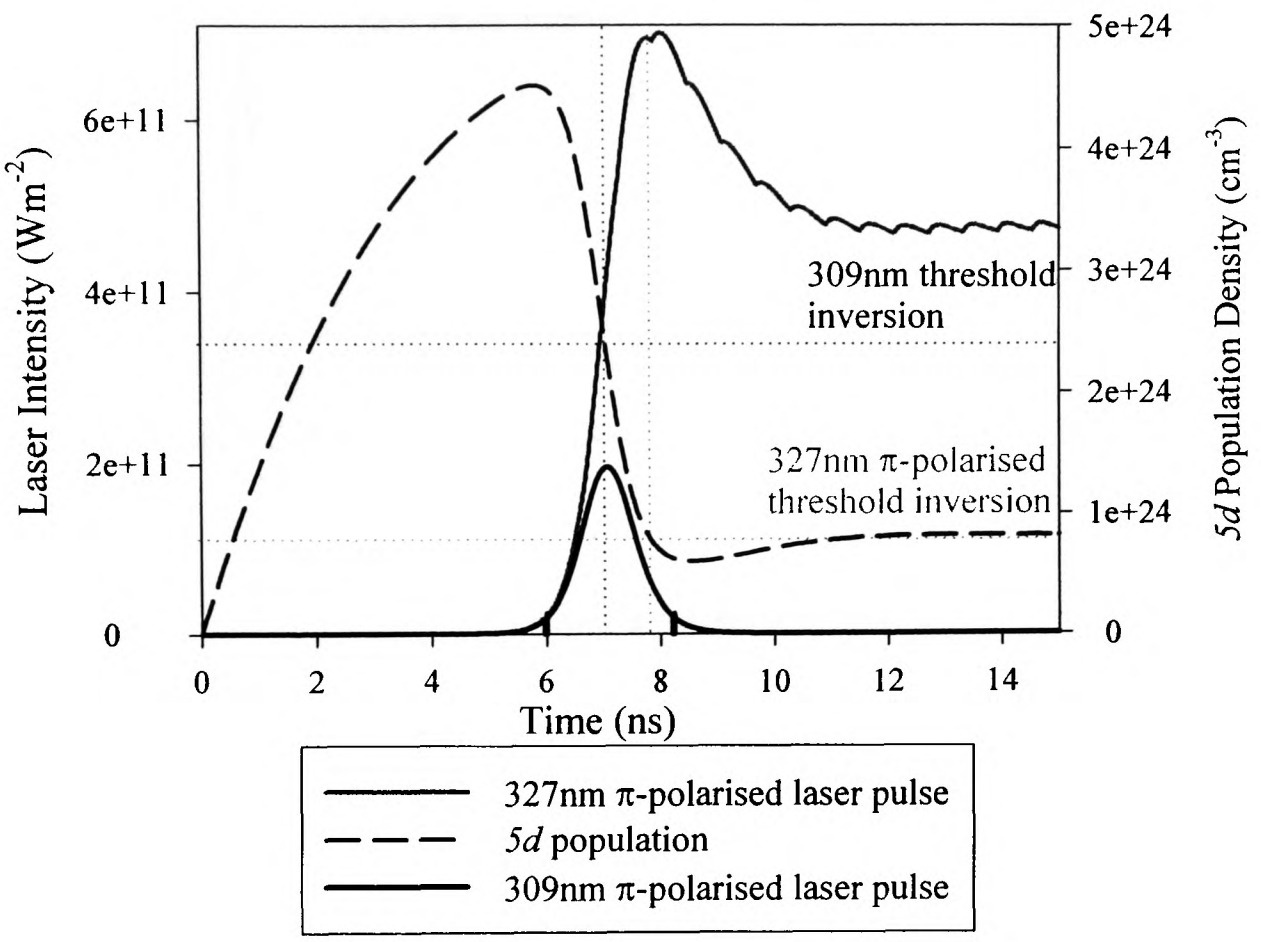


Figure 3.46 shows a detailed view of the M303 output coupler cavity laser output simulated with a top hat pump pulse with a pump power of $1x10^{12}$ Wm^{-2} with a loss in the cavity such that π-lasing is forced. The crystal simulated was cooled to ~0°C.

The simulated results for the M302 output coupler cavity, using the top hat pump pulse are shown in Figure 3.47. The outputs using both a high intensity pump pulse and low intensity pump pulse are shown. The simulated results for the prism-tuned laser cavity, tuned to 327 nm, both with no polarisation bias in the laser cavity and with the π-forcing slide in the cavity are shown in Figure 3.48. The laser output pulses are all on the same scale, with the pump pulses and *5d* populations scaled for convenience. In Figure 3.47 b), in the case of the 309 nm, π-polarised lasing, the lasing starts as soon as the gain overcomes the large output coupler loss (46%). The 309 nm laser pulse grows very fast (due to the high gain at 309 nm) during the initial pumping, once threshold inversion is reached the laser field increases rapidly. Meanwhile the lower gain at 327 nm (π-polarised) results in a slower growth of the 327 nm laser pulse. This laser field has a longer build-up time, with the build-up limited by the time required for the gain to overcome the losses, but overall the lower output coupler loss seen by the 327 nm laser field (8%) results in a low threshold for the 327 nm, π-polarised

lasing thus this lasing eventually dominates. Figure 3.47 shows explicitly the dynamic gain competition effects present in this M302 laser cavity.

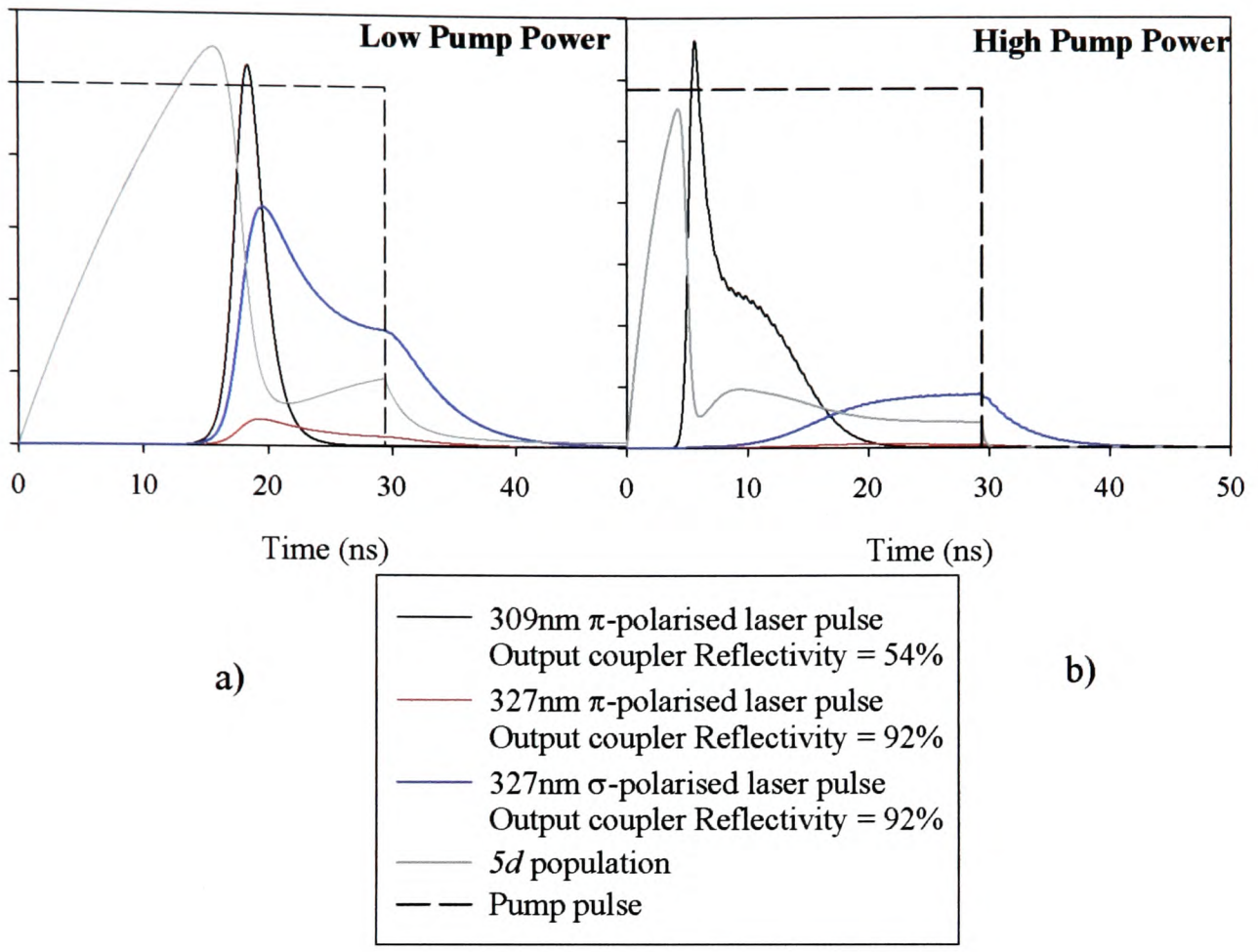


Figure 3.47 shows the simulated output for the M302 output coupler cavity with a top hat pump pulse with a) high pump intensity ($1x10^{12}$ Wm^{-2}) and b) low pump intensity ($1x10^{12}$ Wm^{-2}), with the crystal cooled to ~0°C. The laser output pulses are all on the same scale, the *5d* population and pump pulse have been scaled for convenience.

Using the simulated results from all three Ce:LiLuF cavities various generalisations can be made with regard to the effect of gain competition on the laser output. Firstly that, in general, the laser output that would occur if no spike in the *5d* population, in all three cavities, would be the longer laser pulse seen in the gain switched cavity. For instance in the M303 cavity with no polarisation bias (shown in Figure 3.45a)), the 327 nm, σ-polarised laser output has the long laser pulse thus with no gain spiking the 327 nm, σ-polarised lasing would be dominant. With the π-forced lasing in the M303 cavity as seen in Figure 3.45b) the longer laser pulse corresponds to the π-polarised, 327 nm laser pulse, which is the preferred laser mode for this laser cavity. The laser pulses arising purely from the spike in the upper *5d* population tend to be shorter, shown most obviously by the 309 nm laser pulse in Figure 3.47 with the M302 laser cavity. The reason for this short pulse is because the gain can only overcome the intra-cavity losses whilst the *5d* population spike is greater than the threshold

population inversion for 309 nm lasing. The gain in the short pulse laser modes is high, thus the laser mode grows quickly and the upper population is depleted equally quickly, causing these laser pulses to be short. The pulse length dependence of the experimentally measured laser pulses are in excellent agreement with these generalisations.

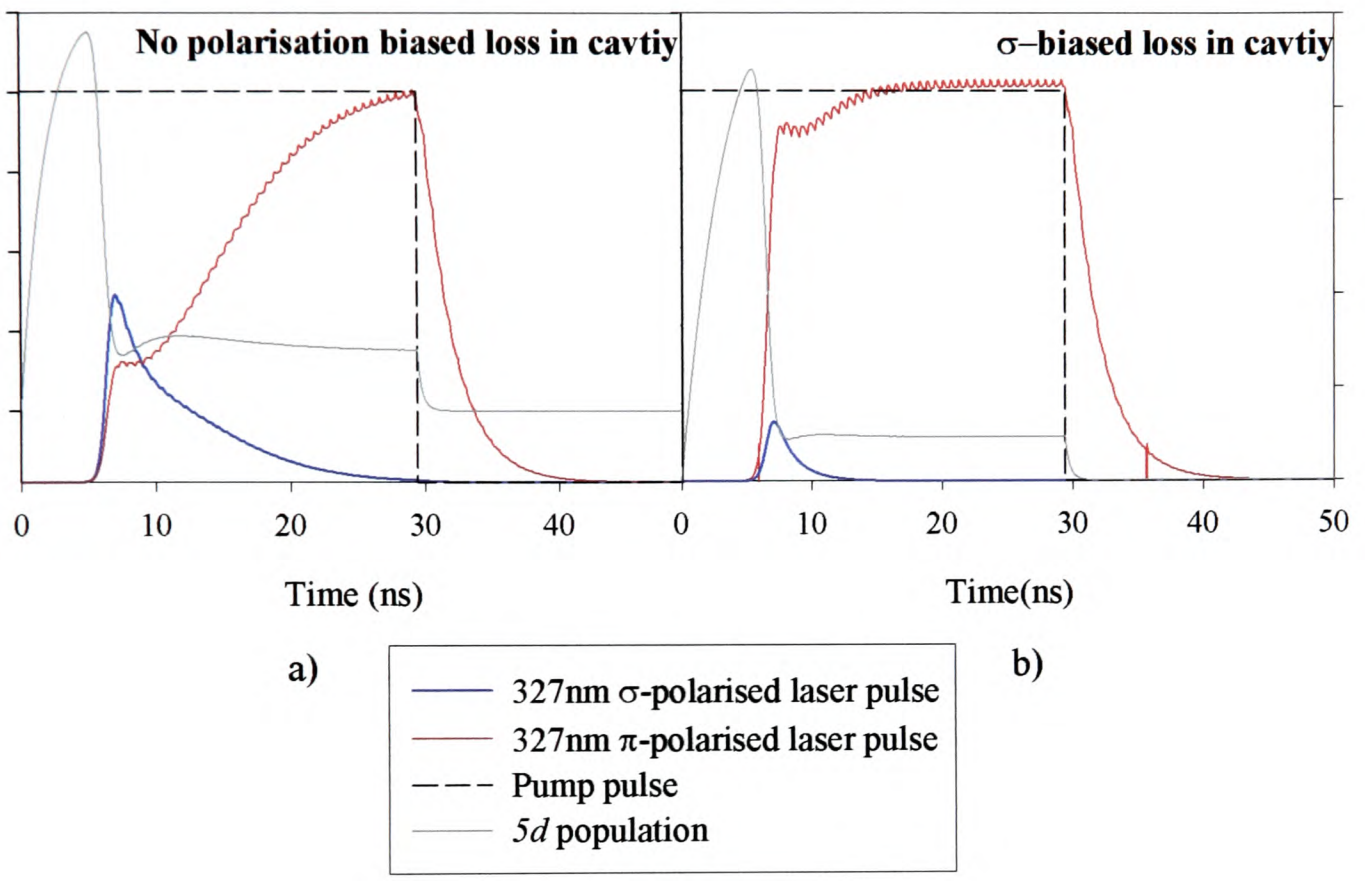


Figure 3.48 shows the simulated output from the prism tuned laser cavity, tuned to 327 nm, with a top hat pump pulse with a pump power of $1x10^{12}$ Wm^{-2} with a) no polarisation-biased loss in the cavity and b) with a loss in the cavity such that π-lasing is forced. The crystal simulated was cooled to ~0°C. The laser output pulses are all on the same scale, the 5d population and pump pulse have been scaled for convenience.

The change in slope efficiency with pump power seen in both the M302 and M303 laser results seen experimentally also arises from the dynamic gain competition effects. The height of the population inversion spike increases with increased pump power, due to the higher peak pump intensity and, as a result, the gain experienced by the each laser component increases. In the M302 output coupler cavity for example, the 327 nm, σ- and π-polarised lasing components overcome their lower losses at lower pump powers. The 309 nm lasing component, however, requires a higher gain spike to overcome its high cavity losses, thus 309 nm lasing only occurs with pump powers above 450 mW. Once 309 nm lasing is above threshold the intensity of the laser emission is high because of the high effective

cross-section, thus the high laser efficiency, increasing the overall lasing efficiency at higher pump powers.

3.6.4 Fluctuations in the laser output in the presence of σ-polarised 327 nm lasing

The laser output with the M302 output coupler cavity (R=54% at 309 nm and R= 92% at 327 nm) was found to fluctuate increasingly with increasing pump power. In the case of the M302 output coupler the fluctuations are coincident with the presence of a narrow 309 nm laser pulse in the laser output. The M302 cavity output showed the laser peak intensity to fluctuate by ~14% for the π-polarised output and ~5% for the σ-polarised output for a pump power of ~800 mW (as shown in Figure 3.11).

In the prism-tuned cavity, tuned to 327 nm, the fluctuations are found to increase with decreasing temperature. The fluctuations in prism-tuned output were found to be coincident with the presence of a narrow σ-polarised 327 nm laser pulse in the output. Experimentally the peak laser intensity was found to fluctuate by ~20% for the σ-polarised output and ~50% for the π-polarised output for a pump power of ~500 mW, as shown in Figure 3.23. In both cases the fluctuations became more prominent as the laser mode arising from the gain spike became large. Thus, on the one hand (M302 cavity) it is the broad pulse emission which is fluctuating and on the other hand (prism-tuned cavity) it is the narrow pulse emission which is fluctuating.

The reasons governing which laser mode fluctuates more and why the fluctuations occur is unclear. The fluctuations may arise from the competition effects between laser modes and are possibly the result of changes in the competitive effects arising from pulse to pulse variation of the pump pulse with time. A change in the pump peak intensity, pump beam quality or pump pulse length may result in such variations. What is known is that the laser output would be most sensitive when the pump power is close to the threshold pump power, because if the pump power is just below threshold no lasing would occur, and if it is above threshold, lasing will occur, thus small fluctuations in the pump will result in a switching on or off of the laser at that wavelength and polarisation resulting in a noticeable fluctuation in the laser output.

Fluctuations resulting from such pump dependence may be more prominent for the laser output components arising only from the gain spike, because the height of the gain spike will be very dependent on the pump pulse intensity, length and beam quality. The fluctuations are coincident with more laser output being due to the narrow pulse laser mode, however the expectation that the laser pulse resulting from the gain spike would fluctuate more does not fit

the experimental results in both cases. In the case of the M302 laser cavity the 309 nm, π-polarised is the laser pulse resulting from the gain spike and it is also found to fluctuate more than the 327 nm, σ-polarised peak. Thus this agrees with the dependence of the laser peak intensity on the pump sensitive gain spike. For the prism-tuned cavity, the π-polarised, 327 nm peak intensity was found to fluctuate more than the σ-polarised peak intensity, but in this case the highly fluctuating laser pulse is not the laser pulse resulting purely to the gain spike, but rather the broad 327 nm, π-polarised pulse.

An explanation of the fluctuations in the laser output, with possibly more substantial evidence, can be gained from a closer look at the simulations results shown in Figure 3.48a) for the prism-tuned cavity, tuned to 327 nm. The dip in the π-polarised pulse intensity at ~10 ns suggests the energy of the π-polarised output pulse may be highly sensitive to the depletion induced by the σ-polarised laser pulse. This depletion may turn off or significantly delay the π-polarised pulse with small changes in the σ-pulse energy. This would result in more pronounced fluctuations in the π-polarised pulse energy as was seen experimentally. In fact, recall the prism-tuned output pulse shapes shown in Figure 3.22, where the two extremes of the fluctuations are shown. In the output with the low π-polarisation content, the π-polarised laser pulse has a dip in the laser output at ~14 ns, probably arising from the quenching of the inversion by the σ-polarised emission. In the output with the high π-polarisation content, this dip is not seen and the build up of both pulses is slightly longer. A comparison of left hand figure in Figure 3.22 and the left hand figure in Figure 3.48 shows a striking similarity of the basic lasing features, in particular the presence of a dip in the π-polarised laser pulses. Since the experimental laser pulses of the fluctuation extremes show mainly a change in the shape of the π-polarised laser pulse, this supports the case that the π-polarised pulse energy is influenced by small changes in the quenching of the population inversion by the σ-polarised pulse, resulting in fluctuations in the π-polarised output.

In a similar manner as the prism-tuned cavity, the tail of the 309 nm, π-polarised laser pulse in the output of the M302 laser cavity, resulting from the overshooting the threshold a second time, may cause fluctuations in the π-polarised pulse, depending on the extent of the overshoot. Jitter in the pump pulse length will change the extent of build up of the population after the initial *5d* population spike, which in turn will affect the 309 nm pulse energy. Thus, with this basic evidence, it is suggested that the fluctuations in the laser output are dependent on the gain switched nature of the lasing. The competition effects between each mode vary from pulse to pulse making the fluctuations in the output a feature of the gain competition for multi-wavelength and multi-polarisation lasing in gain switched Ce:LiLuF lasers.

3.6.5 Conclusions

In this chapter the results of a detailed investigation into the lasing behaviour in Ce:LiLuF have been presented. Experimentally one of the most interesting outcomes of the results was that, overall, the presence of σ-polarised, 327 nm photons in the laser field was found to be detrimental to the total laser output. The introduction of a σ-biased loss into the cavity was found to stop most of the 327 nm, σ-polarised lasing, and as such resulted in an increase in the total laser output obtainable from the laser. This was particularly useful in the prism-tuned cavity as, by cooling the laser crystal to low temperatures, the laser output could be increased over the whole tuning curve, including at 327 nm, which was not possible before. The decreased lasing efficiency caused by the 327 nm, σ-polarised laser field is thought to be solely due to the high ESA cross-section at this wavelength and polarisation.

With the aid of simulations from a computer based laser model, many of the questions posed by the experimental results have been answered. In particular, the presence of a multiple component output from Ce:LiLuF under certain cavity conditions was proved to be present because of the gain switched nature of the lasing.

There are some limitations of the laser model which have yet to be overcome, such as the difference between the depletions predicted by the laser model and those measured experimentally. Other questions still remain as to why the laser model did not simulate the lasing behaviour, in some cases, as close to the experimental laser behaviour as desired. In general however simulated laser behaviour of Ce:LiLuF was in excellent agreement with the experimental laser behaviour, firstly reinforcing the accuracy of the effective gain cross-sections determined in Chapter 2, and secondly, allowing a better understanding of the anomalous Ce:LiLuF lasing behaviour.

[4] Narrow-Bandwidth Lasing in Ce:$LiLuF_4$

4.1 Introduction

In previous work in the Clarendon Laboratory a frequency-doubled Nd:YAG pumped dye laser was built specifically for use in the detection of tropospheric hydroxyl (OH) radicals (Evans and Webb 1994; McGonigle *et al.* 2002). Monitoring the concentration of OH in the atmosphere is an extremely useful tool for atmospheric chemists since the oxidizing capacity of the atmosphere is determined primarily by the concentration of OH radicals in the atmosphere. Because of the high reactivity of the OH radicals, the concentration of OH in the atmosphere is as low as 10^6 radicals/cm^3, making measurements of the OH concentration in the atmosphere very difficult. Direct-absorption and laser-induced fluorescence (LIF) techniques (Holland *et al.* 1995) have been developed for the detection of OH and a number of research groups are currently working on the development of compact, lightweight and inexpensive lasers emitting 308 nm light (Barry *et al.* 2000; Corner *et al.* 2002). Such lasers could be used for the airborne monitoring of OH which has not been possible with the currently used bulky, heavy and relatively expensive dye laser systems. The initial motivation for working on Ce:LiLuF in the Clarendon Laboratory was to replace a frequency-doubled, narrow-bandwidth tunable dye laser with an equivalent all-solid-state cerium system lasing at 308 nm.

LIF involves laser excitation of OH near 308 nm (0-0 band) or near 282 nm (1-0 band). The subsequent fluorescence near 309 nm by the excited OH radicals is then detected and used as a measure of OH concentration. 308 nm is the preferred excitation wavelength, firstly because the absorption cross-section at 308 nm is 4 times larger than the 282 nm absorption cross-section. Secondly, the amount of ozone produced by photolysis at 308 nm is 29 times smaller than the amount produced at 282 nm. The production of ozone is undesirable for OH detection because the ozone reacts with water to produce OH radicals which results in an overestimation of the OH radical concentration. Using 308 nm as the excitation wavelength does however make the detection of the 309 nm fluorescence more difficult because of the close proximity of these wavelengths. The fluorescence signal can, nevertheless, be detected by gating a photon counter off, during the laser excitation and observing only the tail of the fluorescence (lasting 7 ns to a few hundred nanoseconds). To do this it would be obviously advantageous to have a short excitation pulse (few ns), thus allowing more of the fluorescence tail to be detected.

The limited fluorescence detection efficiency and low concentrations of OH in the atmosphere mean that only one in 10^4 emitted fluorescence photons are detected. To overcome the low signal-to-noise ratio, long integration times are required to achieve a decent signal. In the past the lasers used to excite the OH had low repetition rates (Hz) thus the integration times required were extremely long (of the order of minutes). The timescale over which the OH concentrations changes is of the order of 100 s, which makes these long integration times undesirable. Recently, however, high repetition rate lasers (kHz), such as the system used by Holland *et al.* (Holland *et al.* 1995) which had a repetition rate of 8.5 kHz, have made these integration times much shorter (<1minute) allowing more detailed investigations to be undertaken.

Near 308 nm there are a number of OH absorption peaks and in order to excite only one of these rotation-vibration lines, especially for direct-absorption measurements, the spectral bandwidth of the laser must be in the range of 3-5 GHz (~0.1-0.2 cm^{-1}).

In this chapter, the results of the initial investigations into the development of a narrow-bandwidth Ce:LiLuF laser, suitable for OH detection, are reported. This Ce:LiLuF laser was pulsed at 10 kHz and had a short pulse length (~10 ns) both of which make it ideal for atmospheric OH detection.

4.2 Methods of Narrowband tuning

In the past Ti:Sapphire and dye lasers have been the most attractive broadly-tunable lasers. Narrow bandwidth operation of dye lasers, in particular, has been thoroughly investigated by Duarte (Duarte and Piper 1981; Duarte and Piper 1982a; Duarte and Piper 1982b; Duarte and Piper 1984). These narrow-bandwidth dye lasers have been frequency-doubled to produce the desired UV wavelength for OH detection by Evans *et al.* (Evans and Webb 1994) who achieved laser output at 308 nm with output powers approaching 1W and UV bandwidths of less than 2 GHz. Narrow-bandwidth laser operation has been previously achieved in Ce:LiSAF with a linewidth of <0.1 nm (Pinto and Esterowitz 1997). In this laser two 266 nm pump beams were interfered within the Ce:LiSAF laser crystal, creating a dynamic sinusoidal gain grating within the laser crystal and as such a narrow bandwidth output results from the frequency selective properties of the gain grating, with tuning achieved by varying the pump beam intersection angle. This method of laser tuning is commonly referred to as distributed feedback laser action.

There are a variety of cavity designs that can be used to obtain narrow-bandwidth output from high gain laser systems such as the dye lasers. Such cavities generally use a combination of frequency-selective elements including prisms, diffraction gratings and tuning mirrors. These cavity designs are normally only useful in high gain systems as the losses incurred in these cavities are high. With such cavity designs, spectral bandwidths of < 0.001 nm (~1 GHz) can be achieved (Duarte and Piper 1981; Zhou 1984) which is required of the Ce:LiLuF for it to be useful in OH radical LIF measurements. In this chapter various cavity designs were investigated, based on a combination of prisms, gratings and mirrors available. Unfortunately a good quality UV etalon was not available at the times of these experiments. A basic description of these cavities, in which a combination of these elements is used, is given next.

Diffraction gratings are dispersive elements with a wavelength resolution which is directly dependent on the illuminated width of a grating. Increasing the length of grating illuminated therefore results in the ability to resolve a smaller difference in wavelength. There are various methods used to obtain a large illumination of a diffraction grating. One method is to increase the angle of incidence of the beam to the grating as described by Littman and Metcalf (Littman and Metcalf 1978), namely grazing-incidence grating cavities (shown in Figure 4.1a)). This method has a high loss off the grating and as such these cavities are usually used with a highly reflective mirror reflecting the zero order light back onto to the grating. These cavities can be used in an open cavity configuration, in which the output is taken from the grating non-zero order reflection. A closed cavity can also be used, in which the output is not

taken off the grating but rather through an output coupler. Both these open and closed cavity designs are described in detail by Duarte *et al.* (Duarte and Piper 1982b).

The other method of achieving a large illumination length on the grating is for the laser beam to be magnified before reaching the grating. This way the grating can be used in a less lossy Littrow configuration as shown in Figure 4.1b). The loss in these cavities is further reduced by using a grating blazed for the desired wavelength.

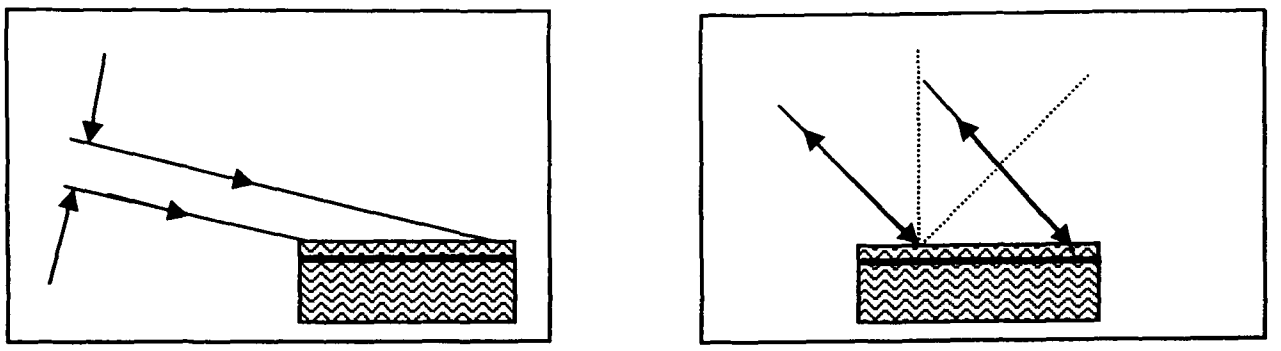


Figure 4.1 shows schematic diagrams of a) Littman and b) Littrow grating configurations.

Two such beam expansion methods include the use of anamorphic prisms or intra-cavity telescopes. The expansion factor of a prism is dependent on the angle of incidence of the laser beam, with the magnification factor increasing with increasing angle of incidence. The reflection losses of the incident surface of the prism on the other hand also increase with increasing angle of incidence. Thus, when using a prism as the beam expansion element (as shown in Figure 4.2a), the angle of incidence must be chosen such that the loss introduced by reflection off the prism surface is balanced with the magnification obtainable. In order to maximise the expansion while simultaneously minimising the cavity losses introduced by the prism, more than one prism is often used such that one face for each prism can be at Brewster's angle. Using multi-prism beam expanders (as shown in Figure 4.2b)), the magnification of the laser beam can be increased whilst using a smaller angle of incidence. This way, the reflection losses are smaller than they that would have been if the same magnification were to be obtained from a single prism. The theory of these prism expanders has been dealt with in detail by Duarte *et al.* (Duarte and Piper 1982a; Duarte and Piper 1983; Duarte 2000). A comparison of the grazing-incidence grating cavities and prism-expanded, Littrow grating cavities is reported by Duarte and Piper (Duarte and Piper 1982b). Another method of achieving beam expansion in a cavity is by using an intra-cavity telescope to expand the beam as shown in Figure 4.2c).

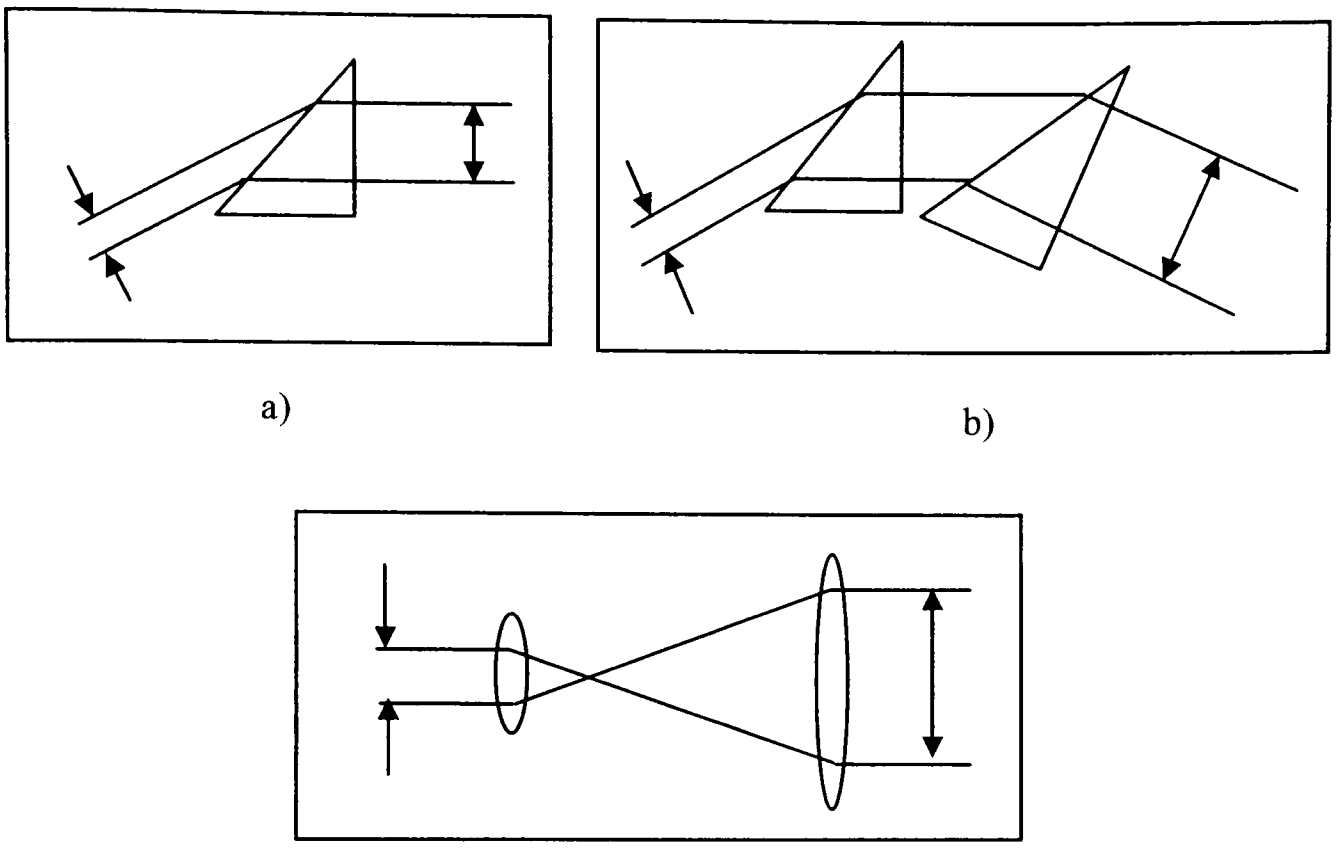


Figure 4.2 shows schematic diagrams of three different methods of beam expansion such that a greater illumination length of a grating can be achieved. Shown are a) single-prism expansion, b) two-prism expansion and c) telescopic expansion.

Other methods of wavelength selection that are used commonly in narrow-bandwidth laser cavities are etalons and birefringent crystals. These methods of wavelength selection introduce less loss into the cavity than the previously described higher loss alternatives.

Ce:LiLuF is a relatively high gain system, thus various combinations of the narrow bandwidth selection techniques described above were investigated with the aim of achieving a linewidth of the order of 0.1 cm^{-1}. The focus of these experiments was to obtain narrow-linewidth lasing of Ce:LiLuF, and as such it was purely the linewidth that was of importance at this initial stage of laser development. Once a cavity was found from which narrow-linewidth output could be obtained, more effort could then be made to maximise the laser output power.

4.3 Cavity 1- Three-mirror, small-mode cavity

4.3.1 Experimental Configuration

The frequency-doubled yellow output of the 10 kHz UV-KE-CVL at 289 nm was used to pump the Ce:LiLuF. The pumping configuration used in the experiments described in this

chapter was identical to that described in Chapter 1. A 100 mm focussing lens was used to focus the pump into the Maine-grown Ce:LiLuF laser crystal (as was used in Chapter 3). As in the previous chapter the crystal was mounted on a water cooled brass mount.

A new laser cavity configuration (Cavity 1) was used in these experiments, since the small crystal-output coupler distance required to achieve high lasing efficiency and low thresholds (both essential for narrow-band lasing) in the cavity described in Chapter 3, did not allow enough room to use a grating as the output coupler, in either Littrow or Littman configuration.

The Cavity 1 laser configuration used in this section is shown in Figure 4.3. The laser cavity consisted of three cavity mirrors, two curved high reflectors (M1 and M2) and an output coupler (M3). The distances L_1, L_2, and L_3 were varied such that a small laser mode existed at the crystal and the laser mode at the output coupler was relatively large. In the experiments reported here, the laser cavity was such that L_1=10 cm, L_2 = 6.8 cm and L_3=15 cm. M4 was used to reflect the unabsorbed pump light back through the laser crystal. This mirror was a curved high reflector with a ROC of 0.1 m and was placed such that L_4 =10 cm. In all results reported here, only one mirror was used in place of both M1 and M4, since in this case L_1 = L_4 = 10 cm. Thus the laser mode and the unabsorbed pump could be reflected back into the pumped region of the laser crystal using a single mirror. It was however possible for a second mirror to be used if desired.

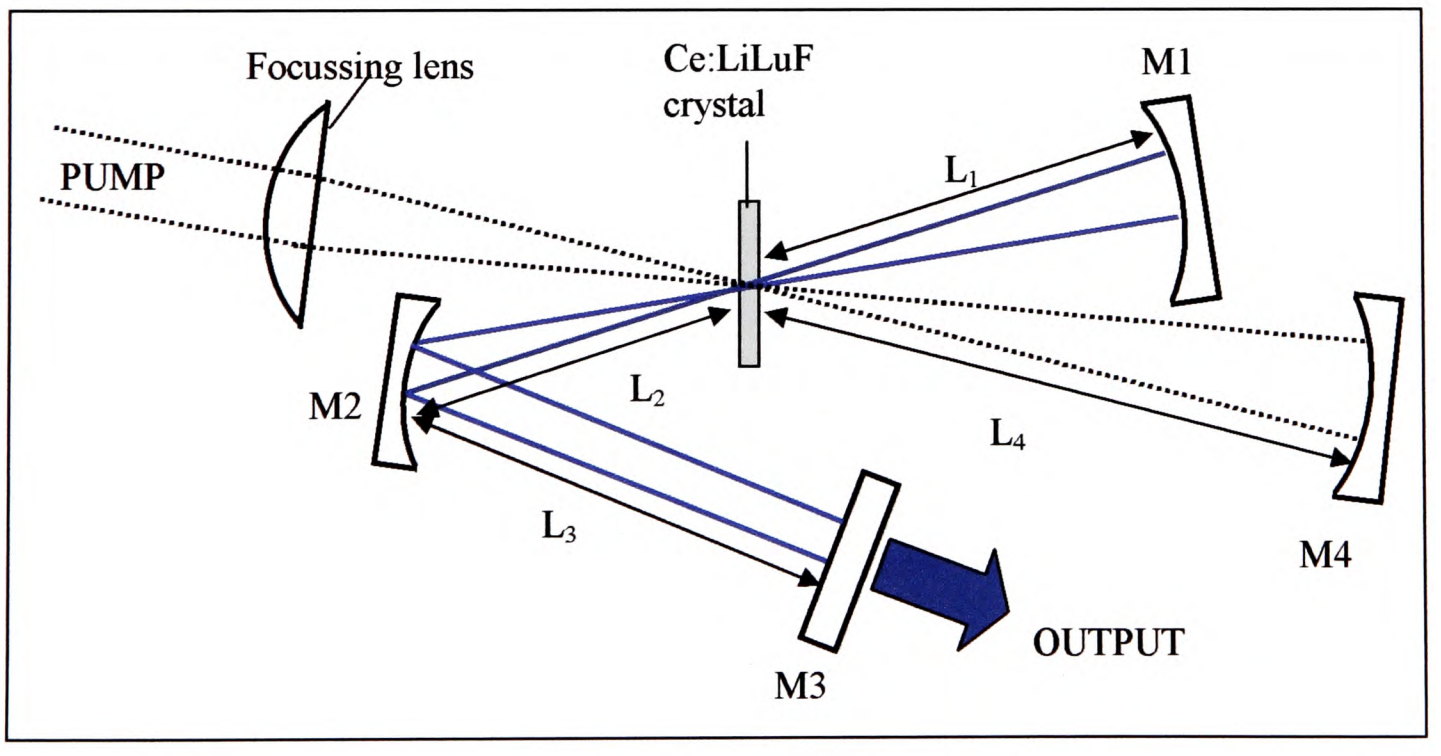


Figure 4.3 shows a schematic diagram of the un-tuned Cavity 1 laser configuration.

During all the Cavity 1 experiments, M1 and M2 both had a radius of curvature (ROC) of 0.1 m. For initial untuned laser experiments, a flat output coupler (M3) was used with a

reflectivity of 80%, 50% or 30% as shown in Figure 4.3. In the different variations of this cavity used for narrow bandwidth lasing, the wavelength selective elements were placed between M2 and M3. These wavelength selective elements were a) a prism in the cavity and a 90% flat reflectivity mirror used as the output coupler (shown in Figure 4.4); b) a Littrow grating in which the zero-order reflection was taken as the laser output (shown in Figure 4.5); c) a Lyott filter aligned at Brewster's angle with a 90% reflectivity flat mirror as the output coupler (as shown in Figure 4.6); and d) again a Littrow grating, however in this cavity a single-prism expander was used to magnify the laser mode onto the grating increasing the resolution of the grating (as shown in Figure 4.7). In the prism-expanded Littrow cavity shown in d), as in b), the zero-order reflection off the grating was taken as the laser output. In a) the prism used was a 60° fused silica prism and in d) the prism used was a right angle quartz prism. The grating used in both b) and d) was blazed for 1st order reflection at 330 nm and a ruling spacing of 2400 lines/nm. The Lyot filter used in c) was made up of three birefringent quartz plates of increasing thickness up to ~6 mm.

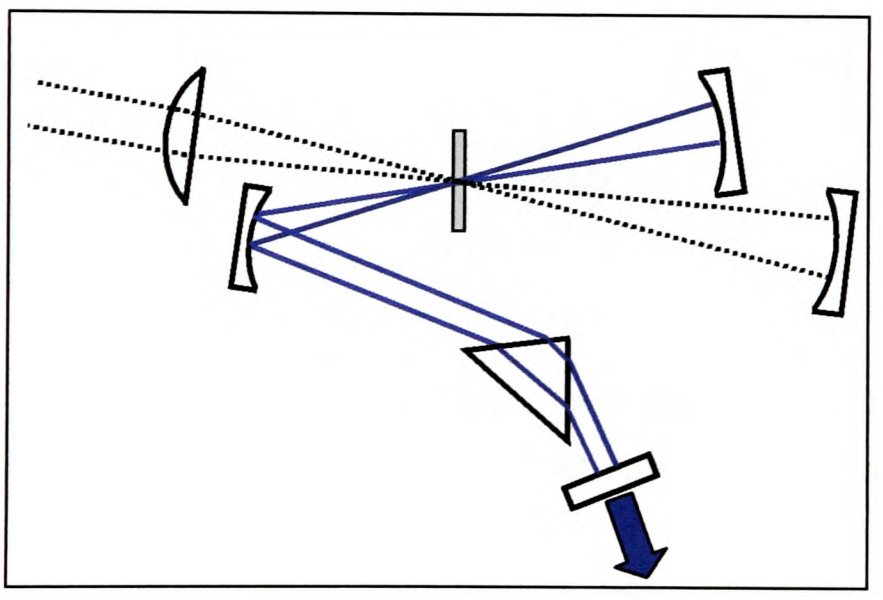


Figure 4.4 shows a schematic diagram of the Cavity 1 laser configuration with a prism as the wavelength-selective element and a 90% reflectivity flat output coupler.

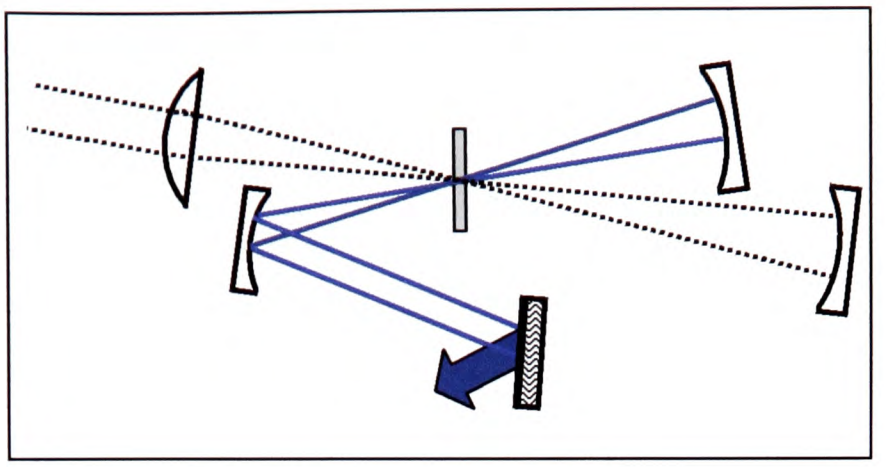


Figure 4.5 shows a schematic diagram of the Cavity 1 laser configuration with a Littrow grating as wavelength-selective output coupler.

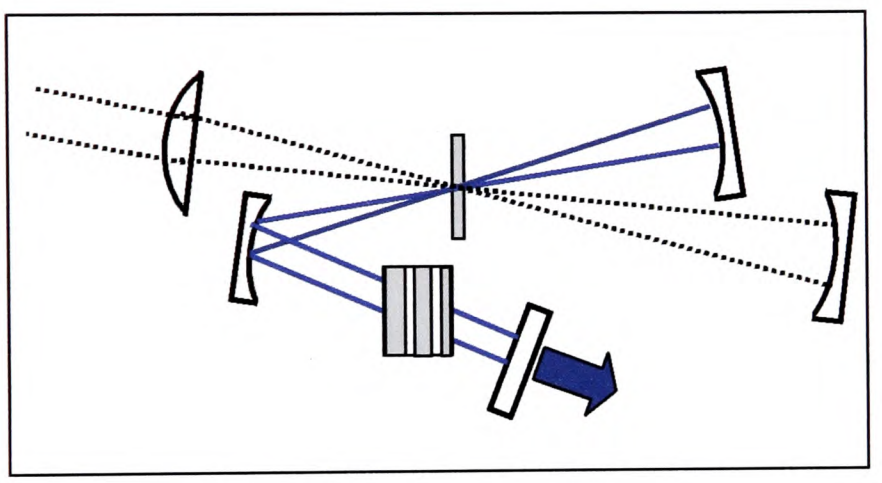


Figure 4.6 shows a schematic diagram of the Cavity 1 laser configuration with a Lyott filter as the wavelength-selective element and a 90% reflectivity flat output coupler.

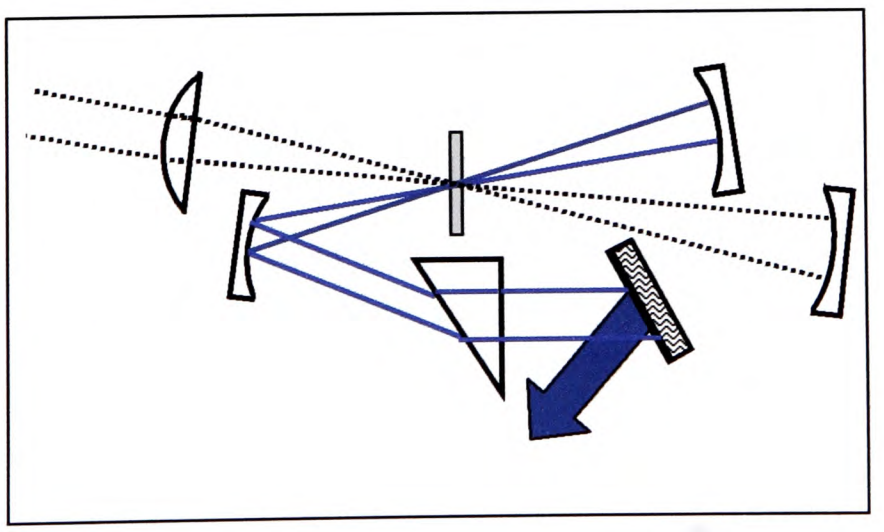


Figure 4.7 shows a schematic diagram of the Cavity 1 laser configuration with a prism expander and Littrow grating as the wavelength-selective element and output coupler.

The spectrometer used to determine the spectral output of the laser from each laser cavity was a Hilger and Watts spectrometer, with a Monospec 600 curved grating (600 lines/mm). The distance between the spectrometer slit and the curved mirror was 0.6 m. The laser output was passed through a 300 μm diameter, UV optical fibre to the spectrometer. A SWH-04 Thorn EMI Electrotube photomultiplier was used to detect the light exiting the spectrometer. In §4.3.2, §4.3.3.1 and §4.3.3.2 the slit-width of the spectrometer used was 50 μm. For the lasing using cavities c) and d) (hence the results reported in §4.3.3.3 and §4.3.3.4) a slit-width of 5 μm was required to resolve the spectral features of the laser output. In both cases the linewidth of the 289 nm pump light was used as reference showing the approximate resolution of the spectrometer, as the yellow CVL linewidth was known to be 11000 MHz, thus the corresponding 289 nm linewidth would be at most 22000 MHz (equivalent to 0.006 nm or ~0.7 cm^{-1}), which is suspected to be much less than the resolution of the 0.6 m spectrometer.

For the spectral bandwidth determination of each laser cavity used, the variation of detected laser output intensity with the wavelength setting of the spectrometer was measured. Using these measurements, a Gaussian approximation was made of the spectral output of the laser in Sigmaplot and as such the bandwidth of the laser output was determined.

4.3.2 Untuned results using Cavity 1

In order to characterise the basic behaviour of Ce:LiLuF with this laser cavity configuration, various experiments were undertaken. Firstly the efficiency of Ce:LiLuF lasing with the Cavity 1 configuration, with a 30%, 50% and 80% output coupler was determined. In these experiments the laser crystal was held at ~25°C. The laser output consisted entirely of ~309 nm, π-polarised laser output. In these experiments the unabsorbed pump was reflected back through the crystal using the 0.1 m ROC high reflector (M1 = M4). The results of these measurements are shown in Figure 4.8. The maximum laser output measured was 51 mW from 680 mW of incident pump power, when the 50% output coupler was used. The laser output was found to roll-over between 600-700 mW with all three output couplers. With the 50% output coupler the output dropped from 51 mW with 680 mW of incident pump power to 44 mW with 840 mW of incident pump power. The corresponding decrease in depletion was from 38% with 680 mW pump power (maximum laser output power) to 32% with 840 mW of pump power (maximum pump power available). The slope efficiency before the roll-off, with the 50% output coupler, was 14% with respect to incident pump power. The lasing threshold with the 50% output coupler was ~ 200 mW. With the 30% and 80% output couplers the slope efficiencies before roll-off were 14% and 10% respectively. Table 4.1 shows a summary of the lasing results for varying output coupler reflectivities.

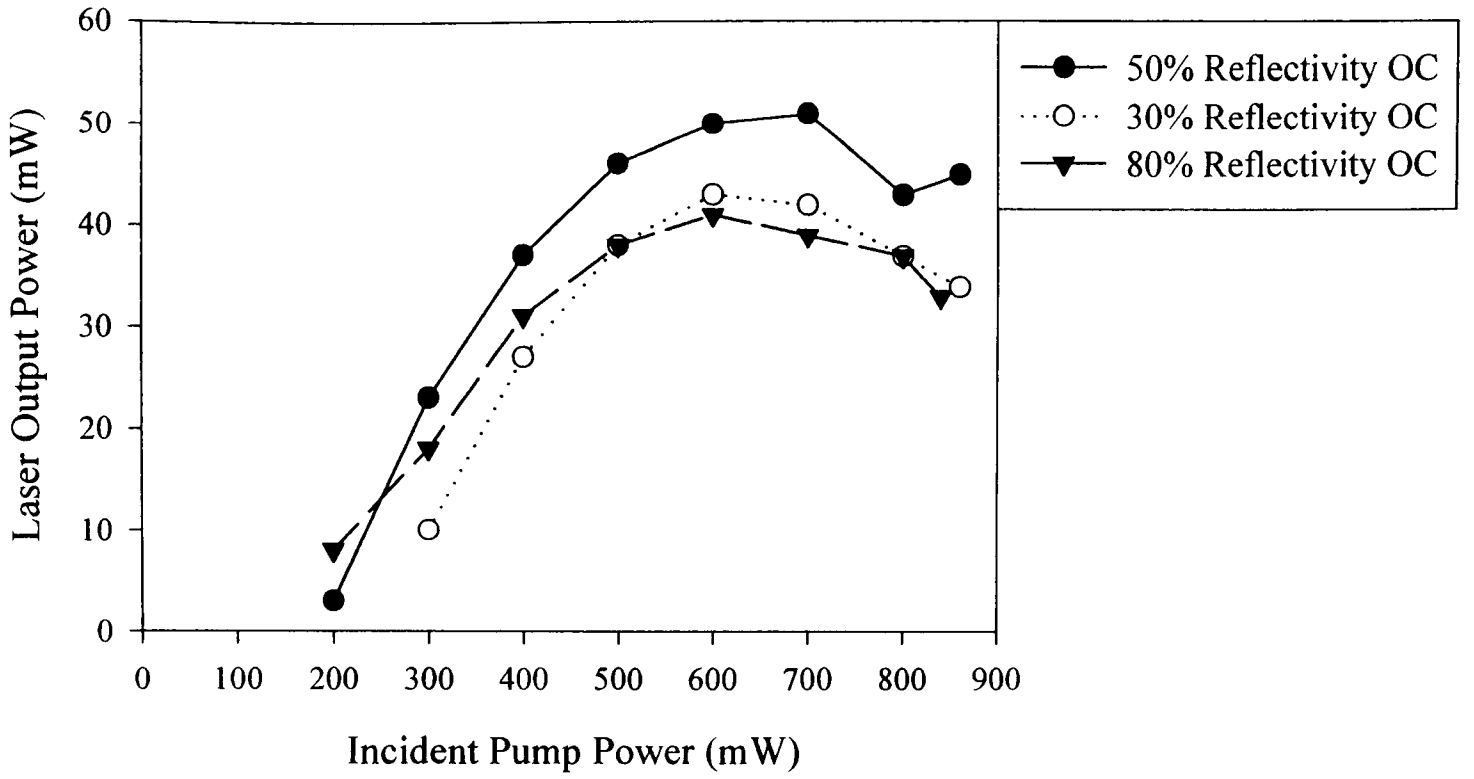


Figure 4.8 shows the variation of laser output power in Ce:LiLuF with Cavity 1 configuration, with pump power. In all these results the crystal temperature was ~25°C.

Table 4.1 is a summary of the Ce:LiLuF Cavity 1 results at room temperature with an 80%, 50% and 30% output coupler.

Output coupler reflectivity	30%	50%	80%
Slope efficiency	14%	14%	10%
Threshold	~200 mW	~220 mW	~150 mW
Maximum Output Power/ Incident Pump Power	42 mW / 640 mW	51 mW / 680 mW	40 mW / 660 mW
Depletion at maximum output	26%	38%	45%
Power with maximum available pump power (~850 mW)	34 mW	44 mW	35 mW
Depletion with the maximum available pump power	20%	32%	40%

Using the 50% output coupler the origin of the roll-off in the laser output with pump power was investigated further by seeing the effect on the output energy of blocking and unblocking the pump beam. The results are shown in Figure 4.9. As can be seen in the figure the laser output decreases from a high initial laser output power to a stable lower output power after

<10 ms. The decrease in laser energy with time, after unblocking the pump beam, was dependent on pump power, with only a 28% decrease in output with 500 mW pump power and room temperature crystal compared to the 64% decrease in laser output power with 840 mW pump power at room temperature. When the crystal was cooled to 4°C, the decrease in output after the unblocking of the pump was reduced to 27% when the incident pump power was 840 mW. This laser behaviour is suggestive of the presence of thermal effects in the laser crystal. The exact nature of these thermal effects was not investigated at the time of these experiments, though it is possible they were related to the temperature ESA effects in Ce:LiLuF.

A comparison was made between the variation of output power with pump power with the 50% output coupler for the room temperature laser crystal and a cooled laser crystal (~2°C). The slope efficiency increased to 16% with a decrease in crystal temperature to 2°C. Up to 91 mW of output power was obtainable from the laser with the crystal cooled to 2°C. A roll-off in the output was observed with the cooled laser crystal however it only occurred with pump powers greater than 800 mW.

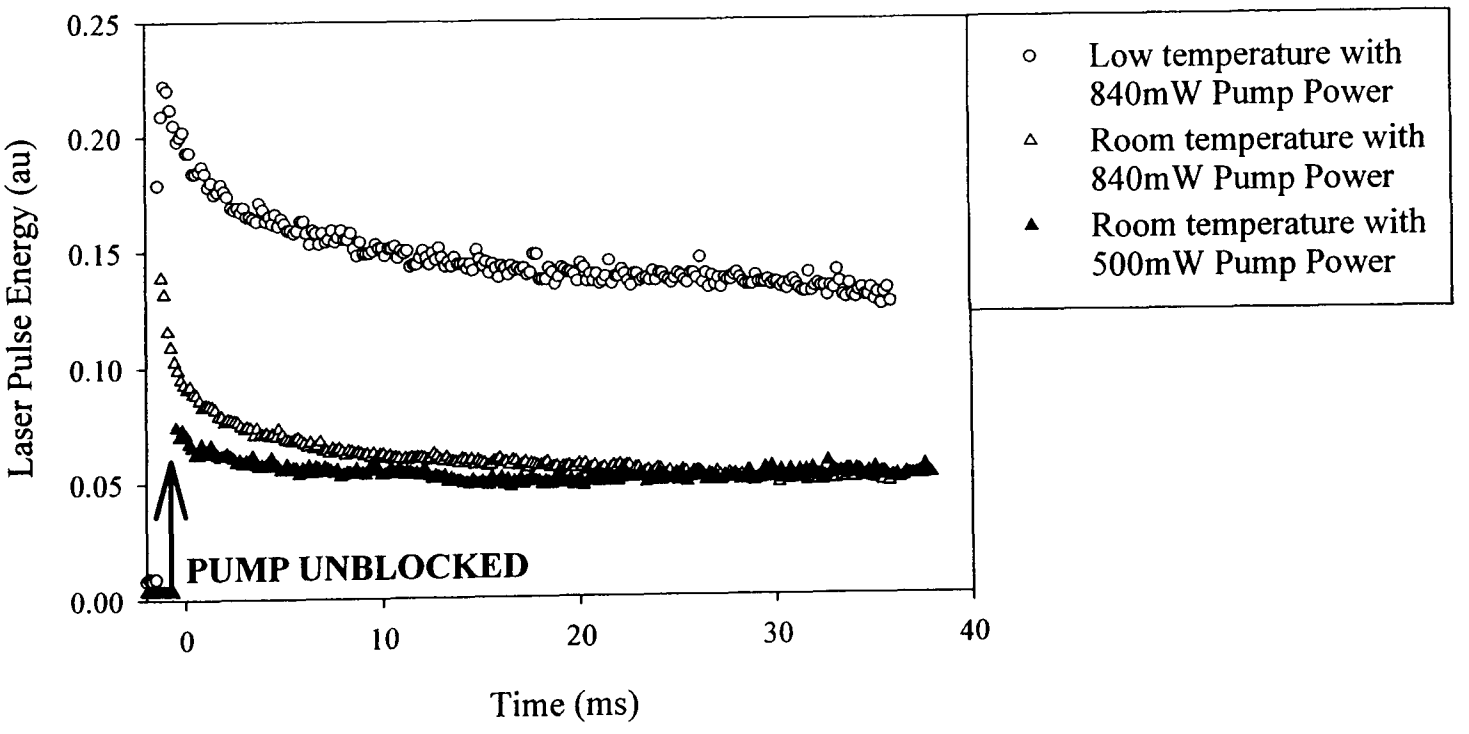


Figure 4.9 shows the variation of Ce:LiLuF laser output for maximum laser output and maximum pump power in the 50% output coupler cavity with both a cooled and uncooled laser crystal.

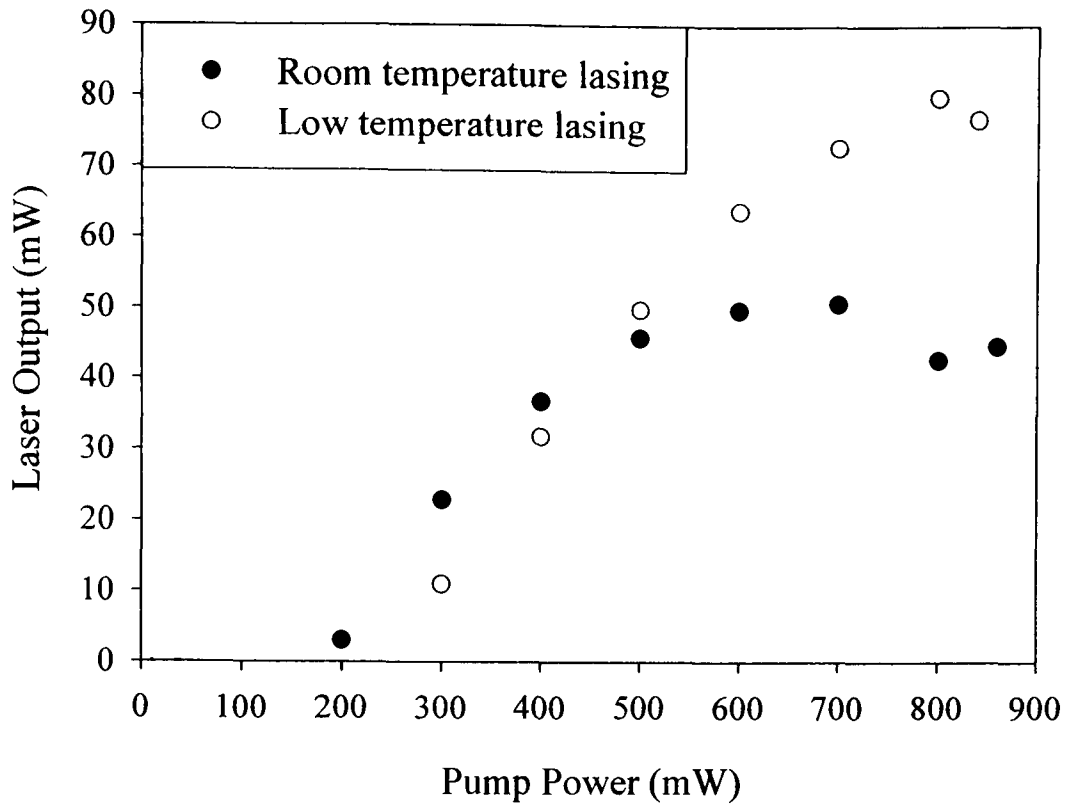


Figure 4.10 shows the temperature dependence of the Cavity 1, Ce:LiLuF lasing slope efficiency with a 50% output coupler.

The effect of reflecting the unabsorbed pump through the pumped laser mode on lasing efficiency was investigated. The laser output power obtained with only a single-pass of the pump, with the 50% output coupler cavity and the crystal at room temperature, was 21 mW from 560 mW of incident pump power. Reflecting the unabsorbed pump (~120mW) through the laser crystal increased the laser output to 44 mW output with 530 mW of incident pump power. The depletion was found to increase from 17% with only the single-pass pump configuration to ~32% with the double-pass pump configuration.

Parasitic lasing between the M1 high reflector and the crystal face furthest from M1 crystal face was found to occur. This lasing resulted in the output laser spot to be made up of two separate spots, one corresponding to the parasitic lasing and the other to the lasing from the whole cavity. Various attempts to attenuate this parasitic lasing were made, however any misalignment of the crystal from the laser mode caused both laser modes to cease. The presence of the parasitic lasing as the only laser mode was found to cause less than 1% depletion of the fluorescence. Minimising the parasitic lasing as much as possible, while still maintaining the cavity controlled lasing (as opposed to the parasitic lasing) resulted in a depletion of 32%. Realigning the laser for maximum depletion (and hence a correspondingly large fraction of parasitic lasing in the output) produced a depletion of 43%. When varying the output coupler alignment, the laser pulse was found to change shape as shown in Figure

4.11. The achievement of maximum output power was found to coincide with a laser pulse which had build-up time similar to the short parasitic lasing build-up time.

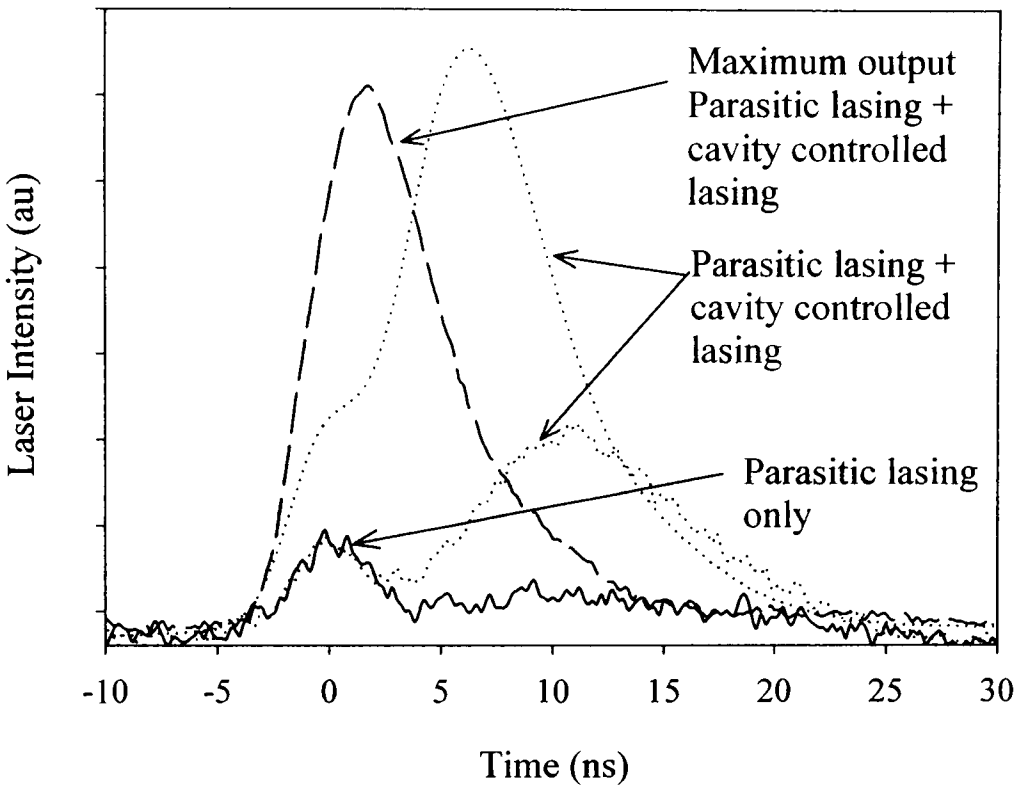


Figure 4.11 shows the laser pulses of the 50% output coupler cavity at room temperature, with the output coupler alignment varied to achieve parasitic lasing (M1-crystal lasing) and cavity-controlled lasing.

Finally, with the untuned Cavity 1 laser cavity configuration the spectral bandwidth (FWHM) of the laser output was determined to be 2.5 nm using the spectrometer with 50 μm slit widths. This bandwidth is shown in Figure 4.12 Also shown in Figure 4.12 is the spectral bandwidth of the pump laser at 289 nm, which is indicative of the resolution of the spectrometer, which was found to be much smaller (0.27 nm) than the laser bandwidth (2.5 nm) indicating that the laser bandwidth was sufficiently resolved.

4.3.3 Results: Narrow bandwidth adaptations of Cavity 1.

4.3.3.1 Prism-tuned cavity

Using the prism-tuned cavity with the 90% reflectivity output coupler, shown in Figure 4.4 up to 19 mW of 310 nm Ce:LiLuF output power was achieved with 670 mW of incident pump power, and the crystal cooled to ~2°C. The spectral bandwidth of the laser output, as shown in Figure 4.13, was found to be 2 nm.

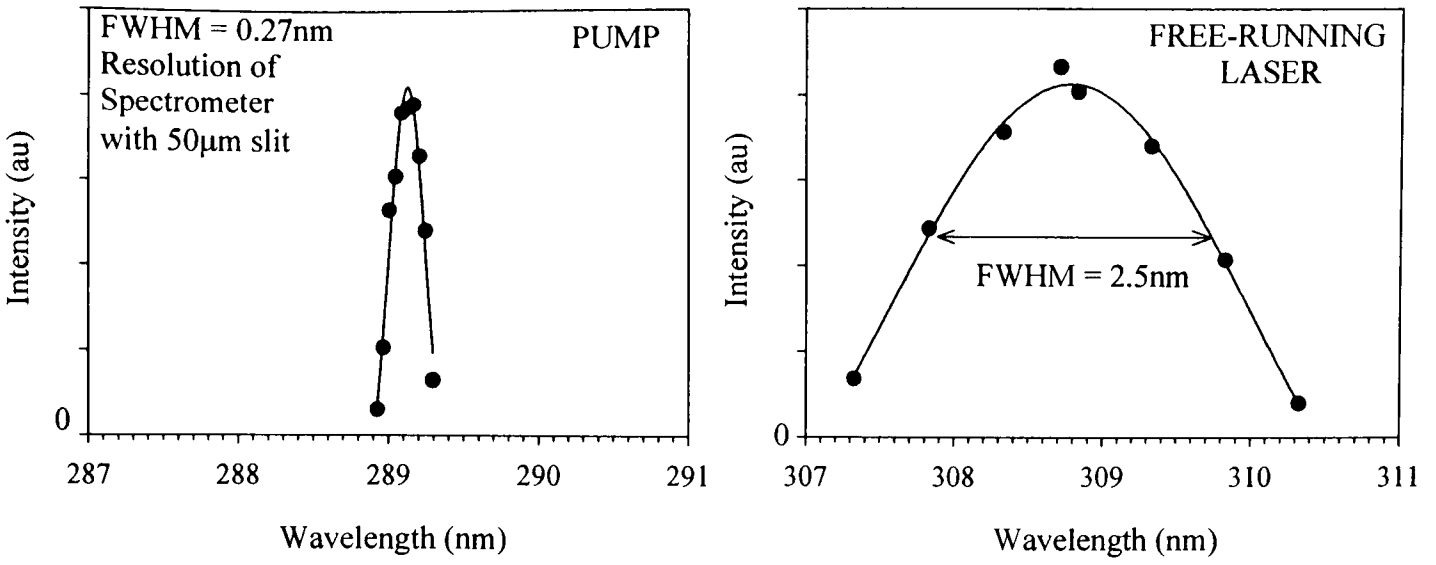


Figure 4.12 shows the pump (left hand side) and laser (right hand side) linewidths of Ce:LiLuF lasing at room temperature with the Cavity 1 laser configuration with 50% output coupler. Note: both y-axes start at zero.

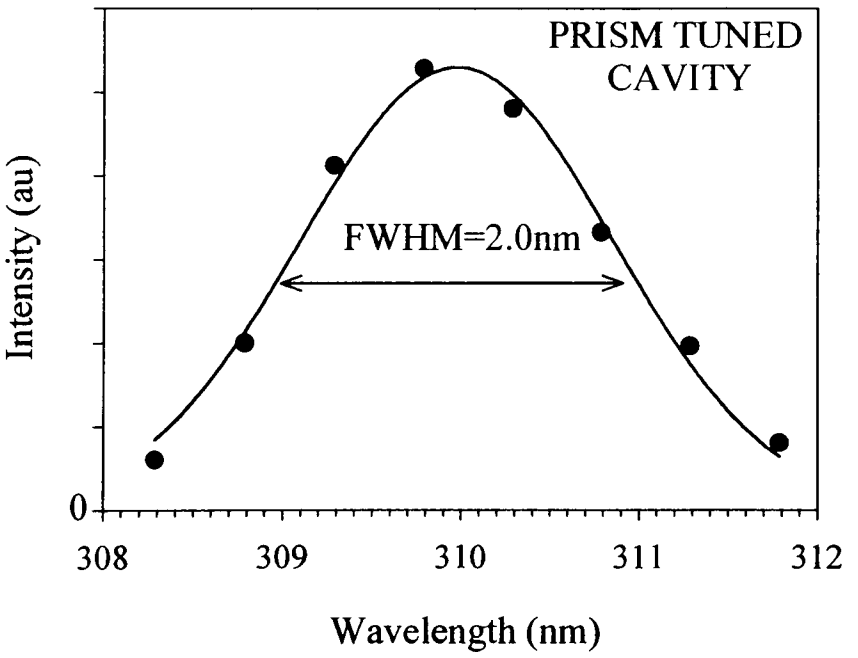


Figure 4.13 shows the spectral bandwidth of the prism-tuned cavity with 50 μm spectrometer slit width.

4.3.3.2 Littrow Grating-tuned cavity

In this grating tuned laser cavity (as shown in Figure 4.5) the maximum output power obtained at the peak of the tuning curve was 25 mW with 690 mW of incident pump power with the crystal cooled to ~2°C. The maximum output achieved with the same pump power at room temperature was 17 mW. The bandwidth of the output and the corresponding Gaussian

fit is shown in Figure 4.14. The spectral bandwidth was found to be 1.9 nm. Tuning of this laser was found to be difficult as the laser mode was found to move along the grating in order to maintain lasing at ~309 nm. It is possible to prevent such jumping of the laser mode by placing a slit in front of the grating. The spectral bandwidth of the output from this cavity was far from that required, thus an investigation into the effect of placing a slit in front of the grating was not undertaken at this time.

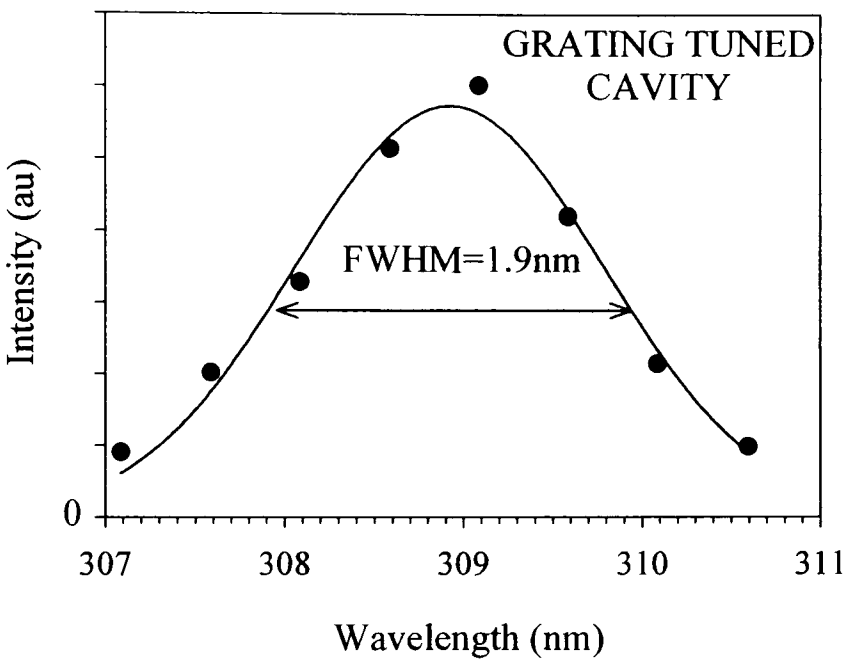


Figure 4.14 shows the spectral bandwidth of the grating-tuned cavity with 50 μm spectrometer slit width.

4.3.3.3 Birefringent crystal-tuned cavity

Figure 4.6 shows the laser cavity in which a Lyot filter was used. The output coupler used had a 90% reflectivity. Initially lasing was maximised without the filter in place. The filter was then placed at Brewster's angle to the laser mode and rotated until maximum laser output was achieved. Up to 6 mW of laser output was achieved with the crystal cooled to ~2°C, with 700 mW of incident pump power.

Using the spectrometer with the 5 μm slit width the pump bandwidth was measured to be 0.067 nm showing that the laser bandwidth was resolved. The output spectral structure is shown in Figure 4.15. The laser output was found to have a variation of intensity with wavelength showing definite maxima and minima. The spectral width of a single peak was found to be 0.16 nm as shown in Figure 4.15a). One could include a prism in the cavity with the Lyott filter which would then enable one of these peaks to be selected preferentially over the others giving a laser output with a bandwidth of 0.16 nm. The linewidth of a single peak

was however not sufficiently narrow for this method of peak selection to be investigated further at this time.

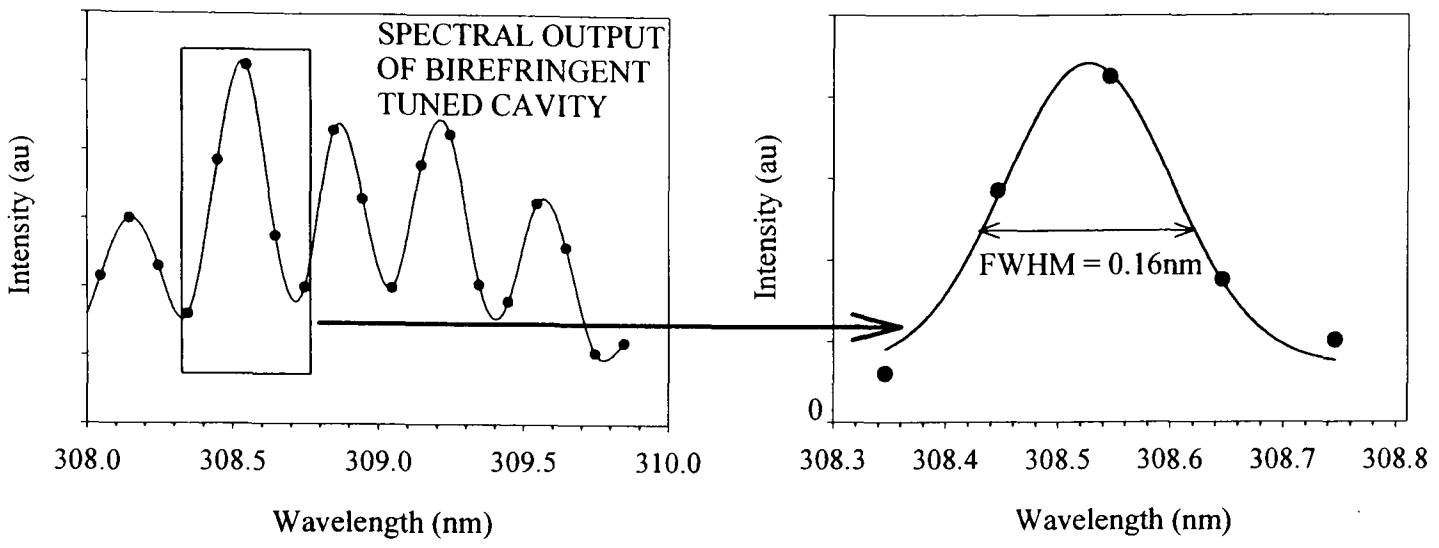


Figure 4.15 shows the spectral bandwidth of the Lyot filter-tuned cavity with 50 μm spectrometer slit width.

4.3.3.4 Prism expanded-Littrow Grating- tuned cavity

The final adaptation of Cavity 1 included a prism-expander and a grating in Littrow configuration as shown in Figure 4.7. The prism was aligned to give the maximum laser mode size on the grating possible while still maintaining lasing. The spot size on the grating was up to 3 mm in width. Up to 6.5 mW of output was obtained with the crystal at room temperature and 430 mW of pump power and up to 10 mW was obtained with 630 mW of pump power, with the crystal cooled to ~2°C. The spectral bandwidth of the laser output was measured to be 0.17 nm as shown in Figure 4.16.

The spectral linewidth of the laser output from all these cavities just described was much greater than the desired 0.1 cm^{-1} (0.001 nm). Use of a four-prism beam expander was investigated, however the expanders available were coated for use in a dye laser (thus for the visible and not the UV) and the magnification factor was found to be comparable and not larger than that obtainable with the single prism thus this cavity was not investigated further.

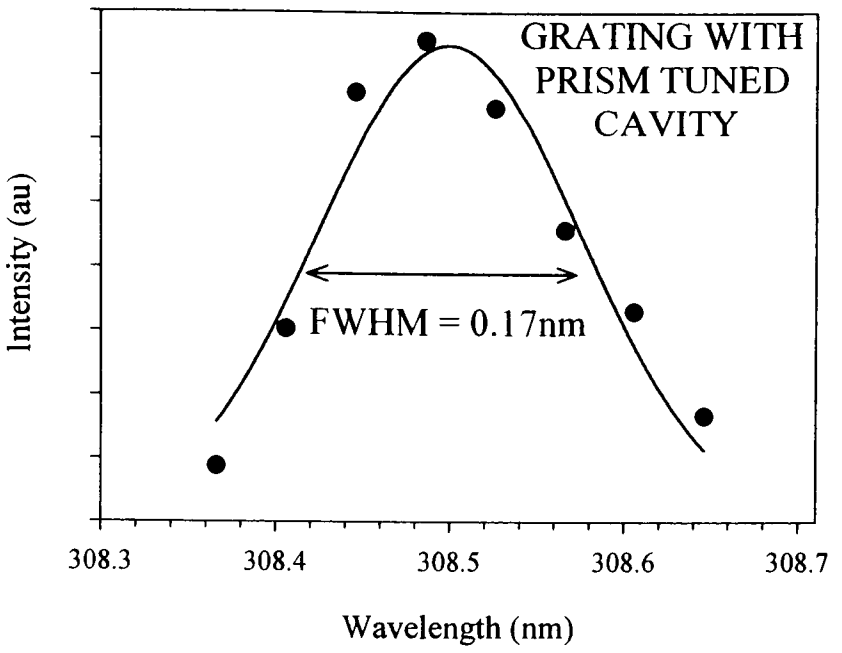


Figure 4.16 shows the spectral linewidth of the prism-expanded grating tuned laser cavity with a 5 μm spectrometer slit width.

4.4 Cavity 2-Telescope cavity

4.4.1 Experimental Configuration

The pump source used in these experiments was the UV-CVL with the pumping configuration identical to that described in §1.3. Note that, in contrast to the previous chapter the CVL used in these experiments was not kinetically-enhanced, thus the UV laser output power in general was lower and the overall beam quality of the UV pump was worse than with the UV-KE-CVL. The pump beam was focussed using an 80 mm focussing lens. In order to keep the angle of overlap between the pumped region of the laser crystal and the laser mode in the crystal small, the focussed pump beam was reflected off a 289 nm high reflector (HR1) into the Ce:LiLuF crystal. There was a little loss of pump power through the high reflector (<5%). The Ce:LiLuF crystal was cooled to ~2°C using a Melcor Chiller throughout the experiments described in this section.

In this cavity (Cavity 2), a telescope was included to magnify the laser mode before it reached the prism expander and Littrow-configured grating. A schematic diagram of the laser cavity used is shown in Figure 4.17 and a photo of the laser cavity is shown in Figure 4.18. The telescope consisted of a 15 mm focal length, 1cm diameter singlet lens and a curved high reflecting mirror with a ROC=0.25m. This telescope enabled the laser mode to be magnified by 6.67 times. The magnified laser mode was then reflected onto an anti-reflection (AR) coated right angle prism, with the angle of incidence onto the prism of ~84°C from the normal

to the prism face. The prism was AR coated for 308 nm light at an 80° incident angle on the long prism face and 0° on the short prism faces, thus the intra-cavity loss introduced by the prism at this large angle was small. The grating used was blazed for 1st order 330 nm light and had 2400 lines/mm rulings. The grating was arranged in Littrow configuration for 1st order reflection off the grating. The spot size on the grating was measured to be between 1-1.5 cm. The zero order reflection was taken as the laser output. A flat 308 nm high reflector (HR2), placed close (<2 mm) to the Ce:LiLuF crystal completed the laser cavity. The total cavity length was ~26 cm, as shown in more detail in Figure 4.17.

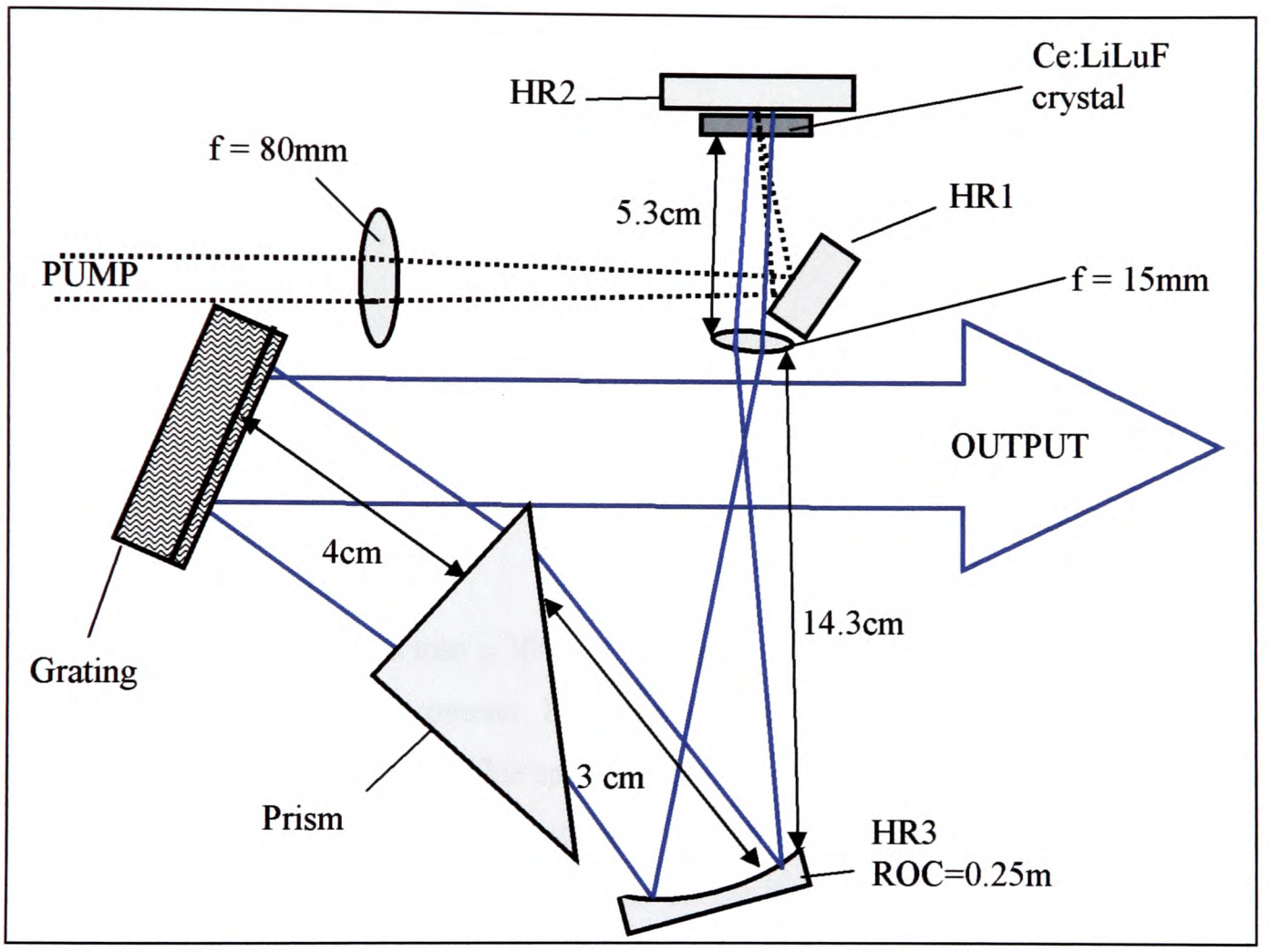


Figure 4.17 shows a schematic diagram of Cavity 2 used to obtain narrow-bandwidth operation of Ce:LiLuF at ~308 nm. Note this diagram is not to scale.

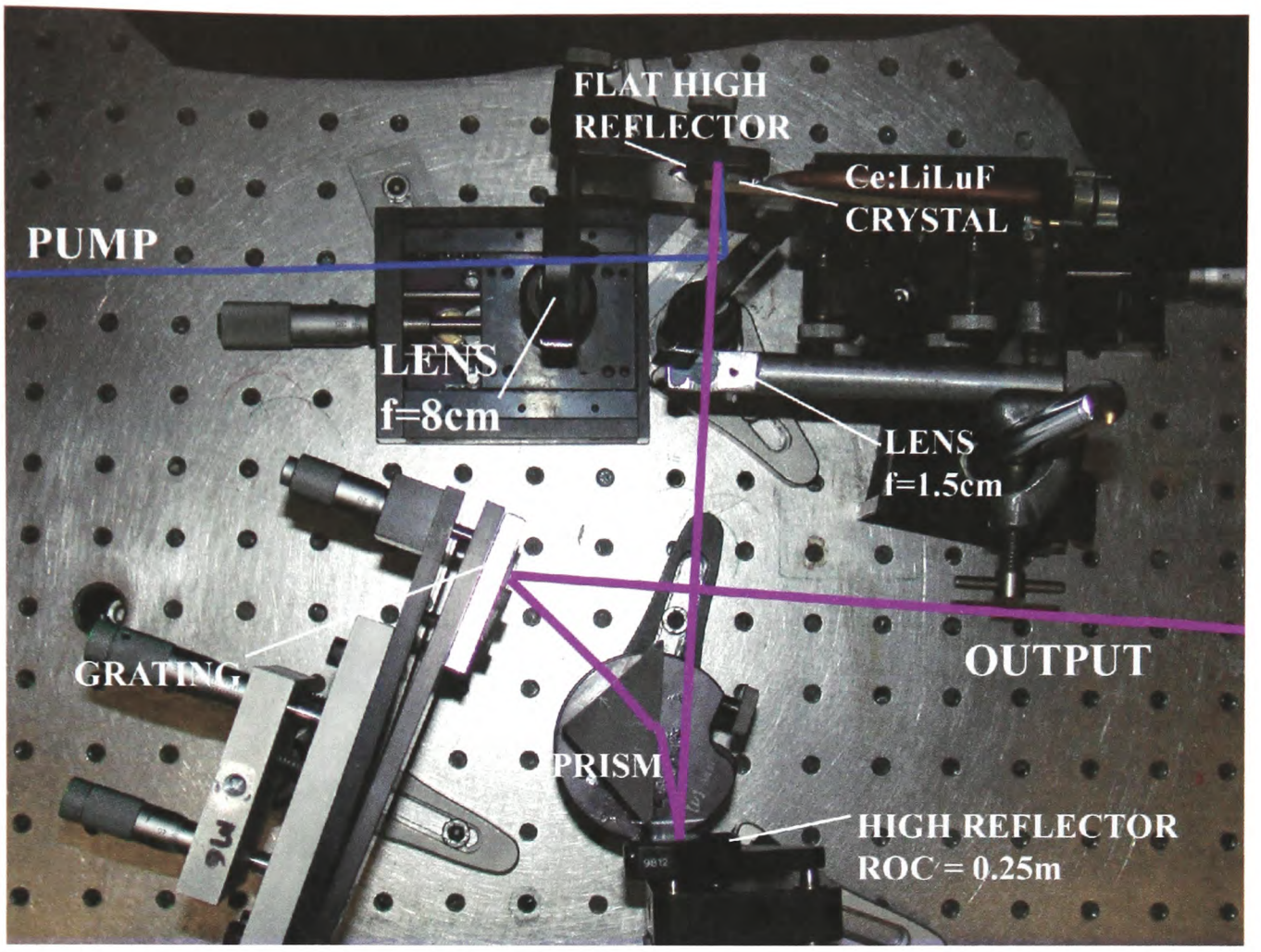


Figure 4.18 is a photograph of Cavity 2, used for narrow-bandwidth lasing of Ce:LiLuF.

The laser output was focussed into a 300 μm UV fibre using a 3 cm focussing lens. The fibre then carried the light to a spectrometer. For the initial spectral determination the 0.6 m Hilger and Watts spectrometer was used. This spectrometer is described in detail in §4.3.1. For more resolution a 1 m Higher and Watts spectrometer was then used. The grating in this spectrometer had 2400 lines/mm and a distance of 1m between the spectrometer slit and the curved mirror. The slit was imaged (1:1) onto a Princeton Instruments Intensified ICCD camera using two silica 10 cm focussing lenses. The CCD had 576 pixels by 384 pixels. The grating in the spectrometer was blazed for 2nd order reflection, thus for the measurements made, in this section, the spectrometer was set to two times the laser wavelength.

The camera was calibrated by tuning the 1 m spectrometer by ~1 nm and determining the distance (in pixels) the image moved on the camera. One pixel was found to correspond to a $\Delta\lambda$ = 0.0048 nm at 613.5 nm and a $\Delta\lambda$ = 0.0024 nm at 306.75 nm. Absolute wavelength calibration of the spectrometer was carried out using an Hg-Zn-Cd lamp. The spectrometer was tuned to 613.5 nm and the lamp spectrum was taken, two peaks were seen, the more intense Zn I peak at 307.5901 nm was used to calibration the spectrometer. The position of the second peak was assigned to the Cd I peak at 308.0827 nm. Using the $\Delta\lambda$/pixel determined earlier the position of the second peak was found to lie within 0.005 nm of the

predicted Cd I wavelength value. The lamp spectrum is shown in Figure 4.19, with the spectrometer set to 613.5 nm.

A Fabry-Perot Interferometer was also used to determine the linewidth of the laser output. Highly reflective 308 nm etalon plates were used, and the distance between the plates could be adjusted. In these measurements, the Ce:LiLuF laser output was diffused using a frosted quartz window. This diffused light illuminated Fabry-Perot plates and the resulting interference rings were focussed onto the Princeton Instruments Intensified ICCD camera using a 15 cm lens.

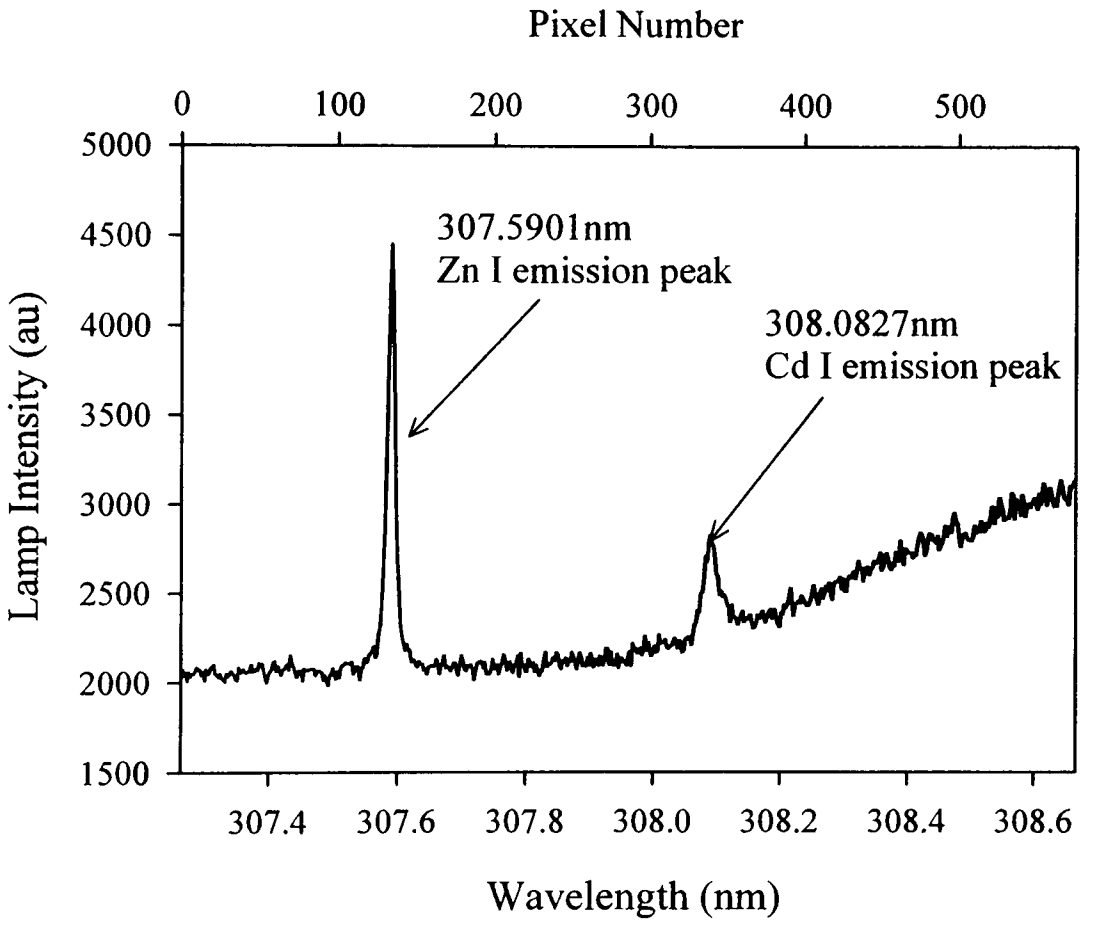


Figure 4.19 is the spectra of Hg-Zn-Cd Lamp with the spectrometer set to 613.5 nm (2^{nd} order =306.75 nm).

4.4.2 Results

In all the Cavity 2 experiments, parasitic lasing between HR2 and the furthest Ce:LiLuF crystal face from HR2 was pronounced. Reducing the pump focus slightly and increasing the Ce:LiLuF crystal temperature was found to have little affect on the parasitic lasing intensity. The parasitic lasing was characterised by a ring structure on the laser output beam spot, possibly resulting from the flat-flat laser cavity resulting in the parasitic lasing. The parasitic lasing was thought to be detrimental to the narrow-bandwidth lasing since it may have acted

as a broad-band seed to the laser cavity. One advantage of the parasitic lasing, however, was the ability to use it to aid the alignment of the laser cavity, since a UV alignment source was not available. The cavity was aligned such that the parasitic lasing travelled from the flat high reflector through to the grating and then back along itself. When the whole cavity was aligned, the laser output, which consisted of parasitic lasing when unaligned, became noticeably more intense. The laser output was found to flash on and off when the grating was adjusted, suggesting some etalon affects in the cavity.

In the initial measurements made using Cavity 2, a four prism-expander was used in place of the single AR coated prism. The spectral output of the laser determined using the 0.6 m spectrometer was found to consist of a broad bandwidth platform on top of which a narrow-band output was found to be superimposed as shown in Figure 4.20. It was thought that the broad-bandwidth peak corresponded to the parasitic lasing output and the narrow-bandwidth peak resulted from lasing in which the whole cavity was used by the laser mode. Tuning the laser by rotating the grating resulted in the movement of the narrow-bandwidth peak, confirming this suggestion. When the cavity was aligned the laser output power was not detectable with the power meters available as the power was less than 1 mW from 360 mW of 289 nm pump power.

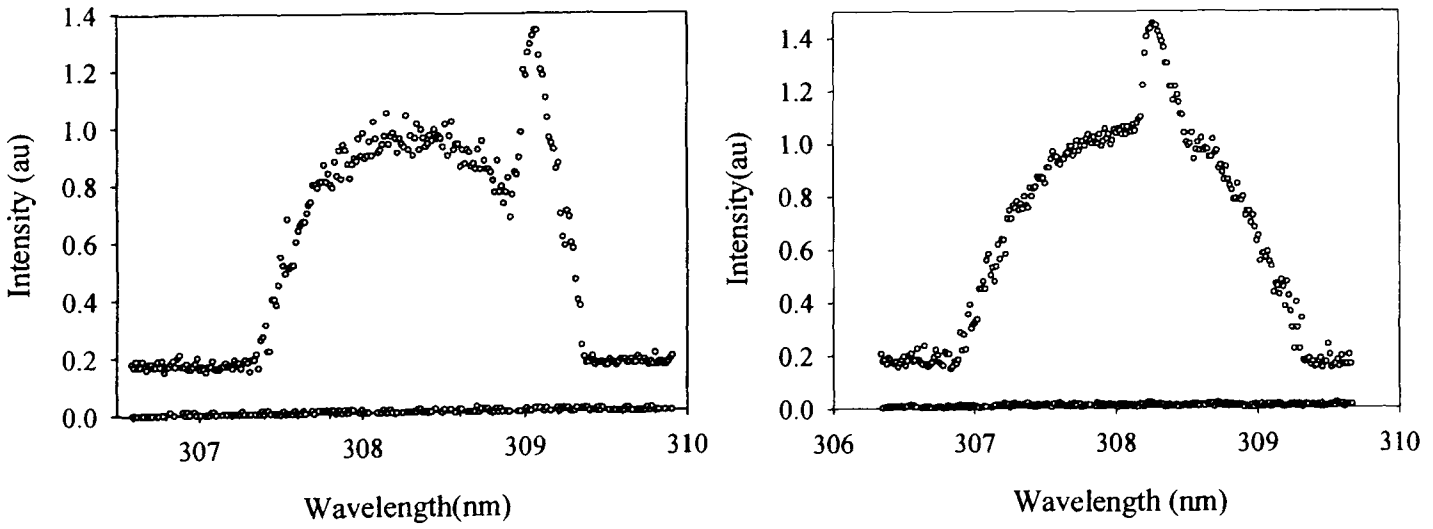


Figure 4.20 shows the spectral output of the Cavity 2 Ce:LiLuF laser with the 4 prism-expander in place of the single AR coated prism. The spectrometer used was the 0.6 m spectrometer.

The 4-prism expander was then replaced with a less lossy AR-coated single prism expander. The laser output was estimated to be ~2 mW with 360 mW of incident pump power. Using the 1 m spectrometer (viewing the peaks for 2nd order diffraction) the spectral output of the laser was better resolved as shown by the CCD images in Figure 4.21. The image of the pump

spectrum is shown (Figure 4.21 bottom) for comparison with the above threshold laser output (Figure 4.21 middle). As can be seen both the laser output and pump light have similar spectral bandwidths suggesting that either the narrow-bandwidth lasing was not fully resolved by this 1 m spectrometer or the pump was fully resolved (0.7 cm^{-1}). Structure within the laser output was resolved and is shown in Figure 4.21 (top).

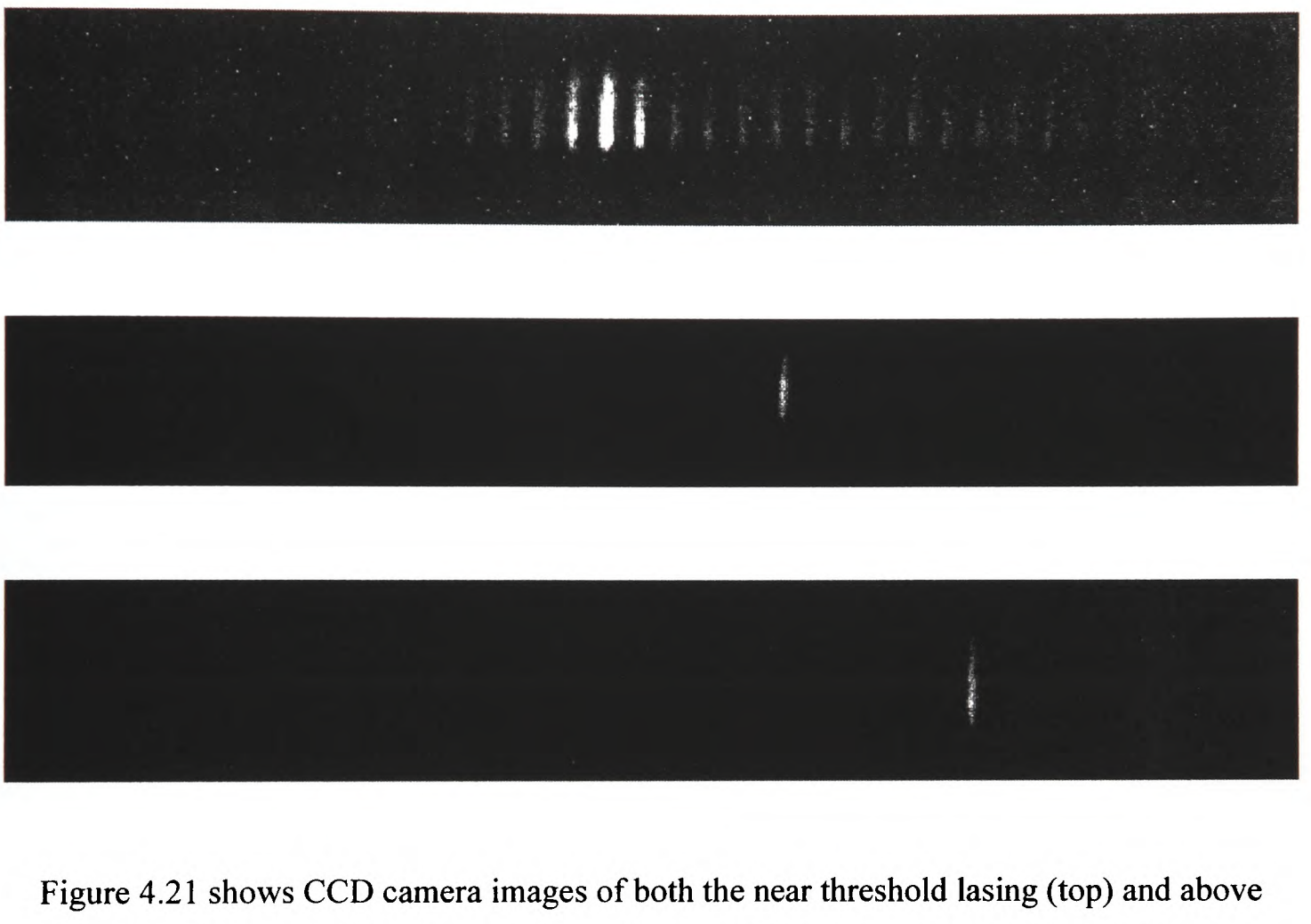
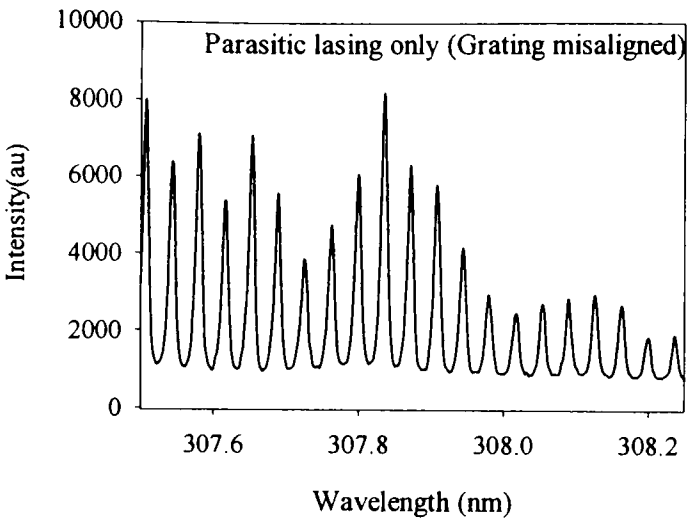
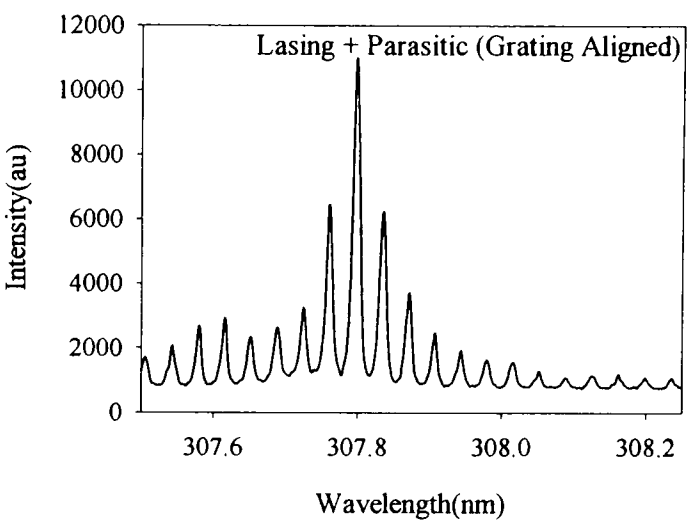


Figure 4.21 shows CCD camera images of both the near threshold lasing (top) and above threshold lasing (middle). Also shown is the spectral image of the pump laser at 289 nm (bottom)

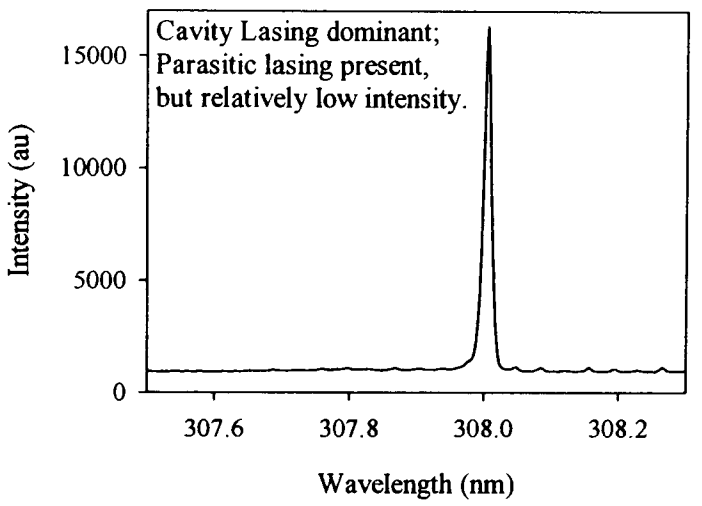
Figure 4.22 shows the sum of multiple consecutive images, giving an integration of the laser output over time. The laser output shown in Figure 4.22(a) consisted only parasitic lasing (with the grating misaligned). The laser output shown in Figure 4.22(b) consisted of both a relatively intense output from the whole laser cavity as well as the parasitic lasing. Figure 4.22(c) shows the laser output with the cavity well aligned. The parasitic lasing was still present in the output however the cavity controlled lasing was obviously dominant over the parasitic lasing.



a)



b)



c)

Figure 4.22 shows the laser output of Cavity 2 using the 1 m spectrometer. a) shows only parasitic output b) shows threshold lasing output (parasitic lasing still obvious) and c) shows above threshold lasing (parasitic lasing present but relatively low intensity).

As can be seen the spectral output of the laser shown in Figure 4.22a) and b) was characterised by many narrow peaks with a spacing of 3.8 cm^{-1}, which would arise from an etalon mirror spacing of ~900 μm. The optical fibre was replaced by a number of different diameter fibres from varying producers with no affect on the spectrum of the laser seen, ruling out any fibre related effects which may have caused these output features. The distance between the laser crystal faces was measured to be ~800 μm, thus it was thought that the etalon effects seen in the laser output arose from the Ce:LiLuF crystal acting as an etalon. The laser output was monitored whilst HR2 (see Figure 4.17) was moved away from the crystal, the spacing of the peaks was found to be unaffected by changing this distance, ruling out HR2-Ce:LiLuF crystal etalon effects.

The Ce:LiLuF crystal was mounted on a translation stage such that it could be moved at right angles to the laser mode, hence, due to the wedged nature of the crystal, the crystal etalon

peak positions were expected to move as the crystal was moved. The result of moving the laser crystal across the laser mode is shown in Figure 4.23. As can be seen the etalon peaks (of the parasitic lasing) do move with change in crystal width (resulting from moving the wedged crystal) to shorter wavelengths with increasing micrometer movement. The movement of the peaks however was not smooth, which was suggestive that either the crystal surfaces were not flat or the micrometer translation stage movement was not smooth. The change in the actual peak separation was very small; too small to determine the change in crystal width with μm changes of the translation stage.

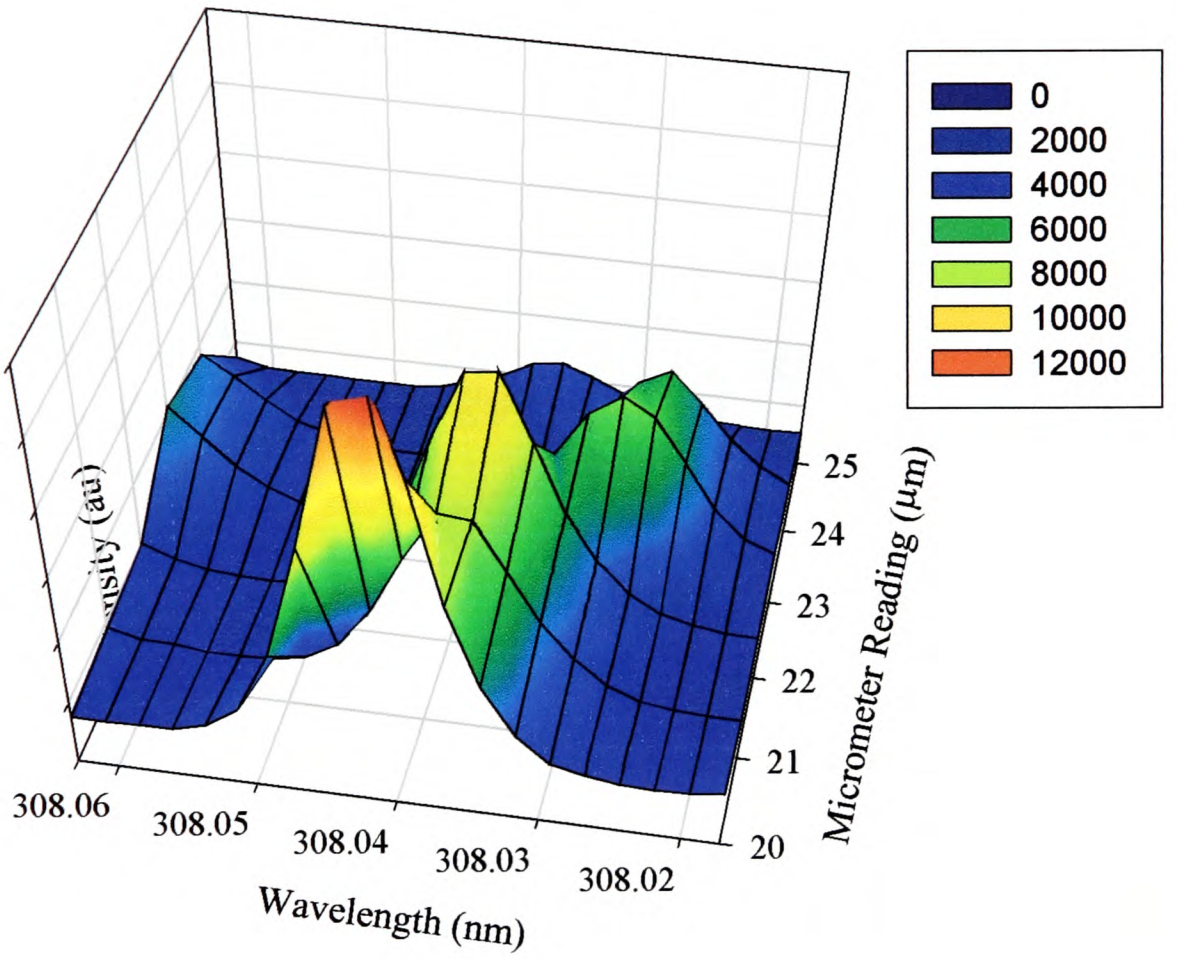


Figure 4.23 shows the movement of crystal etalon peaks with horizontal movement of the wedged Ce:LiLuF crystal.

The variation of the position of the crystal etalon peaks with temperature was also investigated, since increasing the temperature may result in crystal expansion which in turn could result in a shift in the parasitic laser peaks. By blocking and then swiftly unblocking the pump beam and monitoring the peak position with time after the pump was unblocked, the approximate variation of peak position with pump induced temperature increase was measured. The temperature of the crystal was assumed to increase with time, thus each frame detected would show the peak position for an increasing crystal temperature (Frame 1 being taken immediately after the unblocking of the pump, hence corresponding to a colder crystal).

These results are shown in Figure 4.24. As can be seen in the figure, as the crystal temperature increases, the crystal etalon peaks shifted to longer wavelengths. The variation of peak intensity with crystal position and crystal temperature was assumed to be purely due to fluctuations in the parasitic lasing intensity with time and not related to crystal position or temperature. Again the change in peak separation was too small to determine accurately.

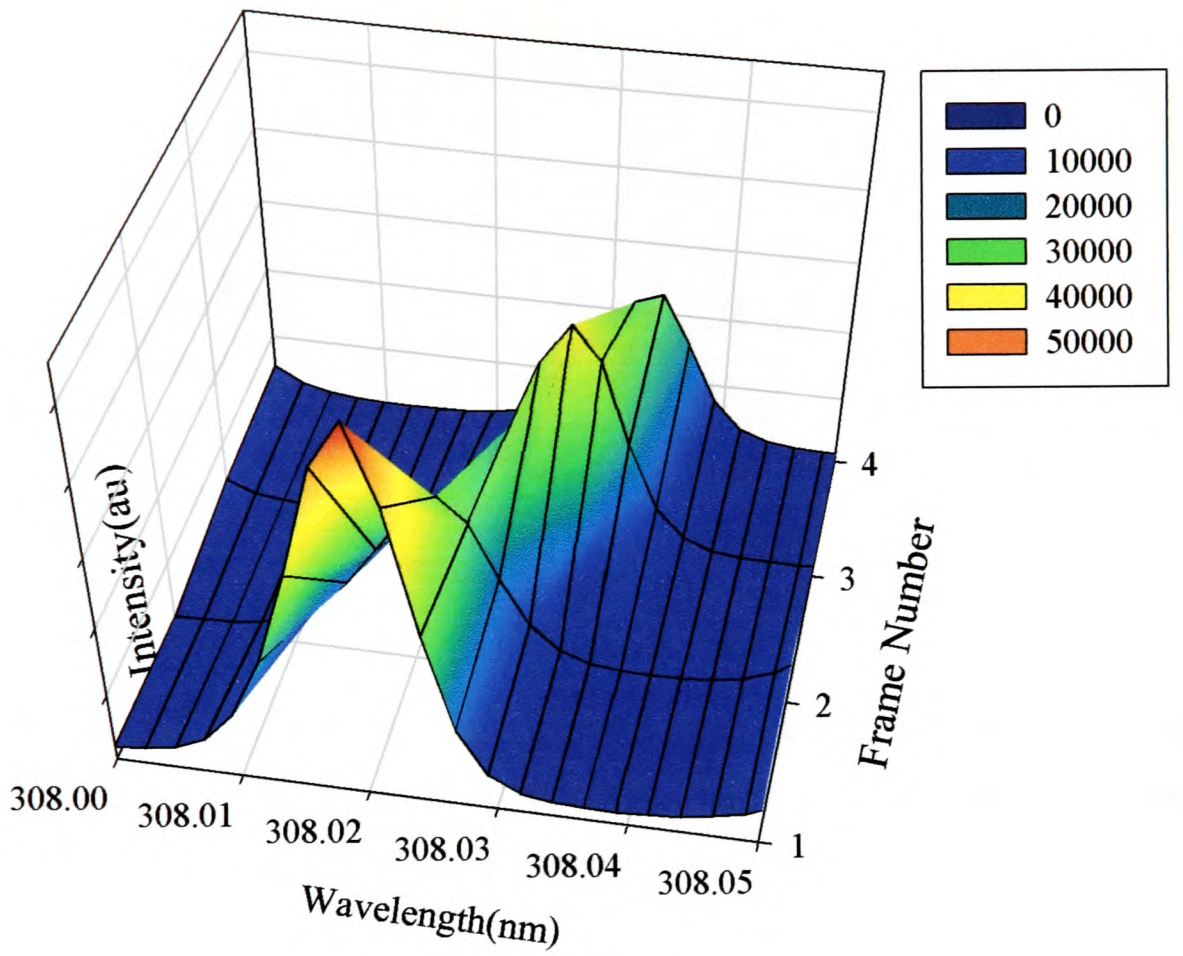


Figure 4.24 shows the movement of crystal etalon peaks with increasing crystal temperature induced by time after pump was unblocked. Frame 1 was taken immediately after the pump was unblocked and Frame 4 was the 4th frame taken after the pump was unblocked, thus corresponds to a higher crystal temperature.

When tuning the laser, achieved by rotating the grating about its vertical axis, the laser output pulse was shown to consist of varying quantities of parasitic lasing in the output and varying quantities of cavity controlled laser output (corresponding to the output resulting form the whole laser cavity). Two well defined laser pulses were present in each pulse, the earlier arriving (1 ns) shorter pulse (3 ns) corresponding to the parasitic lasing output and a later arriving (3-6 ns), longer duration narrow-bandwidth, cavity controlled laser pulse (~7 ns). Figure 4.25 shows the variation of laser pulse shape with wavelength. Arrows indicate the parasitic laser pulse and the cavity-controlled laser pulse as just described.

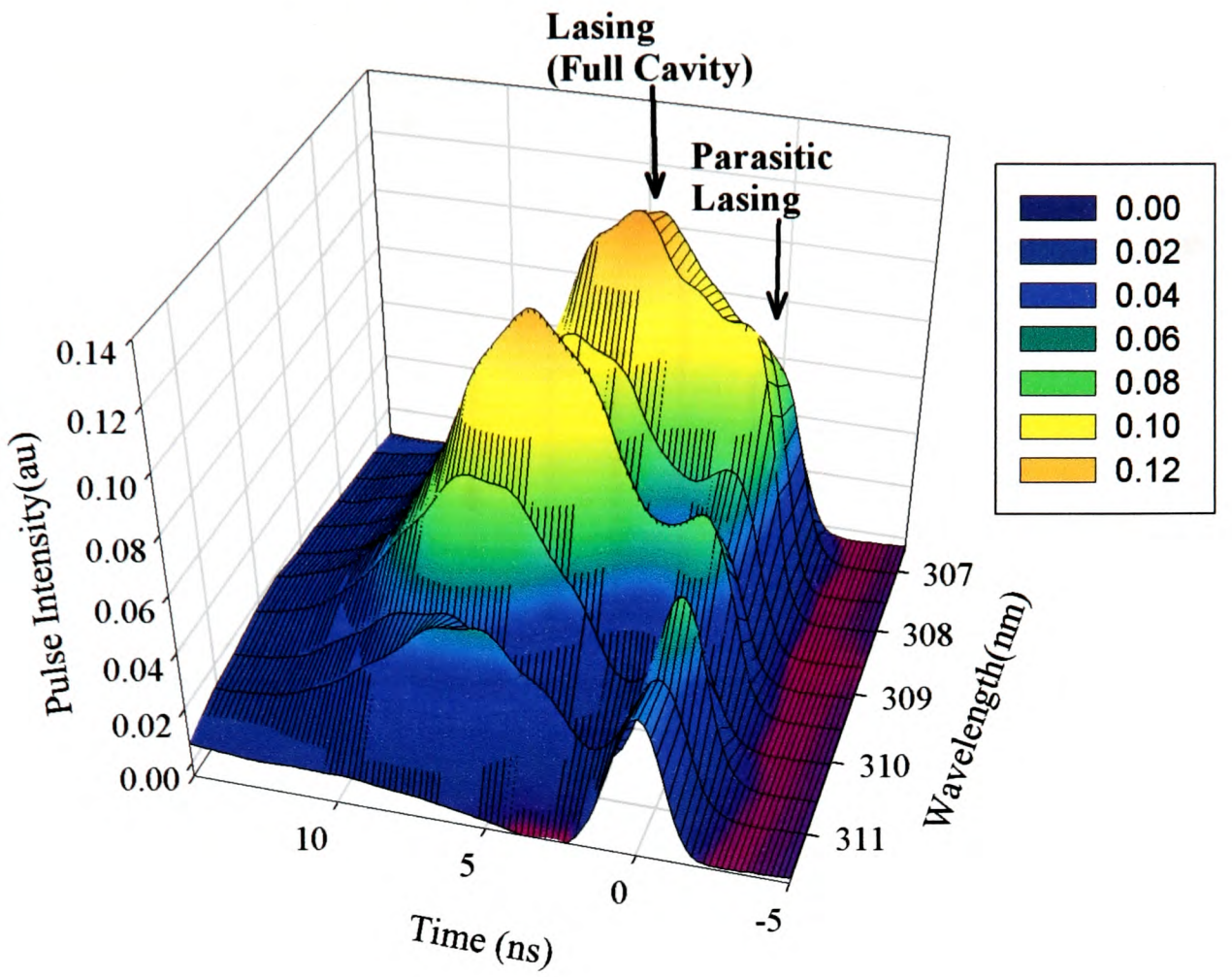


Figure 4.25 shows a 3D representation of the variation in laser pulse shape with tuning between 307.5 nm and 311.6 nm. Note the time axis has time increasing from right to left and the pump pulse arrives at ~-3 ns.

The variation of parasitic laser energy and cavity-controlled energy with wavelength is shown in Figure 4.26. These energies were approximated by determining the area under the corresponding parasitic or cavity-controlled pulse at each wavelength. Also shown in Figure 4.26 are the spectra of the laser output at each wavelength. The spectral output of the parasitic lasing was found to be undetectable relative to the spectral peak of the cavity-controlled lasing, unlike that in Figure 4.22 b). Using this cavity setup tunable output was obtainable between ~306.5 nm and ~311.5 nm.

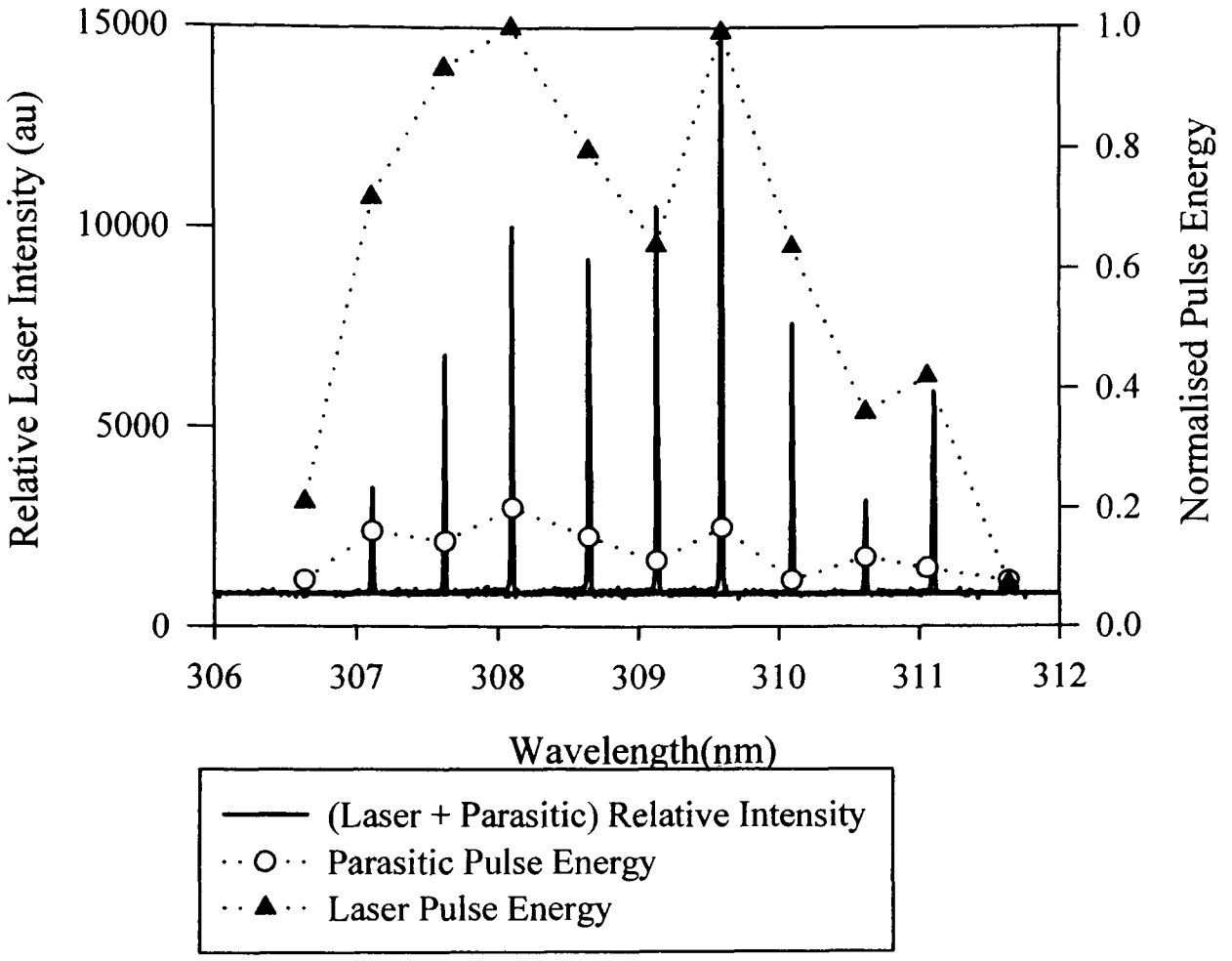


Figure 4.26 shows the tuning curve for Ce:LiLuF in Cavity 2. Shown are the variation of relative intensity with wavelength and the variation of the parasitic lasing pulse energy and laser pulse energy with wavelength. In the relative intensity measurements, the intensities of many frames have been summed over time to give the pulses shown.

The resolution of the spectrometer was determined to be ~0.013 nm (1.4 cm^{-1}) by fitting a Gaussian beam to the cavity controlled laser spectral peak. Because of the similar bandwidths of the pump and laser output, the pump spectral bandwidth and hence the laser spectral bandwidth was confirmed to be not fully resolved by the spectrometer. Thus the linewidth of the laser output was also determined using a Fabry-Perot interferometer. Four different etalon spacings were used; the interferograms from the two larger etalon separations are shown in Figure 4.27 and in more detail in Figure 4.28. The linewidth of the laser output was found to be between 0.67±0.1 cm^{-1} and 0.71±0.1 cm^{-1} as shown in Figure 4.28. Figure 4.27 (bottom) and the corresponding Figure 4.28 b) show the rings to be just resolved; the FSR of the etalon used for these figures was 1.7 cm^{-1}. The presence of well defined rings in the Figure 4.27 (top), made up of only one peak, is indicative of the single mode nature of the laser output, with the parasitic lasing having very low intensity and possibly constituting the ~10% background noise of the image.

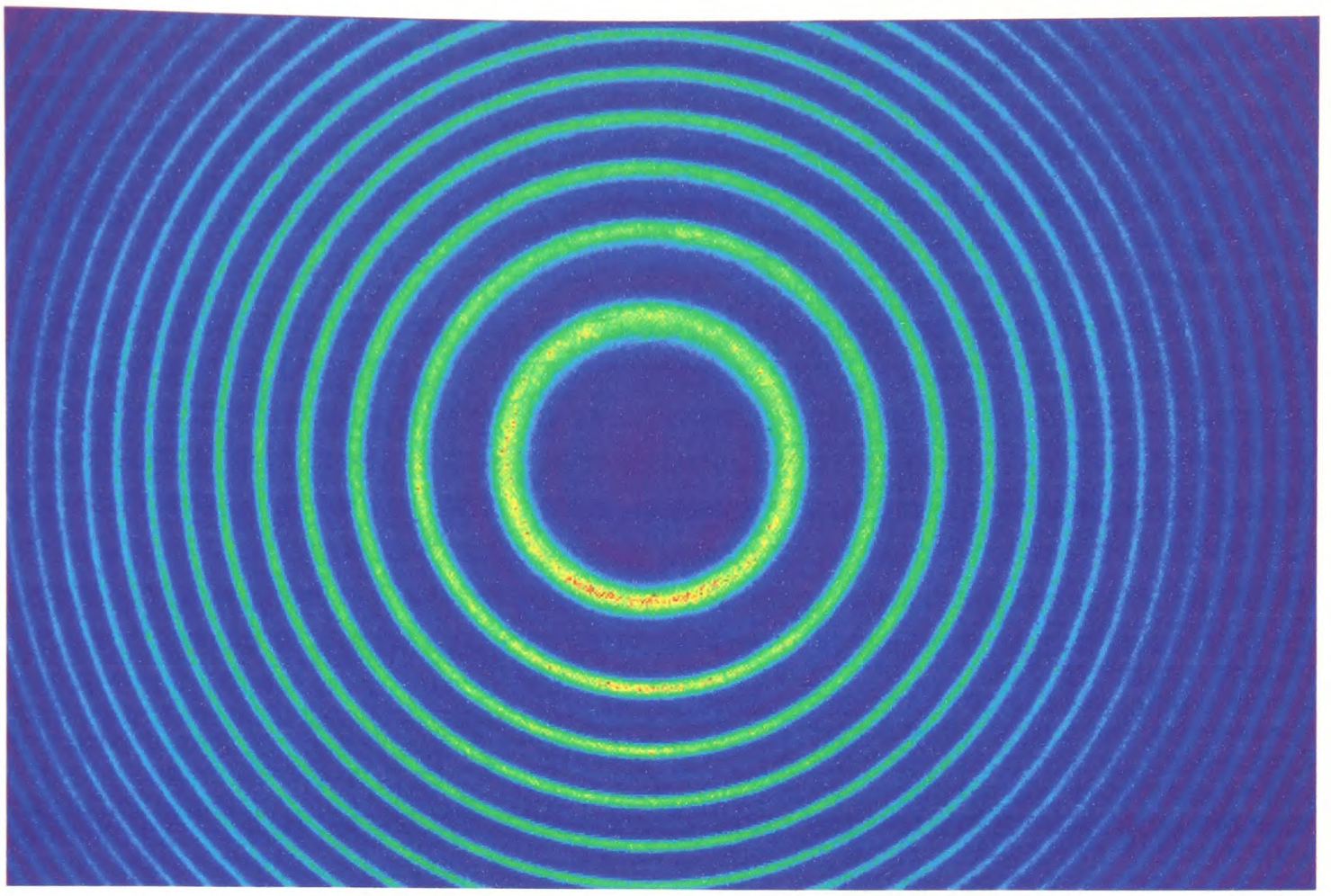


Figure 4.27 shows Fabry-Perot Interferograms with etalon spacings of 0.175cm (top) and 0.290cm (bottom). The top figure shows the rings fully resolved and the bottom show the rings to be just resolved.

previously recorded of 55% (Rambaldi *et al.* 1998). The maximum output obtained with the 80% reflectivity output coupler was 67 mW from 230 mW of incident pump power giving an absolute laser efficiency of 29% with respect to incident pump light at 289nm. Taking into account only the absorbed fraction of the pump power, an absolute efficiency of 41% was achieved. The threshold of the laser with the 80% reflectivity output coupler was approximately 65 mW of absorbed pump power and there was no noticeable saturation at the higher pump powers. The variation of the output power of the cerium laser with time was measured to be ~5%, corresponding to the stability of the pump laser.

When the laser crystal was warmed to room temperature, lasing with the 80% output coupler gave a slope efficiency of 44±3%, with respect to incident pump power, and a maximum output of ~40 mW from 200 mW of incident pump power.

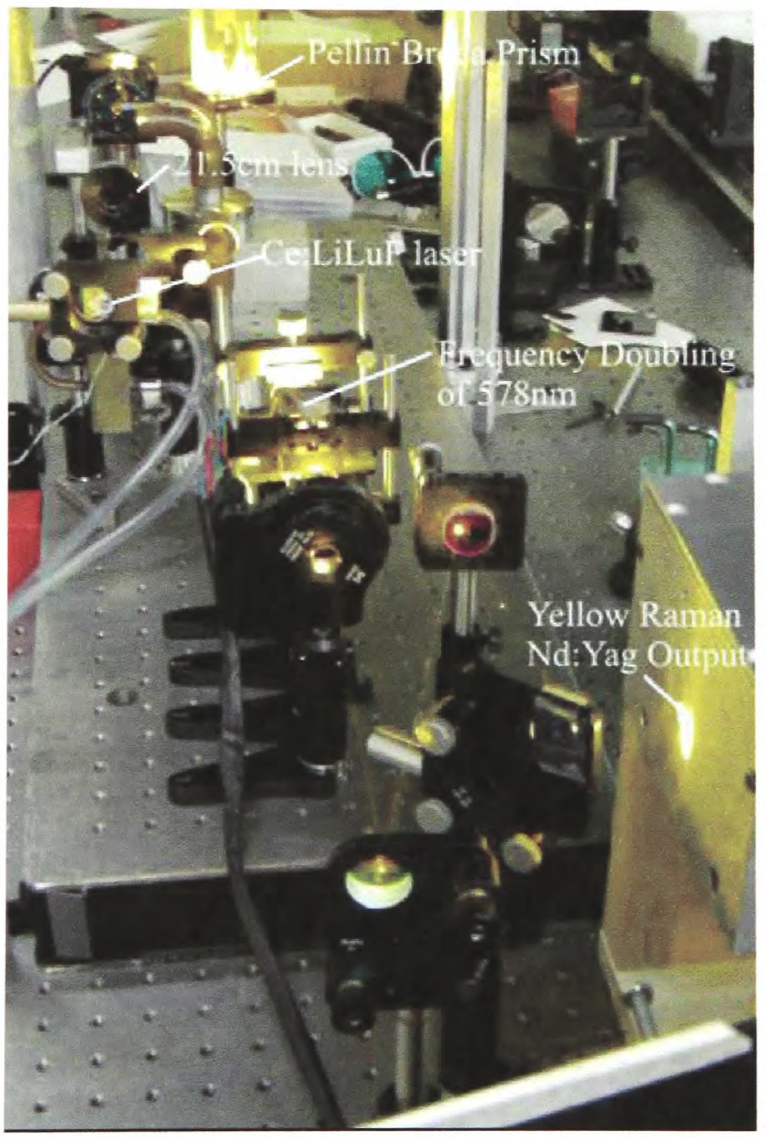


Figure 5.2 shows a photograph of the experimental setup used in the experiments in Chapter 5. Note: the schematic diagram of this setup in Figure 5.1 is rotated 90° anticlockwise relative to this photograph.

With the 90% output coupler, a slope efficiency of 35±2%, with respect to incident pump power, was achieved, which was equivalent to a 46±2% slope efficiency, with respect to absorbed pump power. The maximum output power achieved was 55 mW with 220 mW of

incident pump power. Lasing with a room temperature laser crystal gave a slope efficiency of 24%, with respect to incident pump power and a maximum output of 35 mW from 200 mW of incident pump power.

Lasing was achieved with the 50% output coupler, with the Ce:LiLuF crystal at 7°C, giving a maximum of 17 mW of output at 309 nm, from 200 mW of incident pump power. Lasing with the 50% output coupler was found to fluctuate by ~18% above and below the average 17 mW.

Finally, lasing with the M303 output coupler was obtained, however this lasing was only just above threshold. The maximum laser output achieved was ~7 mW of σ-polarised, 327 nm output, from 200 mW of incident pump power.

Table 5.1 is a summary of the lasing results of the frequency-quadrupled Raman-shifted Nd:YAG pumped Ce:LiLuF laser

Output Coupler Reflectivity	Crystal Temperature 7^0C		Crystal Temperature 25^0C	
	Maximum Output Power	Slope Efficiency	Maximum Output Power	Slope Efficiency
90%	55mW	35±2 %	35mW	24±1 %
80%	67mW	48±3 %	40mW	44±3 %
50%	33mW	n/a	18mW	n/a
7%@308nm 70%@327nm	7mW (@ 327 nm)	n/a	n/a	n/a

The temporal characteristics of the pump and laser pulses (obtained with the 80% output coupler, and for maximum output power) are shown in Figure 5.4. The build up time of the 309 nm laser pulse was found to be ~15±2 ns and the laser pulse length had a FWHM of ~7 ns with the 80% reflectivity output coupler. With the 90% output coupler the build up time was found to be ~19±2 ns and the pulse length was also found to have a FWHM of ~12 ns. The longer build up time found with the 90% output coupler is larger than expected as one would expect a shorter build up with the lower loss cavity. The fluorescence both with and without laser action (cavity blocked and unblocked) is also shown in Figure 5.4. The depletion, measured by comparison of the fluorescence, both with lasing and with the lasing

blocked, was found to be ~45% and 57% with the 80% and 90% reflectivity output couplers respectively.

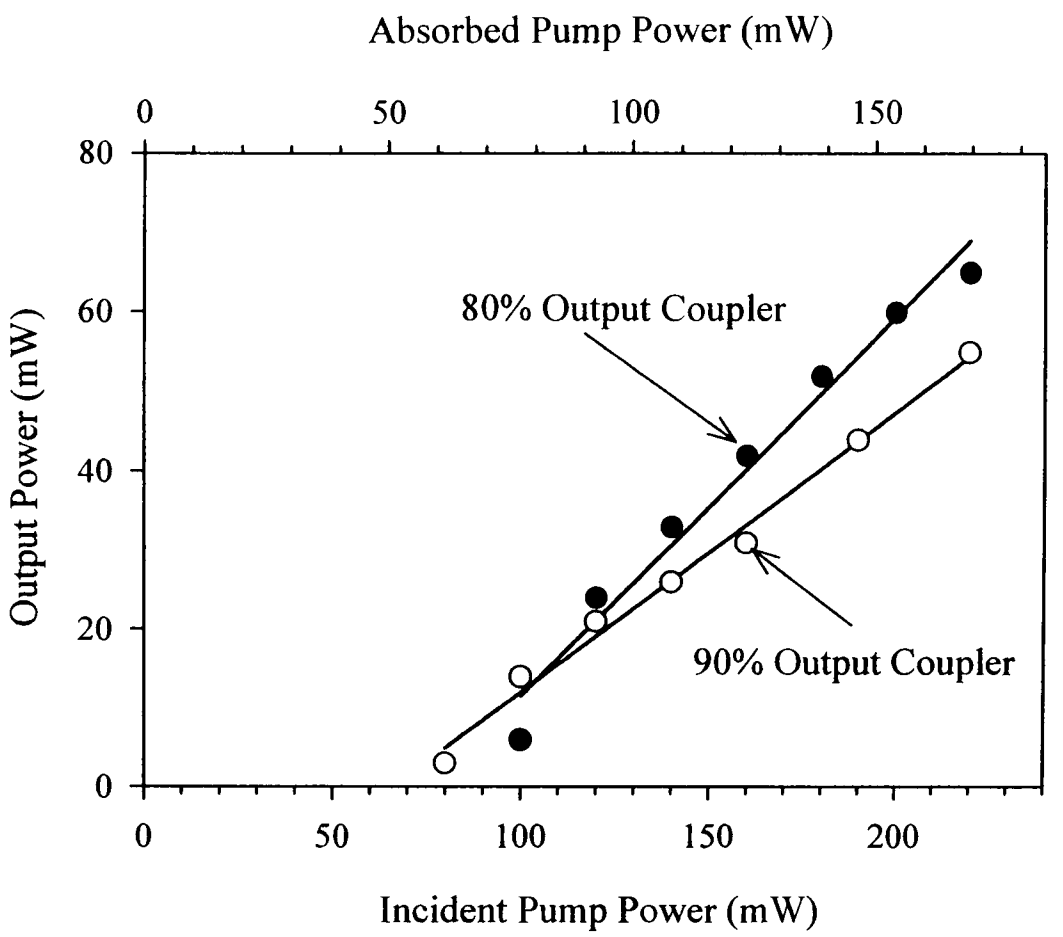


Figure 5.3 shows the 309 nm, π-polarized laser output of a Ce:LiLuF laser (cooled to 7^0C) with an 80% and 90% reflectivity output coupler, pumped by the frequency-quadrupled Raman laser.

5.4 Discussion

A highly efficient all-solid-state UV laser giving up to 67 mW of 309 nm output and 7 mW of 327 nm output has been demonstrated. It is believed that the 62% slope efficiency (with respect to absorbed pump light at 289nm) obtained here is the highest slope efficiency for Ce:LiLuF lasing to date. The optical-to-optical conversion efficiency was up to 41%, with respect to absorbed 289 nm pump power and ~7% with respect to incident 578 nm pump power. The overall IR-to-UV conversion efficiency was ~0.4%, with respect to the 18W laser diode, which is the pump source for the entire system. In comparison, the UV-to-UV conversion efficiency of the UV-CVL pumped Ce:LiLuF laser was up to ~30% corresponding to a visible-to-UV (578 nm-to-309 nm) conversion efficiency of ~2%. Thus results presented in this Chapter reinforce the extremely high efficiencies obtainable from Ce:LiLuF. Using this all-solid-state pump source has in fact proved to be beneficial to the laser performance as well as the having the advantages of an all-solid-state system.

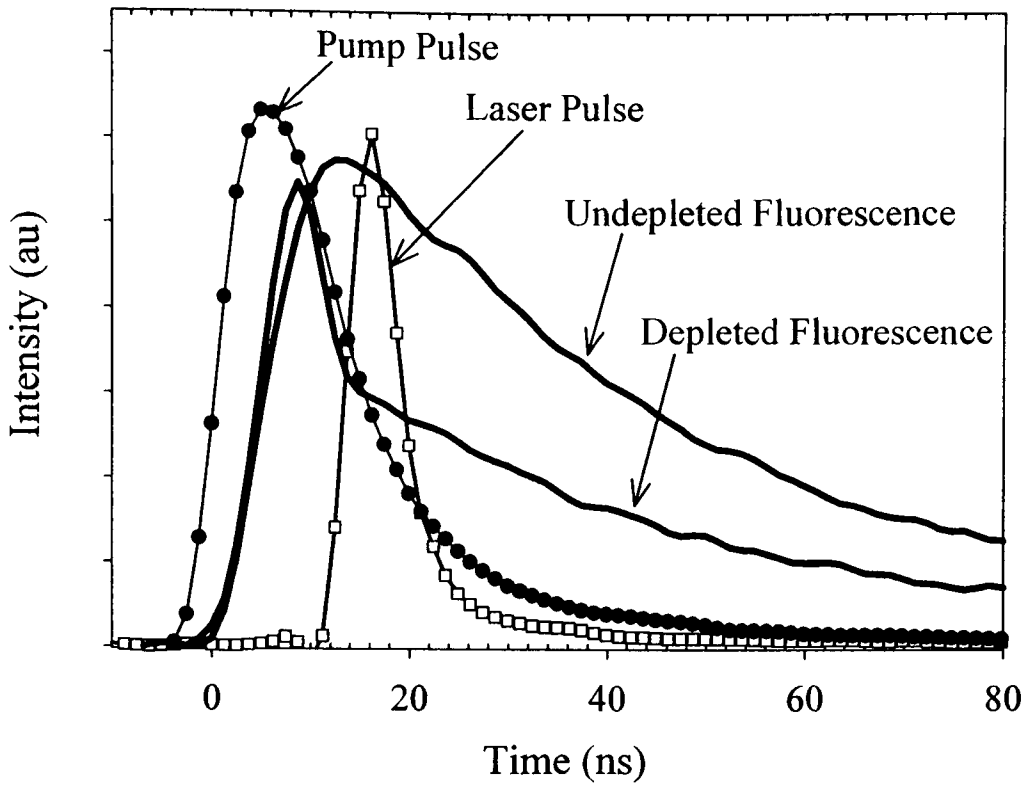


Figure 5.4 shows the fluorescence, laser and pump pulse shapes from the frequency-quadrupled Raman laser pumped Ce:LiLuF laser, with an output power of 67mW, operating with a 80% reflectivity output coupler at 7 ^{0}C.

The excellent performance reported here is thought to be primarily due to the good beam quality of this all-solid-state pump source ($M^2 = 2.8$) compared to that of the UV-CVL pump source ($M^2 = 8$). The good mode-matching (150 μm pump mode diameter and 110 μm laser mode diameter) may have also contributed to the high efficiencies achieved. The near-optimum wavelength of this all-solid-state pump source at 289 nm is also thought to contribute to the high efficiency of this laser compared to the previous all-solid-state pumped Ce:LiLuF lasing efficiencies (Rambaldi *et al.* 1998; Sarukura *et al.* 1998). Comparison of the ESA cross-sections determined in Chapter 2 showed that the ESA cross-section decreased with increasing wavelength, making pumping into the lowest energy absorption band more efficient than pumping into the 210 nm or 245 nm absorption bands. As mentioned previously this has been previously shown to be the case experimentally by Rambaldi *et al.* (Rambaldi *et al.* 1998).

Improved performance is expected through the use of a longer crystal, or double passing the pump beam as in §4.3, which would provide increased pump absorption in the Ce:LiLuF crystal. In the results presented in Chapter 3, the laser output was shown to increase further by decreasing the crystal temperatures below the minimum temperature of 7°C used in the present study. Using a better chiller to cool the laser crystal, such as the Melcor chiller used in the experiments described in Chapter 2, 3 and 4, would allow the crystal temperature to be reduced more, hence a further increase in the output power and slope efficiency could be

expected. Anti-reflection coating or Brewster cutting the Ce:LiLuF crystal, as described in §4.5, would improve both the pumping efficiency and as well as reduce intra-cavity losses, thereby increasing the laser efficiency and decreasing the laser threshold.

The ability to obtain lasing at both 309 nm and 327 nm, corresponding to the two emission peaks for Ce:LiLuF, suggests continuously tunable output will be obtainable between these wavelengths since good tuning over this range has previously been obtained with less efficient lasing with the same crystal, as described in §3.4. Tunable output between 305-333nm from an all-solid-state Ce:LiLuF laser such as this Raman Nd:YAG pumped Ce:LiLuF laser will complement the all-solid-state Ce:LiCAF and Ce:LiSAF lasers available which are tunable between 281-315 nm.

[6] Conclusion

In this thesis Ce:LiLuF has been extensively investigated as a gain and laser medium. The emphasis of this research was directed, firstly, towards gaining an understanding of the anomalous lasing behaviour displayed by Ce:LiLuF. As such the small-signal gain (Chapter 2), excited-state absorption (Chapter 2) and the anomalous lasing behaviour itself (Chapter 3) were studied in detail. The second area of research was focussed on the development of Ce:LiLuF lasers for applied research. As such a narrow-bandwidth, 308 nm Ce:LiLuF laser source was developed, with one of the many applications of such a laser being in the remote sensing of the atmospheric OH radicals (Chapter 4). Finally, a new, efficient, all-solid-state UV pump source for Ce:LiLuF was investigated (Chapter 5). With this new pump source a highly efficient Ce:LiLuF laser was developed.

6.1 Summary of Results

In Chapter 2, the polarised emission cross-sections, across the whole Ce:LiLuF emission spectrum, were reported. These spontaneous emission cross-sections show the 327 nm σ-polarised emission to have the largest emission cross-section of 6.9×10^{-18} cm^2 followed closely by the π-polarised emission cross-section at 309 nm of 6.7×10^{-18} cm^2.

The measured small-signal, single-pass gain in Ce:LiLuF was also presented in Chapter 2. The polarised gain variation over most of the emission spectrum of Ce:LiLuF was presented, showing a slight blue-shift in both short wavelength peaks. This blue-shift was more prominent for the σ-polarised gain and was shown to be the result of a narrow, polarisation dependent excited-state absorption band which had a positive slope in the 300-330 nm region, resulting in the larger blue-shift in the shorter wavelength gain peaks compared to that at the longer wavelength gain peak. Between 314 nm and 316 nm, for the σ-polarisation, absorption was evident as opposed to gain.

At the emission peaks (309 nm and 327 nm), a more detailed investigation into the dependence of the small-signal single-pass gain on polarisation, pump intensity and temperature was undertaken. These results show the π-polarised gain at 309 nm to be the highest with a maximum single-pass gain of 10±1 at -3°C, corresponding to gain coefficient of 30±3cm^{-1}. The low temperature, σ-polarised, 309 nm gain coefficient was found to have a maximum of only 12±1cm^{-1}. The σ-polarised and π-polarised gains at 327 nm were found to be very similar, (both ~15±2 cm^{-1}) at room temperature. This similarity was less apparent at low temperatures where the σ-polarised, 327 nm gain coefficient was 20±2 cm^{-1}, 4±1 cm^{-1} higher than the π-polarised, 327 nm gain coefficient. The temperature dependence of the Ce:LiLuF gain showed, in general, a more dramatic increase in the σ-polarised gain with decreasing temperature (with up to 50% increase in the 309 nm, σ-polarised gain coefficient) compared to the π-polarised gain (with only a 7% increase in the π-polarised gain coefficient at 309 nm).

The excited-state absorption (ESA) in Ce:LiLuF, measured at 261 nm and 349 nm, was also reported in Chapter 2. As in the gain measurements, a polarisation dependence of the ESA was evident, showing more σ-polarised absorption than π-polarised absorption at both wavelengths.

Using the emission and pump absorption cross-sections determined, together with the gain and ESA measurements, the gain and ESA were simulated using a model of the Ce:LiLuF laser. These simulations enabled the polarised effective gain cross-sections at 309 nm and 327 nm to be determined, from which the polarised ESA cross-sections at these wavelengths could be calculated. Further, using this model, the ESA cross-sections at 261 nm and 349 nm were determined and estimates of the 316 nm σ-polarised and 289 nm σ- and π-polarised ESA cross-sections were also made. Overall, the ESA cross-sections determined were of a similar magnitude as the Ce:LiLuF emission and GSA cross-sections, namely of the order of 10^{-18} cm^{-1} suggesting that ESA does in fact have a large influence on the lasing efficiencies in Ce:LiLuF. The σ-polarised ESA cross-sections were found to be larger than the π-polarised ESA cross-sections at all the wavelengths investigated. This polarisation dependence implied that σ-polarised pumping and lasing were more detrimental to the overall laser performance of Ce:LiLuF than π-polarised pumping and lasing. In general it was found that the ESA cross-sections at the shorter wavelengths (2.4 x 10^{-18} cm^2 at 261 nm, σ-polarised) were larger than those at longer wavelengths (1 x 10^{-18} cm^2 at 349 nm, σ-polarised).

The ESA measurements reported in this thesis show a temperature dependent narrow absorption band, coincident with the Ce:LiLuF emission spectrum, superimposed on a broad ESA band (with no temperature dependence). The proposed origin of the broad ESA band

was an absorption resulting in the promotion of an electron from the lowest Ce^{3+} *5d* level to the host conduction band. Evidence of this transition was implied by the determined absorption lifetime and cross-section magnitude of the ESA measured. The narrow absorption band was hypothesised to arise from absorption by colour centres embedded in the conduction band. A temperature dependence of either the formation or relaxation mechanisms of these colour centres was suggested to give rise to the temperature dependence of the narrow-band absorption seen in Ce:LiLuF. The nature of the colour centres could not be ascertained at this stage and further evidence is required to establish exactly how this temperature dependence arises.

A very recent paper (April 2003) by Laroche *et al.* (Laroche *et al.* 2003), previewed online, presented emission cross-sections which were in very close agreement to the values determined in this thesis. Similarly, the π-polarised, 289 nm absorption cross-section for Ce:LiLuF published in the same paper was in excellent agreement with that determined in this thesis. ESA measurements were also reported by Laroche *et al.* (shown in Figure 6.1), which were in excellent agreement with the ESA results reported in this thesis, with similar polarisation and wavelength dependence (Laroche *et al.* 2003). The actual ESA cross-sections were not reported by Laroche *et al.* The ESA measurements reported in Chapter 2, at 309 nm and 327 nm, complement the ESA spectrum reported by Laroche *et al.*, but more importantly give some idea of the ESA behaviour in the emission spectral region of Ce:LiLuF, which was not investigated by Laroche *et al.*

The results of the investigations into the anomalous lasing behaviour displayed by Ce:LiLuF are presented in Chapter 3. Although Ce:LiLuF has been shown to lase at 327 nm or 309 nm when free running, in the laser cavity used in this thesis, the Ce:LiLuF laser preferentially lased at 309 nm with π-polarised output. A Rigrod analysis of the 309 nm Ce:LiLuF lasing enabled an estimated pumping efficiency of 50±5% to be determined for Ce:LiLuF. Further, the temperature dependence of the 309 nm lasing was also investigated. The π-polarised lasing at 309 nm was found to be more sensitive to temperature change than the π-polarised small-signal gain at 309 nm, in that the change in ESA with temperature required to simulate the experimental temperature dependence of laser output was much larger (2×10^{-18} cm^2) than that required to simulate the experimental change in gain with temperature (0.15×10^{-18} cm^2). This increased sensitivity to temperature of the lasing compared to the small-signal gain was tentatively suggested to arise from the presence of additional ESA at 309 nm not seen during the small-signal gain measurements.

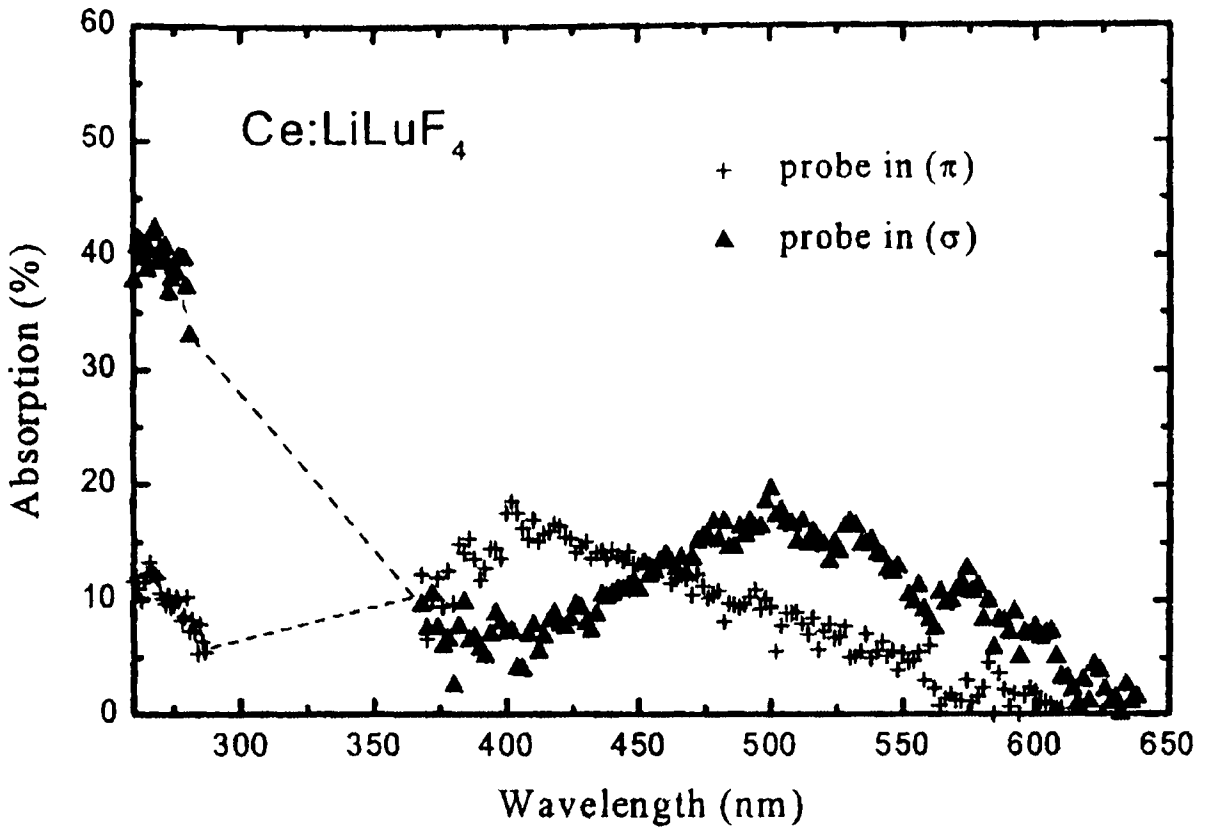


Figure 6.1 shows the absorption spectra of short-lived colour centres in Ce:LiLuF measured by Laroche *et al.* (Laroche *et al.* 2003).

In the laser cavity used in this thesis, Ce:LiLuF lased preferentially at 309 nm and to investigate 327 nm lasing, lasing at 327 nm had to be forced, either by using an output coupler with a higher reflectivity at 327 nm (compared to the reflectivity at 309 nm) or using a prism-tuned cavity. This 327 nm laser showed behaviour with various unusual features. The slope efficiencies and content of the laser output from these cavities were shown to vary with pump power and/or temperature. The laser output was shown to contain multiple polarisation and wavelength output components, the latter particularly with the M302 output coupler (R=92% at 327 nm and R=54% at 309 nm). These multiple components were shown to exist simultaneously and not to be the result of competing laser modes lasing alternately. The effective gain cross-sections determined in Chapter 2 gave some indication of the competition effects to be expected in the lasing but the presence of more than one wavelength or polarisation mode in the output simultaneously was initially not clear. Using a laser model to simulate the lasing in Ce:LiLuF, the presence of multiple polarisation and wavelength components in the laser output with these cavities was shown to be due the gain switched nature of the lasing in Ce:LiLuF when pumped by high peak power, pulsed lasers. The variable slope efficiencies and output content of the Ce:LiLuF laser were shown to arise from the dynamic competition effects between the different laser modes.

Overall, the presence of σ-polarised laser oscillation in the laser cavity was shown to be detrimental to the total laser efficiency. The introduction of a σ-biased loss into a laser cavity,

which forced π-polarised lasing at 327 nm, showed an increase the lasing efficiency by up to 300%. Using such a σ-biased loss in the prism-tuned cavity, the dip in the Ce:LiLuF laser tuning curve at 327 nm, present at low temperatures, was shown to no longer occur. In fact the slope efficiency at 327 nm, in the prism-tuned laser, was found to increase from 1% to 10% with the introduction of the σ-biased loss into the cavity. With the σ-biased loss in the cavity the laser tuning curve for Ce:LiLuF closely followed the π-polarised fluorescence spectrum of Ce:LiLuF.

In Chapter 4, tunable, narrow bandwidth lasing in Ce:LiLuF was achieved using a Littrow grating with telescopic and prism beam expansion. The output bandwidth was ~0.7 cm^{-1} (0.007 nm). Narrow-bandwidth tuning between 306.5 nm and 311.5 nm was presented. The maximum narrow-bandwidth laser output power achieved from this laser however was <2 mW with 360 mW of pump power. Parasitic lasing between a flat high reflector and one crystal face was found to be a prevalent in the high-loss laser cavities investigated in this chapter, however these could be easily overcome with the right coatings and Brewster cut crystals. Laser-crystal induced etalon effects were also shown to be present in this cavity which may in fact prove useful for fine tuning of the laser; however for this the Ce:LiLuF crystal faces would have to be very flat.

Finally in Chapter 5, a new all-solid-state pump source was explored. To the best of the author's knowledge, the Ce:LiLuF pumped by a frequency-quadrupled, Raman-shifted Nd:YAG laser (289 nm) performed with unequalled efficiency. Slope efficiencies as high at 62±3 % were achieved and UV-to-UV optical efficiencies of 41% were achieved with the Ce:LiLuF laser crystal cooled to 7°C. The excellent laser performance is thought to be due to the high 289 nm pump beam quality (M^2=2.8) and good pump (150 μm) and laser (110 μm) mode matching. Lasing at 309 nm and 327 nm was achieved suggesting continuously tunable lasing to be inevitable with this superior pump source. Higher efficiencies can also be expected with further cooling of the Ce:LiLuF crystal.

6.2 *Implications of Results*

The high single-pass gains (G (309 nm, π) = 10) reported in Chapter 2 show the highest gains measured for Ce:LiLuF, with previous gain maximums of 5 measured by Sarukura *et al.* (Sarukura *et al.* 1995a). As mentioned in §1.2, Ce:LiCAF has found application in chirped pulse amplification (CPA) systems. The gain measurements reported here support the application of Ce:LiLuF as an amplifying media in such CPA systems, particularly at 309 nm for π-polarised light. In fact the highest reported single-pass gain determined in Ce:LiCAF and Ce:LiSAF was ~11 (Marshall *et al.* 1994). This gain was obtained with a pump fluence of

2 J/cm^2 which was high compared to the pump fluence used in the experiments reported in this thesis of ~0.5 J/cm^2 from which a gain of 10 at 309 nm was achieved, in Ce:LiLuF. This suggests Ce:LiLuF to be the more desirable choice of amplifying media.

The ESA measurements reported in Chapter 2, provide details of the polarisation dependence of ESA in Ce:LiLuF, both at laser emission wavelengths and pump wavelengths. Of particular interest is the σ-polarised ESA at the 289 nm pump wavelength. This σ-polarised ESA cross-section was estimated to be almost ten times the π-polarised ESA at 289 nm, indicating that one could expect much more efficient lasing with a π-polarised pump. As such the use of unpolarised and σ-polarised pump sources is strongly detrimental to efficient Ce:LiLuF lasing. The ESA measurements reported in this thesis (together with the recently reported ESA results) show the wavelength dependence of ESA in Ce:LiLuF, giving explicit evidence of why lasing is more efficient with a pump source emitting at a wavelength coincident with the longer wavelength GSA peak of Ce:LiLuF at 292 nm, as opposed to the shorter wavelength peaks at 210 nm and 244 nm. Such behaviour was previously reported by Rambaldi *et al.* from comparative experiments (Rambaldi *et al.* 1998).

The detrimental effects of σ-polarised lasing due to ESA in Ce:LiLuF are also of vital importance to the development of these lasers. Such information suggests that intra-cavity polarising elements to force π-polarised lasing are necessary for efficient operation of Ce:LiLuF lasers, particularly at 327 nm. The insignificant amount of ESA at 309 nm and 327 nm for the π-polarisation with crystal temperatures below 0°C indicated by the results presented in this thesis are very encouraging, as this implies better performance can be expected from a cooled Ce:LiLuF crystals than has been obtained from Ce:LiSAF and Ce:LiCAF which are limited by ESA at the laser wavelengths.

Finally, the availability of the efficient, new, all-solid-state pump source at 289 nm, lasing directly into the longest wavelength ground-state absorption peak of Ce:LiLuF is extremely beneficial for Ce:LiLuF laser development. Using the narrow-bandwidth Ce:LiLuF laser described in Chapter 4 with such an all-solid-state pump source constitutes the ideal all-solid-state, narrow-bandwidth, tunable UV laser for airborne remote sensing applications. The use of this all-solid-state pump source may indeed pave the way to a commercial highly efficient Ce:LiLuF-based broadly tunable UV laser.

6.3 *Future work*

Although many answers have been gained from the Ce:LiLuF ESA and gain measurements, many unanswered questions still remain. Firstly the origin of the temperature dependence in Ce:LiLuF requires further investigation to elucidate further details of the proposed origins of

this temperature dependence. A detailed exploration as to the behaviour of the of the narrow-band absorption in Ce:LiLuF is required, in which the wavelength, temperature and polarisation dependence of the absorption could be determined. The measurement of the temperature dependence of the long-lived colour centre absorption between 300 nm and 600 nm, as detected by Sarukura *et al.* (Sarukura *et al.* 1995a) could provide evidence in support of the specific temperature dependence of the narrow-band ESA induced absorption suggested in Ce:LiLuF. Perhaps the more ideal experiments would monitor more explicitly the temperature dependence of the 316 nm, σ-polarised absorption giving direct access to the excited-state absorption within the Ce:LiLuF emission spectrum. Firstly the actual relationship between the 316 nm peak absorption with temperature, pump and probe powers could be ascertained. From such experiments more details as to the absorption mechanism could be obtained, namely whether the mechanism is a single-photon, or multi-photon mechanism and whether the transition is a pump and/or probe-induced absorption process. The temperature dependence of the absorption lifetime may give evidence as to the origin of the temperature dependence, for example whether the temperature dependence arises from the temperature dependence of the creation or decay of the colour centres.

One of the questions still unanswered to date is why, so far, has the temperature dependence of Ce:LiLuF not been reported by other groups working on Ce:LiLuF. Perhaps it has simply not been investigated by other groups. It may also be the case that the origin of the ESA seen in Ce:LiLuF in the Clarendon Laboratory is related to the high repetition rate pump lasers used at the Clarendon Laboratory. High repetition rate lasers may cause cumulative build up of colour centres which are responsible for the temperature effects. Measurements of the lasing or gain with pump sources with varying repetition rates, such as those available from a CVL MOPA system, for which laser repetition rate can be varied between 1 Hz and 12 kHz, may provide some insight into this. The effect of longer-lived transient colour centres on the gain and lasing in Ce:LiLuF can also be obtained from such experiments.

Further cooling of the lasing crystal should also be investigated, however at temperatures much lower than 0°C problems with frosting will arise unless a dry atmosphere is maintained at the crystal faces. It would be interesting to ascertain the extent to which Ce:LiLuF lasing is temperature dependent at temperatures below 0°C, as again this may give some insight into the behaviour observed.

There are a number of other possible paths being investigated toward overcoming detrimental excited state absorption effects in cerium lasers. Such methods include the use of crystal design techniques and improved crystal growth techniques. Crystal growth techniques include the advancement of growth techniques as described by Baldochi *et al.* (Baldochi *et al.* 1999)

who used CF_4 atmospheres in the growth of fluoride crystals as opposed to the previously used inert gas atmospheres. The advantage of this growth atmosphere is that it is highly reactive and as such the number of oxygen induced impurities in the fluoride crystals are greatly reduced, improving the overall mechanical and optical properties of the fluoride crystals.

Crystal design is also becoming a more prominent part of cerium laser research. New crystals have been designed and some have also been shown to display gain such as Ce:$LuPO_4$ (Laroche *et al.* 2003). Co-doping with charge compensators has also been shown to be useful in Ce:LiSAF increasing slope efficiencies by more than 10% (Bayramian *et al.* 1996). Crystal design investigations have also been directed towards alternate pump pathways. For instance Pr^{3+}:LiLuF co-doped with Ce^{3+} has shown electron transfer between excited Pr^{3+} to form excited Ce^{3+}. Such excitation pathways may be useful as alternate pump routes for Ce:LiLuF lasers (Nicolas *et al.* 2001). Similarly in Ce:LiCAF, a new, and possibly useful pump pathway has been discovered via a *VB*→*CB* transition at 112 nm. This pathway may allow the scaling of Ce:LiCAF output powers by pumping this transition with synchrotron emission at 112 nm (Kozeki *et al.* 2001).

In terms of lasing, further work towards the realisation of an efficient narrow-bandwidth tunable laser at 308 nm is required for this laser to be used in remote sensing. The use of a kinetically enhanced UV-CVL, as was used in some of the experiments described in this thesis, would be the first step towards improvement of the output powers from this laser, as the KE-UV-CVL can give up to 900 mW of 289 nm compared to the 400 mW available at the time of the narrow-bandwidth laser experiments. A number of improvements to the laser cavity for improved laser performance as well as narrower bandwidth operation were suggested in the Chapter 4 discussion, including the use of AR coated optics, multiple-prism expanders specifically for 308 nm and a Brewster cut laser crystal. These improvements would result in a reduction of the intra-cavity loss in the cavity and parasitic lasing losses, resulting in lower lasing threshold hence higher output powers. A good quality 308 nm etalon could also aid further narrowing of the spectral bandwidth of the Ce:LiLuF laser. Amplifying the narrow-bandwidth 308 nm output would be of great interest not only in achieving higher output powers for the remote sensing applications, but also for the investigation of amplification in Ce:LiLuF in general. This use of cerium laser crystals as amplifying media is possibly a major direction of the future applications of these cerium-doped fluoride crystals.

Although sum-frequency mixed and frequency-doubled CVLs are ideal sources for research on cerium lasers, all-solid-state lasers, such as the Raman laser described in Chapter 5, are much more user-friendly for the applied research in which these lasers are hoped to be used and for the production of commercial Ce:LiLuF systems. Scaling the output power of this

pump source to >300 mW will enable continuously tunable lasing from Ce:LiLuF. Continuously tunable lasing from an all-solid-state Ce:LiLuF has yet to be obtained by any group working on Ce:LiLuF. Such a laser will complement the already available all-solid-state tunable Ce:LiCAF. Achieving continuously tunable lasing from Ce:LiLuF pumped with the 289 nm frequency-quadrupled Raman laser may give Ce:LiLuF the attention it deserves as a highly efficient, tunable UV solid-state laser.

The Raman laser used in Chapter 5 used a $LiIO_3$ Raman crystal. $LiIO_3$ can give a Raman shift between 770 cm^{-1} and 840 cm^{-1}. In the case of the Raman-shifted Nd:YAG laser used in this thesis the $LiIO_3$ crystal shifted the fundamental from 1064 nm to 1156 nm. Using the 840 cm^{-1} frequency shift of the $LiIO_3$ crystal will provide a shift from 1064 nm to 1168 nm, which when frequency-quadrupled could provide pump light at 292 nm corresponding to the peak of the Ce:LiLuF longer wavelength GSA band. Pumping into this absorption band would result in more pump absorption than is achieved at 289 nm. Pumping the 0.78 mm Ce:LiLuF crystal used in this thesis with 292 nm pump light would result in almost 100% absorption in this very short crystal.

Continuous wave (CW) lasing in Ce:LiLuF has not been investigated as yet, due to the unavailability of an appropriate pump source. The laser simulations shown in §3.6.3, in which lasing with the long (30 ns) pump pulse was used indicate to a first approximation that CW lasing is possible in Ce:LiLuF. However issues such as the thermal properties of Ce:LiLuF and the bottleneck effects (if any) the between the lower laser levels and the ground-state will need to be taken into consideration more explicitly to predict better the operation of a CW Ce:LiLuF laser. The cumulative effects of colour centres would also have to be taken into consideration in a CW laser, however lasing at 309 nm, with π-polarised emission, and the Ce:LiLuF crystal cooled to below 0°C may reduce such affects making them negligible. Frequency-doubled argon ion lasers (FREDs) lasing of 244 nm are a CW source which may be suitable for pumping a Ce:LiLuF CW laser, however the evidence indicated in this thesis suggests ESA may be a problem at this pump wavelength. CW lasers at 266 nm have been developed by Spectraphysics from which 1W of 266 nm can be obtained. Such a laser could be used to pump a CW-Ce:LiCAF or Ce:LiSAF laser.

The work reported in this thesis has concentrated on both the understanding of the dynamics of the processes occurring during lasing in Ce:LiLuF as well as the development of Ce:LiLuF as an efficient solid-state source of tunable UV laser emission. It is hoped that this research has promoted more interest in Ce:LiLuF both spectroscopically and as a highly efficient, all-solid-state, tunable, UV laser medium.

Bibliography

Baldochi, S. L., K. Shimamura, K. Nakano, N. Mujilatu and T. Fukuda (1999). "Growth and optical characteristics of Ce-doped and Ce : Na- co-doped $BaLiF_3$ single crystals." Journal of Crystal Growth **200**(3-4): 521-526.

Barry, H. R., B. Bakowski, L. Corner, T. Freegarde, O. T. W. Hawkins, G. Hancock, R. M. J. Jacobs, R. Peverall and G. A. D. Ritchie (2000). "OH detection by absorption of frequency-doubled diode laser radiation at 308 nm." Chemical Physics Letters **319**(1-2): 125-130.

Basiev, T. T. and R. C. Powell (1999). "Special issue on solid state Raman lasers - Introduction." Optical Materials **11**(4): 301-306.

Bayramian, A. J., C. D. Marshall, J. H. Wu, J. A. Speth, S. A. Payne, G. J. Quarles and V. K. Castillo (1996). "Ce:$LiSrAlF_6$ laser performance with antisolarant pump beam." Journal of Luminescence **69**(2): 85-94.

Buhr, M. and R. Fedosejevs (2002). Ultraviolet Laser Pulse Amplification in Ce:LiLuF. IEEE Canadian Conference on Electrical and COmputer Engineering.

Burshtein, Z., P. Blau, Y. Kalisky, Y. Shimony and M. R. Kokta (1998). "Excited-state absorption studies of Cr^{4+} ions in several garnet host crystals." IEEE Journal of Quantum Electronics **34**(2): 292-299.

Caird, J. A., S. A. Payne, P. R. Staver, A. J. Ramponi, L. L. Chase and W. F. Krupke (1988). "Quantum Electronic-Properties of the $Na_3Ga_2Li_3F1_2$:Cr^{3+} Laser." IEEE Journal of Quantum Electronics **24**(6): 1077-1099.

Cashmore, J. S. (1995). DPhil Thesis Titled: VUV Laser Oscillation in Optically Pumped LaF_3:Nd^{3+}. Atomic and Laser Physics Department, University of Oxford.

Cashmore, J. S., S. M. Hooker and C. E. Webb (1997). "Vacuum ultraviolet gain measurements in optically pumped $LiYF_4$:Nd^{3+}." Applied Physics B-Lasers and Optics **64**(3): 293-300.

Cheung, Y. M. and S. K. Gayen (1994). "Excited-State Absorption in Pr^{3+}-$Y_3Al_5O_{12}$." Physical Review B **49**(21): 14827-14835.

Combes, C. M., P. Dorenbos, C. W. E. vanEijk, C. Pedrini, H. W. DenHartog, J. Y. Gesland and P. A. Rodnyi (1997). "Optical and scintillation properties of Ce^{3+} doped $LiYF_4$ and $LiLuF_4$ crystals." Journal of Luminescence **71**(1): 65-70.

Corner, L., J. S. Gibb, G. Hancock, A. Hutchinson, V. L. Kasyutich, R. Peverall and G. A. D. Ritchie (2002). "Sum frequency generation at 309 nm using a violet and a near-IR DFB diode laser for detection of OH." Applied Physics B-Lasers and Optics **74**(4-5): 441-444.

Coutts, D. W., M. D. Ainsworth and J. A. Piper (1990). "Efficient green/yellow conversion of copper vapour laser output." Optics Communications **75**(3,4): 301-6.

Coutts, D. W., D. J. W. Brown and J. A. Piper (1993). "Measurements of the Divergence Evolution of a Copper-Vapor Laser Output by Using a Cylindrical Imaging Technique." Applied Optics **32**(12): 2058-2061.

Coutts, D. W., J. S. Cashmore and C.E.Webb (1996). Multi kHz PRF cerium lasers pumped by frequency doubled copper vapour lasers. IQEC, Sydney, Australia.

Duarte, F. J. and J. A. Piper (1981). "Prism Pre-Expanded Grazing-Incidence Grating Cavity for Pulsed Dye-Lasers." Applied Optics **20**(12): 2113-2116.

Duarte, F. J. and J. A. Piper (1982a). "Dispersion Theory of Multiple-Prism Beam Expanders for Pulsed Dye-Lasers." Optics Communications **43**(5): 303-307.

Duarte, F. J. and J. A. Piper (1982b). "Comparison of Prism-Expander and Grazing-Incidence Grating Cavities for Copper Laser Pumped Dye-Lasers." Applied Optics **21**(15): 2782-2786.

Duarte, F. J. and J. A. Piper (1983). "Generalized Prism Dispersion Theory." American Journal of Physics **51**(12): 1132-1134.

Duarte, F. J. and J. A. Piper (1984). "Narrow Linewidth, High PRF Copper Laser-Pumped Dye-Laser Oscillators." Applied Optics **23**(9): 1391-1394.

Duarte, F. J. (2000). "Multiple-prism arrays in laser optics." American Journal of Physics **68**(2): 162-166.

Dubinskii, M. A., V. V. Semashko, A. K. Naumov, R. Y. Abdulsabirov and S. L. Korableva (1993a). "Ce-3+-Doped Colquiriite - a New Concept of All-Solid-State Tunable Ultraviolet-Laser." Journal of Modern Optics **40**(1): 1-5.

Dubinskii, M. A., V. V. Semashko, A. K. Naumov, R. Y. Abdulsabirov and S. L. Korableva (1993b). "Spectroscopy of a new active medium of a solid-state UV laser with broadband single pass gain." Laser Physics **3**(1): 216.

Dubinskii, M. A., X. Zhu, A. H. Nur, M. M. Kamal, H. L. Bryant, P. Misra, R. Y. Abdulsabirov, S. L. Korableva, A. K. Naumov and V. V. Semashko (1995).

Analytical application of a LiCAF:Ce laser for combustion studies. Conference on Lasers and Electro Optics.

Dubinskii, M. A. and K. L. Schepler (1998). Tunable UV Ce:LiCAF injection-seeded laser for high brightness. Advanced Solid-State Lasers - Postdeadline papers, Idaho.

Dubinskii, M. A., K. L. Schepler, V. V. Semashko, R. Y. Abdulsabirov, S. L. Korableva and A. K. Naumov (1998). "Spectroscopic analogy approach in selective search for new Ce^{3+}-activated all-solid-state tunable ultraviolet laser materials." Journal of Modern Optics **45**(2): 221-226.

Ehrlich, D. J., P. F. Moutlon and R. M. Osgood (1979). "Ultraviolet solid-state Ce:YLF laser at 325nm." Optics Letters **4**(6): 184.

Ehrlich, D. J., P. F. Moutlon and R. M. Osgood (1980). "Optically pumped Ce:LaF_3 laser at 286nm." Optics Letters **5**(8): 339-341.

Evans, I. J. and C. E. Webb (1994). "A 10-KHz Pulsed Tunable Laser Source at 308-Nm for Tropospheric OH Detection." Chemical Physics Letters **230**(1-2): 127-130.

Gororkov, S. V., A. O. Weissner, T. Schroder, U. Stamm, W. Zschocke and D. Bastings (1998). Efficient high average power and narrow spectral linewidth operation of Ce:LiCAF at 1kHz repetition rate. Advanced Solid State Lasers. W. R. Bosenberg and M. M. Fejer. Optical Society of America, Washington DC. **19:** 2-5.

Hamilton, D. S. (1985). Trivalent cerium doped crystals as tunable laser systems: Two bad apples. Tunable Solid State Lasers. Berlin, Springer**:** 80-90.

Hamilton, D. S., S. K. Gayen, G. J. Pogatshnik, R. D. Ghen and W. J. Miniscalco (1989). "Optical-Absorption and Photoionization Measurements from the Excited-States of Ce^{3+}-$Y_3Al_5O_{12}$." Physical Review B **39**(13): 8807-8815.

Hanna, S. F., R. Barron-Jimenez, T. N. Anderson, R. P. Lucht, J. A. Caton and T. Walther (2002). "Diode-laser-based ultraviolet absorption sensor for nitric oxide." Applied Physics B-Lasers and Optics **75**(1): 113-117.

Henderson, B. and R. H. Bartram (2000). Crystal-Field Engineering of Solid-State Laser Materials, Cambridge University Press.

Holland, F., M. Hessling and A. Hofzumahaus (1995). "In situ measurement of tropospheric OH radicals by laser-induced fluorescence - A description of the KFA instrument." Journal of the Atmospheric Sciences **52**(19): 3394.

Ilev, I. K., H. Kumagai and K. Toyoda (1997). "Ultraviolet and blue discretely tunable double-pass fiber Raman laser." Applied Physics Letters **70**(24): 3200-3202.

Jacobs, R. R., W. F. Krupke and M. J. Weber (1978). "Measurement of excited-state-absorption loss for Ce^{3+}:$Y_3Al_5O_{12}$ and implications for tunable 5d - 4f rare-earth lasers." Applied Physics Letters **33**(5): 410.

Kodama, N., M. Yamaga and B. Henderson (1998). "Energy levels and symmetry of Ce^{3+} in fluoride and oxide crystals." Journal of Applied Physics **84**(10): 5820-5822.

Koepke, C., K. Wisniewski, M. Grinberg, A. Majchrowski and T. P. J. Han (2001). "Excited state absorption in chromium doped $Li_2B_4O_7$ glass." Journal of Physics-Condensed Matter **13**(11): 2701-2716.

Kozeki, T., Y. Suzuki, M. Sakai, H. Ohtake, N. Sarukura, Z. L. Liu, K. Shimamura, K. Nakano and T. Fukuda (2001). "Observation of new excitation channel of cerium ion through highly vacuum ultraviolet transparent LiCAF host crystal." Journal of Crystal Growth **229**(1): 501-504.

Kuck, S., K. L. Schepler, S. Hartung, K. Petermann and G. Huber (1997). "Excited state absorption and its influence on the laser behavior of Cr4+-doped garnets." Journal of Luminescence **72-4**: 222-223.

Laroche, M., S. Girard, R. Moncorge, G. J. Quarles and J. Y. Gesland (10 -15 September 2000). Compact and tunable UV-Visible lasers based on Ce-doped laser crystals. CLEO EUROPE, Nice, France.

Laroche, M., S. Girard, R. Moncorge, M. Bettinelli, R. Y. Abdulsabirov and V. V. Semashko (2003). "Beneficial effect of Lu^{3+} and Yb^{3+} ions in UV materials." Optical Materials **22**: 147-154.

Lawson, J. K. and S. A. Payne (1993). "Excited-State Absorption of Eu^{2+}-Doped Materials." Physical Review B **47**(21): 14003-14010.

Lim, K. S. and D. S. Hamilton (1988). "UV-Induced Loss Mechanisms in a Ce^{3+}-$YLiF_4$ Laser." Journal of Luminescence **40-1**: 319-320.

Lim, K. S. and D. S. Hamilton (1989). "Optical Gain and Loss Studies in Ce^{3+}-$YLiF_4$" Journal of the Optical Society of America B-Optical Physics **6**(7): 1401-1406.

Little, C. E. (1999). Metal Vapour Lasers, John Wiley and Sons Ltd.

Littman, M. G. and H. J. Metcalf (1978). "Spectrally narrow pulsed dye laser without beam expander." Applied Optics **17**(14): 2224.

Liu, Z., S. Izumida, H. Ohtake, N. Sarukura, K. Shimamura, N. Mujilatu, S. L. Baldochi and T. Fukuda (1998). "High-pulse-energy, all-solid-state, ultraviolet laser oscillator using large Czochralski-grown Ce : LiCAF crystal." Japanese Journal of Applied Physics Part 2-Letters **37**(11A): L1318-L1319.

Liu, Z. L., K. Shimamura, K. Nakano, N. Mujilatu, T. Fukuda, T. Kozeki, H. Ohtake and N. Sarukura (2000). "Direct generation of 27-mJ, 309-nm pulses from a Ce^{3+}: $LiLuF_4$ oscillator using a large-size Ce^{3+}: $LiLuF_4$ crystal." Japanese Journal of Applied Physics Part 2-Letters **39**(2A): L88-L89.

Liu, Z. L., T. Kozeki, Y. Suzuki, N. Sarukura, K. Shimamura, T. Fukuda, M. Hirano and H. Hosono (2001). "Chirped-pulse amplification of ultraviolet femtosecond pulses by

use of Ce^{3+}: $LiCaAlF_6$ as a broadband, solid-state gain medium." Optics Letters **26**(5): 301-303.

Marshall, C. D., J. A. Speth, S. A. Payne, W. F. Krupke, G. J. Quarles, V. Castillo and B. H. T. Chai (1994). "Ultraviolet-Laser Emission Properties of Ce^{3+}-Doped $LiSrAlF_6$ and $LiCaAlF_6$." Journal of the Optical Society of America B-Optical Physics **11**(10): 2054-2065.

Marshall, G. D. and D. W. Coutts (2000). "Repetition rate scaling up to 100 kHz of a small-scale (50W) kinetically enhanced copper vapor laser." IEEE Journal of Selected Topics in Quantum Electronics **6**(4): 623-628.

McGonigle, A. J. (2000). DPhil Thesis Titled: Tunable UV Lasers. Department of Atomic and Laser Physics. Oxford, UK, University of Oxford.

McGonigle, A. J. S., D. W. Coutts and C. E. Webb (1999a). "A 380-mW 7-kHz cerium LiLuF laser pumped by the frequency doubled yellow output of a copper-vapor-laser." IEEE Journal of Selected Topics in Quantum Electronics **5**(6): 1526-1531.

McGonigle, A. J. S., D. W. Coutts and C. E. Webb (1999b). "530-mW 7-kHz cerium LiCAF laser pumped by the sum-frequency- mixed output of a copper-vapor laser." Optics Letters **24**(4): 232-234.

McGonigle, A. J. S., S. Girard, D. W. Coutts and R. Moncorge (1999c). "10kHz continuously tunable Ce : $LiLuF_4$ laser." Electronics Letters **35**(19): 1640-1641.

McGonigle, A. J. S., D. W. Coutts, S. Girard and R. Moncorge (2001a). "A 10 kHz Ce : LiSAF laser pumped by the sum-frequency-mixed output of a copper vapour laser." Optics Communications **193**(1-6): 233-236.

McGonigle, A. J. S., R. Moncorge and D. W. Coutts (2001b). "Temperature-dependent polarization effects in Ce : LiLuF." Applied Optics **40**(24): 4326-4333.

McGonigle, A. J. S., A. J. Andrews, D. W. Coutts, G. P. Hogan, K. S. Johnston, J. D. Moorhouse and C. E. Webb (2002). "Compact 2.5-W 10-kHz Nd : YLF-pumped dye laser." Applied Optics **41**(9): 1714-1717.

Miniscalco, W. J., J. M. Pellegrino and W. M. Yen (1978). "Measurement of excited-state absorption in Ce^{3+}:YAG." Journal of Applied Physics **49**(12): 6109.

Mohamed, A. K., A. Mustellier, J. P. Faleni and E. Rosencher (2002). "Tunable ultraviolet intracavity tripled Ti : sapphire laser." Optics Letters **27**(16): 1457-1459.

Moncorge, R. and T. Benyattou (1988). "Excited-State-Absorption and Laser Parameters of V-2+ in Mgf2 and Kmgf3." Physical Review B **37**(16): 9177-9185.

Nebel, A. and R. Beigang (1991). "External Frequency-Conversion of Cw Mode-Locked Ti-Al_2O_3 Laser- Radiation." Optics Letters **16**(22): 1729-1731.

Nicolas, S., E. Descroix, Y. Guyot, M. F. Joubert, R. Y. Abdulsabirov, S. L. Korableva, A. K. Naumov and V. V. Samashko (2001). "$4f^2$ to 4f5d excited state absorption in Pr^{3+}doped crystals." Optical Materials **16**(1-2): 233-242.

Okada, F., S. Togawa, K. Ohta and S. Koda (1994). "Solid-State Ultraviolet Tunable Laser - a Ce^{3+} Doped $LiYF_4$, Crystal." Journal of Applied Physics **75**(1): 49-53.

Ono, S., Y. Suzuki, T. Kozeki, H. Murakami, H. Ohtake, N. Sarukura, H. Sato, S. Machida, K. Shimamura and T. Fukuda (2002). "High-energy, all-solid-state, ultraviolet laser power-amplifier module design and its output-energy scaling principle." Applied Optics **41**(36): 7556-7560.

Owen, J. F., P. B. Dorian and T. Kobayasi (1981). "Excited-state absorption in Eu^{2+}:CAF_2 and Ce^{3+}:YAG single crystals at 298 and 77K." Journal of Applied Physics **52**(3): 1216-1223.

Pask, H. M. and J. A. Piper (3-6 Feb. 2002). Design and operation of an efficient 1.4W diode pumped Raman laser at 578nm. Advanced Solid State Lasers, Quebec, Canada.

Pask, H. M. and J. A. Piper (1998). "Practical 580nm source based on frequency doubling of an intracavity-Raman-shifted Nd : YAG laser." Optics Communications **148**(4-6): 285-288.

Pask, H. M. and J. A. Piper (1999). "Efficient all-solid-state yellow laser source producing 1.2-W average power." Optics Letters **24**(21): 1490-1492.

Pask, H. M. and J. A. Piper (2000). "Diode-pumped LiIO3 intracavity Raman lasers." IEEE Journal of Quantum Electronics **36**(8): 949-955.

Payne, S. A., L. L. Chase and G. D. Wilke (1988). "Excited-State Absorption-Spectra of V^{2+} in $KMgF_3$ and MgF_2." Physical Review B **37**(2): 998-1006.

Petersen, A. B., C. D. Marshall and G. J. Quarles (1996). High repetition rate Ce:LiCAF tunable UV laser. Conference for Lasers and Electro-Optics.

Petersen, A. B. (1997). All solid-state 228-240 nm source based on Ce:LiCAF. OSA Advanced Solid-State-Lasers, ASSL, Washington DC, Paper PD-2.

Pinto, J. F., G. H. Rosenblatt, L. Esterowitz, V. Castillo and G. J. Quarles (1994). "Tunable Solid-State Laser Action in $Ce^{3+}LiSrAlF_6$." Electronics Letters **30**(3): 240-241.

Pinto, J. F., L. Esterowitz and G. J. Quarles (1995). "High-Performance $Ce^{3+}LiSrAlF_6$/$LiCaAlF_6$ Uv Lasers with Extended Tunability." Electronics Letters **31**(23): 2009-2011.

Pinto, J. F. and L. Esterowitz (1997). "Distributed-feedback, tunable Ce^{3+}-doped colquiriite lasers." Applied Physics Letters **71**(2): 205-207.

Pinto, J. F., L. Esterowitz and T. J. Carrig (1998). "Extended wavelength coverage of a Ce^{3+}: LiCAF laser between 223 and 243 nm by sum frequency mixing in beta-barium borate." Applied Optics **37**(6): 1060-1061.

Pogatshnik, G. J., S. K. Gayen and D. S. Hamilton (1984). "Laser-Induced Defect Centers in Ce^{3+}:CaF_2." Journal of Luminescence **31-2**(DEC): 251-253.

Pogatshnik, G. J. and D. S. Hamilton (1987). "Excited-State Photoionization of Ce-$^{3+}$ Ions in Ce^{3+}:CaF_2." Physical Review B **36**(16): 8251-8257.

Rambaldi, P., M. Douard and J. P. Wolf (1995). "New UV Tunable Solid-State Lasers for Lidar Applications." Applied Physics B-Lasers and Optics **61**(1): 117-120.

Rambaldi, P., R. Moncorge, J. P. Wolf, C. Pedrini and J. Y. Gesland (1998). "Efficient and stable pulsed laser operation of Ce : $LiLuF_4$ around 308 nm." Optics Communications **146**(1-6): 163-166.

Ranieri, I. M., K. Shimamura, K. Nakano, T. Fujita, Z. Liu, N. Sarukura and T. Fukuda (2000). "Crystal growth of Ce : $LiLuF_4$ for optical applications." Journal of Crystal Growth **217**(1-2): 151-156.

Sarukura, N., M. A. Dubinskii, Z. L. Liu, V. V. Semashko, A. K. Naumov, S. L. Korableva, R. Y. Abdulsabirov, K. Edamatsu, Y. Suzuki, T. Itoh and Y. Segawa (1995a). "Ce^{3+}-Activated Fluoride-Crystals as Prospective Active Media for Widely Tunable Ultraviolet Ultrafast Lasers with Direct 10- ns Pumping." IEEE Journal of Selected Topics in Quantum Electronics **1**(3): 792-804.

Sarukura, N., Z. L. Liu, Y. Segawa, K. Edamatsu, Y. Suzuki, T. Itoh, V. V. Semashko, A. K. Naumov, S. L. Korableva, R. Yu, R. Y. Abdulsabirov and M. A. Dubinskii (1995b). "Ce^{3+}:LuLiF4 as a Broad-Band Ultraviolet Amplification Medium." Optics Letters **20**(3): 294-296.

Sarukura, N., Z. L. Liu, H. Ohtake, Y. Segawa, M. A. Dubinskii, V. V. Semashko, A. K. Naumov, S. L. Korableva and R. Y. Abdulsabirov (1997). "Ultraviolet short pulses from an all-solid-state Ce:LiCAF master-oscillator-power-amplifier system." Optics Letters **22**(13): 994-996.

Sarukura, N., Z. L. Liu, S. Izumida, M. A. Dubinskii, R. Y. Abdulsabirov and S. L. Korableva (1998). "All-solid-state tunable ultraviolet subnanosecond laser with direct pumping by the fifth harmonic of a Nd : YAG laser." Applied Optics **37**(27): 6446-6448.

Skripko, G. A., S. G. Bartoshevich, I. V. Mikhnyuk and I. G. Tarazevich (1991). "LiB_3O_5 - a Highly Efficient Frequency-Converter for Ti-Sapphire Lasers." Optics Letters **16**(22): 1726-1728.

Staebler, D. L. and S. E. Schnatterly (1971). "Optical studies of a photochomic colout centre in rare-earth-doped CaF_2." Physical Review B **3**(2): 516.

Waynant, R. W. and P. H. Klein (1985). "Vacuum Ultraviolet-Laser Emission from Nd^{+3}-LaF_3." Applied Physics Letters **46**(1): 14-16.

Weber (1986). Handbook of Laser Science and Technology; Optical Materials Part 2, CRC Press.

Weber, M. J. (1973). "Nonradiative decay from 5d states of rare earths in crystals." Solid State Communications **12**: 741-744.

Withford, M. J., D. J. W. Brown, D. W. Coutts and J. A. Piper (1995). "Increased Efficiency of High-Beam Quality Extraction from a Copper-Vapor Laser with H-2-Ne Admixtures." Ieee Journal of Quantum Electronics **31**(5): 898-902.

Withford, M. J., D. J. W. Brown and J. A. Piper (1996). "Optimization of H_2 -Ne buffer gas mixtures for copper vapor lasers." Ieee Journal of Quantum Electronics **32**(8): 1310-1315.

Withford, M. J., D. J. W. Brown, R. J. Carman and J. A. Piper (1997). "Investigation of the effects of bromine and hydrogen bromide additives on copper vapour laser performance." Optics Communications **135**(1-3): 164-170.

Withford, M. J., D. J. W. Brown, R. J. Carman and J. A. Piper (1998a). "Kinetically enhanced copper vapour lasers employing H_2-HCl-Ne buffer gas mixtures." Optics Communications **154**(1-3): 160-166.

Withford, M. J., D. J. W. Brown, R. J. Carman and J. A. Piper (1998b). "Enhanced performance of elemental copper-vapor lasers by use of H_2-HCl-Ne buffer-gas mixtures." Optics Letters **23**(9): 706-708.

Yamaga, M., N. Kodama, T. Yosida, B. Henderson and K. Kindo (1997). "An electron-spin-resonance study of substitutional disorder in Ce^{3+}-doped $CaYAlO_4$." Journal of Physics-Condensed Matter **9**(44): 9639-9649.

Yamaga, M., D. Lee, B. Henderson, T. P. J. Han, H. G. Gallagher and T. Yosida (1998). "The magnetic and optical properties of Ce^{3+} in $LiCaAlF_6$." Journal of Physics-Condensed Matter **10**(14): 3223-3237.

Yamaga, M., N. Kodama and T. Imai (1999). "Optical spectroscopy of Ce^{3+} in $CaNaYF_6$ and $BaMgF_4$." Radiation Effects and Defects in Solids **149**(1-4): 335-339.

Yamaga, M., M. Honda, K. Shimamura, T. Fukuda and T. Yosida (2000). "Electron spin-resonance study on Ce^{3+} in $BaLiF_3$." Journal of Physics-Condensed Matter **12**(27): 5917-5928.

Yamaga, M., K. Hattori, N. Kodama, N. Ishizawa, M. Honda, K. Shimamura and T. Fukuda (2001a). "Superlattice structure of Ce^{3+}-doped $BaMgF_4$ fluoride crystals - x-ray diffraction, electron spin-resonance, and optical investigations." Journal of Physics-Condensed Matter **13**(48): 10811-10824.

Yamaga, M., T. Imai, K. Shimamura and T. Fukuda (2001b). "Optical and ESR studies of Ce^{3+} in perovskite fluoride crystals $BaLiF_3$ and $KMgF_3$." Journal of Crystal Growth **229**(1): 487-491.

Yamaga, M., T. Inoue, S. Yabashi, M. Honda, J. P. R. Wells, K. Shimamura and T. Fukuda (2002a). "Site symmetry and crystal field splittings of Ce3+ in LiLuF4 and LiSr0.8Ca0.2AlF6." Radiation Effects and Defects in Solids **157**(6-12): 977-982.

Yosida, T., M. Yamaga, D. Lee, T. P. J. Han, H. G. Gallagher and B. Henderson (1997). "The electron spin resonance and optical spectra of Ce3+ in LiYF4." Journal of Physics-Condensed Matter **9**(18): 3733-3739.

Zhou, C. S. (1984). "Design of a pulsed single-mode dye laser." Applied Optics **23**(17): 2879.

Appendix A–Laser Simulation Code in C

```
#include <stdio.h>
#include <math.h>
#include <string.h>
#include "nrutil.h"
#include "nrutil.c"
#include "stdio.h"
#include "stdlib.h"
void initialise(int loop);                          /*allocation of memory and setting starting intensities*/
double *n4f, *n5d, *Ipump;                          /*define matracies*/
double *I308piL, *I308piR, *I308sigL, *I308sigR, *I327piL, *I327piR, *I327sigR, *I327sigL;
double *loop308pi, *loop308sig, *loop327pi, *loop327sig;
double I308piLoutput, I308sigLoutput, I327piLoutput, I327sigLoutput;
double I327sigLloss, I308sigLloss, I327piLloss, I308piLloss;
void shiftlaser(int q, int loop, int a);            /*shifts the laser + intensity along every j*/
void shiftIpump(int j);                             /*shifts a fixed pump intensity every j*/
void openfile();                                    /*opens input pump file*/
void closefile();                                   /* closes input pump file when finished*/
void shiftIpumpprofile(int d, int j);               /*shifts the pump from file every d*/
void shiftprobepulse(int j);
double dn4f(int i);                                 /*determines dn4f*/
double dn5d(int i);                                 /*determines dn5d*/
double dn4f308pilaser(int i);                       /*determines dn4f due to stimulated emission 308*/
double dn4f308siglaser(int i);                      /*determines dn4f due to stimulated emission 308*/
double dn4f327pilaser(int i);                       /*determines dn4f due to stimulated emission 327pi*/
double dn4f327siglaser(int i);                      /*determines dn4f due to stimulated emission 327sig*/
double dn5d308pilaser(int i);                       /*determines dn5d due to stimulated emission 308*/
double dn5d308siglaser(int i);                      /*determines dn5d due to stimulated emission 308*/
double dn5d327pilaser(int i);                       /*determines dn4f due to stimulated emission 327pi*/
double dn5d327siglaser(int i);                      /*determines dn4f due to stimulated emission 337sig*/
double dIpump(int i);                               /*determines dIpump*/
double dIpump2(int i);      /*determines dIpump2 - taking into account ESA @pump wavelength*/
double dI308piL(int i);                             /*determines change in probe intensity @308nm, pi*/
double dI308sigL(int i);                            /*determines change in probe intensity @308nm, pi*/
double dI308sigR(int i);                            /*determines change in probe intensity @308nm, pi*/
double dI327sigL(int i);                            /*determines change in probe intensity @327nm, sig*/
double dI327piL(int i);                             /*determines change in probe intensity @327nm, pi*/
```

```
double dI308piR(int i);                 /*determines change in probe intensity @308nm, pi*/
double dI327sigR(int i);                /*determines change in probe intensity @327nm, sig*/
double dI327piR(int i);                 /*determines change in probe intensity @327nm, pi*/
double spontemission308sig(int i);
double spontemission308pi(int i);
double spontemission327sig(int i);
double spontemission327pi(int i);
double update();                /*updating all values in matrices taking delta fns into account*/
double updatelaser();           /*updates n5d and n4f levels due to stimulated emission*/
void outputIpump2(void);        /*outputs intensity to file I2.XXX*/
void outputn4f(void);           /*outputs n4f to file n4f.XXX*/
void outputn5d(void);           /*outputs to file n5d.XXX*/
void outputI308piL(void);       /*outputs to file I308pid.XXX*/
void outputI327piL(void);       /*outputs to file I327pi.XXX*/
void outputI327sigL(void);      /*outputs to file I327sig.XXX*/
void outputI308piR(void);       /*outputs to file I308pid.XXX*/
void outputI327piR(void);       /*outputs to file I327pi.XXX*/
void outputI327sigR(void);      /*outputs to file I327sig.XXX*/
void outputlaser(void);
void laserloss(void);           /*outputs energy lost*/
void info(void);
double Iprobeintensity(void);   /* Outputs probe intensity*/
double probe;                   /*outputs an information file to info.XXX*/
double timedt(void);            /*determines time step length from crystal width and slicenumber*/
int stepnumber();               /*determines number if time steps duration of pulse and dt*/
int inpulse() ;                 /*determines whether we are still in a pulse*/
int Ipumpstepwidth();           /*determines how many steps to split intensity pulse into*/
int looplength();               /*determines no of steps in loop*/
double dt;                      /*takes value of timedt*/
double plancktimesfreqpump;     /*calculates hv*/
double plancktimesfreq308;
double plancktimesfreq327;
double deltaz;                  /*calculates c x dt*/
double dz;
void outputprobeintensity(void);
float temp;


/*FILE DETAILS TO BE UPDATED EVERYTIME*/

char prefix[] = ".pag";
const double pumppower = 800;           /*average pump power mW*/
const double peakintensity=1e12;        /*peak intensity of pump*/
const int slicenumber = 101;            /*determines how many z steps there are*/

/*experimental variables*/

const double duration = 5e-8;           /*duration of entire experiment*/
const double pulselength = 2.94e-8;     /*entire length in time of pump pulse NOT FWHM*/
const double spotsize=2.1e-9;           /*spotsize of pump m2 */
const double outputcoupler308 = 0.9;    /*output coupler reflectivity*/
const double outputcoupler327 = 0.9;
const double cavitylength = 180e-3;/* round trip length m*/
const double notloss308pi = 0;          /*transmitted intensity not lost due to refl & scat etc*/
const double notloss308sig = 0;
const double notloss327sig = 0.3;
const double notloss327pi = 0.9;

int Ipumpvaluenumber = 148;
const double abscoeff= 3.35e-22;        /*in m(2)*/
```

```
const double ESAcoeff= 0.2e-22;
const double nonabsem308 = 2.35e-15;
const double em308pi = 6.72e-22;
const double esa308pi= 0e-22;
const double em327pi = 3.7e-22;
const double esa327pi = 0e-22;
const double em327sig = 6.85e-22;
const double esa327sig = 2.4e-22;
const double em308sig = 4.01e-22;
const double esa308sig =1.3e-22;
const double reprate = 10000;
const double probelength = 23.6e-9;
const double probepower = 1e8;

/*initial values*/
const double initialn4f=5.47e24;          /*number density of atoms in the n4f state*/
const double initialn5d=0;                /* number of atoms in excited n5d state*/
const double initialIpump=0;              /*initial pump intensity*/
//const double initialIloop=10;
//const double initialIlaserL=(notloss*initialIloop);
//const double initialIlaserR=(initialIloop*notloss*outputcoupler);
                                          /*initial probe intensity*/
const double initialIloop = 0;
const double initialIlaserL=0;
const double initialIlaserR=0;

/*constants for crystal*/
const double crystalwidth = 0.8e-3;
const double dlifetime= 40e-9;
const double flifetime =2e-9;
const double planck=1.05e-34;
const double frequencypump=6.518e15;
const double frequency308=6.1157e15;
const double frequency327=5.7604e15;
const double c=299.79e6;
const double solidangle = 2.25e-6;        /* solid angle containing seed in right direction*/

FILE *flprofile;


/*MAIN PART OF PROGRAM, INCLUDING ALL THE VARIOUS PARTS*/
int main(void)
{
        int j;
        int p;
        int f;
        int a;
        int b;
        int g;
        int d;
        int s;
        int q;
        int loop;

        dt=timedt();
        deltaz=c*dt;
        plancktimesfreqpump = planck*frequencypump;
        plancktimesfreq308 = planck*frequency308;
        plancktimesfreq327 = planck*frequency327;
        loop = looplength();
```

```
p = 1;
temp = 0;
        info();
initialise(loop);           /*set initial level pops. and intensity waveform shape*/
q=1;
g= Ipumpstepwidth();
a= stepnumber();
b=(g-1);
s= a/(looplength()+ (2*slicenumber));
                            /*s is the number of times program goes around loop*/
f = a/5000;                 /*ensures that only 5000 time steps are sent to file*/
openfile();
for (j=1; j<=a; ++j) {
                b++;
                if (p == f) {
                        outputn4f();
                        outputn5d();
                        outputIpump2();
                        outputlaser();
                        laserloss();

                p = 0;
        }
                update();
                /*deduce dn4f, add to n4f, replace original value with new one*/
                /*deduce dn5d, add to n5d, replace original value with new one*/
                /*deduce dI, add to I, replace original value with new one*/

        if (b == g){
                d=1;
                printf("%.1f \t", (j*100.0)/a);
                printf("%d \t %d \t %d \n ", q, j, a);
        //      printf(" %.1f \t %.1f \n", spontemission308pi, I308piR[slicenumber]);
                b=0;
        }
        else d=0;

//      shiftIpump(j);
//      shiftprobepulse(j);
        shiftIpumpprofile(d,j);         /*shift pump one step*/
        p++;

        shiftlaser (q, loop, a);        /*shift laserL one step L and laserR one step R*/
        if (q == loop)
        {
                q = 1;
        }
        else q++;
        }

        closefile();
        return 0;
}

/* OPEN INTENSITY FILE*/
        void openfile(void)
        {
                char name[]="L800pump.txt";     /* input file name */
                flprofile=fopen(name,"r");      /*file opened for reading*/
        }
```

```
/*ALLOCATION OF MEMEORY AND INITIALISATION OF n4f, n5d AND I ARRAYS*/
void initialise(int loop)
{
        int i;
        int k;                                  /*declaring integers for loops*/

        n4f=dvector(1,slicenumber);             /* setting size of n4f matrix to slicenumber*/
        n5d=dvector(1,slicenumber);             /*setting size of n5d matrix to slicenumber*/
        Ipump=dvector(1,slicenumber);           /*setting size of I matrix to slicenumber*/
        I308piL=dvector(1,slicenumber);
        I308sigL=dvector(1,slicenumber);
        I327piL=dvector(1,slicenumber);
        I327sigL=dvector(1,slicenumber);
        I308sigR=dvector(1,slicenumber);
        I308piR=dvector(1,slicenumber);
        I327piR=dvector(1,slicenumber);
        I327sigR=dvector(1,slicenumber);
        loop308pi=dvector(1,loop);              /* size of loop is 80 time crystal length*/
        loop327pi=dvector(1,loop);
        loop327sig=dvector(1,loop);
        loop308sig=dvector(1,loop);

        i=1;                                    /* setting the starting intensity to a step of initialI*/
        for (i =1; i<=slicenumber; ++i)         /* over all the crystal*/
        {               I308piL[i] = initialIlaserL;
                        I308sigL[i] = initialIlaserL;
                        I308sigR[i] = initialIlaserR;
                        I327piL[i] = initialIlaserL;
                        I327sigL[i] = initialIlaserL;
                        I308piR[i] = initialIlaserR;
                        I327piR[i] = initialIlaserR;
                        I327sigR[i] = initialIlaserR;
                        n4f[i] = initialn4f;
                        n5d[i] = initialn5d;
                        Ipump[i] = initialIpump;
        }
        k=1;
        for (k =1; k<=loop; ++k){
                loop308pi[k] = initialIloop;
                loop327sig[k] = initialIloop;
                loop327pi[k] = initialIloop;
                loop308sig[k] = initialIloop;
        }

/*      for (k =1; k<=loop; ++k)  {             /* over all loop*/

//      }

}

/*SHIFTING THE Ilaser + */
void shiftlaser(int q, int loop, int a)
{
        int k;
        int m;
        int s;
        s= a/(loop + (2*slicenumber));
                /*s is the number of times program goes around loop*/
```

```
        if (q == 1) {
                loop308pi[loop] = I308piR[1];                   /* last value is to loop*/
                loop327pi[loop] = I327piR[1] ;
                loop327sig[loop] = I327sigR[1];
                loop308sig[loop] = I308sigR[1];
        }
        else {
                loop308pi[q-1] = I308piR[1];                    /* last value is to loop*/
                loop327pi[q-1] = I327piR[1] ;
                loop308sig[q-1] = I308sigR[1];
                loop327sig[q-1] = I327sigR[1];
}
        m= 2;                                                   /*starting counting from 2*/

        for (m = 2; m<=slicenumber; ++m)            /* shifting all the values from right to left  */
        {       I308piR[m-1] = I308piR[m];
                I327piR[m-1] = I327piR[m];
                I308sigR[m-1] = I308sigR[m];
                I327sigR[m-1] = I327sigR[m];
        }
                I308piR[slicenumber] = outputcoupler308*I308piL[slicenumber];
                I327piR[slicenumber] = outputcoupler327*I327piL[slicenumber];
                I308sigR[slicenumber] = outputcoupler308*I308sigL[slicenumber];
                I327sigR[slicenumber] = outputcoupler327*I327sigL[slicenumber];

                k= (slicenumber - 1);       /*starting counting from one from end of crystal*/


                for (k = (slicenumber-1); k>=1; --k)
                                                /* shifting all the values from left to right*/
        {       I308piL[k+1] = I308piL[k];
                I327piL[k+1] = I327piL[k];
                I327sigL[k+1] = I327sigL[k];
                I308sigL[k+1] = I308sigL[k];
                }

        I308piL[1] = notloss308pi*loop308pi[q];             /* first value is from loop*/
        I327piL[1] = notloss327pi*loop327pi[q];
        I327sigL[1] = notloss327sig*loop327sig[q];
        I308sigL[1] = notloss308sig*loop308sig[q];


}

/*SHIFTING THE INTENSITY (square pulse) MATRIX ELEMENT BY +1 EVERY TIME STEP for
k steps*/
void shiftIpump(int j)
{
        int k;                                  /*declaring number so steps for which step is 1/0*/

        k= (slicenumber - 1);
                                        /*step is 1 for 1000 time steps, but end of step not defined*/
        for (k = (slicenumber-1); k>=1; --k)
                                                /* shifting all the values of the */
                Ipump[k+1] = Ipump[k];  /* Intensity from matrix element 1 to 2 etc.*/

        if (j <= inpulse())                             /*this governs pulse length of a step pulse*/
                {Ipump[1]= peakintensity;}              /*this governs the peak intensity*/
        else Ipump[1] = 0;                              /*this governs min intensity*/
```

```
}
/* CLOSE INTENSITY FILE */
        void closefile(void)
        {

        fclose(flprofile);
        }

/*SHIFTING THE INTENSITY (variable) MATRIX ELEMENT BY +1 EVERY TIME STEP for k
steps*/
void shiftIpumpprofile(int d, int j)
{
        int k;
        int x=0;
                /*declaring number so steps for which step is 1/0*/
        if (d ==1) {
        fscanf(flprofile, "%f\n", &temp);    /*read jth value into intensityinput()*/
        printf("%e \n",Ipump[1]);
        }

        k= (slicenumber - 1);                 /*step is 1 for 1000 time steps,
                                              /*but end of step not defined*/
        for (k = (slicenumber-1); k>=1; --k) /* shifting all the values of the */
                Ipump[k+1] = Ipump[k];   /* Intensity from matrix element 1 to 2 etc.*/
        if (j <= inpulse()){                  /*this governs pulse length of a step pulse*/
                Ipump[1]= temp; }             /*this governs the input intensity for jth step*/
        else Ipump[1] = 0;                    /*this governs min intensity*/
}
/*DETERMINATION OF dn4f*/
double dn4f(int i)
{
        double calcdn4f;                      /*definition of output of eqn for dn4f*/

        calcdn4f=(-1*((abscoeff*n4f[i]* pump[i])/(plancktimesfreqpump))+(n5d[i]/dlifetime)) * dt;

/*equation for change in n4f population*/
        return calcdn4f;                      /*output of eqn for dn4f for i*/
}

/*DETERMINATION OF dn5d due to tha pump*/
double dn5d(int i)
{
        double calcdn5d;                      /*definition of output of eqn for dn5d*/

        calcdn5d=(((abscoeff * n4f[i] * Ipump[i])/(plancktimesfreqpump))-(n5d[i]/dlifetime)) * dt;
                                              /*equation for change in n5d population*/
        return calcdn5d;                      /*output of eqn for dn5d for i*/
}

/*DETERMINATION OF dn4f due to the laser*/
double dn4f308pilaser(int i)
{
        double calcdn4f;                      /*definition of output of eqn for dn4f*/

        calcdn4f = ((em308pi*n5d[i] * (I308piR[i] + I308piL[i]) )/(plancktimesfreq308))*dt;
                                              /*equation for change in n4f population*/
        return calcdn4f;                      /*output of eqn for dn4f for i*/
}

/*DETERMINATION OF dn5d due to the laser*/
```

```
double dn5d308pilaser(int i)
{
        double calcdn5d;                    /*definition of output of eqn for dn4f*/

        calcdn5d = (-(em308pi*n5d[i]* (I308piR[i] + I308piL[i]) )/(plancktimesfreq308))*dt;
                                            /*equation for change in n4f population*/
        return calcdn5d;                    /*output of eqn for dn4f for i*/
}

/*DETERMINATION OF dn4f due to the laser*/
double dn4f308siglaser(int i)
{
        double calcdn4f;                    /*definition of output of eqn for dn4f*/

        calcdn4f = ((em308sig*n5d[i]*(I308sigR[i]+I308sigL[i]) )/(plancktimesfreq308))*dt;
                                            /*equation for change in n4f population*/
        return calcdn4f;                    /*output of eqn for dn4f for i*/
}

/*DETERMINATION OF dn5d due to the laser*/
double dn5d308siglaser(int i)
{
        double calcdn5d;                    /*definition of output of eqn for dn4f*/

        calcdn5d=(-em308sig*n5d[i]*(I308sigR[i]+I308sigL[i]) /(plancktimesfreq308))*dt;
                                            /*equation for change in n4f population*/
        return calcdn5d;                    /*output of eqn for dn4f for i*/
}

/*DETERMINATION OF dn4f due to the laser*/
double dn4f327pilaser(int i)
{
        double calcdn4f;                    /*definition of output of eqn for dn4f*/

        calcdn4f = ((em327pi* n5d[i] * (I327piR[i] + I327piL[i]) )/(plancktimesfreq327))*dt;
                                            /*equation for change in n4f population*/
        return calcdn4f;                    /*output of eqn for dn4f for i*/
}

/*DETERMINATION OF dn5d due to the laser*/
double dn5d327pilaser(int i)
{
        double calcdn5d;                    /*definition of output of eqn for dn4f*/

        calcdn5d = (-(em327pi*n5d[i] * (I327piR[i] + I327piL[i]))/(plancktimesfreq327))*dt;
                                            /*equation for change in n4f population*/
        return calcdn5d;                    /*output of eqn for dn4f for i*/
}
/*DETERMINATION OF dn4f due to the laser*/
double dn4f327siglaser(int i)
{
        double calcdn4f;                    /*definition of output of eqn for dn4f*/

        calcdn4f =((em327sig*n5d[i]*(I327sigR[i] + I327sigL[i]))/(plancktimesfreq327))*dt;
                                            /*equation for change in n4f population*/
        return calcdn4f;                    /*output of eqn for dn4f for i*/
}

/*DETERMINATION OF dn5d due to the laser*/
double dn5d327siglaser(int i)
```

```
{
        double calcdn5d;                    /*definition of output of eqn for dn4f*/

        calcdn5d=(-(em327sig*n5d[i]*(I327sigR[i]+ I327sigL[i]))/(plancktimesfreq327))*dt;
                                            /*equation for change in n4f population*/
        return calcdn5d;                    /*output of eqn for dn4f for i*/
}

/*DETERMINATION OF dI - FIRST APPROXIMATION*/
double dIpump(int i)
{
        double calcdIpump;                                  /*definition of output of eqn for dI*/

        calcdIpump = -1 *( abscoeff * n4f[i] * Ipump[i] * deltaz);
                                            /*equation for change in I with z*/
        return calcdIpump;                  /*output of eqn for dI for i*/
}

/*DETERMINATION OF dI - SECOND APPROXIMATION (WITH ESA)*/
double dIpump2(int i)
{
        double calcdIpump2;                 /*definition of output of eqn for dI*/

        calcdIpump2 = -((abscoeff * n4f[i])+(ESAcoeff * n5d[i])) * Ipump[i] *deltaz;
                                            /*equation for change in I with z*/
        return calcdIpump2;                 /*output of eqn for dI for i*/
}

/*DETERMINATION OF Ilaser 308*/
double dI308pioutL(int i)
{
        double calcIlaserout;
        calcIlaserout=(em308pi - esa308pi) * n5d[i] * I308piL[i] * deltaz;
                                            /*equation for change in I with z*/
        return calcIlaserout;               /*output of eqn for dI for i*/
}


double dI308sigoutL(int i)
{
        double calcIlaserout;
        calcIlaserout=(em308sig - esa308sig) * n5d[i] * I308sigL[i] * deltaz;
                                            /*equation for change in I with z*/
        return calcIlaserout;               /*output of eqn for dI for i*/
}

/*DETERMINATION OF Ilaser 327*/
double dI327sigoutL(int i)
{
        double calcIlaserout;
        calcIlaserout=(em327sig - esa327sig) * n5d[i] * I327sigL[i] * deltaz;
                                            /*equation for change in I with z*/
        return calcIlaserout;               /*output of eqn for dI for i*/
}

/*DETERMINATION OF Ilaser 327*/
double dI327pioutL(int i)
{
        double calcIlaserout;
        calcIlaserout=(em327pi - esa327pi) * n5d[i] * I327piL[i] * deltaz;
```

```
                                        /*equation for change in I with z*/
        return calcIlaserout;           /*output of eqn for dI for i*/
}

/*DETERMINATION OF Ilaser 308*/
double dI308pioutR(int i)
{
        double calcIlaserout;
        calcIlaserout=(em308pi - esa308pi) * n5d[i] * I308piR[i] * deltaz;
                                        /*equation for change in I with z*/
        return calcIlaserout;           /*output of eqn for dI for i*/
}

double dI308sigoutR(int i)
{
        double calcIlaserout;
        calcIlaserout=(em308sig - esa308sig) * n5d[i] * I308sigR[i] * deltaz;
                                        /*equation for change in I with z*/
        return calcIlaserout;           /*output of eqn for dI for i*/
}

/*DETERMINATION OF Ilaser 327*/
double dI327sigoutR(int i)
{
        double calcIlaserout;
        calcIlaserout=(em327sig - esa327sig) * n5d[i] * I327sigR[i] * deltaz;
                                        /*equation for change in I with z*/
        return calcIlaserout;           /*output of eqn for dI for i*/
}

/*DETERMINATION OF Ilaser 327*/
double dI327pioutR(int i)
{
        double calcIlaserout;
        calcIlaserout=(em327pi - esa327pi) * n5d[i] * I327piR[i] * deltaz;
                                        /*equation for change in I with z*/
        return calcIlaserout;           /*output of eqn for dI for i*/
}

/* determination of spontaneous emission*/
double spontemission308pi(int i)
{
        double calcse;
        calcse = n5d[i] * (1/dlifetime) * solidangle * plancktimesfreq308 * deltaz;
        return calcse;
}

/* determination of spontaneous emission*/
double spontemission308sig(int i)
{
        double calcse;
        calcse = n5d[i]* (1/dlifetime)* solidangle*plancktimesfreq308*deltaz;
        return calcse;
}

/* determination of spontaneous emission*/
double spontemission327sig(int i)
{
        double calcse;
        calcse = n5d[i]* (1/dlifetime)* solidangle*plancktimesfreq327*deltaz;
```

```
        return calcse;
}

/* determination of spontaneous emission*/
double spontemission327pi(int i)
{
        double calcse;
        calcse = n5d[i]* (1/dlifetime)* solidangle*plancktimesfreq327*deltaz;
        return calcse;
}

/* ADDITION OF DELTA n4f, n5d AND I, UPDATING MATRIX ELEMENT*/
double update()
{
        int i;
        double a, b, c, x,y, A, B, C, D, M, N, O, P, Q, R;
        double aa, bb, cc, dd,ee, ff, mm, hh;
        i=1;
        for (i = 1; i<=slicenumber; ++i) {
                a = dn4f(i);
                b = dn5d(i);

                c = dIpump2(i);
                x = dI308pioutL(i);
                y = dI308pioutR(i);
                A = dI327pioutL(i);
                B = dI327sigoutL(i);
                C = dI327pioutR(i);
                D = dI327sigoutR(i);
                Q = dI308sigoutL(i);
                R = dI308sigoutR(i);
                M = spontemission308pi(i);
                N = spontemission308sig(i);
                O = spontemission327sig(i);
                P = spontemission327pi(i);
                aa = dn4f308pilaser(i);
                bb = dn5d308pilaser(i);

                mm = dn4f308siglaser(i);
                hh = dn5d308siglaser(i);

                cc = dn4f327pilaser(i);
                ee = dn5d327pilaser(i);

                dd = dn4f327siglaser(i);
                ff = dn5d327siglaser(i);


                n4f[i] = n4f[i] + a;            /*addition n4f+dn4f and update matrix point*/
                n5d[i] = n5d[i] + b;            /* Addition n5d+dn5d, replace matrix element*/
                n4f[i] = n4f[i] + aa + dd + cc + mm;
                                                /*addition n4f+dn4f and update matrix point*/
                n5d[i] = n5d[i] + bb + ff + ee + hh;
                                                /* Addition n5d+dn5d, replace matrix element*/
//              n5d[i] = 1 - n4f[i];
                Ipump[i] = Ipump[i] + c;
                                                /* Addition nI+dI, replace matrix element*/
                I308piL[i] = I308piL[i] + x + M;    /* new I laser has gain factor included*/
                I308piR[i] = I308piR[i] + y + M;
                I308sigL[i] = I308sigL[i] + Q + N; /* new I laser has gain factor included*/
```

```
                I308sigR[i] = I308sigR[i] + R + N;
                I327piL[i] = I327piL[i] + A + P;
                I327piR[i] = I327piR[i] + C + P;
                I327sigL[i] = I327sigL[i] + B + O;
                I327sigR[i] = I327sigR[i] + D + O;
                        /* Addition of probe dI and replace matrix element*/
                }
                return 0;
}

/*OUTPUT ALL OF INTENSITIES*/
void outputIpump2(void)
{
        FILE *fIpump2;                  /*fn4f is file reference*/
        char name[]="Ipump2";           /*filename will eventually be the name outputed*/
                strcat(name, prefix);
                fIpump2=fopen(name,"a");
                int i;
                i=1;
                for(i=1; i<=slicenumber; i=i+(slicenumber/10))
                        fprintf(fIpump2, "%f\t", Ipump[i]); /*print to file*/
                fprintf(fIpump2, "\n");
                                        /*if i=slicenumber finish writing out result*/
                                        /*with a new line*/
        fclose(fIpump2);
}

/* OUTPUT OF n4f[i] VALUES TO FILE*/
void outputn4f(void)
{
        FILE *fn4f;                     /*fn4f is file reference*/
        char name[]="n4f";              /*filename will eventually be the name outputed*/
                strcat(name, prefix);
                fn4f=fopen(name,"a");
                int i;
                i=1;
                for(i=1; i<=slicenumber; i=i+(slicenumber/10))
                                        /* for all values of i to slicenumber*/
                fprintf(fn4f, "%f\t", n4f[i]);          /*print to file*/
                                        /*if i=slicenumber finish writing out result*/
                fprintf(fn4f, "\n");    /*with a new line*/
        fclose(fn4f);
}
/* OUTPUT OF n5d[i] VALUES TO FILE*/
void outputn5d(void)
{
        FILE *fn5d;                     /*fn4fis file reference*/

        char name[]="n5d";              /*filename will eventually be the name outputed*/
                strcat(name, prefix);
                fn5d=fopen(name,"a");
                int i;
                i=1;
                for(i=1; i<slicenumber; i=i+(slicenumber/10))
                                                /* for all values of i to slicenumber*/
                        fprintf(fn5d, "%f\t", n5d[i]);          /*print to file*/
                        fprintf(fn5d, "\n");

        /*if i=slicenumber finish writing out result*/
        /* with a new line*/
```

```
                fclose(fn5d);
}

/* OUTPUT OF n5d[i] VALUES TO FILE*/
void outputI308piL(void)
{
        FILE *fI308piL;                 /*fn4fis file reference*/

        char name[]="I308piL";          /*filename will eventually be the name outputed*/
                strcat(name, prefix);
                fI308piL=fopen(name,"a");
                                        I308piL[slicenumber]=(1-
outputcoupler308)*I308piL[slicenumber];
                /*output coupler reducing output*/
                        fprintf(fI308piL, "%f\t", I308piL[slicenumber]);        /*print to file*/
                        fprintf(fI308piL, "\n");
                                                /*if i=slicenumber finish writing out result*/
                                                /* with a new line*/
                fclose(fI308piL);
}

/* OUTPUT OF n5d[i] VALUES TO FILE*/
void outputI327piL(void)
{
        FILE *fI327piL;                         /*fn4fis file reference*/

        char name[]="I327piL";                  /*filename will eventually be the name
outputed*/
                strcat(name, prefix);
                fI327piL=fopen(name,"a");
                I327piL[slicenumber]=(1-outputcoupler327)*I327piL[slicenumber];
                        fprintf(fI327piL, "%f\t", I327piL[slicenumber]);        /*print to file*/
                        fprintf(fI327piL, "\n");
                                                /*if i=slicenumber finish writing out result*/
                                                /* with a new line*/
                fclose(fI327piL);
}

/* OUTPUT OF n5d[i] VALUES TO FILE*/
void outputI327sigL(void)
{
        FILE *fI327sigL;                /*fn4fis file reference*/

        char name[]="I327sigL";         /*filename will eventually be the name outputed*/
                strcat(name, prefix);
                fI327sigL=fopen(name,"a");
                        I327sigL[slicenumber]=(1-outputcoupler327)*I327sigL[slicenumber];
                        fprintf(fI327sigL, "%f\t", I327sigL[slicenumber]);
                                                /*print to file*/
                        fprintf(fI327sigL, "\n");
                                                /*if i=slicenumber finish writing out result*/
                                                /* with a new line*/
                fclose(fI327sigL);
}

void outputlaser(void)
{
        FILE *fIlaser;                  /*fn4fis file reference*/
```

```
        char name[]="Ilaser";                   /*filename will eventually be the name outputed*/
        strcat(name, prefix);
                fIlaser=fopen(name,"a");

                I308piLoutput=(1-outputcoupler308)*I308piL[slicenumber];
                I327piLoutput=(1-outputcoupler327)*I327piL[slicenumber];
                I327sigLoutput=(1-outputcoupler327)*I327sigL[slicenumber];
                I308sigLoutput=(1-outputcoupler308)*I308sigL[slicenumber];
                                                        /*output coupler reducing output*/
                fprintf(fIlaser, "%f\t", I308piLoutput);
                fprintf(fIlaser, "%f\t", I327piLoutput);
                fprintf(fIlaser, "%f\t", I308sigLoutput);
                fprintf(fIlaser, "%f\t", I327sigLoutput);
                                /*print to file*/

                        fprintf(fIlaser, "\n");
                                                /*if i=slicenumber finish writing out result*/
                                                /* with a new line*/
                fclose(fIlaser);
}

void laserloss(void)
{
        FILE *fIloss;                           /*fn4fis file reference*/

        char name[]="Iloss";                    /*filename will eventually be the name outputed*/
                strcat(name, prefix);
                fIloss=fopen(name,"a");

                I308piLloss=(1-notloss308pi)*I308piL[1]/notloss308pi;       /*energy loss*/
                I327piLloss=(1-notloss327pi)*I327piL[1]/notloss327pi;
                I308sigLloss=(1-notloss308sig)*I327sigL[1]/notloss308sig;
                I327sigLloss=(1-notloss327sig)*I308sigL[1]/notloss327sig;

                fprintf(fIloss, "%f\t", I308piLloss);
                fprintf(fIloss, "%f\t", I327piLloss);
                fprintf(fIloss, "%f\t", I308sigLloss);
                fprintf(fIloss, "%f\t", I327sigLloss);

                fprintf(fIloss, "\n");
                                                /*if i=slicenumber finish writing out result*/
                                                /* with a new line*/
                fclose(fIloss);
}

/* OUTPUT OF n5d[i] VALUES TO FILE*/
void outputI308piR(void)
{
        FILE *fI308piR;                         /*fn4fis file reference*/

        char name[]="I308piR";                  /*filename will eventually be the name outputed*/
                strcat(name, prefix);
                fI308piR=fopen(name,"a");

                        fprintf(fI308piR, "%f\t", I308piR[slicenumber]);    /*print to file*/
                        fprintf(fI308piR, "\n");
                                                /*if i=slicenumber finish writing out result*/
                                                /* with a new line*/
                fclose(fI308piR);
}
```

```
/* OUTPUT OF n5d[i] VALUES TO FILE*/
void outputI327piR(void)
{
        FILE *fI327piR;                 /*fn4fis file reference*/

        char name[]="I327piR";          /*filename will eventually be the name outputed*/
                strcat(name, prefix);
                fI327piR=fopen(name,"a");
                int i;
                i=1;
                for(i=1; i<slicenumber; i=i+(slicenumber/10))
                                                /* for all values of i to slicenumber*/

                        I327piR[i] = (1-outputcoupler327)*I327piR[i]         ;
                /*output coupler reducing output*/
                        fprintf(fI327piR, "%f\t", I327piR[i]);              /*print to file*/
                        fprintf(fI327piR, "\n");
                                                /*if i=slicenumber finish writing out result*/
                                                /* with a new line*/
                fclose(fI327piR);
}

/* OUTPUT OF n5d[i] VALUES TO FILE*/
void outputI327sigR(void)
{
        FILE *fI327sigR;                                /*fn4fis file reference*/

        char name[]="I327sigR";  /*filename will eventually be the name outputed*/
                strcat(name, prefix);
                fI327sigR=fopen(name,"a");
                int i;
                i=1;
                for(i=1; i<slicenumber; i=i+(slicenumber/10))
                                        /* for all values of i to slicenumber*/
                        I327sigR[i] = (1-outputcoupler327)*I327sigR[i]       ;
                                        /*output coupler reducing output*/

                                        /*if i=slicenumber finish writing out result*/
                                        /* with a new line*/
                fclose(fI327sigR);
}

/*SETUP PRINTED TO FILE INFO*/
void info(void)
{
        FILE *finfo;                    /*fn4fis file reference*/
        char name[]="INFO";
        strcat(name, prefix);
                                        /*filename will eventually be the name outputed*/

                finfo=fopen(name,"a");

                fprintf(finfo, "n4f = \t %e \n", initialn4f );
                fprintf(finfo,"n5d= \t %e \n" ,initialn5d );
                fprintf(finfo,"crystal = \t %e m \n",crystalwidth );
                fprintf(finfo,"5dlifetime = \t %e s \n",dlifetime );
                fprintf(finfo,"dur= \t %e  s \n",duration );
                fprintf(finfo,"pulse =\t %e s \n \n",pulselength  );
                fprintf(finfo,"spot size =\t %e s \n \n",spotsize );
```

```
                fprintf(finfo,"absx = \t %e m2 \n",abscoeff );
                fprintf(finfo,"esax = \t %e m2 \n",ESAcoeff );
                fprintf(finfo,"pump power =\t  %e mW\n",pumppower );
                fprintf(finfo,"deltat = \t %e \n",dt );
                fprintf(finfo,"stepnumber= \t %e \n \n",stepnumber());
                fprintf(finfo,"slices = \t %d \n", slicenumber) ;
                fprintf(finfo,"308piem = \t %e m2 \n",em308pi );
                fprintf(finfo,"308piesa = \t %e m2 \n",esa308pi );
                fprintf(finfo,"327piem = \t %e m2 \n",em327pi );
                fprintf(finfo,"327piesa = \t %e m2 \n",esa327pi );
                fprintf(finfo,"327sigem = \t %e m2 \n",em327sig );
                fprintf(finfo,"327sigesa = \t %e m2\n",esa327sig );
                fprintf(finfo,"outputcoupler 327nm= \t %e %\n",outputcoupler327);
                fprintf(finfo,"outputcoupler 308nm= \t %e %\n",outputcoupler308);
                fprintf(finfo,"losses due to cavity for 308 pi= \t %e %\n",notloss308pi);
                fprintf(finfo,"losses due to cavity for 308 sig= \t %e %\n",notloss308sig);
                fprintf(finfo,"losses due to cavity for 327 pi= \t %e %\n",notloss327pi);
                fprintf(finfo,"losses due to cavity for 327 sig= \t %e %\n",notloss327sig);
                fclose(finfo);

}


/* DETERMINATION OF TIME STEP dt*/
double timedt(void)
{
        double dz;
        double calcdt;
        dz = crystalwidth/slicenumber;                  /*work out dz*/
//      printf("%e \n",dz);
        calcdt = dz/c;                                  /* from dz work out the corresponding dt*/

        return calcdt;
}

/* DETERMINATION OF NUMBER OF TIME STEPS */
int stepnumber(void)
{

        double calcstepnumber;
        calcstepnumber = duration/dt;                   /* number of steps =duration of exp/dt*/
//      printf("%e \n %e \n ",calcstepnumber,dt);       /*print out number of steps and dt*/

        return calcstepnumber;
}

/*DETERMINATION OF inpulse IN TERMS OF TIME STEPS*/
int inpulse(void)
{
        int calcpulsestep;
                calcpulsestep = pulselength/dt;         /*work out the number of steps for which */

                                                        /*the intensity is high from the pulselength*/
                return calcpulsestep;
}

/* DETERMINATION OF INTENSITY STEPWIDTH*/
int Ipumpstepwidth()
{
        double calcstepwidth;
```

```
        calcstepwidth = inpulse()/Ipumpvaluenumber;
                return calcstepwidth;
}

/* DETERMINATION OF no of steps in loop*/
int looplength()
{
        double calclength;
        calclength = (slicenumber/crystalwidth)*cavitylength ;
                return calclength;
}
```